

## IMMUNE PHENOTYPES OF ALS & AOA2

IMMUNOLOGICAL PHENOTYPES ASSOCIATED WITH NEURODEGENERATIVE  
DISEASE

By  
JONATHAN MAPLETOFT, B.Sc, M.Sc.

*A Thesis  
Submitted to the School of Graduate Studies  
in Partial Fulfilment of the Requirements  
for the Degree  
Doctor of Philosophy*

DOCTOR OF PHILOSOPHY (2020)  
(Biochemistry & Biomedical Sciences)

McMaster University  
Hamilton, Ontario

Title: Immunological Phenotypes Associated with Neurodegenerative Disease

Author: Jonathan Mapletoft, B.Sc. *Hons*, M.Sc. (Laurentian University)

Supervisor: Dr. Matthew Miller

Number of pages: xx, 236

## Lay Abstract

The causes of most neurodegenerative diseases remain poorly understood. These diseases are highly complex, as they are influenced by both genetics and the environment and involve many different cell types. However, neurodegenerative diseases also share common hallmarks. The immune system is known to behave abnormally in several neurodegenerative diseases. Therefore, we set out to study the involvement of the immune system in two related neurodegenerative diseases, ataxia with oculomotor apraxia type 2 (AOA2) and amyotrophic lateral sclerosis (ALS). We demonstrate that AOA2-like mutations in *senataxin* (*SETX*) affect the formation of specific antibodies due to problems repairing broken DNA. We also find that viral infections activate immune cells within the spinal cord which can promote ALS progression. Taken together, this body of work suggests that the immune system plays an important role in AOA2 and ALS, and that drugs that prevent abnormal immune responses might help to treat these diseases.

## Abstract

The etiology of most neurodegenerative diseases remains a mystery. Environmental factors seemingly play an important role in neurodegenerative diseases, as does the immune system. Here, we describe immunological phenotypes associated with the neurodegenerative diseases AOA2 and ALS.

During CSR, B-cells and neurons share a preferred pathway for DNA repair, NHEJ. SETX, the gene implicated in AOA2, has been implicated in the DDR. In SETX-deficient conditions, B-cells exhibit a defect in IgA class-switching as a result of impaired NHEJ and enhanced alternate-end joining, a slower process with higher mutational burden. These results suggest that neurons in SETX-deficient patients may also demonstrate defects in DNA repair, leaving them more susceptible to death. Further, IgA plays an important role in both protection from infections and as an anti-inflammatory mediator at mucosal surfaces. Defects in IgA class switching might lead to immune dysregulation in AOA2, similar to that observed in other neurodegenerative diseases.

Viral infections have been associated with several neurodegenerative diseases, including ALS. However, a causal role for viruses in the etiology of ALS has never been established. Common viral infections can impact immune cell phenotypes within the CNS. Microglia are the primary immune cell of the CNS and are able to respond to subtle changes in the microenvironment. Microglia have neurotoxic properties upon hyper-activation. Influenza infection of SOD1<sup>G93A</sup> mice accelerated ALS disease progression and reduced overall survival. Exacerbated microgliosis was evident within the spinal cords of infected

mice. Thus, the immune response stimulated by viral infections may result in toxic microgliosis that accelerates the progression of ALS.

Together, this body of work describes a series of novel immunological abnormalities associated with AOA2 and ALS4. A deeper understanding of the role played by the immune system in patients with neurodegenerative disorders may unveil new targets for future therapies.

## Acknowledgements

First and foremost, I would like to thank Dr. Matthew Miller for all his support and guidance throughout my graduate studies at McMaster University. Thank you, Dr. Miller, for constantly challenging me to strive for greatness and thank you for trusting me as your first Ph.D. student. You have always made the lab an enjoyable place to be with your humour and \*gentle\* roasting throughout the years. I have thoroughly enjoyed my studies in the Miller laboratory and I would not have achieved what I have without your tutelage. I would also like to thank my supervisory committee, Dr. Karen Mossman and Dr. John Turnbull, for providing useful insight and support throughout my studies.

Without the help of the Miller lab team I would not be the researcher I am today. For that I would like to thank all members of the Miller lab, both past and present, for their support throughout the years. Watching the lab build to where it is today has been one of the highlights of my time at McMaster University and I will not soon forget any member of the Miller lab. Jann, the lab would fall apart without you and you have been so fantastic during my time here, never change. Peter, thank you for your brilliance in all areas of computing and data analysis. Julia, thank you for all the “q’s” and I am happy that you turned out to be so great a researcher, despite my involvement. Braeden, thank you for being a brother in arms and helping to get the SOD1 model up and running. Art, I am leaving the SOD1 project in great hands and I wish you all the luck. Hannah, it has been a joy working with you and I am lucky that I was assigned to be your TA all those years ago. Ali, I will miss you and your constant positive attitude! Mike, although you are the new guy you have already fit in with the lab so perfectly and I wish you every success in the

future. To everyone there is not space to mention thank you for everything you've done for me, my Ph.D. experience has been made greater by all of you.

No acknowledgements would be complete without thanking the people behind the scenes. I would like to thank my family for always being supportive and believing in me even though they have no idea what I am talking about when it comes to work. Finally, for my wife, Charlotte, thank you so much for all that you are. My Ph.D. would have been insurmountable without you and your support over the years. Thank you for listening to my complaints, to offering helpful criticisms, and being my lay audience for abstract writing, your presence is felt throughout this body of work. Thank you from the bottom of my heart.

## Table of Contents

<b>Title Page</b> .....	<b>i</b>
<b>Descriptive Note</b> .....	<b>ii</b>
<b>Lay Abstract</b> .....	<b>iii</b>
<b>Abstract</b> .....	<b>iv</b>
<b>Acknowledgements</b> .....	<b>vi</b>
<b>Table of Contents</b> .....	<b>viii</b>
<b>List of Figures and Tables</b> .....	<b>xii</b>
<b>List of Abbreviations and Symbols</b> .....	<b>xiv</b>
<b>Declaration of Academic Achievement</b> .....	<b>xix</b>
<b>CHAPTER 1: General Introduction</b> .....	<b>1</b>
1.1 Autosomal Recessive Cerebellar Ataxia.....	2
1.2 B Cell Biology and the Germinal Center .....	3
1.2.1 Class Switch Recombination .....	6
1.2.2 Somatic Hypermutation .....	10
1.3 The DNA Damage Response and CSR.....	13
1.4 Non-Homologous End Joining.....	13
1.5 Alternate End Joining.....	15
1.6 Amyotrophic Lateral Sclerosis.....	16
1.7 The Innate Immune System of the CNS .....	17
1.7.1 The Blood Brain Barrier .....	18
1.7.2 Glial Cells .....	19
1.7.2.1 Astrocytes.....	19
1.7.2.2 Microglia.....	20
1.8 Hypothesis.....	22
<b>CHAPTER 2: Materials and Methods</b> .....	<b>23</b>

**CHAPTER 3: Elucidating the Role of Senataxin on Class Switch Recombination ..... 42**

3.1 Introduction.....	43
3.1.1 Senataxin.....	43
3.1.2 RNA:DNA hybrids .....	44
3.1.3 RNA Helicases and CSR.....	48
3.1.4 DNA Damage Factors and CSR.....	49
3.1.5 Alternate End Joining during CSR.....	52
3.1.6 Hypothesis.....	53
3.2 Results.....	54
3.2.1 SETX deficiency alters the magnitude and kinetics of class switch recombination <i>ex-vivo</i> .....	54
3.2.2 SETX deficiency alters the rate of B cell proliferation.....	54
3.2.3 SETX deficiency alters the kinetics of IgA production during a primary immune response.....	56
3.2.4 SETX deficiency has little effect on IgA titers during secondary immune responses following homologous vaccination .....	58
3.2.5 SETX deficiency reduces the diversity of the IgA repertoire post-vaccination .....	60
3.2.6 SETX deficiency alters the distribution of R-loops within the IgH locus .....	62
3.2.7 SETX deficiency alters the kinetics of the DNA damage response.....	64
3.2.8 SETX deficiency results in a preference for the alternate end-joining DNA repair pathway .....	68
3.3 Discussion .....	70
3.3.1 The Role of SETX on CSR is IgA Specific.....	70
3.3.2 SETX Deficiency alters CSR but Does Not Globally Alter SHM.....	72
3.3.3 SETX Impacts CSR in a B-cell Intrinsic Manner.....	74
3.3.3.1 SETX Deficiency Alters R-loop Accumulation Within the IgH Locus.....	74
3.3.3.2 DNA Damage Response Kinetics are Altered in SETX Deficient Cells... ..	74
3.3.4 SETX Deficiency Induces Similar Deficits to those in DNA Repair Deficient B cells .....	77
3.3.5 SETX Deficiency Promotes a-EJ Repair of DNA During CSR .....	79
3.3.6 Limitations .....	81
3.3.7 Concluding Remarks.....	81

**CHAPTER 4: A Role for Viral Infection on the Onset and Progression of Amyotrophic Lateral Sclerosis ..... 84**

4.1 Introduction.....	85
4.1.1 Genetics of ALS.....	85
4.1.2 Possible Etiology of ALS.....	86
4.1.2.1 Toxic Protein Aggregation and Spreading.....	87
4.1.2.2 Glutamate Excitotoxicity .....	88
4.1.2.3 Mitochondrial Abnormalities.....	89

4.1.2.4	Oxidative and Endoplasmic Reticulum Stress .....	90
4.1.2.5	Neuroinflammation .....	91
4.1.3	CNS Response to Peripheral Inflammation .....	93
4.1.4	The Role of Astrocytes in Neurodegenerative Disease .....	95
4.1.5	The Role of Microglia in Neurodegenerative Disease .....	98
4.1.6	Neurodegeneration, TLR Signaling, and Microgliosis .....	100
4.1.7	Environmental Triggers of ALS .....	101
4.1.8	Implications for Environmental Factors as Triggers of ALS.....	107
4.1.9	Hypothesis.....	110
4.2	Results .....	111
4.2.1	IAV infection accelerates ALS progression.....	111
4.2.2	IAV infection does not cause more severe morbidity in the SOD1 <sup>G93A</sup> ALS mouse model .....	113
4.2.3	Effect of IAV infection on ALS progression does not require viral replication .....	116
4.2.4	Cytokine profiles of SOD1 <sup>G93A</sup> mice are similar to WT <i>in vitro</i> and <i>in vivo</i> ..	118
4.2.5	Microgliosis levels are elevated in SOD1 <sup>G93A</sup> mice at later disease stages following IAV infection.....	122
4.2.6	Misfolded SOD1 levels are unaltered in the spinal cords of previously-infected SOD1 <sup>G93A</sup> mice at day 60 post-infection .....	125
4.3	Discussion .....	127
4.3.1	IAV Infection Accelerates ALS Progression Independent of Infection Severity .....	127
4.3.2	The Effects of IAV Infection on the SOD1 <sup>G93A</sup> Model is not Virus Specific.	128
4.3.3	The Immune Response to Infection is Sufficient to Induce ALS Acceleration .....	129
4.3.4	Cytokine Responses Induced by IAV Infection are not Globally Altered in SOD1 <sup>G93A</sup> Mice.....	130
4.3.5	Peripheral Infection and Inflammation Induces Gliosis in the CNS.....	132
4.3.6	Protein Misfolding and Microglial Priming.....	134
4.3.7	Limitations .....	136
4.3.8	Concluding Remarks.....	136
4.4	Appendix .....	139
4.4.1	HSV-1 infection is more severe in SOD1 <sup>G93A</sup> mice.....	139
<b>CHAPTER 5: General Discussion.....</b>		<b>143</b>
5.1	IgA Deficiency and Neurodegeneration .....	144
5.2	Implications of SETX Deficiency on the DDR in Neurodegeneration.....	145
5.3	CNS Immunity and Glial Cell Activation.....	147
5.4	Microglial Priming in Neurodegenerative Disorders.....	149
5.5	The Mechanism of Motor Neuron Death Remains a Mystery in ALS .....	152
5.6	Peripheral Immune Cell Involvement in the Pathogenesis of ALS .....	154

5.7 Concluding Remarks.....	156
<b>Bibliography .....</b>	<b>159</b>

## List of Figures and Tables

### Chapter 1

Figure 1.1.1: A diagrammatical representation of class switch recombination .....	7
-----------------------------------------------------------------------------------	---

### Chapter 2

Table 2.1: Primer information for antiviral gene expression .....	41
-------------------------------------------------------------------	----

### Chapter 3

Figure 3.1.1: The structure of an R-loop.....	46
Figure 3.1: SETX deficiency alters the magnitude and kinetics of class-switch recombination <i>ex vivo</i> .....	55
Figure 3.2: SETX deficiency alters the rate of B-cell proliferation.....	57
Figure 3.3: SETX deficiency alters the kinetics of a primary immune response.....	59
Figure 3.4: SETX deficiency alters the diversity within the IgA repertoire .....	61
Figure 3.5: SETX deficiency alters the localization and magnitude of R-loops within the IgH locus .....	63
Figure 3.6: SETX alters the induction of p-ATM foci following DNA damage .....	66
Figure 3.7: $\gamma$ -H2AX foci formation is unaltered in SETX deficient conditions.....	67
Figure 3.8: SETX deficiency alters the microhomology usage in switch region repair .....	69
Figure 3.3.1: A model for the role of SETX on IgA class switching.....	83

### Chapter 4

Figure 4.1.1: Inflammation is mediated by glial cells within the CNS during neurodegenerative disorders .....	92
Figure 4.1.2: Pathophysiological pathways associated with ALS are perturbed during viral infection .....	106
Figure 4.1: Sublethal Influenza A infection accelerates ALS disease progression and reduces overall survival in the SOD1 <sup>G93A</sup> ALS model .....	112
Figure 4.2: Lethal Influenza A infection accelerates ALS disease progression and reduces overall survival in the SOD1 <sup>G93A</sup> ALS model .....	114
Figure 4.3: SOD1 <sup>G93A</sup> expressing mice exhibit similar morbidity to wildtype mice during an influenza A infection .....	115
Figure 4.4: Administration of inactivated influenza A results in an intermediate effect on ALS progression in the SOD1 <sup>G93A</sup> ALS model .....	117
Figure 4.5: <i>In vitro</i> inflammatory and antiviral response to inactivated influenza A virus in WT and SOD1 <sup>G93A</sup> expressing conditions .....	120
Figure 4.6: <i>In-vivo</i> inflammatory response to influenza A virus infection in WT and SOD1 <sup>G93A</sup> mice .....	121

Figure 4.7: Influenza A infection of SOD1 <sup>G93A</sup> mice induces elevated levels of microgliosis.....	123
Figure 4.8: Influenza A infection of SOD1 <sup>G93A</sup> mice induces a slight elevation in astrogliosis .....	124
Figure 4.9: Influenza A infection of SOD1 <sup>G93A</sup> mice does not affect misfolded SOD1 accumulation.....	126
Figure 4.3.1: A model for viral infection as an environmental trigger of ALS .....	138
Figure 4.10: SOD1 <sup>G93A</sup> expressing mice exhibit enhanced morbidity to a HSV-1 infection .....	141
Figure 4.11: HSV-1 infection accelerates ALS disease progression in the SOD1 <sup>G93A</sup> ALS model.....	142

## List of Abbreviations and Symbols (In alphabetical order)

<b><math>\alpha</math></b>	Alpha
<b><math>\beta</math></b>	Beta
<b><math>\gamma</math></b>	Gamma
<b><math>\mu</math></b>	Micro
<b>%</b>	Percentage
<b>×g</b>	Times the force of gravity
<b>°C</b>	Celsius
<b>bp</b>	Base pair
<b>g</b>	Grams
<b>h</b>	hours
<b><i>i.m.</i></b>	Intra Muscular
<b><i>i.n.</i></b>	Intra Nasal
<b>L</b>	Litre
<b>LD<sub>50</sub></b>	Lethal Dose - 50
<b>m</b>	Milli
<b>M</b>	Molar
<b>min</b>	Minutes
<b>n</b>	Nano
<b>nt</b>	Nucleotide
<b>PFA</b>	Para-formaldehyde
<b>PFU</b>	Plaque Forming Units
<b>PR8</b>	A/Puerto Rico/8/1934
<b>qRT-PCR</b>	Quantitative reverse transcription polymerase chain reaction
<b>rpm</b>	Revolutions per minute
<b>RT</b>	Room Temperature
<b>s (sec)</b>	Seconds
<b>S.D.</b>	Standard Deviation
<b>SEM</b>	Standard Error of the Mean
<b><math>\alpha 7nAChR</math></b>	Nicotinic acetylcholine receptor subunit $\alpha$ -7
<b>a-EJ</b>	Alternate End Joining
<b>A-T</b>	Ataxia-Telangiectasia
<b>AD</b>	Alzheimer's Disease
<b>AID</b>	Activation-Induced cytidine Deaminase
<b>ALS</b>	Amyotrophic Lateral Sclerosis
<b>AOA1</b>	Ataxia with Oculomotor Apraxia type 1
<b>AOA2</b>	Ataxia with Oculomotor Apraxia type 2
<b>APE(n)</b>	Apurinic/Apyrimidinic Endonuclease (n)
<b>APTX</b>	Aprataxin
<b>ARCA</b>	Autosomal Recessive Cerebellar Ataxia

<b>ATF6</b>	Activating transcription factor 6
<b>ATM</b>	Ataxia-Telangiectasia Mutated
<b>ATP</b>	Adenosine Triphosphate
<b>ATXN2</b>	Ataxin-2
<b>A<math>\beta</math></b>	Amyloid- $\beta$
<b>BBB</b>	Blood Brain Barrier
<b>BCR</b>	B-cell Receptor
<b>BER</b>	Base Excision Repair
<b>BMAA</b>	$\beta$ -methylamino-I-alanine
<b>BSA</b>	Bovine Serum Albumin
<b>Ca<sup>+2</sup></b>	Calcium
<b>CDC</b>	Center for Disease Control
<b>CNS</b>	Central Nervous System
<b>CSR</b>	Class Switch Recombination
<b>CVO</b>	Circumventricular Organs
<b>CXCR (L)</b>	C-X-C chemokine receptor (ligand)
<b>CX3CR (L)</b>	CX3C chemokine receptor (ligand)
<b>DAMP</b>	Damage associated molecular pattern
<b>DDR</b>	DNA Damage Response
<b>DMEM</b>	Dulbecco's minimal essential media
<b>DNA</b>	Deoxyribonucleic Acid
<b>DNA-PKcs</b>	DNA dependent protein kinase catalytic subunit
<b>dpi</b>	Days post-infection
<b>DRIP</b>	DNA:RNA Immunoprecipitation
<b>DSB</b>	Double Strand Break
<b>DZ</b>	Dark Zone
<b>ELISA</b>	Enzyme-linked immunosorbent assay
<b>ELIspot</b>	Enzyme-linked immune absorbent spot
<b>ER</b>	Endoplasmic Reticulum
<b>Exo1</b>	Exonuclease 1
<b>fALS</b>	Familial ALS
<b>FBS</b>	Fetal bovine serum
<b>FDC</b>	Follicular Dendritic Cells
<b>FUS</b>	Fused in sarcoma RNA binding protein
<b>G4</b>	G-quadruplexes
<b>GC</b>	Germinal Center

<b>GFAP</b>	Glial Fibrillary Acid Protein
<b>GLT</b>	Germline Transcript
<b>Grn</b>	Progranulin
<b><math>\gamma</math>-H2AX</b>	Phosphorylated H2AX
<b>H2AX</b>	Histone 2A.X
<b>HA</b>	Hemagglutinin
<b>HD</b>	Huntington's Disease
<b>HERV-K</b>	Human endogenous retrovirus K
<b>HR</b>	Homologous Recombination
<b>HSV-1</b>	Herpes simplex virus type 1
<b>IAV</b>	Influenza A virus
<b>IFN</b>	Interferon
<b>Ig</b>	Immunoglobulin
<b>Igf1</b>	Insulin-like growth factor 1
<b>IgH</b>	Immunoglobulin Heavy Chain
<b>IHC</b>	Immunohistochemistry
<b>IRE1</b>	Inositol requiring enzyme 1
<b>IRF(n)</b>	Interferon Regulatory Factor (n)
<b>ISG</b>	Interferon Stimulated Gene
<b>KO</b>	Knockout
<b>LPS</b>	Lipopolysaccharide
<b>LZ</b>	Light Zone
<b>MBC</b>	Memory B Cell
<b>MCP-1</b>	Monocyte Chemoattractant Protein-1
<b>MDCK</b>	Madin-Darby canine kidney
<b>MEF</b>	Mouse embryonic fibroblast
<b>MEM</b>	Minimal essential media
<b>MHC</b>	Major Histocompatibility Complex
<b>MMR</b>	Mismatch Repair
<b>MN</b>	Motor Neuron
<b>MOI</b>	Multiplicity of infection
<b>MRN complex</b>	Mre11-Rad50-Nbs1 complex
<b>mSOD1</b>	Misfolded SOD1
<b>MyD88</b>	myeloid differentiation factor 88
<b>NHEJ</b>	Non-Homologous End Joining
<b>NMJ</b>	Neuromuscular Junction

<b>NO</b>	Nitric Oxide
<b>p-ATM</b>	Phosphorylated ATM
<b>PAMP</b>	Pathogen Associated Molecular Pattern
<b>PBS (T)</b>	Phosphate Buffered Saline (Tween)
<b>PC</b>	Plasma Cell
<b>PD</b>	Parkinson's Disease
<b>PERK1</b>	Double-stranded RNA-activated protein kinase-like ER kinase
<b>Pol-<math>\theta</math></b>	DNA polymerase $\theta$ (theta)
<b>POL<math>\eta</math></b>	DNA Polymerase- $\eta$ (eta)
<b>PRR</b>	Pattern Recognition Receptor
<b>R-loop</b>	RNA:DNA hybrid
<b>RNA</b>	Ribonucleic acid
<b>ROS</b>	Reactive Oxygen Species
<b>S-region</b>	Switch Region
<b>sALS</b>	Sporadic ALS
<b>SETX (<sup>-/-</sup>)</b>	Senataxin (knockout)
<b>SG</b>	Stress Granule
<b>SHM</b>	Somatic Hypermutation
<b>SIgAD</b>	Selective IgA Deficiency
<b>SMA</b>	Spinal Muscular Atrophy
<b>SMN1</b>	Survival of Motor Neuron 1
<b>SOD1 (<sup>G93A</sup>)</b>	Superoxide Dismutase 1 (G93A substitution)
<b>SSB</b>	Single Strand Break
<b>TDP-43</b>	TAR DNA binding protein 43
<b>Tfh</b>	T follicular helper cells
<b>TGF<math>\beta</math></b>	Transforming Growth Factor beta
<b>TLR</b>	Toll-like Receptor
<b>TLS</b>	Translesion Synthesis
<b>TNF-<math>\alpha</math></b>	Tumour Necrosis Factor alpha
<b>TOP1</b>	Topoisomerase 1
<b>T<sub>reg</sub></b>	T-regulatory cells
<b>TRIF</b>	TIR domain containing adaptor inducing interferon- $\beta$
<b>UNG</b>	Uracial DNA Glycosylase
<b>UPR</b>	Unfolded Protein Response
<b>VDJ</b>	Variable-Diversity-Joining

**WT**

Wildtype

## Declaration of Academic Achievement

The work presented in this thesis is the result of my research in the Miller lab over the past 4 years at McMaster University. Dr. Miller and I designed and interpreted experiments in a collaborative effort. I was the primary researcher on all experiments presented with collaborations occurring as described below.

For analysis of the data presented in Chapter 3, regarding the role of SETX on CSR, I collaborated with Peter Zeng, an undergraduate student in the Miller lab. While I performed the physical experiments and the interpretation, Peter performed the bioinformatic analysis of both the IgH repertoire analysis and the S-region sequencing. Additionally, while I performed the DRIP experimentation and interpretation, Julia Avolio, a previous undergraduate student in the Miller lab, performed the necessary qRT-PCR. Further, flow cytometric analysis of cell proliferation and IgA production was performed in collaboration with Joshua McGrath, a Ph.D. candidate in the Stampfli lab at McMaster University.

The data presented in Chapter 4, regarding the role of viral infection on ALS onset and progression, is the result of collaboration between me and many members of the Miller lab. I was primarily involved in all experiments with assistance being provided by other students for the infecting of mice with IAV/HSV and the performing of the rotarod assay. Collaborations included Braeden Cowbrough, Art Marzok, Hannah Stacey, Ali Zhang, Daniel Celeste, and Andrew Chen. Cytokine analysis of *in-vitro* and *in-vivo* samples were performed in collaboration with Braeden Cowbrough, Art Marzok, and Daniel Celeste, who assisted with the homogenizing and sending of samples for cytokine analysis. I performed

all immunohistochemical analysis of the spinal cord with assistance from the Core Histology Facility at the McMaster Immunology Research Center for tissue embedding and slicing.

# CHAPTER 1

## General Introduction

## 1.1 Autosomal Recessive Cerebellar Ataxia

Autosomal recessive cerebellar ataxias (ARCA) are a rare group of neurological disorders characterized by cerebellar atrophy. ARCAs are separated into subgroups based on the cellular function of the mutated genes leading to the disease<sup>1</sup>, one such division is the ataxias associated with a DNA repair defect<sup>1</sup>. Three distinct diseases make up this subcategory: ataxia-telangiectasia (A-T), ataxia with oculomotor apraxia type 1 (AOA1), and AOA2. A-T is the second most common ataxia with a prevalence of approximately 1-2.5/100,000 people<sup>2</sup>. The prevalence of AOA1 and AOA2 is less certain as they are rare disorders<sup>1</sup>. However, the mutated genes associated with all three diseases have been defined. Mutations in ataxia-telangiectasia mutated (ATM), aprataxin (APTX), and senataxin (SETX) are implicated in A-T, AOA1, and AOA2, respectively<sup>3-6</sup>. In addition to neurological symptoms, A-T patients commonly present with selective IgA deficiency (SIgAD)<sup>7</sup>. Immunodeficiency phenotypes have not been reported for AOA1 or AOA2, however, given the rarity of these diseases, possible immunodeficiencies have not been extensively studied<sup>1</sup>.

AOA2 is characterized by peripheral sensorimotor neuropathy<sup>6</sup>, elevated  $\alpha$ -fetoprotein levels in the circulation<sup>8</sup>, and progressive cerebellar atrophy<sup>9</sup>. Oculomotor apraxia only occurs in 50% of individuals afflicted with AOA2<sup>9</sup>. Diagnosis of AOA2 is primarily one of exclusion, as AOA2 lacks features of both AOA1 and A-T<sup>6</sup>. While loss-of-function SETX mutations are associated with AOA2, gain-of-function SETX mutations can result in a separate neurological disease, amyotrophic lateral sclerosis type 4 (ALS4), a juvenile form of amyotrophic lateral sclerosis (ALS)<sup>10,11</sup>. ALS4 is characterized by

pyramidal signs of degeneration of both brain and spinal cord motor neurons (MNs). Unlike classical ALS, disease progression in ALS4 is incredibly slow and there is a lack of degeneration of bulbar and respiratory muscles<sup>10</sup>. The etiology of the ARCA's listed above is not fully understood, however the adaptive immune system appears to be affected, especially in A-T, and may hold clues to unlock the etiology driving disease.

## **1.2 B Cell Biology and the Germinal Center**

B cells are characterized by the expression and secretion of antibodies, or immunoglobulins (Ig). A hallmark of the antibody response to pathogens is the progressive increase in the affinity of antibodies over time. Antibody affinity is altered by somatic hypermutation (SHM) during the process of a germinal center (GC) reaction<sup>12</sup>. GC's are specialized microstructures that form in lymphoid tissues upon infection or immunization. Within the GC there is intense competition between B cells for antigen, T cell help, and survival signals<sup>13</sup>. This intense competition ensures that only B cells that increase their antibody affinity for antigen are capable of receiving the survival signals. Ultimately a GC reaction results in the formation of both memory B cells (MBCs) and plasma cells (PCs)<sup>14</sup>. Recent work using an elegant BrdU-based tracking system demonstrated that MBCs are produced early post-immunization, with PCs appearing later<sup>15</sup>. IgM+ MBCs peak approximately 1-week post-immunization, while IgG+ MBCs appear 2-3 weeks post-immunization. In comparison, IgG+ PCs are not produced until approximately 1 month post-immunization<sup>15</sup>.

B cells, T cells, and follicular dendritic cells (FDCs) are the central cell types involved in the GC reaction<sup>13</sup>. Within lymphoid organs, B cells can be found clustered into follicles, composed of IgM+IgD+ B cells. The GC begins within these follicles. Resting B cells acquire antigen and migrate into the interfollicular zone. Here, the antigen presenting B cells receive signals from CD4+ T cells. B cell and T cell interactions begin as early as 1 day after immunization<sup>16</sup>. T cells that interact with B cells within the GC are called T follicular helper cells (Tfh) and are characterized by high expression of BCL-6, a key regulator of the GC reaction, among other markers<sup>17,18</sup>.

The B cell/T cell interaction induces rapid proliferation of the B cell, and a tight cluster of B cells begin near FDCs within the follicle, thus initiating a GC reaction. This typically happens at 3-4 days post-immunization<sup>16</sup>. In roughly 7 days a full mature GC forms, which is defined by the clear delineation of two zones, the light zone (LZ) and the dark zone (DZ). The LZ is defined by less cellularity, however it is more diverse in the cell types present, while the DZ is defined by clusters of highly proliferative B cells<sup>13</sup>.

B cells within the DZ are characterized by high expression of C-X-C chemokine receptor type 4 (CXCR4). Within the DZ, CXCL12 expressing stromal cells maintain the localization of proliferating B cells to the DZ, via the CXCR4-CXCL12 interaction<sup>19</sup>. B cells undergo rapid proliferation and SHM while in the DZ. In comparison, the LZ consists of FDCs, B cells, and Tfh cells. The LZ is the site of selection<sup>20</sup>, wherein B cells that have undergone SHM within the DZ now vie for antigen uptake from the FDCs and compete to receive Tfh help. As was aforementioned, BCL-6 is a key regulator of GC dynamics<sup>18</sup>.

BCL-6 acts as a transcriptional regulator for many genes associated with the GC including CXCR4, c-MYC, and integrins which enhance T cell interactions with B cells<sup>18</sup>.

The shuttling of B cells within the DZ and LZ is critical for increasing antibody affinity<sup>20-22</sup> with recent research attempting to understand the mechanism behind B cell shuttling. The most commonly used, and widely accepted, markers of mouse B cells in the LZ are CXCR4<sup>lo</sup>CD83<sup>hi</sup>CD86<sup>hi</sup>, while the DZ B cells are CXCR4<sup>hi</sup>CD83<sup>lo</sup>CD86<sup>lo</sup><sup>20,21,23</sup>. The importance of CXCR4 expression is clear given its aforementioned interaction with CXCL12<sup>19</sup>. CD86 and CD83 expression has also been well studied. CD86 expression is induced on B cells following stimulation by IL-21, which has been demonstrated to be expressed by Tfh cells. Therefore, CD86 is a marker of T cell help<sup>24</sup>. CD83 is a marker of both activated and LZ B cells and has been suggested to play a role in antigen presentation to Tfh during the GC reaction<sup>25,26</sup>. Interestingly, these markers are also found on human DZ/LZ B cells<sup>21</sup>, suggesting an evolutionarily conserved mechanism for the shuttling of B cells within the GC<sup>21</sup>.

After shuttling between LZ and DZ, B cells eventually receive signals to differentiate into either MBCs or PCs, as discussed earlier. CD40 stimulation of B cells by Tfh cells initiates a signaling cascade leading to NF- $\kappa$ B activation, induction of interferon regulatory factor 4 (IRF4) expression, and repression of BCL-6. These signals cause cells to exit the DZ<sup>27-29,30</sup>. Epigenetic changes induced by high IRF4 expression result in the expression of Blimp-1, a key mediator of PC differentiation<sup>31</sup>. MBCs rely on the expression of Bach2 to repress Blimp-1<sup>32,33</sup>. B cell receptor (BCR) affinity is also an important determinant of differentiation, with lower affinity BCRs having a higher propensity for

becoming MBCs<sup>32</sup>, while high affinity BCRs are more likely to become PCs<sup>34</sup>. The BCR affinity model supports the early MBC and late PC production during a GC response<sup>15</sup>.

The function of the GC is to ensure an appropriate antibody response by 1) enhancing the affinity of antibodies, 2) stimulating the differentiation of B cells, and 3) selecting for the best B cell clones. At the genetic level, two major processes govern antibody generation in B cells: 1) class switch recombination (CSR) and 2) SHM, which result in Ig isotype switching and affinity maturation, respectively.

### **1.2.1 Class Switch Recombination**

CSR is the process by which B cells switch the isotype of antibody produced, thereby altering antibody effector function and increasing antibody diversity<sup>35</sup>, as illustrated in Figure 1.1.1. All B cells begin IgM<sup>+</sup> and have the ability to switch from IgM to IgG, IgA, or IgE. CSR is mediated by a rearrangement of chromosomal DNA, resulting in an irreversible switch of antibody isotype<sup>13</sup>. The chromosomal rearrangements occur between regions in the immunoglobulin heavy chain (IgH) locus known as switch (S) regions. The S-regions are located upstream of the constant heavy regions of each antibody isotype such as C $\mu$  (IgM), C $\gamma$  (IgG), or C $\alpha$  (IgA). The upstream S-regions are G-rich and vary in length<sup>36</sup>. High G nucleotide content is important within the S-regions as they promote the formation of RNA:DNA hybrids (R-loops) during CSR<sup>37-42</sup>.

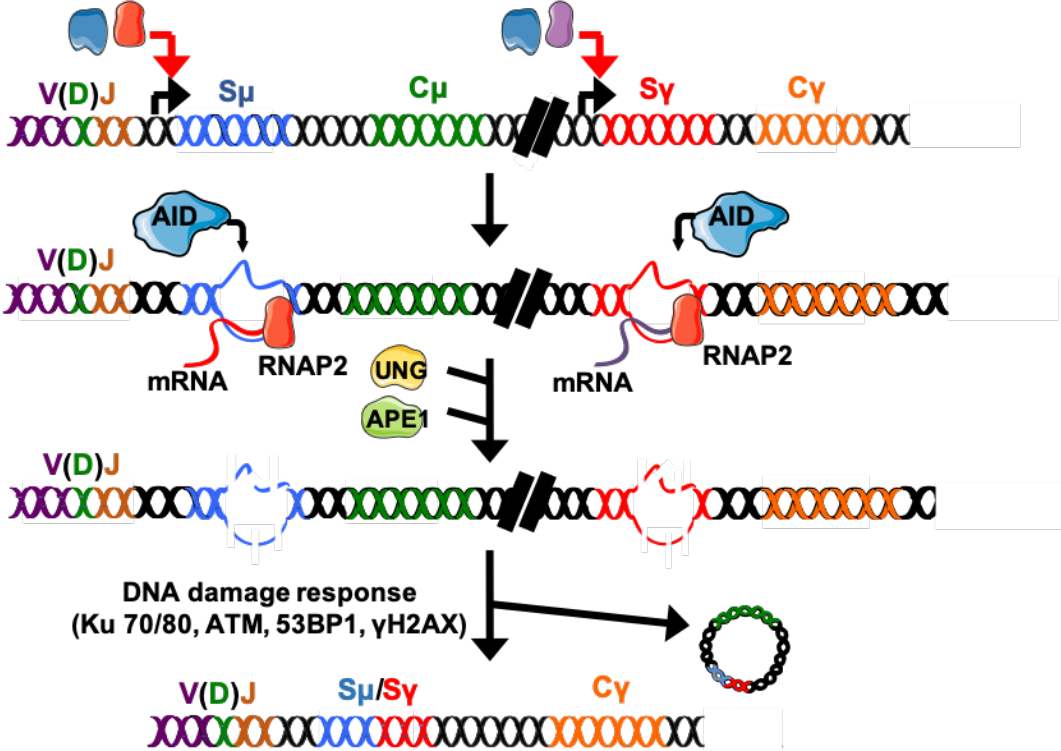


**Figure 1.1.1: A diagrammatical representation of class switch recombination.**

Herein we depict a simplified view of CSR showing the IgH locus undergoing a switch from IgM (C $\mu$ ) to IgG (C $\gamma$ ) antibody isotype. Within the GC, cytokines from Tfh cells activate specific transcription factors to induce transcription of S-regions, located upstream of the constant isotype regions, within the B cell. During transcription of the S-regions, an R-loop will form behind RNA polymerase II, as the S-regions are highly G:C rich resulting in an increased propensity for R-loop formation. R-loop formation within S-regions is crucial for CSR, providing a ssDNA substrate for the enzyme AID, which converts cytosines to uracils in ssDNA. UNG and APE work in concert on the mutated uracil to remove uracil from the DNA leaving a SSB. If these SSBs within the S-region are in close proximity to each other a spontaneous DSB will occur. Finally, via NHEJ, the IgM constant heavy region is removed from the DNA resulting in a switch to the IgG constant heavy region thereby creating an IgG producing B cell.

Cytokines produced by Tfh cells determine which S-regions are transcribed by activating transcription factors that then bind to the promoters of specific S-regions, inducing transcription<sup>43-45</sup>. Common cytokines associated with CSR are CD40L and IL-4, for IgG switching<sup>46</sup>, and CD40L, IL-4, and transforming growth factor beta (TGF $\beta$ ), for IgA switching<sup>47</sup>. Nascent S-region mRNA anneals to the template DNA strand resulting in the formation of an R-loop<sup>37-40,48</sup>. R-loop formation causes the opposite DNA strand to remain single-stranded, making it a target for the enzyme Activation-Induced cytidine Deaminase (AID)<sup>49</sup>. The function of AID is to convert cytosines to uracils via deamination<sup>42,43,50,51</sup>. The resulting uracil in the DNA is removed via uracil DNA glycosylase (UNG) leaving an abasic site<sup>41</sup>. The abasic site is then removed by apurinic/apyrimidinic endonuclease (APE), leaving a single strand break (SSB) within the DNA<sup>44,52,53</sup>. Recent studies suggest that APE1 is primarily involved in CSR, while APE2 is involved in the process of SHM<sup>54</sup>.

If the AID/UNG/APE induced SSBs are found in close proximity, a spontaneous double strand break (DSB) can form in the DNA. Spontaneous DSBs occur relatively frequently due to clustering of AID induced damage within the S-region. However, if the SSBs are not in close proximity they may be simply repaired. Alternatively, mismatch repair (MMR) can create a DSB using two distal SSBs<sup>55</sup>. In such a scenario, MSH2-MSH6 recognizes the AID induced U:G mismatches and recruits Mlh1-Pms2<sup>55</sup>. The complex formed by these proteins recruits Exonuclease 1 (Exo1), which excises nucleotides starting at the nearest 5' SSB heading in the 5' to 3' direction toward the mismatched U:G. Exo1 continues along the DNA beyond the U:G mismatch until it reaches another distal SSB, on

the other DNA strand, thereby creating a DSB within the S-region<sup>56-58</sup>. Following the formation of the DSB, there remains a single-strand overhang, which must be either removed or filled to complete CSR<sup>57,59</sup>. Ku70 and Ku80, key proteins in the non-homologous end joining (NHEJ) pathway, play a key role in DSB repair during CSR<sup>60</sup>. In fact, Ku-deficient B cells undergo apoptosis following the activation of CSR<sup>60,61</sup>. Ku70/80 heterodimers bind the ends of DNA and position the DNA to promote NHEJ while also acting as scaffolding for recruitment of DNA damage response (DDR) proteins<sup>61-65</sup>. Ultimately, CSR utilizes the NHEJ DNA repair process to complete the DNA repair and finalize switching to a new antibody isotype.

A key marker of active CSR is the expression of germline transcripts (GLTs)<sup>45,66-68</sup>, GLTs are spliced, polyadenylated RNA released from promoters upstream of S-regions<sup>68</sup>. Interestingly, a recent publication by Roco *et al.* discovered that GLTs peak before the GC develops, and rapidly decline upon B cell entry into the GC<sup>54</sup>. Prior to this study, how B cells balanced CSR and SHM was unclear. However, in this paper the authors clearly demonstrate that CSR occurs prior to SHM. Both GLT and AID expression was detectable approximately 3 days after immunization. GLT expression quickly fell to undetectable levels by 5 days post-vaccination, while AID expression increased further and remained detectable beyond 8 days post-vaccination, indicating that SHM was likely occurring<sup>54</sup>. The repression of GLT expression during the GC reaction is thought to be due to BCL-6 expression, which is expressed in B cells within the GC<sup>18</sup>. BCL-6 is a transcriptional repressor and a BCL-6 binding site is found within the promoter region of

*Apex1* gene which encodes for APE1, thereby decreasing the CSR-promoting APE1 and stimulating the switch to APE2 and SHM<sup>54</sup>.

### **1.2.2 Somatic Hypermutation**

SHM is the process of introducing point mutations within the variable region of heavy and light chain exons in an effort to increase antigen-antibody binding affinity<sup>13</sup>. In a manner similar to CSR, SHM relies on AID activity and R-loop formation across the variable region, which creates a ssDNA substrate for AID to act upon<sup>69</sup>. Mutations are most often found in the complementarity determining regions, which are the regions that primarily mediate antibody-antigen interactions, although framework regions can also be mutated<sup>70</sup>. The utilization of AID for both CSR and SHM to induce mutations within the DNA suggests that the DNA repair process of SHM must utilize a different mechanism than that used during CSR, since the purpose is to introduce mutations, and not faithfully repair the DNA. B cells undergoing SHM therefore rely upon error-prone DNA polymerases to introduce these mutations. During a typical DNA repair process following uracil insertion the base excision repair (BER) pathway is utilized<sup>71</sup>, resulting in faithful DNA repair. BER is induced in B cells for SHM, however other mechanisms can be used such as MMR<sup>72</sup>. Ultimately, both pathways end up converging at translesion synthesis (TLS) which fills gaps in the DNA using error-prone enzymes such as DNA polymerase- $\eta$  (POL $\eta$ ), which lacks proof reading capacity<sup>59,73</sup>, and REV1, which tolerates abasic sites during nucleotide addition<sup>74-77</sup>.

Both SHM and CSR are reliant upon the cell cycle. Research has demonstrated that AID is active during the G1 phase of the cell cycle, and therefore CSR and SHM must also occur during the G1 phase<sup>78–81</sup>. Interestingly, expression of AID during the S/M/G2 phases of the cell cycle did not result in induction of mutations, further solidifying the selectivity of AID activity during the G1 phase<sup>82</sup>.

Mutations introduced via SHM are ultimately stochastic and as a result, the mutation may be beneficial or detrimental to antigen binding. In some cases SHM may result in antibody recognition of self-antigens. Therefore, selection must occur during SHM to prevent proliferation of B cells that produce defective antibodies. One proposed determinant of B cell selection involves direct competition for antigen being presented upon FDCs within the GC. Higher affinity BCR's outcompete those with a lower affinity allowing for increased antigen uptake. Increased antigen uptake correlates with increased antigen presentation resulting in an increased interaction with Tfh cells. Greater Tfh interactions result in higher affinity B cells receiving more survival signals and out surviving the low affinity B cell clones<sup>20,83,84</sup>. Studies have demonstrated that the greater the T cell interactions made by B cells, the greater the number of cellular divisions B cells undergo upon re-entry into the DZ<sup>83</sup>. Proliferation is directly correlated with the rate of SHM, providing the link between Tfh interactions and SHM<sup>83</sup>. Additionally, interactions between Tfh and GC B cells induces the expression of IL-4, IL-21, and CD40L on the surface of Tfh cells<sup>84,85</sup>, all of which provide survival signals to B cells. In turn, CD40 signaling in B cells stimulates ICOSL expression, which signals Tfh cells to express

CD40L providing a feed-forward system in which B cells and Tfh cells receive mutual stimulation and strengthen their interactions<sup>85</sup>.

Peptide/major histocompatibility complex-II (MHC-II) complex density may not fully explain how competition drives B cell selection. Yeh *et al.* used B cells expressing half the level of MHC-II on their surface and demonstrated that B cells with lower MHC-II expression were recruited at a slower rate to the GC. However, during the GC reaction, B cell selection rates were unaltered<sup>86</sup>. In this system, enhanced MHC-II expression increased the ability of a B cell to enter the GC but did not alter selection of the cells within the GC<sup>86</sup>. Given the lack of MHC-II mediated selection, selection may be mediated by antibody masking of antigen on the surface of FDCs. Antibodies have been found to coat the antigen displayed on FDCs and compete with B cells for antigen binding<sup>87</sup>. In the antibody masking model, if a BCR is unable to outcompete pre-existing antibodies, the B cell is unable to receive survival signals. Finally, B cells are highly dynamic and constantly cycle through the zones of the GC. Recent research has demonstrated that B cells within the GC recycle the BCR prior to leaving the DZ (areas of SHM), thereby facilitating accurate selection of recently mutated BCRs within the LZ (area of B cell selection)<sup>88</sup>. Thus, selection of B cells during GC reactions may be determined by several factors. How these factors come together to determine which cells are ultimately selected remains incompletely understood.

### **1.3 The DNA Damage Response and CSR**

The DDR is incredibly nuanced with intricate levels of built in redundancy. DNA damage can be broadly divided into either SSBs or DSBs<sup>89</sup>. Within this thesis I will focus primarily on DSBs and their repair as they relate to CSR. The DDR to DSBs can be further subdivided into either the homologous recombination (HR) or the NHEJ pathways, whose mechanisms of repair differ substantially<sup>90</sup>. The mechanism of repair that is employed to fix DSBs depends on the cell type and the stage of the cell cycle<sup>91</sup>. For example, neurons are post-mitotic, and therefore, they rely solely upon NHEJ<sup>92</sup>. Interestingly, dividing cells can use NHEJ at all stages of the cell cycle, while HR is only possible during the S and G2 phases<sup>93</sup>. B cells, which divide rapidly during GC responses, use NHEJ during CSR. CSR occurs during the G1 phase/early S phase of the cell cycle<sup>78-82</sup> and as a consequence B cells must rely upon NHEJ to complete the DNA repair necessary for effective CSR<sup>94</sup>.

### **1.4 Non-Homologous End Joining**

DNA damage is a physiological consequence of active cell division and if left unrepaired (or ineffectively repaired) can cause cell death or oncogenesis. However, DNA damage can also be specifically induced during V(D)J recombination and CSR. NHEJ is a form of DNA damage repair resulting in the ligation of blunt DNA ends without microhomology<sup>95</sup>. NHEJ occurs when DNA breaks are recognized by a Ku70-80 heterodimer which exhibits a high affinity for DNA ends<sup>96,97</sup>. Following Ku recognition of DNA breaks, XRCC4-DNA ligase IV binds to the Ku/DNA complex<sup>98</sup>. The XRCC4-Ligase IV complex exists as a 2:1 stoichiometry; XRCC4 recognizes the two DNA ends to

be repaired and ensures close proximity for DNA ligase IV to efficiently initiate repair<sup>99</sup>. The cooperative nature of Ku-XRCC4-Ligase IV is highly efficient *in vitro* at repairing DNA ends<sup>100</sup>. However, *in vivo* the repair of DNA breaks is not so straightforward.

During spontaneous DNA breaks the DNA ends are frequently not blunt ends and cannot be recognized by the Ku-XRCC4-Ligase IV complex. These breaks rely on different NHEJ pathways. If a break results in an overhang the DNA overhang can be 1) cleaved to create a blunt end, 2) be filled to create a blunt end, or 3) microhomology within the overhang can be used as a template to initiate repair<sup>95</sup>. When DNA ends are incompatible, nuclease activity occurs to ensure that the ends can be efficiently ligated. During such a scenario, DNA-dependent protein kinase catalytic subunit (DNA-PKcs) is recruited to DNA ends in a Ku-dependent manner<sup>101</sup>, DNA-PKcs activates enzymes for DNA end processing, including Artemis<sup>102-104</sup>. Upon DNA-PKcs interaction with the Ku heterodimer, Ku transitions away from the break, along the DNA, allowing DNA-PKcs direct access to the damaged DNA site<sup>105,106</sup>. DNA-PKcs is phosphorylated at Thr2609, an essential phosphorylation site required for the activity of DNA-PKcs in NHEJ<sup>107</sup>. DNA-PKcs recruits the nuclease Artemis, which acts to resect overhangs, resulting in blunt ends and ultimately allowing for ligation of blunt ends<sup>103</sup>. Artemis, while essential for variable-diversity-joining (VDJ) recombination<sup>108</sup>, is dispensable for CSR<sup>109</sup>, meaning that different nucleases are recruited for different forms of DNA damage. DNA-PK, the complex consisting of DNA, Ku, and DNA-PKcs<sup>110</sup>, has been demonstrated to act as an inhibitory signal for other DNA repair pathways, thereby promoting NHEJ<sup>111</sup>. In addition to Artemis, DNA-PKcs interacts with XRCC4 to complete the ligation of DNA ends<sup>112</sup>. NHEJ is the

primary form of DSB repair however, research has suggested an alternate end joining (a-EJ) pathway can repair DNA when NHEJ is compromised<sup>113</sup>.

### **1.5 Alternate End Joining**

In comparison to NHEJ, a-EJ is a longer process and has elevated rates of mutation associated with this form of DNA repair. a-EJ functions as a backup for classical NHEJ<sup>113</sup>. A hallmark of a-EJ is the requirement for microhomology-mediated end joining during repair, with microhomologies of 4-20 base pairs (bp) typically being required for a-EJ while NHEJ utilizes 0-4bp<sup>114</sup>. Key proteins involved in a-EJ include PARP1<sup>115,116</sup>, CtIP<sup>117</sup>, the MRN complex<sup>118</sup>, and Pol- $\theta$ <sup>119</sup>. Another defining feature of a-EJ is independence from Ku-mediated DNA repair<sup>120</sup>.

PARP1 acts as a sensor of DNA damage and catalyzes PARylation of proteins within the DNA damage site<sup>121</sup>. PARP1 is proposed to be a key mediator of a-EJ, given findings that PARP1 deficient B cells are deficient in microhomology mediated repair<sup>122</sup>. PARP1 directly competes with Ku for the binding of DNA ends<sup>123</sup>, and thereby promotes a-EJ over the Ku-dependent NHEJ. Further, PARP1, via PARylation, recruits various repair factors associated with a-EJ, including DNA ligase III<sup>115</sup> and the MRN complex<sup>118</sup>.

The MRN complex consists of MRE11, RAD50, and NBS1<sup>124</sup>, and acts as an endonuclease to create DNA overhangs, upon activation by CtIP, which generates microhomology<sup>117,125-127</sup>. Knockdown of CtIP reduces both CSR rates and microhomology usage<sup>117</sup>.

Following endonuclease activity by MRN/CtIP, the DNA polymerase  $\theta$  (Pol- $\theta$ ) stabilizes the annealing of ssDNA overhangs allowing for ligation to occur. Pol- $\theta$  can add nucleotides to create microhomology where none exists<sup>128</sup>. While other polymerases have been proposed to play a role in a-EJ, Pol- $\theta$  has recently been demonstrated to be indispensable for a-EJ<sup>129</sup>. Further, Pol- $\theta$  lacks proofreading capabilities<sup>130</sup>, which is of particular importance for the role of Pol- $\theta$  in SHM. The role of Pol- $\theta$  in SHM has been challenged, with Pol- $\eta$  potentially being the more relevant polymerase during SHM<sup>131</sup>. Pol- $\theta$  may also play an active role in the repair of DSBs involved in replication fork collapses induced by DNA damage, and is often overexpressed in cancers<sup>132</sup>.

Ultimately, ligation can occur via either DNA ligase I or III<sup>133</sup>. A common method of studying a-EJ is to use cells that are deficient in DNA ligase IV, which forces cells to use a-EJ. In such systems, both ligase I and III are able to repair DNA, with knockout of one or the other having little effect. However, knockdown of both abrogates DNA repair<sup>133,134</sup>. Despite inbuilt redundancy, the ligases do exhibit preferences with regards to the type of DNA ends they ligate, with DNA ligase I preferring longer microhomologies and DNA ligase III preferring blunt ends<sup>134</sup>.

## **1.6 Amyotrophic Lateral Sclerosis**

ALS (also known as Lou Gehrig's disease) is a progressive and fatal MN disease. The mean age of onset of ALS is 50 – 65 years old. Males and females have nearly equal risk, with incidence rates of approximately 2-4 / 100,000 people. The average survival for ALS is 2-5 years post diagnosis and there is no cure for the disease<sup>135</sup>. Current treatments,

riluzole<sup>136–139</sup> and edaravone<sup>140–143</sup>, are woefully inadequate, and at best offer modest survival increases. In fact, edaravone may prove to be harmful to ALS patients, given the daily intravenous administration required, as both placebo and edaravone treated patients experienced worse disease progression than patients receiving no treatment<sup>144</sup>.

ALS can occur at either the spinal or the bulbar level, with bulbar onset being associated with more rapid disease progression<sup>145</sup>. Both bulbar and spinal cases of ALS are characterized by the rapid development of muscle weakness and atrophy throughout the body, caused by the progressive loss of both upper and lower MNs<sup>146</sup>. Patients ultimately succumb to ALS when innervation of the diaphragm is lost, and patients lose the ability to breathe<sup>135</sup>. The etiology of ALS remains a mystery, although evidence suggests that ALS is a non-cell autonomous disorder with glial cell activation being a major driver of disease<sup>147–152</sup>. Interestingly, wildtype (WT) neurons surrounded by mutant SOD1-expressing glia show signs of degeneration<sup>153</sup>. Therefore, innate immune cells within the central nervous system (CNS) may play an important role in the etiology of ALS.

## **1.7 The Innate Immune System of the CNS**

The innate response is nonspecific and generally relies upon pattern recognition receptors (PRRs) and phagocytic cells to recognize and destroy foreign invaders. The innate immune system can be divided into physical and cellular barriers. Physical barriers include the skin and mucosa, while cellular barriers include granulocytes, dendritic cells, natural killer cells, and monocytes/macrophages<sup>154</sup>. In addition to having a general role as the first response to an infection, the innate response can differ depending on tissue resident cells

and tissue specific characteristics. Herein, we will focus on the innate response as it relates to the CNS. The CNS is somewhat unique given that it has historically been considered an “immune privileged” site<sup>155</sup>. However, we know now that the CNS and the immune system cross talk extensively in an attempt to maintain healthy homeostasis<sup>156</sup>. The innate immune system within the CNS consists of both a physical (the blood brain barrier (BBB)) and cellular (glial cells) component<sup>157</sup>.

### **1.7.1 The Blood Brain Barrier**

The BBB is the physical barrier separating the CNS from the periphery. The BBB is composed of tight junctions between endothelial cells and a secondary layer of astrocytic endfeet and pericytes<sup>158</sup>. The function of the BBB is to prevent access of circulating pathogens and cells into the CNS and thus to protect the CNS from injury, inflammation, toxins, and disease<sup>158</sup>. The endothelial cells of the BBB limit the transmission of molecules from the blood into the CNS. As such, they are highly polarized cells and are highly restrictive with regards to passive transport<sup>159</sup>. Pericytes have the ability to control the contraction of the blood vessels and strengthen the tight junctions between endothelial cells<sup>160</sup>. Astrocytic endfeet are found at the end of astrocytic processes and are capable of covering the vasculature<sup>161</sup>. The astrocytes play a key role in the sensing and uptake of molecules from the periphery. For example, aquaporins on the surface of endfeet are essential for maintaining the homeostasis of water within the CNS<sup>162</sup>. Additionally, astrocytic endfeet are capable of sending signals to alter the blood flow of the vasculature. The BBB is a key component of the innate immune response within the CNS, and

neurodegeneration often results in a breakdown of the BBB. Neurodegenerative disorders that have been demonstrated to have a disrupted BBB include Alzheimer's disease (AD), Parkinson's disease (PD), and ALS<sup>163</sup>. The implications of BBB disruption on progression of neurodegenerative diseases is poorly understood<sup>164</sup>.

### **1.7.2 Glial Cells**

Glial cells are the nonneuronal cells within the CNS and consist of astrocytes, microglia, and oligodendrocytes. Glia in the human brain make up roughly 50% of the cellular mass<sup>165</sup>. Glial cells were thought to be inert, simply the glue that holds the CNS together. However, glial cells are designed to support the healthy function of neurons within the CNS. Astrocytes, so called because of their star-like morphology, have the broadest functionality within the CNS, with roles in neuronal maintenance, BBB maintenance, and neurotransmitter uptake and release<sup>166</sup>. Microglia are small oval shaped cells with long processes extending from the cell body and are considered the primary immune cell of the CNS, harbouring phagocytic capabilities<sup>167</sup>. Oligodendrocytes myelinate and provide support to axons within the CNS<sup>168</sup>. Both astrocytes and microglia have been extensively studied in neurodegenerative disorders, while the contribution of oligodendrocytes has only recently been explored. Therefore, the focus herein will be on astrocytes and microglia.

#### **1.7.2.1 Astrocytes**

Within the healthy CNS astrocytes exhibit branching processes that expand into 3-dimensional space. Astrocytes can be found in all areas of the CNS<sup>166</sup>. A major function of

astrocytes is their interaction with blood vessels, whereby astrocytes receive and propagate signals from the blood and restrict blood flow within areas of the CNS<sup>169</sup>. Astrocytes can release molecular mediators of vasodilation such as prostaglandins<sup>170</sup>. In addition to regulating blood flow, astrocytes are essential in maintaining synaptic health<sup>171</sup>.

Astrocytic processes can be found enveloping synapses. Within the synapse, astrocytes regulate fluid, ion, and neurotransmitter levels<sup>171</sup>. Astrocytes can coordinate a diverse array of functions through astrocytic processes, which are able to interact with many areas of the CNS simultaneously. For example, a single astrocyte may interact with blood vessels, synapses, and microglia simultaneously allowing for the orchestration of complex functions<sup>172</sup>. One such function includes CNS metabolism. Astrocytes are able to uptake and store glucose from the blood and produce energy metabolites, such as glucose, glycogen, and lactate, that can be supplied to all manner of neuronal cells<sup>173</sup>. For example, astrocytes have been demonstrated to store glycogen at synaptic processes<sup>174,175</sup>. During periods of high activity, glycogen can be released allowing the neuron to use glycogen as an energy substrate<sup>175</sup>. Finally, astrocytes are involved in the maintenance of the BBB, although the mechanism through which astrocytes support the BBB remains poorly understood. While astrocytes demonstrate many functions in the healthy CNS, astrocytes also have the ability to become reactive in neurodegenerative disorders.

### **1.7.2.2 Microglia**

Microglia are the innate immune cells within the CNS. Microglia constantly survey the CNS for alterations to homeostasis with protrusions extending from the soma. The

protrusions are highly motile and are in constant motion while surveying the CNS<sup>176</sup>. Microglial protrusions scan blood vessels, astrocytes, neurons and synapses assessing their functional health. CX3C chemokine receptor (CX3CR)-1 is expressed on the microglial protrusions and binds to CX3CL1. CX3CL1 is constitutively expressed on neuronal cells and signals to the microglia that a cell is healthy through negative regulation of microglial activation<sup>177,178</sup>. However, decreased expression of CX3CL1, which occurs when a cell is too damaged to survive, signals microglia to become activated. Microglia are the macrophages of the CNS and, similar to a macrophage, once activated become phagocytic and phagocytose damaged neurons<sup>180</sup>.

In the healthy CNS microglia have a diverse array of functions. During development, microglia are involved in the shaping of neural circuits by modulating the strength of synaptic transmission as well as by pruning nonreceptive synapses<sup>179</sup>. Together, both microglia and astrocytes are involved in synaptic pruning. Pruning is mediated by TGF $\beta$  activation of C1q expression within neurons, ultimately signaling to microglia that the synapse must be pruned<sup>179,180</sup>. While microglia perform these functions, they are termed to be “resting”, however, microglia can also be activated. Following CNS injury, microglia migrate to the site of damage, typically through adenosine triphosphate (ATP) gradients, and direct their processes towards the site of damage to enhance phagocytosis<sup>181</sup>. If the injury is more drastic, microglia become more ameboid in morphology, which is a signature of activation and is accompanied by enhanced phagocytic function and proinflammatory cytokine secretion. Additionally, microglia can induce programmed cell

death in an effort to prevent inflammation from occurring by secreting superoxide ions or tumour necrosis factor alpha (TNF- $\alpha$ )<sup>182-185</sup>.

In a similar fashion to macrophages, microglia have been characterized as either M1 or M2, pro- or anti-inflammatory, respectively. The M1/M2 paradigm is useful for the characterization of microglial activity *in vitro*. However, studies have demonstrated that microglia can exist in many different permutations *in vivo*<sup>186</sup>. M2 activation is induced by IL-4, IL-10, IL-13, and the detection of apoptotic cells<sup>187-190</sup>. M2 activation induces secretion of anti-inflammatory cytokines, such as IL-10 and TGF- $\beta$ , growth factors, and neurotrophic factors<sup>191</sup>. In comparison, M1 activation can be induced by signaling through PRRs such as the toll-like receptor (TLR) and interferon (IFN)- $\gamma$  receptor, and results in the release of proinflammatory factors, such as TNF- $\alpha$ , IL-1 $\beta$ , and CCL2, ROS, and induces high MHC-II expression levels<sup>189,192</sup>. The M1/M2 paradigm is less clear *in vivo*. Instead, microglia exhibit a wide heterogeneity with regard to their transcriptomic profiles<sup>193</sup>. The differences between microglial phenotypes *in vitro* and *in vivo* are likely due to 1) excessive levels of stimulants used *in vitro*, and 2) microglia undergo extensive interactions with other cells within the CNS which modulate their activity.

## 1.8 Hypothesis

We hypothesize that neurodegenerative disease associated mutations in both SETX and SOD1 will result in immune dysregulation.

# CHAPTER 2

## Materials and Methods

### ***Ethics statement***

Mouse experiments described herein were approved by the McMaster University Animal Research Ethics Board.

### ***Mice***

SETX mice were a generous gift from Dr. Martin Lavin. SETX<sup>+/+</sup> and SETX<sup>-/-</sup> mice were bred using SETX<sup>+/-</sup> parents and genotyped using the methods described in Becherel *et al.* 2013<sup>194</sup>. Mouse experiments were performed using 6-12 week old mice. SOD1<sup>G93A</sup> mice and WT control mice were purchased from The Jackson Laboratory (B6SJL-Tg(SOD1\*G93A)1Gur/J), and genotyped according to The Jackson Laboratory protocol. The mice were raised on a mixed B6SJL genetic background and contain a high copy number of the SOD1<sup>G93A</sup> gene resulting in elevated protein expression. Mice were bred up to second generation and experiments were performed on littermate controls at the mentioned days of age.

### ***Cells and Viruses***

HeLa cells were originally obtained from the American Type Culture Collection (ATCC), and maintained in Dulbecco's minimal essential media (DMEM) supplemented with 2 mM glutamine, 10 % fetal bovine serum (FBS) (Gibco, Life Technologies), 100 U/mL penicillin and 100 µg/mL streptomycin (Gibco, Life Technologies) at 37 °C with 5 % CO<sub>2</sub>. Mouse embryonic fibroblasts (MEFs) were isolated from embryos at 13.5 days post-conception<sup>195</sup> and maintained as described above, but with 15 % FBS. CH12-WT and CH12-SETX KO

cells were a kind gift from Dr. Uttiya Basu<sup>196</sup>. Splenocytes, CH12s, and primary B cells were cultured in complete RPMI-1640 (cRPMI-1640), 2 mM glutamine, 10 % FBS (Gibco, Life Technologies), 100 U/mL penicillin and 100 µg/mL streptomycin (Gibco, Life Technologies), and 10 µM β-mercaptoethanol (MilliporeSigma) at 37 °C with 5 % CO<sub>2</sub>. Madin-Darby canine kidney (MDCK) cells were maintained in DMEM supplemented with 2 mM glutamine, 15 % FBS (Gibco, Life Technologies), 100 U/mL penicillin and 100 µg/mL streptomycin (Gibco, Life Technologies) at 37 °C with 5 % CO<sub>2</sub>. Vero cells were maintained in DMEM supplemented with 2 mM glutamine, 15 % FBS (Gibco, Life Technologies), 100 U/mL penicillin and 100 µg/mL streptomycin (Gibco, Life Technologies) at 37 °C with 5 % CO<sub>2</sub>. The Influenza A virus (IAV) strain used herein was A/Puerto Rico/8/1934 (PR8) which was propagated in 8 – 10 day old embryonated chicken eggs (Canadian Food Inspection Agency). HSV-1 strain 17 syn was grown and titred on Vero cells.

### ***Virus Inactivation***

PR8 was inactivated using formalin. Briefly, 100× inactivation solution (0.925% formaldehyde in phosphate buffered saline (PBS)) was combined with 1 mg/mL of virus suspension to a final concentration of 1× inactivation solution. Samples were incubated at 4 °C on a rotator for 72 h, following which the inactivated virus was stored at -80 °C.

### ***Recombinant hemagglutinin (HA) production***

To assess HA specific antibodies, recombinant PR8 HA was produced in HighFive cells as described in Margine *et al.*<sup>197</sup>.

### ***Immunization***

Mice were immunized intramuscularly (i.m., quadricep muscle) with 100  $\mu$ L of 0.5 mg/mL formalin-inactivated PR8. Blood was drawn at designated time points, 7, 14, and 30 days post-vaccination. Serum was separated by incubating blood overnight at 4 °C and centrifuged at 16,000  $\times$ g for 5 min. Serum was frozen at -20 °C prior to further analyses.

### ***Spleen and B cell isolation***

Mice were euthanized via cervical dislocation and spleens were removed. Following spleen removal, tissue was homogenized and passed through a 70  $\mu$ m filter. Cells were centrifuged at 200  $\times$ g for 5 min at 4 °C, RBC's were then lysed using ACK lysis buffer for 5 min at room temperature (RT) and centrifuged at 200  $\times$ g for 5 min at 4 °C. B cells were isolated from splenocytes using the EasySep Mouse B cell isolation kit (StemCell Technologies) according to the manufacturer's instructions. Briefly, spleens were suspended in PBS + 2 % FBS + 1 mM EDTA and blocked with rat serum. Next, antibody isolation cocktail was added and incubated at RT for 10 min. Magnetic beads were added and further incubated at RT for 3 min. Samples were placed in the EasySep magnetic stand and incubated at RT for 5 min. Following incubation, B cells were decanted and used for downstream purposes.

### ***B cell stimulation***

For general polyclonal stimulation, cells were treated with 10 µg/mL lipopolysaccharide (LPS) (MilliporeSigma), 1 µg/mL R848 (Invivogen), 1 µg/mL pokeweed mitogen (MilliporeSigma), *Staphylococcus aureus* Cowan (SAC, 1/10000) (MilliporeSigma), and 0.5 mM β-mercaptoethanol (MilliporeSigma) in RPMI-1640<sup>198</sup>. For IgA stimulation, cells were treated with 1 µg/mL CD40 (eBioscience), 10 ng/mL IL-4 (Peprotech), 2 ng/mL TGF-β (R&DSystems), and 0.5 mM β-mercaptoethanol (MilliporeSigma) in RPMI-1640<sup>199</sup>.

### ***Enzyme-linked immune absorbent spot (ELISpot)***

ELISpot assays were performed in 96 well MultiScreen Filter Plates (Millipore). Plates were coated with 100 µL of capture antibody, goat anti-mouse IgG, IgA or IgM (ThermoFisher Scientific), or recombinant HA at 10 µg/mL for 24 h at 4 °C in PBS. Plates were washed 3× with PBS-T (0.1% Tween) and were blocked with cRPMI-1640 for 1 h at 37 °C. Splenocytes were plated in a 96-well plate and were diluted 1:2 across the plate 11 times in cRPMI-1640, leaving the last well as a blank negative control. Plates were incubated overnight at 37 °C. Cells were removed and the plate was washed 3× with PBS-T. HRP-conjugated secondary antibodies, goat anti-mouse IgM, IgG, and IgA (ThermoFisher Scientific), at a 1:1000 dilution, were diluted in PBS-T and were incubated on plates for 1 h at RT. Secondary antibodies were aspirated and the plate was washed 3× with PBS-T. AEC substrate (Millipore) was prepared according to the manufacturer's protocol and incubated on the plate for 20 min at RT. AEC substrate was discarded and the plates were washed with distilled water before being left at RT overnight to dry. Plates were

read using an ImmunoSpot plate reader (Image Acquisition 4.5) and the number of spots were analyzed using the ImmunoSpot 3 software.

### ***Live/dead cell analysis***

Isolated B cells received polyclonal stimulation for 3 or 5 days. At each time point cells were stained with the ReadyProbes cell viability imaging kit (Thermo Fisher Scientific) according to the manufacturer's protocol. Briefly, cells were incubated with PBS containing 2 drops of stain per mL and incubated at 37 °C for 15 min. Following staining, cells were imaged using the EVOS-FL system at 10X magnification. The percentage of dead cells was quantified by overlaying the live (blue) and dead (green) channels and counting the proportion of cells which exhibited dual staining.

### ***Flow cytometry for IgA positive cells***

Splenocytes were stimulated with polyclonal stimulation, IgA stimulation, or left untreated for 72 h. Following stimulation, cells were resuspended in 100 µL PBS and plated in U-bottom 96 well plates. Cells were centrifuged at 200 ×g for 5 min at 4 °C, resuspended in 50 µL LIVE/DEAD (LD) fixable yellow dead cell stain kit (1:400 dilution in PBS, Molecular Probes) and incubated on ice for 30 min. Cells were centrifuged at 200 ×g for 5 min at 4 °C, then resuspended in 50 µL of blocking antibody (1:100 dilution in 0.5% bovine serum albumin [BSA], 2mM EDTA in PBS [FACS buffer]) and incubated on ice for 30 min. Cells were centrifuged at 200 ×g for 5 min at 4 °C, and cells were stained with IgD-BV711 (Biolegend) and CD19-APC/Cy7 (Biolegend) diluted in FACS buffer for 30 min at

4 °C. Following staining, cells were washed with FACS buffer and centrifuged at 200 ×g for 5 min at 4 °C. Cells were suspended in fixation/permeabilization solution (BD Biosciences) and incubated for 30 min at 4 °C, at which point the fixation/permeabilization was stopped by adding permeabilization/wash (P/W) buffer and cells were centrifuged at 200 ×g for 5 min at 4 °C. Cells were resuspended in P/W buffer and stained with IgM-BV786 (Biolegend), IgG1-BV421 (Biolegend), and IgA-BV650 (Biolegend) for 30 min at 4 °C. Following staining, cells were centrifuged at 200 ×g for 5 min at 4 °C and washed twice with P/W buffer and then washed 2× in FACS buffer. Cells were assayed on the BD LSRFortessa (BD Biosciences), and analyzed using FlowJo v.10 (FlowJo, LLC, BD Biosciences).

### ***Enzyme-linked immunosorbent assay (ELISA)***

ELISAs were performed in 96 well plates (ThermoFisher Scientific). Plates were coated with 100 µL of capture antibody goat anti-mouse IgG, IgA, IgM (ThermoFisher Scientific), or recombinant HA at 2 µg/mL for 24h at 4 °C in bicarbonate/carbonate coating buffer (5.3 g Na<sub>2</sub>CO<sub>3</sub>, 4.2 g NaHCO<sub>3</sub>, pH 9.4, in 1 L of H<sub>2</sub>O). Following the 24h coating period, plates were blocked using 100 µL of 5 % milk in PBS with 0.1 % tween (PBS-T) for 1 h at RT. Following blocking, serum samples were added and diluted 1:2 across the plate 11 times in blocking buffer, leaving the last well as a blank control. Samples were incubated for 1 h at RT. Following the 1 h incubation period, plates were washed 3× with PBS-T. Following the 3 washes, 100 uL of secondary antibodies goat anti-mouse IgG-HRP, IgA-HRP, and IgM-HRP (ThermoFisher Scientific) were added at 0.1 µg/mL, diluted in PBS-T, and

incubated for 1 h at RT. Following the incubation period, plates were washed 3× with PBS-T and 100 µL of Sigmafast OPD substrate (MilliporeSigma) was added for 10 min, following which the reaction was neutralized with 50 µL of 3 M HCl. Plates were then analyzed on the Spectramax i3 plate reader (Molecular Devices) at an absorbance of 490 nm. Data was transformed into a log(X) scale and a nonlinear fit was performed using the log(agonist) vs. response with a variable slope (four parameters). The log(EC50) value was then plotted and statistical analysis was performed using a one-way ANOVA with a Tukey post-hoc test.

### *Immunofluorescence*

MEFs were cultured overnight on coverslips and treated with either 0.5 mM H<sub>2</sub>O<sub>2</sub> (MilliporeSigma) or 20 µM phleomycin (Invivogen). At indicated time points cells were fixed using ice-cold methanol for 20 min at -20 °C. Following methanol fixation, cells were washed 3× with PBS. Coverslips were permeabilized using 0.2 % Triton-X-100/0.1 % BSA/PBS for 15 min at RT, and then washed 3× PBS. Following permeabilization, cells were blocked with 10 % normal goat serum (Abcam)/1 % BSA/PBS for 30 mins. Cells were incubated with primary antibodies overnight at 4 °C. Primary antibodies included rabbit anti-human SETX (Bethyl Laboratories, Inc.), mouse anti-mouse/human  $\gamma$ -histone 2A.X (H2AX) (Abcam), mouse anti-human 53BP1 (MilliporeSigma), mouse anti-mouse/human phospho-ATM (p-ATM) (ThermoFisher Scientific), and mouse anti-R-loop S9.6 (Kerafast). Cells were then washed 5× with PBS and probed with compatible AlexaFluor-conjugated secondary antibodies (all at 1:1000 dilution) (Life Technologies).

Cells were washed 3× with PBS and DNA was counterstained using Hoechst 33342 (1 µg/mL) (Life Technologies) and mounted with EverBrite mounting medium (Biotium). Images were taken with the Zeiss Imager M2 microscope (Carl Zeiss Canada Ltd.) at the indicated magnification. For DNA damage kinetics experiments, cells were considered to be positive for p-ATM and γ-H2AX foci formation based on the average number of p-ATM/γ-H2AX foci in the SETX<sup>+/+</sup> untreated conditions + 3 S.D. Any cell with more foci than this was considered positive for DNA damage induction following treatment.

#### ***Germline transcript quantification***

RNA was isolated from stimulated splenocytes using RNeasy isolation kit (QIAGEN) and 1 µg of complimentary DNA was synthesized according to manufacturer's instructions (Maxima First Strand cDNA Synthesis kit, Thermo Fisher Scientific). Expression levels of AID, IgM GLT (M-GLT), and IgA GLT (A-GLT) were assessed using SensiFAST SYBR reaction kit (Bioline) and quantitative reverse transcriptase polymerase chain reaction (qRT-PCR) along with previously published primers in Ribeiro de Almeida *et al.*<sup>200</sup>.

#### ***DNA:RNA Immunoprecipitation (DRIP)***

DRIP was performed using methods described in Halász *et al.* as a framework<sup>201</sup>. Briefly, genomic DNA was isolated from stimulated splenocytes using the DNeasy isolation kit (QIAGEN), according to the manufacturer's protocol. Total DNA was quantified and DNA was sonicated (pulse; on for 20 s, off for 30 s; at an amplitude of 30 %) to a size ranging from 250-1000 bp. 6 µg of total DNA was then precleared using protein G agarose beads

(Invitrogen) for 1h at 4 °C while shaking, following which samples were either treated with RNaseH (New England Biolabs) or left untreated. Samples were incubated with 10 µg S9.6 antibody (Kerafast), or 10 µg of control mouse IgG (Invitrogen), whilst shaking overnight at 4 °C. Protein G agarose beads (Invitrogen) were then added to the samples and incubated at 4 °C while shaking overnight. Protein G agarose beads (Invitrogen) were then spun at 16,000 ×g for 5 min and washed 4× with buffers of differing ionic strength. First, low salt IP buffer (16.7 mM TRIS (pH 8), 1.2mM EDTA, 167 mM NaCl, 0.01 % SDS, and 1.1 % Triton X-100), second, high salt IP buffer (16.7 mM TRIS (pH 8), 1.2 mM EDTA, 500 mM NaCl, 0.01 % SDS, and 1.1 % Triton X-100), third, high LiCl buffer (10 mM TRIS (pH 8), 1 mM EDTA, 250 mM LiCl, and 1 % NP-40), and the final wash, low LiCl buffer (10 mM TRIS (pH 8), 1 mM EDTA, and 50 mM LiCl). Following the washes, DNA was eluted from protein G agarose beads (Invitrogen) using 100 µL elution buffer (50 mM TRIS (pH 8), 10 mM EDTA, and 1% SDS) at 65 °C for 15 min. After the 15 min incubation, an additional 100 µL of PBS was added and the DNA was purified using the DNeasy isolation kit (QIAGEN). Following DNA isolation, samples were assessed via q-PCR using SensiFAST SYBR reaction kit (Bioline) and previously published primers against areas of the IgH locus by Ribeiro de Almeida *et al.*<sup>200</sup>.

### ***High-Throughput IgH Sequencing***

High throughput-sequencing analysis of mouse immunoglobulin repertoire was performed as previously described in Turchaninova *et al.*<sup>202</sup>. Briefly, SETX<sup>+/+</sup> and SETX<sup>-/-</sup> mice were vaccinated *i.m.* with inactivated-PR8 and spleens were isolated 14 days post-vaccination. Total RNA was isolated using the RNeasy Qiagen RNA isolation kit, according to the

manufacturer's protocol. 1  $\mu$ g of total RNA was used for the sequencing of the IgH repertoire, according to the Turchaninova *et al.* protocol<sup>202</sup>. Illumina adaptors were added to the library according to the manufacturer's protocol. Sequencing was performed on an Illumina Mi-Seq platform using asymmetric 400+200-nt paired-end sequencing. The MIGEC software was used to demultiplex the samples and perform UMI-based assembly of full-length variable regions. ChangeO package was used to perform IgBLAST and perform clonal clustering. Immunoglobulin gene usage analysis was conducted using the Alakazam package. The ShazaM package was used to quantify mutations within the full variable region or in the CDR/FDR regions.

### ***Switch-Region Sequencing***

WT and SETX knockout (SETX-KO) CH12 cells were stimulated using IgA specific stimulation for 72h. Following stimulation, genomic DNA was extracted using the DNeasy isolation kit, according to manufacturer's protocol (QIAGEN). Following which, PCR amplification was performed with primers upstream of the S $\mu$  and downstream of the S $\alpha$  DNA regions taken from Ribeiro de Almeida *et al.*<sup>200</sup>. Briefly, using PrimeSTAR HS DNA polymerase (Tanaka) genomic S-regions were amplified at 35 cycles of 98 °C for 10 s and 68 °C for 2 min 30 s. PCR amplicons were ran on 1 % agarose gels and bands ranging from 1 – 3 kb were extracted from the gel using the NEB Monarch gel extraction kit (New England BioLabs) according to the manufacturer's protocol. DNA was then inserted into the TOPO-TA cloning kit (ThermoFisher Scientific), 6  $\mu$ L of DNA was combined with 1  $\mu$ L of plasmid and 1  $\mu$ L of salt solution and incubated at RT for 30 min. Following which,

the 8  $\mu$ L of TOPO/S-region insert was combined with 50  $\mu$ L DH5 $\alpha$  and incubated on ice for 30 min. Bacteria were heat-shocked for 45 s at 42  $^{\circ}$ C, incubated on ice for 2 min, and 1 mL of LB was added and samples were shaken at 37  $^{\circ}$ C for 1 h. Cells were centrifuged at 16,000  $\times$ g for 3 min and the whole cell pellet was grown on LB-Amp (100  $\mu$ g/mL) plates overnight at 37  $^{\circ}$ C. Colonies were selected and further propagating in 3 mL of LB shaking overnight at 37  $^{\circ}$ C. Plasmids were isolated using the NEB Monarch miniprep plasmid isolation kit (New England BioLabs) according to the manufacturer's protocol. Individual sequences were assessed using M13F and M13R specific primers.

Samples were sent for Sanger sequencing and then sequences were analyzed with custom Python script. Briefly, ABI files were converted to FASTA and then aligned to S-region using the aligner Yara (PMID: 23358824), which is sensitive for deletions and rearrangements. The blast8 file of the forward read and reverse read was then compared to look for signs of microhomology mediated repair or NHEJ. Sequences were defined as microhomology mediated repair if the overlap was less than 20 nucleotides and NHEJ if there was no overlap.

### ***IAV Infection of the SOD1<sup>G93A</sup> model***

WT and SOD1<sup>G93A</sup> mice were anesthetized using isoflurane and infected with IAV intranasally in 40  $\mu$ L inoculums. 300 plaque forming units (pfu) of PR8 was administered as a 0.1 LD<sub>50</sub> infection, and 3000 pfu as a 1 LD<sub>50</sub> infection, at 60 days of age and mice were monitored by weight loss for 14 days post-infection (dpi). Endpoint was considered to be mice reaching 80 % of their initial body weight.

***HSV-1 Infection of the SOD1<sup>G93A</sup> model***

2.5 mg of Depo-Provera, a progesterone derivative, was administered subcutaneously to female WT and SOD1<sup>G93A</sup> mice 4 days prior to infection (56 days of age). One day prior to infection, the vaginal lumen of mice was washed with 20 µL of sterile PBS and cellular morphology was analyzed to confirm effective synchronization of estrous cycle<sup>203</sup>. The wash should appear to have many small dense cells, indicative of lymphocyte infiltration. This means that these mice have entered diestrus, allowing for efficient infection since the uterine walls are thinned at this stage. Mice were infected at day 60 of age with 10<sup>5</sup> pfu of HSV-1 Syn 17. To infect with HSV-1, an anesthetic mixture of Ketamine and Xylazine (3:1) diluted in PBS (1 part anesthetic: 5 parts PBS) was used to anesthetize the mice. Mice were administered 150 µL of anesthetic *i.p.* Following anesthetization, mice were administered 10<sup>5</sup> pfu of HSV-1 Syn 17 intravaginally and placed on a heating pad and monitored until mice regained full mobility. Infected mice were monitored daily over 14 days for disease morbidity, measured by weight loss and HSV-1 pathogenesis. HSV-1 pathogenesis was rated on a 4 point scoring criteria, beginning at minor hair loss around the genitals to severe genital lesioning and/or rectal paralysis. Vaginal lavage samples were collected at 1, 3, 5, and 7 dpi. Infected mice were flushed twice with 20 µL of sterile PBS (40 µL total). Viral titers were determined via the standard Vero plaque assay.

***Inactivated IAV Administration to the SOD1<sup>G93A</sup> model***

Inactivated IAV was administered to WT and SOD1<sup>G93A</sup> mice *i.m.* (quadricep muscle) with 100  $\mu$ L of 0.5 mg/mL inactivated IAV. For intranasal (*i.n.*) administration of inactivated IAV, 0.5 mg/mL was administered in a 40  $\mu$ L inoculum. Stimulation of mice with inactivated IAV was performed at 60 days of age while controls received an equivalent dilution of inactivation solution in PBS.

***ALS Clinical Signs and Endpoint Monitoring in the SOD1<sup>G93A</sup> model***

To assess the clinical signs of ALS in the SOD1<sup>G93A</sup> mice we used the common instrument, the rotarod (Harvard Apparatus). The rotarod is a complex test measuring a combination of limb strength, coordination, and gait. The rotarod consists of a rotating rod with a set acceleration (4 – 15 rpm in 60 s, or 0.2 rpm/s) and a set maximum rotation speed (15 rpm). WT and SOD1<sup>G93A</sup> mice were placed on the rod and the latency to fall was timed. Monitoring via the rotarod began the week following infection recovery and was performed weekly until mice were unable to complete the test due to ALS clinical signs. Rotarod times were averaged for each condition, weekly, and normalized to week 1 as 100%. The data was analyzed using a sigmoidal dose response with a least-squares fit modelled to the average latency to fall at each week. SOD1<sup>G93A</sup> mice were followed until they reached endpoint due to ALS progression. Mice were considered to be at endpoint when unable to right themselves within 30 s, on both sides.

### ***IAV Growth Curves***

WT and SOD1<sup>G93A</sup> MEFs were infected with a multiplicity of infection (MOI) of 3 IAV, or MOI 2 HSV-1, and viral growth rates were assessed using the plaque assay at 0, 2, 4, 8, 12, 24, and 48 h post-infection. WT and SOD1<sup>G93A</sup> mice were infected with 0.1LD<sub>50</sub> IAV at day 60, lungs were harvested and homogenized 4 dpi. Plaque assays were performed to assess viral titre against both media from MEFs and lung homogenates. MDCK cells were plated at  $6.5 \times 10^5$  cells per well in a 6-well plate and incubated overnight at 37 °C in 5 % CO<sub>2</sub>. Following incubation, viral samples were serially diluted 6× in 2× MEM (2× MEM (Minimum Essential Media), 40 mM L-glutamine, 1.5 % sodium bicarbonate, 200 mM HEPES, 2 mg/mL penicillin/streptomycin, 7 % BSA). Cells were infected with 250 µL of diluted viruses and incubated for 1 h at 37 °C in 5 % CO<sub>2</sub>. During the infection period, overlay was prepared by combining 1 % oxoid agar with 2× MEM at a 1:1 dilution, additionally 1 % DEAE-Dextran and 1 µg/mL TPCK-treated trypsin was added at a 1:100 dilution to the overlay. Following, the 1 h viral incubation, virus was removed, wells were washed with PBS, and 2 mL of overlay was added and incubated for 10 min at RT to allow agar to harden. Following overlay, plaque assays were incubated at 37 °C in 5 % CO<sub>2</sub> for 48 h. After the 48 h incubation, wells were fixed with 3.7 % PFA for 30 min at RT. PFA and agar overlay were removed, and cells were stained with crystal violet for 20 min at RT. Pfu/mL was calculated based on dilution factor and the number of plaques visualized per well.

### ***HSV-1 Growth Curves***

WT and SOD1<sup>G93A</sup> MEFs were plated in 6 well plates at a seeding density of  $5 \times 10^4$  cells per well and stored overnight at 37 °C with 5 % CO<sub>2</sub>. MEFs were then incubated with 400 uL HSV-1 Syn 17 at MOI 2 for 1 h. MEFs were washed once with sterile PBS and 2 mL of serum free media was added, denoting time 0 h. Supernatant was collected at 0, 6, 12, 18, 24, 48 and 72 h post-infection and frozen at -80 °C. Viral titres were determined via plaque assay on Vero cells. Vero cells were plated at a density of  $4 \times 10^5$  cells per well in a 6 well plate and stored overnight at 37 °C with 5 % CO<sub>2</sub>. Cells were then washed once with PBS and administered HSV-1 in a serial dilution. Cells were incubated with HSV-1 for 1 h, following which, HSV-1 containing media was removed and replaced with 2 mL of DMEM containing 5 % FBS and 1 % human serum. Plates were stored at 37 °C with 5 % CO<sub>2</sub> 48 h. Following the 48 h, media was removed and replaced with 2 mL of 3.7 % PFA for 20 min. Crystal violet was used to visualize plaque formation. Pfu/mL was calculated based on dilution factor and the number of plaques visualized per well

### ***Cytokine Analysis***

We assessed cytokine expression both *in-vitro* and *in-vivo*. *In-vitro*, WT and SOD1<sup>G93A</sup> MEFs were stimulated with the equivalent of MOI 10 of inactivated IAV and media was taken at 0, 4, 8, and 24 h post-stimulation. Cytokine levels in the media were assessed using a 32-plex cytokine array (EVE Technologies Corp.). Data was represented relative to the WT unstimulated cells at time 0. *In-vivo*, both lungs and brain were extracted from WT and SOD1<sup>G93A</sup> mice at 4- and 30-dpi, or 64 and 90 days of age. Tissue was homogenized with

a bullet homogenizer and cytokine levels within the homogenates were assessed using a 32-plex cytokine array (EVE Technologies Corp.). Data was represented relative to WT uninfected mice at the relative timepoints.

### ***Fluorescent Immunohistochemistry (IHC)***

Spinal cord sections were isolated using hydraulic extrusion, wherein WT and SOD1<sup>G93A</sup> mice were anesthetized and transcardially perfused with PBS. Lumbar spinal regions were hydraulically removed using 5 mL of PBS<sup>204</sup>. Following extrusion, the spinal sections were incubated in 3.7 % PFA for 48 h. Following which, spines were mounted in paraffin and sliced at 5 µm thickness. Sections were deparaffinized with 15 min of xylene twice and subsequently dehydrated using descending ethanol concentrations, 100%, 95%, 95%, 75%, and 75%, for 5 min each. Finally, slices were rehydrated in H<sub>2</sub>O for 5 min. Antigen retrieval was performed with either TRIS-EDTA (10mM TRIS, 1mM EDTA, pH 9) or citrate buffer (1×, pH 6) (Abcam Inc.) for 20 min at 95 °C. Following antigen retrieval, slices were washed 3× with PBS-T (0.1 % tween). Slices were permeabilized using 0.2 % Triton-X-100/0.1 % BSA/PBS for 15 min at RT, and then washed 3× PBS-T. Following permeabilization, slices were blocked with 10 % normal goat serum (Abcam Inc.)/1 % BSA/PBS for 30 mins. Spinal cord slices were incubated with primary antibodies overnight at 4 °C. Primary antibodies included Iba-1 [1:300] (Abcam Inc.), GFAP [1:500] (Abcam Inc.), NeuN [1:300] (Abcam Inc.), and AMF7-63 [1:1000] (Kind gift from Dr. Cashman), to target microglia, astrocytes, neurons, and misfolded SOD1 (mSOD1), respectively. Slices were then washed 5× with PBS-T and probed with compatible AlexaFluor-

conjugated secondary antibodies (all at 1:1000 dilution) (Life Technologies). Slices were washed 3× with PBS-T and DNA was counterstained using Hoechst-33342 (1 µg/mL) (Life Technologies) and mounted with EverBrite mounting medium (Biotium Inc.). Images were taken with the Zeiss Imager M2 microscope (Carl Zeiss Canada Ltd.) at the indicated magnification. Quantification of slices was performed using ImageJ. Iba-1 positive cells were counted per slice and quantified. Whereas GFAP and AMF7-63 spinal slices were quantified based on total fluorescence normalized to Hoechst-33342 fluorescence and the area of the slice.

#### ***Antiviral Gene Expression Quantification***

WT and SOD1<sup>G93A</sup> MEFs were plated and stimulated with 10 MOI of inactivated IAV for 0, 4, 8, and 24 h. RNA was isolated from stimulated MEFs using RNeasy isolation kit (QIAGEN) and 1 µg of complimentary DNA was synthesized according to manufacturer's instructions (Maxima First Strand cDNA Synthesis kit, Thermo Fisher Scientific). Expression levels of *ISG15*, *DDX58*, *IFIT1*, and *IFITM3* were assessed using SensiFAST SYBR reaction kit (Bioline Reagents Ltd.) and qRT-PCR. Relative fold change is demonstrated using unstimulated WT MEFs as the baseline for expression.

**Table 2.1: Primer information for antiviral gene expression**

<b>Gene Target</b>	<b>Primer Information</b>
<i>ISG15</i>	F 5' – TGGTACAGAACTGCAGCGAG – 3'
	R 5' – AGCCAGAACTGGTCTTCGTG – 3'
<i>DDX58</i>	F 5' – ATGTGCCCTACTGGTTGTG – 3'
	R 5' – CCCCAGAAATGCTCGCAATG – 3'
<i>IFIT1</i>	F 5' – CTTTACAGCAACCATGGGAGAGA – 3'
	R 5' – TGATGTCAAGGAACTGGACCTG – 3'
<i>IFITM3</i>	F 5' – GACAGCCCCCAAACCTACGAA – 3'
	R 5' – ATTGAACAGGGACCAGACCAC – 3'
<i>18S</i>	F 5' – GTAACCCGTTGAACCCATT – 3'
	R 5' – CCATCCAATCGGTAGTAGCG – 3'

***Statistical Analysis***

All data is represented using GraphPad Prism (v. 8) (GraphPad Software) and statistical analysis was performed using GraphPad Prism (GraphPad Software).

## CHAPTER 3

# Elucidating the Role of Senataxin on Class Switch Recombination

## 3.1 Introduction

### 3.1.1 Senataxin

Functional studies of SETX have unveiled pleiotropic functions within the cell. The primary role of SETX is to resolve R-loops via its helicase activity<sup>10,196,205–208</sup>. By resolving aberrant R-loops SETX acts to preserve genomic stability<sup>206</sup>. Additionally, our group has shown that SETX suppresses the anti-viral transcriptional response, such that a deficiency in SETX results in amplified expression of anti-viral mediators and inflammatory cytokines/chemokines following infection<sup>209</sup>. Interestingly, SETX<sup>-/-</sup> mice do not spontaneously develop any neurological clinical signs<sup>194</sup>. However, male SETX<sup>-/-</sup> mice are infertile and female SETX<sup>-/-</sup> mice have decreased fertility in comparison to WT mice. The infertility of SETX<sup>-/-</sup> male mice is the result of an accumulation of R-loops in actively transcribing/proliferating spermatocytes, as well the presence of unrepaired DSBs<sup>194</sup>. Interestingly, decreased fertility in male and female patients with AOA2 has also been reported<sup>9,210,211</sup>. Further, SETX colocalizes with a number of proteins involved in the DDR<sup>194,212–215</sup>, however, its specific role in the DDR remains unclear.

Intriguingly, the roles that have been demonstrated for SETX in terms of unwinding R-loops are unlikely to be influential in post-mitotic cells, such as neurons, which do not display high levels of R-loop formation<sup>216</sup>. This has led to the speculation that there may be other important functions for SETX that have not yet been discovered. As previously mentioned, SETX acts as a regulator of the antiviral response<sup>209</sup>. During viral infection the first line of defense is often the induction of type 1 IFNs and interferon stimulated genes (ISGs)<sup>217</sup>. Upon sensing of viral infection, IRF3 is activated. SETX seems to regulate the

antiviral response by promoting the early termination of RNA polymerase II at IRF3-dependent genes. Following viral infection, expression of antiviral genes was elevated in cells that were SETX deficient. Additionally, cells that were derived from AOA2 patients showed a marked increase in the expression of antiviral mediators during a viral infection<sup>209</sup>. Based on these results it is possible that over time, viral infections cause exaggerated inflammatory responses which eventually lead to neurotoxic effects.

SETX has been demonstrated to co-localize with 53BP1 and  $\gamma$ -H2AX (the phosphorylated form of H2AX)<sup>194,212,213</sup>. Both of these proteins have also been shown to play a role in CSR and are important in NHEJ. 53BP1 localizes to sites of DNA damage, particularly DSBs<sup>62</sup>, where it phosphorylates ATM<sup>64</sup>, which is involved in the activation of repair factors required for the DDR. CSR is reduced by approximately 90% in 53BP1-deficient B cells. However, there was no visible effect on cell viability<sup>65</sup>.  $\gamma$ -H2AX is also a DSB sensing protein that gets phosphorylated by ATM<sup>218</sup> and recruits various DNA repair proteins to the site of the DNA break. CSR is also reduced in mouse B cells with diminished levels of H2AX<sup>63</sup>.

### **3.1.2 RNA:DNA Hybrids**

R-loops are genomic structures consisting of 3 nucleic acid strands, 2 DNA strands and 1 RNA strand, wherein the nascent mRNA produced by RNA pol II reanneals to the DNA from which it was transcribed<sup>219</sup>, as depicted in Figure 3.1.1. As a result of the RNA-DNA hybridization, a strand of ssDNA becomes a vulnerable target for DNA damage. R-loops are normal physiological phenomena and can be either beneficial or detrimental

depending upon size, location, and duration prior to resolution. Prevalence of R-loops is tightly regulated, and alterations in R-loop formation can have pathogenic consequences<sup>219</sup>. R-loops are involved in a variety of cellular functions including CSR<sup>42</sup>, mitochondrial DNA replication<sup>220</sup>, and transcriptional regulation<sup>221</sup>. R-loops across promoters have been demonstrated to decrease methylation of the promoter which results in elevated transcription rates<sup>207</sup>. In comparison, R-loop formation across terminators promotes transcriptional termination<sup>222</sup>. R-loops can be induced by DNA strand breaks, negative supercoiling, high G:C content, repetitive DNA sequences, and DNA secondary structures such as G-quadruplexes (G4s)<sup>223,224</sup>.

Normally, R-loops are approximately 8bp in length, though this can range drastically<sup>225,226</sup>. During transcription, Pol II produces an mRNA transcript which can then “thread back” into the DNA as it feeds out of the polymerase<sup>48</sup>. R-loops are highly stable once formed, since DNA-RNA interactions are stronger than DNA-DNA interactions<sup>227</sup>. Additionally, G4s can form on the remaining ssDNA, increasing stability of the ssDNA, and thereby enhancing the stability of the entire R-loop structure<sup>228</sup>. Stable unresolved R-loops can be particularly problematic. During DNA replication, stalled RNA pol II, induced by R-loop accumulation, can collide with the replication machinery leading to DNA breaks and elevated genomic instability<sup>229–231</sup>.

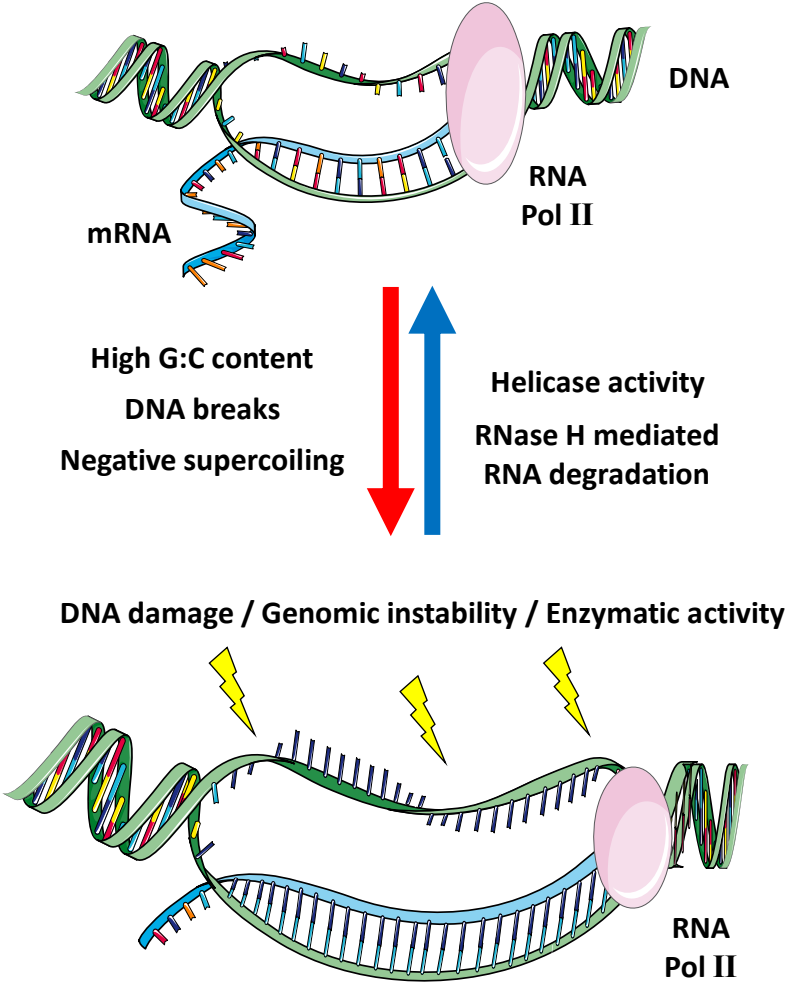


**Figure 3.1.1: The structure of an R-loop**

R-loops are 3-stranded genomic structures which form behind RNA Pol II during transcription. Following transcription, recently formed mRNA anneals to the DNA from which it was formed. R-loops form physiologically and are found at lengths of 8-10 bp. However, as a result of breaks in the DNA, regions of negative supercoiling, or a high G:C content, R-loops become extended and are found in higher abundance. As a result of the elevated RNA-DNA hybridization, a ssDNA strand remains unannealed and is a target for DNA damage leading to elevated genomic instability. R-loops can be resolved via RNaseH- and helicase-mediated mechanisms which act to restore genomic stability by reducing R-loop levels in the genome.

Given the potential risks posed by R-loops, it is unsurprising that the cell has evolved mechanisms of resolving these structures. These include the THO complex, RNase H1, topoisomerases, and R-loop specific helicases. The THO complex recruits mRNA export factors to promote the efficient packaging of pre-mRNA, thereby preventing R-loop formation by preventing free mRNA<sup>232</sup>. A more direct countermeasure for R-loops involves R-loop specific enzymes such as RNase H1. RNase H1 targets RNA within an R-loop and results in its degradation<sup>233–235</sup>. An additional way the cell can attempt to prevent R-loop formation is via topoisomerase 1 (TOP1). In order to prevent R-loop formation, TOP1 acts to relax negative supercoiling, which promotes R-loop formation<sup>236,237</sup>. Finally, R-loop specific helicases can unwind R-loops in an ATP-dependent manner, thus releasing and preserving the RNA moiety. R-loop specific helicases include Mtr4<sup>196,238</sup>, DDX1<sup>200</sup>, and SETX<sup>10,194,196,205–208</sup>. Therefore, while R loop formation is a normal cellular process, it must be tightly regulated to prevent DNA damage from occurring.

R-loops have been implicated in diseases ranging from cancers to neurodegenerative disorders. In disease states, R-loops can originate from expansion repeats, which increase the propensity for R-loop formation, or mutations in proteins known to antagonize R-loop formation, thereby preventing the resolution of R-loops<sup>219</sup>. An example of R-loops originating from repeat expansions can be illustrated by C9orf72 mutations implicated in ALS. Normal C9orf72 alleles consist of approximately 30 GGGGCC repeats. However, patients with C9orf72-associated ALS can have as many as 1000 hexanucleotide repeats<sup>239</sup>. The repeat expansion within C9orf72 results in an elevated propensity for R-loops and G4, resulting in increased DNA damage and DSB

accumulations<sup>240,241</sup>. The accumulation of R-loops, and the resulting DNA damage, has been suggested as a potential etiology for C9orf72-associated ALS. A further expansion associated with ALS is the polyQ expansion within the Ataxin-2 (ATXN2) gene<sup>242</sup>. ATXN2 interacts with TAR DNA binding protein 43 (TDP-43), promoting TDP-43 aggregation. The propensity for TDP-43 aggregation increases with the number of CAG repeats in the ATXN2 gene<sup>243</sup>. The yeast homolog of ATXN2 regulates R-loop formation by preventing the induction of R-loops at sites with high propensity for G4 formation. CAG repeat expansions also results in elevated R-loop accumulation<sup>244</sup>. Mutations in R-loop resolving enzymes can also cause disease, such is the case for SETX. As previously mentioned SETX acts to resolve R-loops. Most interestingly, SETX mutations are associated with both AOA2<sup>6</sup> and ALS4<sup>10</sup>, depending upon whether those mutations are a loss-of-function or a gain-of-function, respectively.

### **3.1.3 RNA Helicases and CSR**

RNA helicases have been reported to play an active role during CSR, namely the helicases Mtr4<sup>196</sup> and DDX1<sup>200</sup>. Interestingly, the aforementioned RNA helicases have been demonstrated to impact CSR via differing mechanisms, suggesting multiple roles for RNA helicases in CSR. Mtr4 recruits the RNA exosome to the sites of R-loops within the S-regions. The RNA exosome targets the RNA moiety of R-loops within S-regions, allowing AID access to the sense strand of the DNA<sup>196</sup>. The RNA exosome plays an important role in facilitating AID targeting of both strands within a S-region<sup>245</sup>, and Mtr4 is required to ensure appropriate localization of the RNA exosome<sup>196</sup>.

Comparatively, DDX1 binds to, and unwinds, G4 structures in intronic S-region RNA resulting in the targeting of AID to S-regions<sup>200</sup>. In this model, the intronic S-region RNA acts as a trans-R-loop, rather than a cis-R-loop. A cis-R-loop refers to the typical R-loop model in which nascent RNA exiting RNA pol II binds to the template DNA, while a trans-R-loop is when external RNA is introduced to open DNA causing an R-loop to form. DDX1 promotes R-loop formation with the non-template DNA strand thereby recruiting AID to the S-region<sup>200</sup>. DDX1 has also been implicated in the DDR. DDX1 is phosphorylated by ATM following DSBs<sup>246</sup>. Additionally, DDX1 depletion alters the microhomology usage at S-region recombination sites<sup>200</sup>. Therefore, DDX1 may influence CSR at multiple levels.

Interestingly, the authors of the Mtr4 paper used SETX-KO CH12 cells as a RNA:DNA helicase control<sup>196</sup>. The CH12 murine cell line is a unique system that has been used for over 30 years for the study of CSR<sup>247</sup>. CH12 cells are only capable of switching from IgM to IgA upon cytokine stimulation<sup>248</sup>, making them an excellent model for the study of CSR. CRISPR-mediated knockout of SETX in murine CH12 cells caused a modest defect in the ability of these cells to become IgA<sup>+</sup> upon initiation of CSR<sup>196</sup>. However, whether this occurs in B cells under physiological conditions was unclear.

### **3.1.4 DNA Damage Factors and CSR**

In addition to the proteins classically associated with NHEJ, many sensors of the DDR are crucial for efficient CSR. Sensors of the DDR that are involved in CSR include  $\gamma$ -H2AX, 53BP1, MDC1, and ATM<sup>249</sup>. During CSR DNA damage is induced by AID

activity in a highly regulated manner and locus of the genome<sup>49</sup>. The programmed nature of DNA damage induction during CSR ensures a more controlled program of DNA repair than when damage occurs via physical or environmental insult.

ATM is a major orchestrator the DDR, activating a variety of cellular pathways in response to DSBs<sup>250</sup>. ATM is the gene mutated in A-T<sup>251</sup>, a form of ARCA, which is also characterized by an SIgAD in 60-80% of afflicted individuals<sup>7</sup>. The function of ATM in CSR remains unclear, though reduced expression of ATM has been reported to cause CSR rates to decrease by 30%<sup>252</sup>, and concomitant increases in microhomology usage<sup>249</sup>. However, ATM phosphorylates, and activates, a panel of DDR-associated proteins including 53BP1, H2AX, MDC1, and many others<sup>253</sup>. Indeed, upon activation ATM has been demonstrated to potentially interact with and activate 100s of proteins with distinct cellular roles<sup>254</sup>, including induction of AID phosphorylation. AID phosphorylation by ATM increases the localization of AID to S-regions but does not affect the functionality of AID<sup>255</sup>. Therefore, the role of ATM in both DDR and CSR is likely associated with the recruitment and activation of DDR factors.

H2AX is a histone that plays an important role in the recognition of DNA damage. Upon induction of DSBs H2AX is phosphorylated ( $\gamma$ -H2AX) by ATM, ATR, and/or DNA-PKcs<sup>256-258</sup>. Foci of  $\gamma$ -H2AX are rapidly formed flanking DSBs up to a megabase<sup>259</sup>, and recruit DNA repair proteins<sup>258,260</sup>. The role of  $\gamma$ -H2AX in the DDR is not restricted to CSR, but rather is a general response to DSBs in the DNA that promotes recognition of DNA damage and recruitment of DNA repair factors<sup>261</sup>. B cells deficient in H2AX exhibit a deficiency in switching to all isotypes<sup>63</sup>. Upon further analysis it was discovered that in B

cells that switched the S-region junctions were normal. However, IgH locus chromosomal breaks were elevated<sup>262,263</sup>, suggesting that  $\gamma$ -H2AX may act as a facilitator of long-range DNA repair necessary for CSR. MDC1 deficient mice demonstrate a similar phenotype to that of  $\gamma$ -H2AX deficient mice<sup>264</sup>. MDC1 acts to retain DDR factors at sites of DNA damage in a  $\gamma$ -H2AX dependent manner and amplifies the ATM response by retaining active ATM in the area of DNA damage<sup>264,265</sup>. MDC1 functionality may be more important during HR rather than NHEJ, which relies more upon 53BP1<sup>266</sup>.

53BP1 is also a target of ATM and becomes phosphorylated in response to DNA DSBs following recruitment by  $\gamma$ -H2AX<sup>267</sup>. 53BP1 is an important mediator of DSB repair. It acts as a scaffold for DNA repair factors, promotes checkpoint signalling, and regulates DNA repair pathway usage<sup>267,268</sup>. The major function of 53BP1 is to promote NHEJ by preventing the resection of DNA ends<sup>269</sup>. 53BP1 has no enzymatic activity but is a large, approximately 350 kDa protein, with many interaction partners<sup>270,271</sup>. 53BP1 promotes checkpoint signalling by amplifying ATM activity via anchoring ATM and further downstream targets of ATM such as p53 and BRCA1<sup>272</sup>. 53BP1 also prevents the resection of DNA following a DSB which greatly promotes NHEJ<sup>273</sup>. The role of 53BP1 in CSR is not entirely understood, however, it clearly plays a critical role. In 53BP1 deficient B cells CSR is reduced by 90%, with no increase in microhomology<sup>65,274</sup>. 53BP1 brings donor S $\mu$  DNA ends in close to proximity to acceptor S-regions using chromosomal conformation capture<sup>275</sup>. Further, 53BP1 deficiency results in an increase in a-EJ due to elevated rates of ATM mediated DNA-end resection<sup>273</sup>.

The factors discussed above all play active roles in the DDR. Deficiencies in these proteins cause phenotypes which include stunted growth, immunodeficiencies, male-specific infertility, enhanced sensitivity to radiation, elevated genomic instability, and accelerated aging<sup>1,266,276–279</sup>.

### **3.1.5 Alternate End Joining during CSR**

While NHEJ is the main driver of the DDR, a-EJ also plays a role in CSR. The DNA damage that occurs during CSR results in a recombination between specific DNA regions. While CSR typically relies on NHEJ, CSR can still occur in the absence of proteins essential for NHEJ, as discussed above. When NHEJ is unavailable, a-EJ can be used to complete the DNA repair, which is characterized by an increase in the rate of microhomology usage<sup>114,280,281</sup>.

CSR is also unique in that the DNA repair occurs over a long range within the DNA, up to 200kb. An essential component of DNA repair during CSR is the tethering of DNA ends within close proximity, which is an important role of 53BP1<sup>275</sup>. As a result, 53BP1 depletion results in a severe defect in CSR<sup>274,282</sup>. ATM<sup>252</sup> and H2AX<sup>63,283</sup> depletion also affect CSR and like 53BP1 depletion, result in an increased usage of microhomology for DNA repair. Together, these results indicate that a-EJ is used as a back-up pathways for DNA repair when cells are deficient in NHEJ<sup>249</sup>.

Under normal conditions, even when NHEJ is fully functional, there are still some rates of microhomology usage in S-region repair<sup>280,281</sup>, suggesting that a-EJ occurs in normal B cells during CSR. Whether the usage of a-EJ in CSR is specific to certain isotypes,

or if a-EJ is simply employed stochastically during intense periods of DNA damage remains to be explored.

### **3.1.6 Hypothesis**

Herein, we hypothesize that SETX is involved in the regulation of CSR and SHM based on its roles in resolving R loops and facilitating the DDR. To explore this hypothesis, we have multiple aims.

1. To determine the role of SETX on CSR *ex vivo* in an antigen-independent B cell intrinsic manner.
2. To determine the role of SETX on CSR during an *in vivo* immunization model.
3. To determine the mechanistic role of SETX during CSR.

## 3.2 Results

### ***3.2.1 SETX deficiency alters the magnitude and kinetics of class switch recombination ex-vivo***

To explore the role of SETX on CSR in an antigen-independent system, we isolated splenocytes from naïve SETX<sup>+/+</sup> or SETX<sup>-/-</sup> mice and stimulated them *ex vivo* with polyclonal stimulants to induce CSR<sup>198</sup>. Following stimulation, we assessed the frequency of IgM-, IgG- and IgA-secreting B cells by ELISpot at days 0, 1, 3, and 5 post-stimulation (Fig. 3.1). Frequencies of both IgM- and IgG-producing B cells were similar throughout the time-course of stimulation (Fig. 3.1A and 3.1B). Ultimately, following 5 days of stimulation, we observed a higher frequency of IgA-producing B cells from SETX<sup>+/+</sup> mice relative to SETX<sup>-/-</sup> mice at this timepoint (Fig. 3.1C). Furthermore, the frequency of IgA-producing B cells from SETX<sup>+/+</sup> mice increased over the 5 days of stimulation, while IgA-producing B cells from SETX<sup>-/-</sup> mice remained relatively unchanged (Fig. 3.1C). These results demonstrate that SETX<sup>-/-</sup> B cells display impaired IgA class-switching upon *ex vivo* polyclonal/antigen-independent stimulation.

### ***3.2.2 SETX deficiency alters the rate of B cell proliferation***

Given that SETX deficiency impaired IgA class-switching *ex vivo*, we explored whether this might reflect differences in B cell death or proliferation. Using a live/dead stain we observed no statistical difference in the percentage of apoptotic SETX<sup>+/+</sup> and SETX<sup>-/-</sup> B cells at days 3 and 5 post-stimulation (Fig. 3.2A). Therefore, the deficiency in IgA-secreting SETX<sup>-/-</sup> B cells is unlikely to be due to a gross increase in apoptotic cells.

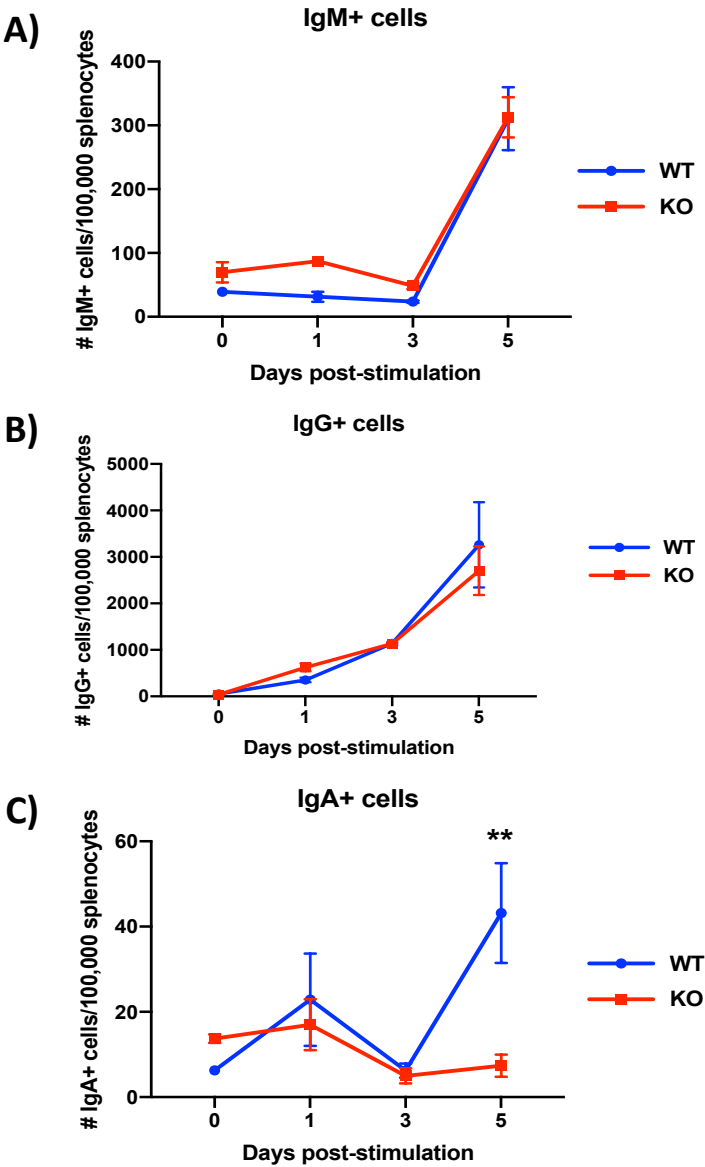


**Figure 3.1: SETX deficiency alters the magnitude and kinetics of class-switch recombination *ex vivo*** SETX<sup>+/+</sup> (WT) and SETX<sup>-/-</sup> (KO) naïve splenocytes were isolated and stimulated with a polyclonal stimulation. Antibody isotype switching was observed following 0, 1, 3, and 5 days of stimulation and demonstrated as IgM (A), IgG (B), and IgA (C) isotypes. n = 3 and p < 0.01, \*\* was determined using two-way ANOVA with a Bonferroni post-hoc test.

Switching to IgA requires 5-7 rounds of cellular division<sup>284</sup> and consequently, differences in the frequencies of IgA-secreting B cells may reflect differences in rate of proliferation between SETX<sup>+/+</sup> and SETX<sup>-/-</sup> B cells. Following 72 h of polyclonal stimulation, SETX<sup>-/-</sup> B cells had a higher proportion of cells with 0-2 cell divisions compared to SETX<sup>+/+</sup> B cells, additionally a subsequent decrease in the percentage of cells at later divisions, 4-6, compared to the SETX<sup>+/+</sup> B cells (Fig. 3.2B). Using flow cytometry, we also analyzed the expression of IgA in CD19<sup>+</sup> cells (Fig. 3.2C and 3.2D), we confirmed the ELISpot data (Fig. 3.1C) and demonstrated that SETX<sup>-/-</sup> and SETX<sup>+/+</sup> have similar IgA expression (Fig. 3.2D). We chose 72 h post-stimulation for our assessment because SETX<sup>+/+</sup> and SETX<sup>-/-</sup> B cells diverge in IgA expression at 5 days post-stimulation therefore proliferation deficits were more likely to be seen at 3 days post-stimulation. SETX deficiency results in proliferative defects in B cells post-stimulation.

### ***3.2.3 SETX deficiency alters the kinetics of IgA production during a primary immune response***

Given the deficiency in IgA-secreting SETX<sup>-/-</sup> cells observed *ex-vivo*, we next explored the profile of antibodies in serum following a primary vaccination. To assess the role of SETX in a natural model of antigen-dependent CSR, we vaccinated SETX<sup>+/+</sup> and SETX<sup>-/-</sup> mice with formalin-inactivated IAV and analyzed the titers of both total and antigen-specific IgM, IgG, and IgA antibodies in serum at days 7, 14, and 30 post-vaccination (Fig. 3.3A-C). At day 7 post-vaccination (Fig. 3.3A) we observed no differences in total antibody levels when comparing SETX<sup>+/+</sup> and SETX<sup>-/-</sup> mice.

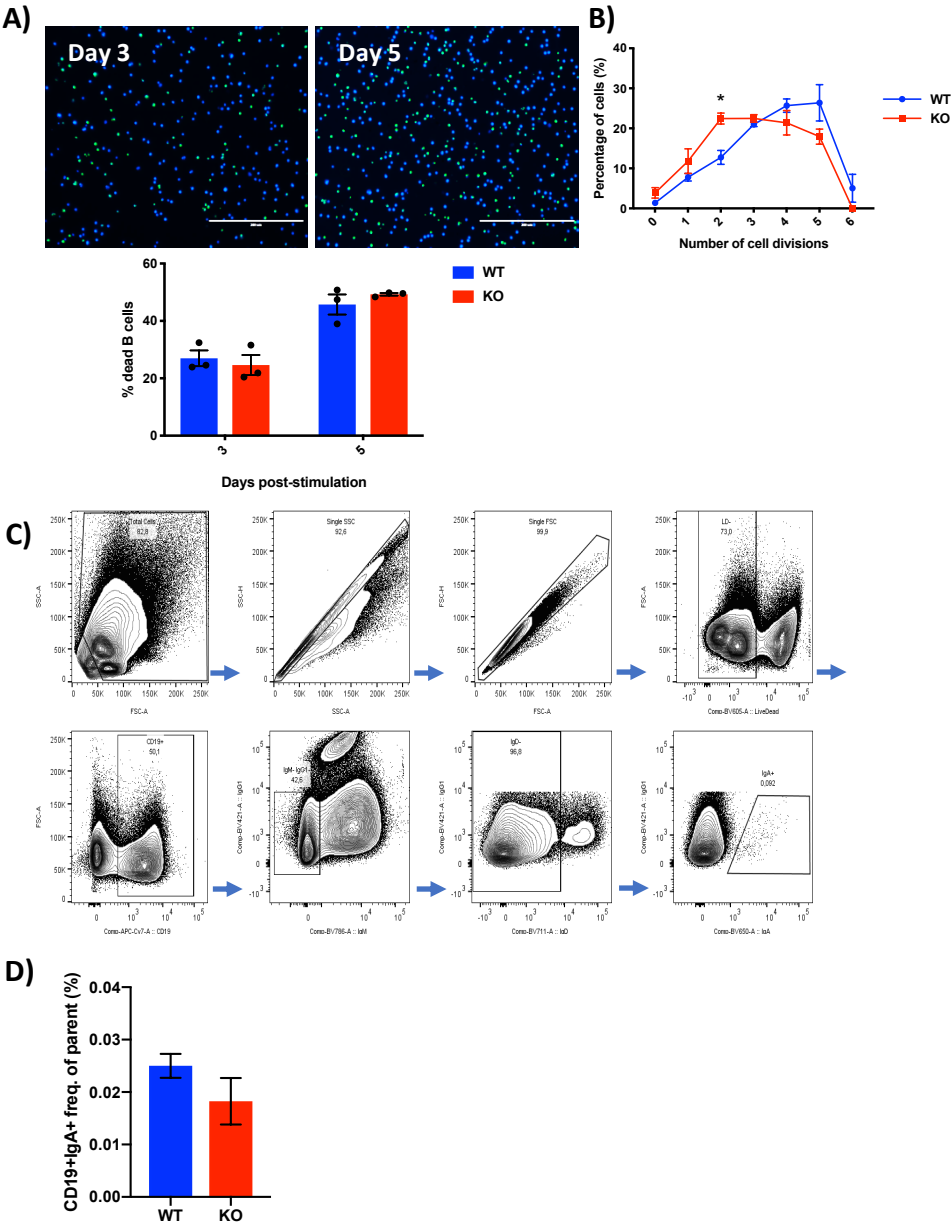


**Figure 3.2: SETX deficiency alters the rate of B cell proliferation**  
 SETX<sup>+/+</sup> (WT) and SETX<sup>-/-</sup> (KO) naïve splenocytes and B cells were isolated and stimulated with a polyclonal stimulation. (A) B cells were stained with live/dead stain at days 3 and 5 post-stimulation. The percentage of dead cells were quantified by the overlap of the live (blue) and dead (green) staining of cells. N = 3. (B) B cells were stained with 10uM CFSE prior to stimulation and stimulated for 72hrs. CFSE stained cells were assessed using flow cytometry with a minimum cell count of 1,000,000 cells. B cells were quantified for the percentage of cells per cellular division using the proliferation tool in FlowJo. N = 3, p < 0.05, \*, was determined using two-way ANOVA with a Bonferroni post-hoc test. (C) The gating strategy for CD19+/IgM-/IgG1-/IgD-/IgA+ cells isolated from whole splenocytes following polyclonal stimulation for 72hrs. (D) The percentage of CD19+/IgA+ cells were compared between SETX<sup>+/+</sup> and SETX<sup>-/-</sup> populations. N = 4.

Equivalent total antibody titers persisted at days 14 (Fig. 3.3B) and 30 (Fig. 3.3C) post-vaccination. We also measured antigen-specific antibody titers. At day 7 we observed a slight elevation in both antigen-specific IgG and IgM and a complete absence of antigen-specific IgA in SETX<sup>-/-</sup> mice (Fig. 3.3A). At day 14 post-vaccination there was a slight elevation in antigen-specific IgM in SETX<sup>-/-</sup> mice, however, antigen-specific IgG levels had normalized, and antigen-specific IgA remained substantially lower in SETX<sup>-/-</sup> mice (Fig. 3.3B). By day 30, antigen-specific antibodies of all isotypes had equalized (Fig. 3.3C). However, we explored the IgA expression at 14 days post-vaccination via the ELISpot assay for total (Fig. 3.3D) and antigen-specific (Fig. 3.3E) antibody producing cells, isolated from the spleen, and demonstrated no difference in IgA production at this time point. These results demonstrate that SETX<sup>-/-</sup> mice exhibit a kinetic delay in the generation of antigen-specific IgA during a primary immune response.

#### ***3.2.4 SETX deficiency has little effect on IgA titers during secondary immune responses following homologous vaccination***

In SETX deficient mice, class switching of antigen-specific B cell to IgA was delayed. To explore whether SETX deficiency also affected IgA production during a memory response, we performed a homologous vaccination with formalin-inactivated PR8 H1N1. At day 7 post-boost, we observed no statistical difference between total or PR8-specific antibody IgM, IgG, or IgA (Fig. 3.3F). These results suggest that SETX deficiency specifically affects the primary switching to the IgA isotype and not the reactivation of previously switched IgA B cells.

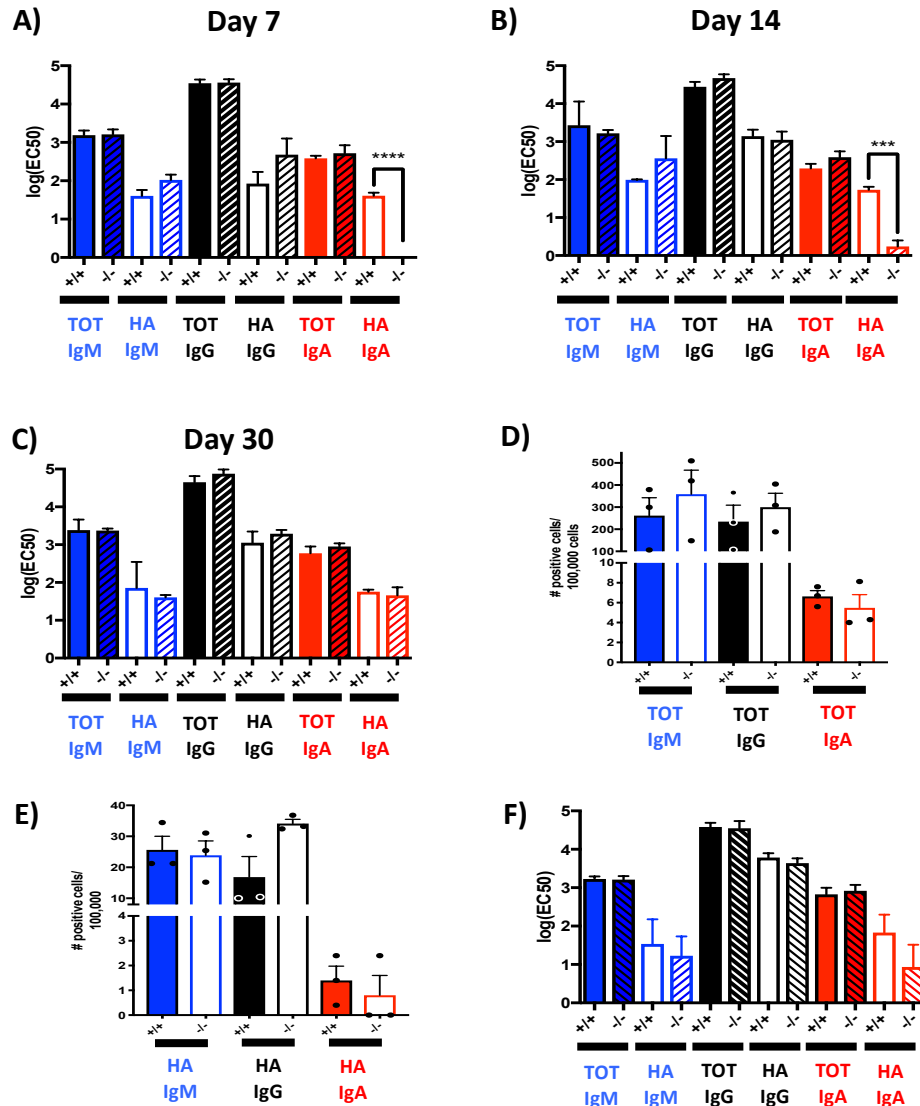


**Figure 3.3: SETX deficiency alters the kinetics of a primary immune response**

SETX<sup>+/+</sup> and SETX<sup>-/-</sup> mice were vaccinated with 50µg of formalin-inactivated PR8 influenza virus *i.m.*. Following vaccination, we performed cheek bleeds on days 7 and 14 followed by a cardiac bleed on day 30. Serum was isolated from the blood samples and via ELISA we quantified both total and PR8-HA specific antibody isotype levels. The log(ELISA) values for the antibody titers were averaged for day 7 (A), day 14 (B), and day 30 (C) post-vaccination. N = 4. D) Splenocytes were isolated from vaccinated mice at day 14 and assessed via ELISPOT for total antibody secreting cells. N = 3. E) Splenocytes were isolated from vaccinated mice at day 14 and assessed via ELISPOT for antigen-specific antibody secreting cells. N = 3. F) A secondary immune response was elicited via homologous boost at 30 days post-primary vaccination and antibody levels in sera were assessed via ELISA 7 days post-boost. N = 3. Statistical analysis was performed using the one-way ANOVA with Bonferroni post-hoc test, p < 0.001, \*\*\*, and p < 0.0001, \*\*\*\*.

Further experimentation needs to be performed to determine the significance of SETX on a secondary immune response. However, a primary IgA response is kinetically altered in SETX deficient conditions.

### ***3.2.5 SETX deficiency reduces the diversity of the IgA repertoire post-vaccination***

Our data indicates that SETX regulates class switching to the IgA isotype. Given the initial defect in IgA switching observed post-primary vaccination that equalized at later times, it is possible that the IgA repertoire is likely less diverse in SETX deficient conditions due to a bottleneck in the number of B cell clones that become IgA-positive. To explore diversity within the IgA repertoire, SETX<sup>+/+</sup> and SETX<sup>-/-</sup> mice were vaccinated with inactivated IAV *i.m.* and spleens were isolated at 14 days post-vaccination, chosen for our ELISA data of the antigen-specific antibodies in the serum of vaccinated mice (Fig. 3.3). To assess the diversity of the IgH repertoire we used a molecular barcoding high-quality sequencing approach<sup>202</sup>.

To this end, total RNA was isolated from whole splenocytes, and sequencing was performed on an Illumina Mi-Seq platform using asymmetric 400+200-nt paired-end sequencing. The IgH repertoire was visualized using Circo plots for both SETX<sup>+/+</sup> (Fig. 3.4A) and SETX<sup>-/-</sup> (Fig. 3.4B). Circo plots can be read as follows, all sequences, on the bottom half of the circle, are mapped to the various isotypes, on the top half of the circles, with the size of the connecting coloured lines representing the number of reads that mapped to that sequence. Quantification of the diversity of both the IgA and IgG repertoires was calculated using the Hill's diversity measure for both SETX<sup>+/+</sup> and SETX<sup>-/-</sup> repertoires.

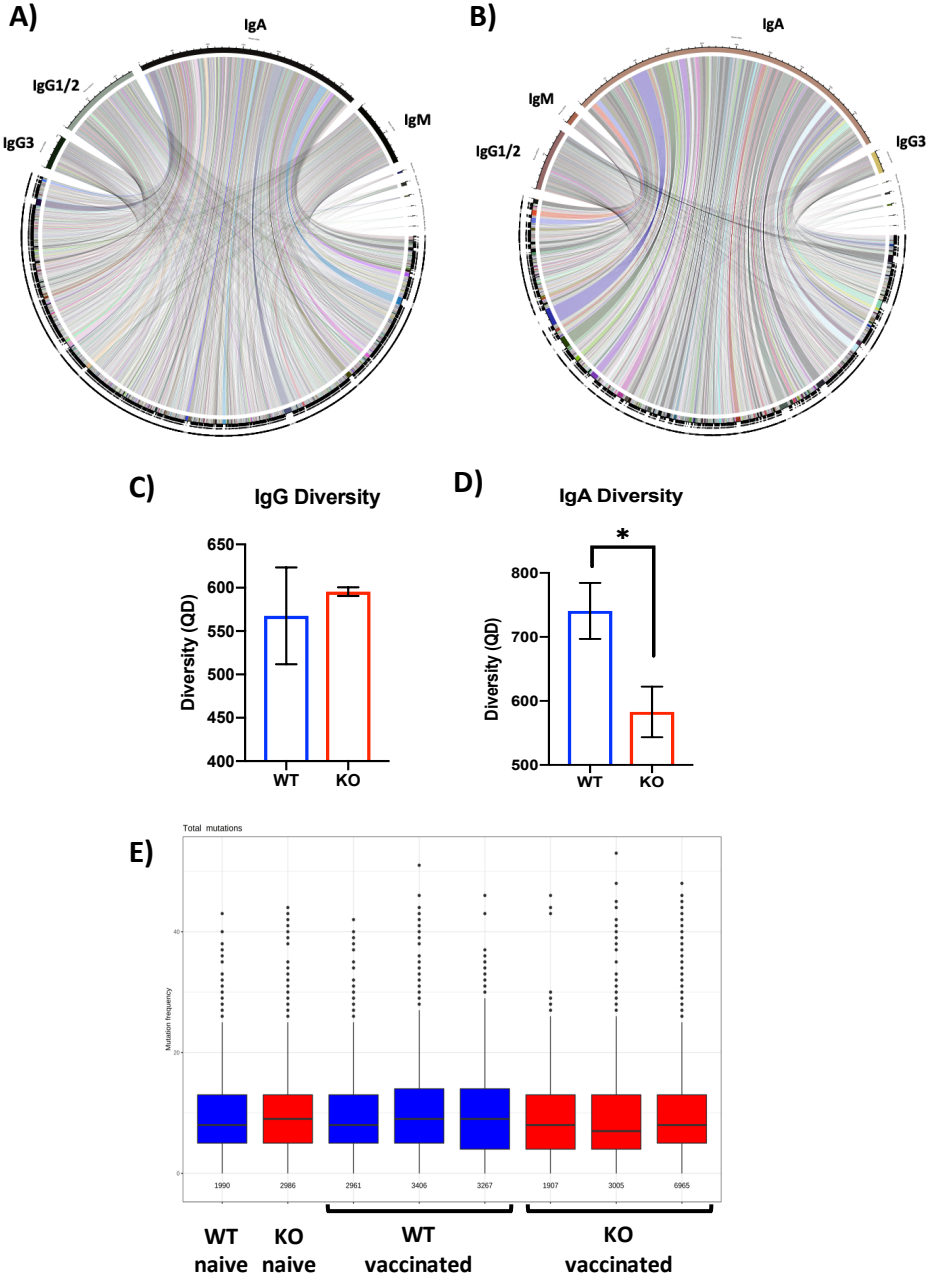


**Figure 3.4: SETX deficiency alters the diversity within the IgA repertoire**  
 SETX<sup>+/+</sup> (WT) and SETX<sup>-/-</sup> (KO) mice were vaccinated with formalin-inactivated IAV *i.m.*. 14 days post-vaccination, spleens were removed, and RNA isolated from whole splenocytes. A and B) The Ig repertoire was assessed via deep-sequencing and diversity was visualized using circo plots, WT (A) and KO (B). C and D) The Hills diversity of the IgG (C) and IgA (D) repertoire was quantified at q = 0. Statistics were performed on n = 3 with p < 0.05, \* determined via student's T-test. E) The WT and KO mice IgA variable regions were assessed for the overall mutation rate compared to a germline sequence, n = 3.

The Hill's diversity measure is a method which takes different diversity measures into account with different preferences given to species abundance at varying  $q$  values. At  $q = 0$ , an equal weight is given to each sequence and therefore is the most direct measure of diversity. Therefore, we used the Hill's diversity measure at  $q = 0$  for both SETX<sup>+/+</sup> and SETX<sup>-/-</sup>. The IgG repertoire was found to have no difference in diversity between SETX<sup>+/+</sup> and SETX<sup>-/-</sup> repertoires (Fig. 3.4C), whereas the SETX<sup>-/-</sup> IgA repertoire was significantly less diverse than the SETX<sup>+/+</sup> IgA repertoire (Fig. 3.4D). Interestingly, the mutation rates within the IgA repertoire (Fig. 3.4E) was unaffected suggesting that SETX deficiency does not affect SHM rates. These results suggest that fewer B cells are filling the IgA repertoire in SETX deficient conditions, indicating a difficult class switching to the IgA isotype.

### ***3.2.6 SETX deficiency alters the distribution of R-loops within the IgH locus***

SETX acts directly upon R-loops as an RNA:DNA helicase, and R-loops are known to be important during CSR<sup>10,37-42,55,205,207,208,285</sup>. To quantify the relative abundance of R-loops at specific regions of the IgH locus (Fig. 3.5A) B cells received either no treatment, polyclonal stimulation, or IgA-specific stimulation for 24h. Chromatin was then isolated from cells and DRIP was performed. SETX deficiency resulted in a general increase in R-loops at different loci within the IgH locus (Fig. 3.5B-D). This trend was consistent after cells were treated with polyclonal stimulation (Fig. 3.5C) and IgA-specific stimulation conditions (Fig. 3.5D). Additionally, we explored the relative expression levels of GLT and AID. SETX<sup>+/+</sup> and SETX<sup>-/-</sup> cells demonstrated equal expression of GLT and AID following stimulation (Fig. 3.5E).

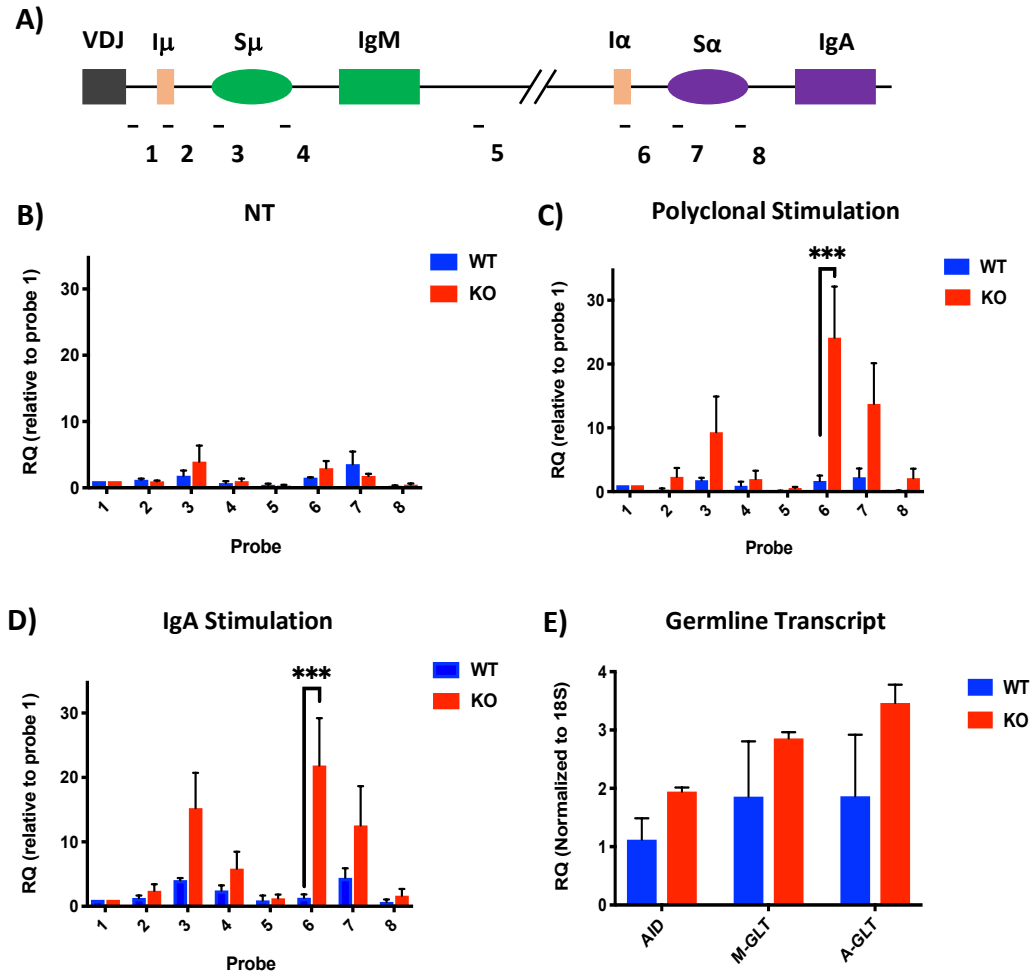


**Figure 3.5: SETX deficiency alters the localization and magnitude of R-loops within the IgH locus**

To assess the role of SETX on R-loop formation within the IgH locus we isolated R-loops from whole DNA and probed the IgH locus for their prevalence (A) A not to scale representative image of the mouse IgM and IgA regions within the IgH locus, approximate probe locations are marked. DNA was isolated from whole splenocytes and R-loops were immunoprecipitated following 24hours of (B) no treatment, (C) polyclonal stimulation, and (D) IgA specific stimulation. (E) RNA was isolated from splenocytes treated with IgA stimulation for 72 hours and the expression levels of AID, IgM-GLT, and IgA-GLT were assessed via q-PCR. n = 3. Statistics were determined via two-way ANOVA with Bonferroni post-hoc test,  $p < 0.001$ , \*\*\*.

These results suggest that all mechanisms up to and including transcription of the IgA locus are intact in SETX deficient conditions, suggesting that the defect in switching to IgA lies downstream of transcriptional activation of the IgA locus.

### ***3.2.7 SETX deficiency alters the kinetics of the DNA damage response***

SETX has been previously demonstrated to colocalize with multiple markers of the DDR in HeLa cells<sup>213</sup>. Many of these DDR proteins have essential functions during CSR. Therefore, we hypothesized that SETX might play a role in the DDR induced in B cells during CSR. We explored the role of SETX on the kinetics of the DDR. Since this is difficult to track in non-adherent B cells, we utilized MEFs treated with various DNA damaging agents. SETX<sup>+/+</sup> and SETX<sup>-/-</sup> MEFs were treated for 30 min with 0.5 mM H<sub>2</sub>O<sub>2</sub> or 20 μM phleomycin, which act as a general DNA damaging agent and an intercalating agent that induces DSBs, respectively. The DNA damaging agents were then removed, and cells were monitored for 24 h. As markers of DNA damage, we tracked p-ATM foci formation (Fig. 3.6) and γ-H2AX foci formation (Fig. 3.7).

We assessed the role of SETX on the DDR by quantifying p-ATM foci formation. ATM responds to DSB induction and is rapidly auto-phosphorylated upon activation<sup>286</sup>. Following induction of DNA damage cells were stained with anti-p-ATM antibodies (Fig. 3.6A). Upon treatment with H<sub>2</sub>O<sub>2</sub>, SETX<sup>+/+</sup> MEFs responded strongly and rapidly to DNA damage, inducing high levels of p-ATM foci positive cells. In comparison, SETX<sup>-/-</sup> MEFs exhibit minimal induction of p-ATM foci following treatment with H<sub>2</sub>O<sub>2</sub> (Fig. 3.6B). Further, upon treatment with phleomycin, p-ATM foci formation was potently induced in

SETX<sup>+/+</sup> MEFs, while p-ATM foci induction was much lower in the SETX<sup>-/-</sup> MEFs (Fig. 3.6C). These results suggest that there is a deficit in the recruitment or activation of DNA repair factors in SETX deficient conditions.

In addition to p-ATM, we assessed the effect of SETX deficiency on  $\gamma$ -H2AX foci formation after inducing DNA damage. Cells positive for  $\gamma$ -H2AX induction were quantified in the same manner as p-ATM positive cells (Fig. 3.7A). We found that at baseline there were slightly more  $\gamma$ -H2AX-positive SETX<sup>-/-</sup> MEFs in comparison to SETX<sup>+/+</sup> MEFs. However, upon induction of the DDR with H<sub>2</sub>O<sub>2</sub> treatment the SETX<sup>-/-</sup> MEFs had slightly less  $\gamma$ -H2AX-positive cells compared to SETX<sup>+/+</sup> MEFs. Following removal of H<sub>2</sub>O<sub>2</sub>, the SETX<sup>-/-</sup> MEFs exhibited similar numbers of  $\gamma$ -H2AX-positive cells over time when compared to SETX<sup>+/+</sup> MEFs (Fig. 3.7B). Following treatment with phleomycin, SETX<sup>+/+</sup> MEFs exhibit peak  $\gamma$ -H2AX foci formation at 1 h following agent removal, whereas SETX<sup>-/-</sup> MEFs exhibit the peak response at 2 h following agent removal (Fig. 3.7C). Together, these results suggest that SETX<sup>-/-</sup> cells have a defect in recognizing and/or repairing DNA damage, which would be consistent with our earlier observations of a defect in CSR to IgA downstream of IgA locus transcription.

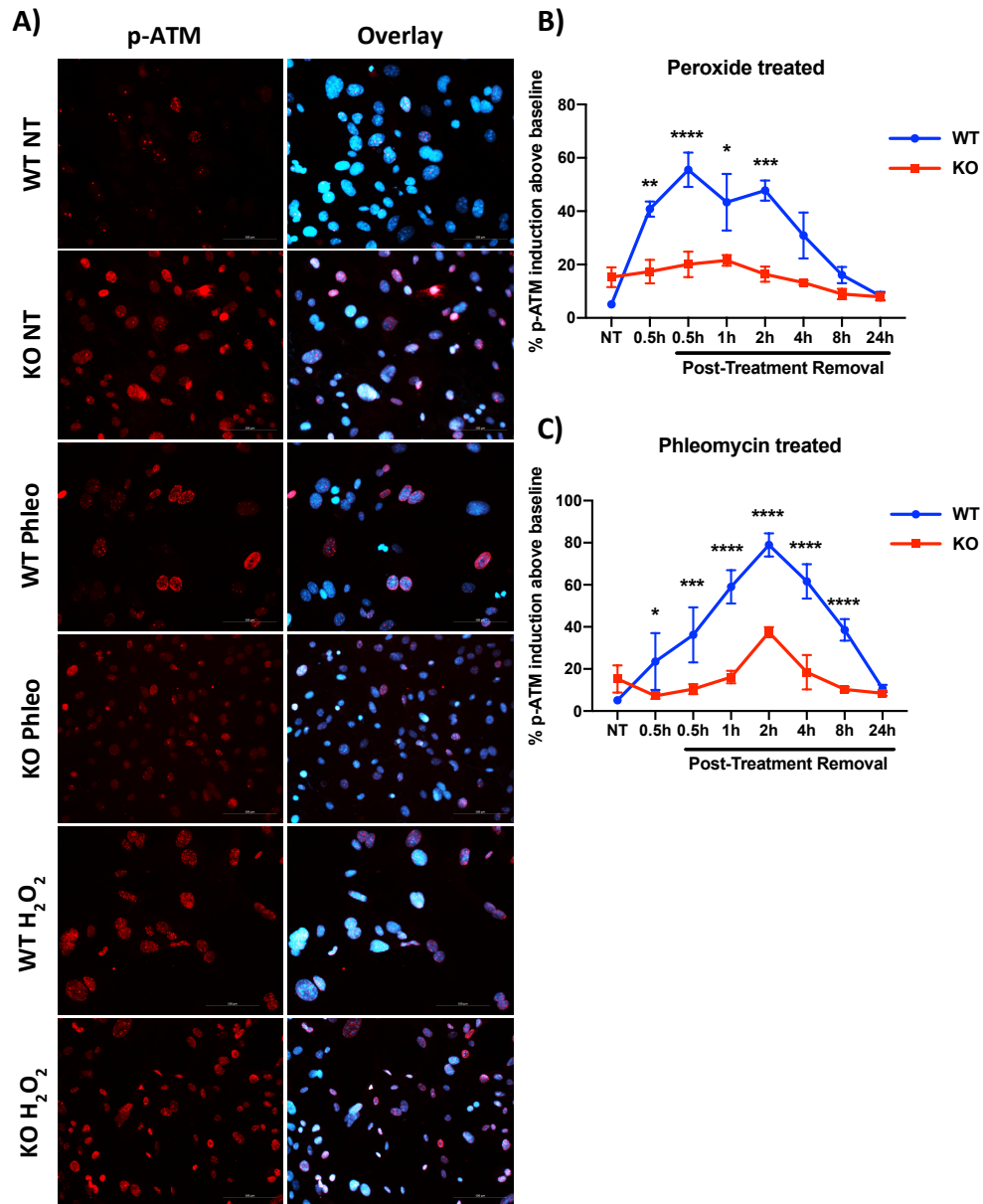


**Figure 3.6: SETX alters the induction of p-ATM foci following DNA damage**

SETX<sup>+/+</sup> (WT) and SETX<sup>-/-</sup> (KO) MEFs were treated with 0.5 mM H<sub>2</sub>O<sub>2</sub> or 20 μM phleomycin (Phleo) for 30mins, following which the damaging agent was removed and replaced with fresh media and cells were fixed with ice cold methanol, 0.5, 1, 2, 4, 8, and 24 h post peroxide removal. Immunofluorescence for the DNA damage marker p-ATM was performed at each time point. (A) Representative images for SETX<sup>+/+</sup> and SETX<sup>-/-</sup> either untreated (NT), 30 min H<sub>2</sub>O<sub>2</sub>, or 30 min phleomycin treatment stained with anti-p-ATM and Hoescht. Images were taken at 20X magnification using a Zeiss M2 Imager. (B) Quantification of p-ATM induction levels following treatment with 0.5 mM H<sub>2</sub>O<sub>2</sub> over the indicated time course. (C) Quantification of p-ATM induction levels following treatment with 20 μM phleomycin over the indicated time course. Statistics were performed on n = 3 with p < 0.05, \*, p < 0.01, \*\*, p < 0.001, \*\*\*, and p < 0.0001, \*\*\*\*, determined via two-way ANOVA with Bonferroni post-hoc test.

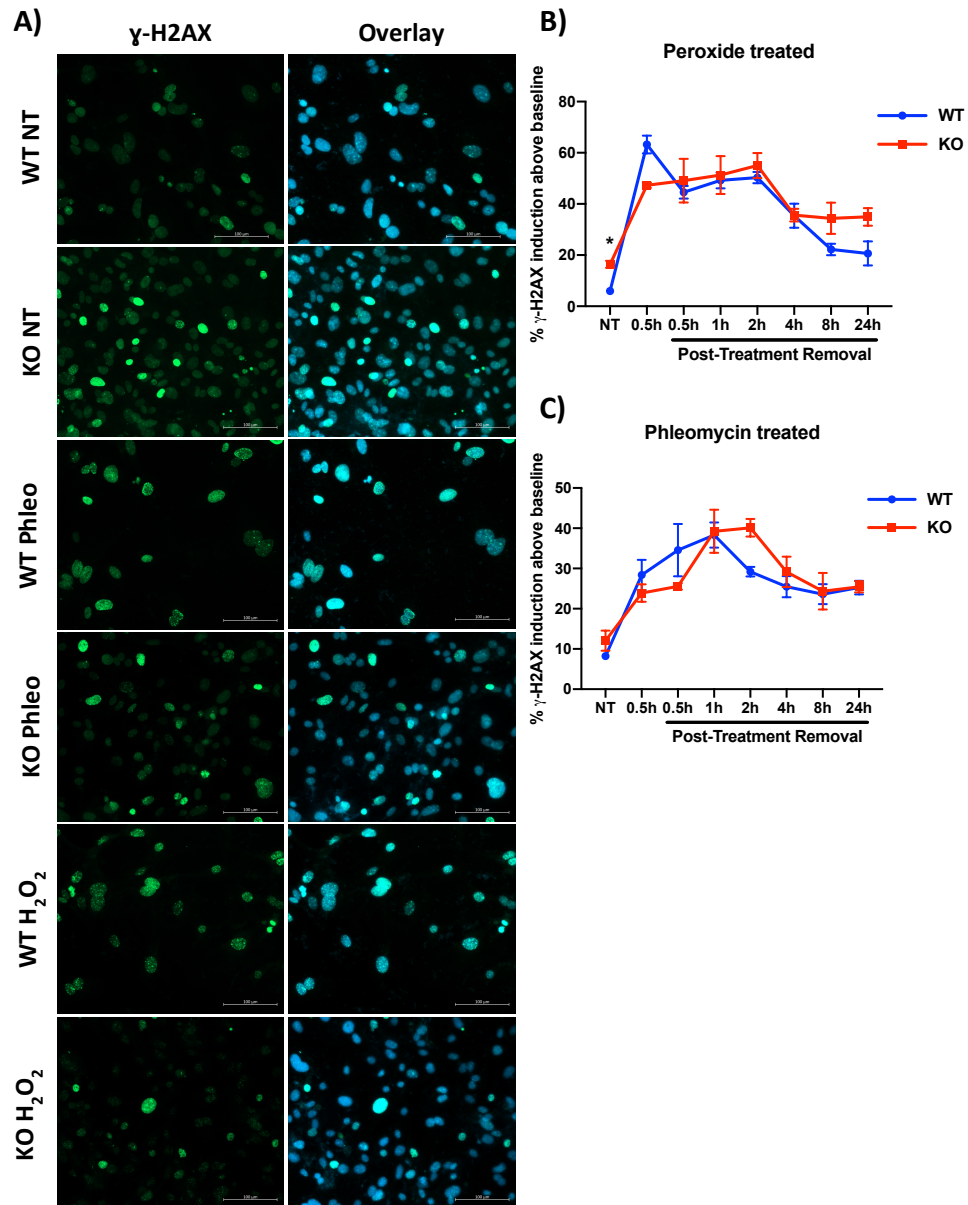


**Figure 3.7:  $\gamma$ -H2AX foci formation is unaltered in SETX deficient conditions**

SETX<sup>+/+</sup> (WT) and SETX<sup>-/-</sup> (KO) MEFs were treated with 0.5 mM H<sub>2</sub>O<sub>2</sub> or 20  $\mu$ M phleomycin (Phleo) for 30 mins, following which the damaging agent was removed and replaced with fresh media and cells were fixed with ice cold methanol, 0.5, 1, 2, 4, 8, and 24 h post peroxide removal. Immunofluorescence for the DNA damage marker  $\gamma$ -H2AX was performed at each time point. (A) Representative images for SETX<sup>+/+</sup> and SETX<sup>-/-</sup> either untreated (NT), 30 min H<sub>2</sub>O<sub>2</sub>, or 30 min phleomycin treatment stained with anti-  $\gamma$ -H2AX and Hoescht. Images were taken at 20X magnification using a Zeiss Imager M2. (B) Quantification of  $\gamma$ -H2AX induction levels following treatment with 0.5 mM H<sub>2</sub>O<sub>2</sub> over the indicated time course. (C) Quantification of  $\gamma$ -H2AX induction levels following treatment with 20  $\mu$ M phleomycin over the indicated time course. Statistics were performed on n = 3 with p < 0.05, \*, determined via two-way ANOVA with Bonferroni post-hoc test.

### ***3.2.8 SETX deficiency results in a preference for the alternate end-joining DNA repair pathway***

During CSR DSBs are ultimately repaired using classical NHEJ<sup>94</sup>. However, a secondary pathway termed a-EJ can also repair DSBs when NHEJ is compromised. Key features of a-EJ are that 1) the a-EJ process takes longer than NHEJ, and 2) a-EJ relies upon microhomology within DNA sequences to initiate repair of the DSBs<sup>114,280,281</sup>. Our earlier results which indicated a delay in the kinetics of DNA repair suggested that a-EJ may be more prevalent in SETX-deficient conditions. To determine whether this was the case we utilized a CRISPR SETX knockout CH12 B cell line. Given that a-EJ relies upon microhomology for DNA repair, we sequenced recombined S-regions from IgA<sup>+</sup> CH12 cells and analyzed the microhomologies within the S-regions (Fig. 3.8). There was a statistically different trend between the WT and SETX-deficient CH12 cells with regards to the microhomology usage. The majority of WT cells had only 1 nt of microhomology, whereas many SETX-KO cells had microhomologies of 3 nt or more. The results herein suggest that SETX is relied upon during CSR for the promotion of NHEJ over a-EJ allowing for faithful repair of the DNA during CSR.

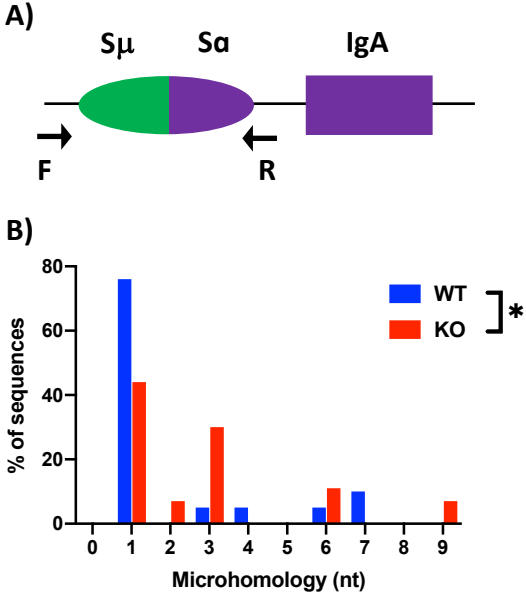


**Figure 3.8: SETX deficiency alters the microhomology usage in switch region repair**  
 CH12-WT and CH12-SETX KO cells were stimulated for 72 h with IgA specific stimulation, following which DNA was isolated and microhomology within S-regions was assessed using primers specific for Sμ and Sα. (A) A graphical representation of the location of primers used for S-region sequencing. (B) The percentage of sequences with the number of nt microhomology at the Sμ/Sα junction in stimulated CH12-WT and CH12-SETX KO cells. WT N = 21, and KO N = 27. \* p < 0.05 determined via Fisher’s exact test.

### 3.3 Discussion

#### 3.3.1 *The Role of SETX on CSR is IgA Specific*

RNA helicases have recently been demonstrated to play an active role in CSR<sup>196,200</sup> with the role of SETX on CSR only being explored tangentially<sup>198</sup>. Many of the known cellular functions of SETX are key players required for CSR, such as R-loop resolution<sup>10,194,196,205–208</sup>, cytokine regulation<sup>209</sup>, DNA DSB repair<sup>194</sup>, and the DDR more generally<sup>194,212–215</sup>. We explored the role of SETX during CSR. Herein, we have described a new role for SETX in facilitating class switching to IgA, in the context of a primary immune response, by facilitating NHEJ.

The role of SETX on CSR was most pronounced for switching to IgA. SETX is an RNA helicase which acts to unwind R-loops<sup>10,194,196,205–208</sup>, and SETX<sup>-/-</sup> mice have previously been demonstrated to exhibit an accumulation of R-loops within specific tissues, such as the testes<sup>194</sup>. R-loops can be either beneficial or detrimental depending on their location and abundance within a cell<sup>206</sup>. Having observed an early elevation in both IgM and IgG isotype production as well as a lack of IgA isotype production in the SETX<sup>-/-</sup> compared to the SETX<sup>+/+</sup> mice, we reasoned that SETX deficiency might lead to an increase in cell death and/or a proliferative defect due to R-loop accumulation, as was previously observed in the testes of SETX<sup>-/-</sup> mice<sup>194</sup>.

Using a live/dead stain we found no appreciable difference between SETX<sup>+/+</sup> and SETX<sup>-/-</sup> cells with regards to cell death during stimulation. We found that SETX<sup>-/-</sup> B cells did exhibit a reduced rate of proliferation in comparison to SETX<sup>+/+</sup> B cells following stimulation. This suggested that while SETX<sup>-/-</sup> B cells were not dying due to R-loop

accumulation, they proliferated at a slower rate than SETX<sup>+/+</sup> B cells. IgA switching requires several rounds of cell division<sup>284</sup> and therefore, a delay in proliferation is consistent with the lack of IgA we observed following *ex-vivo* stimulation of SETX<sup>-/-</sup> cells. At 72h post-stimulation we observed no difference in IgA production via either ELISpot or flow cytometry. However, by 5 days post-stimulation IgA production was defective in SETX<sup>-/-</sup> B cells but not SETX<sup>+/+</sup> and consistent this observation, proliferation was also reduced. We reasoned that the role of SETX on CSR is likely a B cell intrinsic role, given that IgA production was altered *in-vitro* in a situation where cytokines for class switching were provided in abundance and irrespective of other cell types required for *in-vivo* CSR.

To confirm the role of SETX on IgA production that was observed *in-vitro*, we assessed the role of SETX on CSR in an *in-vivo* setting using formalin-inactivated IAV as an antigen. The vaccination model allowed us to explore CSR in a more physiologically natural setting. In the sera of vaccinated mice we detected no differences in total antibody titres. However, by assessing the levels of antigen-specific antibodies, we observed a lack of HA-specific IgA that persisted for up to 14 days post-vaccination. This was consistent with ELISpot data at day 14, as SETX<sup>-/-</sup> mice had lower levels of HA-specific IgA with 2 out of 3 mice showing no HA-specific IgA production. However, the number of replicates will need to be increased in order to determine whether this difference is statistically significant.

SIgAD is the most common form of primary immunodeficiency<sup>287</sup>. Additionally, patients with SIgAD often exhibit elevated levels of IgM antibodies<sup>287,288</sup>. SIgAD often goes unnoticed in patients however, patients with SIgAD have been shown to be more

susceptible to infections of mucous membranes<sup>287,289</sup>. Patients with SIgAD are also known to exhibit higher incidence of autoimmune disorders<sup>290,291</sup>. The SETX<sup>-/-</sup> mice do not exhibit true SIgAD, as their total levels of IgA are comparable to those of SETX<sup>+/+</sup> mice. However, the observed lack of antigen-specific IgA production in the sera up to 14 days post-primary vaccination suggests a potentially unique phenotype of a delayed primary IgA response. This finding was less pronounced in the context of secondary homologous immune responses. A homologous boost largely relies upon the reactivation of MBCs and, given the lack of total IgA deficiency in the SETX<sup>-/-</sup> mice, we can surmise that reactivation of IgA MBCs would be unaltered. However, IgG MBCs can also re-enter a GC reaction and further class switch<sup>13</sup>, along with new naïve B cells entering the GC, which could suggest the slight difference observed between SETX<sup>+/+</sup> and SETX<sup>-/-</sup> antigen-specific IgA production following a homologous boost.

### ***3.3.2 SETX Deficiency Alters CSR but Does Not Globally Alter SHM***

Antigen specificity is gradually improved through a process known as affinity maturation and occurs in lymphoid structures known as GCs<sup>12</sup>. Affinity maturation typically increases with the number of cell divisions. Both the extent of SHM and cell division number are indicative of a longer period of time within the GC<sup>83,292–294</sup>. SHM shares many similarities to the process of CSR<sup>295</sup> and therefore, it was possible that SETX could impact the process of SHM in addition to CSR.

We explored the mutation rate within the variable region of IgA switched B cells and observed no difference between SETX<sup>+/+</sup> and SETX<sup>-/-</sup> cells with regards to overall

mutation rate. Thus, while SETX deficiency alters CSR, SETX appeared to be dispensable for efficient SHM. However, the B cells studied were a total population of B cells rather than a population of only antigen-specific B cells, therefore we may see a defect in SHM if we explored the antigen-specific population. The lack of apparent involvement of SETX in SHM further suggests that the role of SETX is not in the initial targeting of AID to the genome. SHM and CSR share many similarities with regards to AID targeting and activity, however, they differ in that CSR induces DSBs and SHM introduces mutations into the variable region without inducing DSBs<sup>51</sup>. The mechanistic differences between SHM and CSR are incompletely understood. Nevertheless, our data suggests that SETX acts on CSR downstream of AID activity, potentially on the DSB DDR, as this is a point at which CSR and SHM differ.

Further, we demonstrated that the IgA repertoire within vaccinated SETX<sup>-/-</sup> mice was less diverse than that of the SETX<sup>+/+</sup> counterparts, while the diversity of the IgG repertoire was unaltered. The decreased diversity of the IgA repertoire in SETX deficient conditions further demonstrates an issue switching to the IgA isotype, wherein diversity was defined by the number of B cell clones in the repertoire. The decreased diversity observed is indicative of less B cells maintaining the repertoire in the SETX deficient mice. However, once a B cell has switched to the IgA isotype, cell viability and ability to produce IgA is unaltered, allowing the repertoire to be populated by fewer clones, which is capitulated as a less diverse repertoire. Given the CSR defect, and apparent unaltered SHM, the ability of SETX deficient B cells to repair the DNA DSBs during CSR appears to be the mechanism being affected in SETX deficient conditions.

### ***3.3.3 SETX Impacts CSR in a B cell Intrinsic Manner***

#### ***3.3.3.1 SETX Deficiency Alters R-loop Accumulation Within the IgH Locus***

SETX is responsible for the resolution of R-loops<sup>10,205,207,208</sup>, and therefore SETX deficient cells may exhibit elevated levels of R-loops. Using the DRIP assay<sup>201</sup> we explored the levels of R-loops within the IgH locus. SETX deficiency altered the localization and increased the relative prevalence of R-loops in the IgH locus, post-stimulation. R-loops within S-regions are essential for the process of CSR<sup>48,80,285,296</sup>. Genetically altering B cells to prevent the formation of R-loops also inhibited CSR<sup>46,81</sup>. We found that R-loops were elevated across both the IgM and IgA regions of the IgH locus in SETX<sup>-/-</sup> cells. The elevation of R-loops within the IgH locus could potentially be detrimental to class switching. However, we also assessed the expression levels of IgM and IgA GLTs and demonstrated that SETX<sup>-/-</sup> resulted in a trend towards increased GLT expression. Interestingly, GLT expression is a key indicator that CSR to a specific isotype is taking place<sup>45,66–68</sup> and yet we observed that SETX<sup>-/-</sup> cells had difficulty class switching to the IgA isotype. Suggesting that SETX<sup>-/-</sup> B cells are receiving the appropriate upstream signals to induce class switching towards the IgA isotype, but IgA switching is still deficient, which suggests that the problem must be downstream of GLT transcription.

#### ***3.3.3.2 DNA Damage Response Kinetics are Altered in SETX Deficient Cells***

SETX-deficient cells appeared to be receiving the signals to switch to the IgA isotype and yet were unable to switch efficiently. The fact that the defect in switching to

IgA could be detected *in vitro* using purified B cell cultures also suggest that this is a B cell intrinsic effect, rather than a secondary effect of alterations in cytokine expression levels or interactions with another cell type. SETX has been associated with the DDR through interactions with the DDR markers 53BP1 and  $\gamma$ -H2AX in HeLa cells<sup>194,212–214</sup>. Phleomycin treatment has previously been demonstrated to increase the number of SETX foci in HeLa cells, through elevated DSB induction<sup>213</sup>. The DDR is integral for efficient CSR. 53BP1 is essential for efficient CSR<sup>65</sup>, although it is not necessary for either V(D)J recombination or SHM, suggesting different mechanisms of DNA repair for these B cell processes<sup>297</sup>. Recently, 53BP1 has been shown to be important for the 3D reconstruction of the IgH locus during CSR and therefore acts to orient the DNA for long-range interactions occurring between S-regions during CSR<sup>275,298</sup>. Given the DDR proteins with which SETX colocalizes following DNA damage, SETX may act as a scaffold linking 53BP1 to the IgH locus via SETX/R-loop interactions. Additionally, there has been evidence suggesting that SETX can act as a dimer<sup>299</sup>. Leading to the potential of a SETX-dimer binding two R-loops at distinct regions within the IgH locus thereby bringing them in close proximity and allowing 53BP1 to act on the DNA and promoting NHEJ, given the 3D looped structure of the IgH locus during CSR<sup>300,301</sup>.

While SETX has been demonstrated to interact with DDR proteins, the effect of SETX on the kinetics of the DDR has not been explored. Using SETX<sup>+/+</sup> and SETX<sup>-/-</sup> MEFs we assessed the role of SETX on the ability of a cell to resolve DNA damage. MEFs were used as they are adherent and allow for immunofluorescent analysis of DDR factors rather than nonadherent B cell lines. SETX<sup>-/-</sup> cells exhibited elevated levels of DNA damage (as

measured by p-ATM and  $\gamma$ -H2AX foci) at baseline, but upon addition of H<sub>2</sub>O<sub>2</sub> the SETX<sup>-/-</sup> MEFs had similar  $\gamma$ -H2AX foci to SETX<sup>+/+</sup> MEFs. Upon the removal of H<sub>2</sub>O<sub>2</sub>  $\gamma$ -H2AX foci persisted for longer times in SETX<sup>-/-</sup> cells as well. In addition to H<sub>2</sub>O<sub>2</sub> we treated MEFs with phleomycin to specifically induce DSBs<sup>302</sup>, and found that SETX<sup>-/-</sup> MEFs exhibited a similar number of  $\gamma$ -H2AX foci to SETX<sup>+/+</sup> MEFs. Therefore  $\gamma$ -H2AX foci induction was similar between SETX<sup>-/-</sup> and SETX<sup>+/+</sup> MEFs irrespective of DNA damage inducer. Induction of  $\gamma$ -H2AX foci is essential for the appropriate clustering of DDR factors to sites of damage<sup>261</sup>.

In addition to  $\gamma$ -H2AX foci formation we assessed the role of SETX on p-ATM activation using an antibody specific for ATM phosphorylation at site serine 1981. S1981-phosphorylation of ATM was chosen as this phosphorylation event stabilizes ATM at the sites of DSBs, allowing for an appropriate DDR and DNA repair<sup>286</sup>. p-ATM phosphorylates H2AX<sup>218</sup> and anchors many of the proteins involved in the DDR<sup>303</sup>, including those known to interact with SETX during DNA damage<sup>213</sup>. ATM is a major sensor involved in the repair of DSB and mutations in ATM can cause the ARCA A-T<sup>2</sup>. In contrast to  $\gamma$ -H2AX, p-ATM foci formation was dramatically delayed in SETX<sup>-/-</sup> MEFs in comparison to SETX<sup>+/+</sup> MEFs following DNA damage by both peroxide and phleomycin. The effect of SETX-deficiency on the DDR was more severe for p-ATM foci induction than  $\gamma$ -H2AX foci formation. While p-ATM phosphorylates H2AX, ATR, another mediator of the DDR, also phosphorylates H2AX<sup>258</sup>, suggesting that when ATM activity is defective, ATR is able to replace the functionality of ATM, at least partially. Additionally, DNA-PK can phosphorylate H2AX<sup>257</sup>, allowing for redundancy between activators of H2AX, thereby allowing for  $\gamma$ -

H2AX foci formation being unaltered in SETX<sup>-/-</sup> cells. The functional roles of ATM and  $\gamma$ -H2AX on the DDR suggests an issue with the appropriate activation of essential DNA repair factors through p-ATM while recruitment of factors likely remains intact given  $\gamma$ -H2AX foci formation is unaltered in SETX<sup>-/-</sup> cells.

### ***3.3.4 SETX Deficiency Induces Similar Deficits to those in DNA Repair Deficient B cells***

Mice that are deficient in ATM also demonstrate impaired CSR for all isotypes via B cell intrinsic mechanisms<sup>252</sup>. Interestingly, in the SETX<sup>-/-</sup> MEFs we detected a larger discrepancy in p-ATM foci formation than  $\gamma$ -H2AX foci formation. The DDR requires complex coordination of many proteins to achieve repair. One such factor is MDC1, which interacts with both ATM<sup>264</sup> and  $\gamma$ -H2AX<sup>304</sup>. MDC1 functions to amplify the ATM-dependent DNA damage signals. MDC1<sup>-/-</sup> male mice are also infertile, like SETX<sup>-/-</sup> mice, and MDC1<sup>-/-</sup> causes a mild IgG switching deficiency<sup>264</sup>. Additionally, in MDC1<sup>-/-</sup> conditions, p-ATM foci do not form following ionizing radiation<sup>264</sup>. MDC1 and SETX have been shown to interact previously<sup>213</sup> and deficiencies in both proteins result in similar phenotypes. Therefore, understanding the relationship between MDC1 and SETX during DDR may shed more light on the molecular mechanism through which SETX is involved in CSR.

Our results suggest that SETX deficiency may influence the DDR in two ways: 1) a problem recognizing DNA damage and therefore, a defect in recruiting the necessary repair factors, 2) a problem repairing DNA damage. While phosphorylation of H2AX is crucial for the recruitment of DDR factors<sup>304</sup>, p-ATM is key to the activity of these

factors<sup>303</sup>. Therefore, we can propose that in SETX<sup>-/-</sup> conditions DDR factors will be recruited and yet the function of such factors may be altered resulting in a problem repairing DNA appropriately although not recognizing DNA damage.

Further, B cells isolated from ATM<sup>-/-</sup> mice demonstrate elevated levels of microhomology usage, suggesting that a-EJ is occurring, rather than NHEJ, in ATM deficient conditions. As aforementioned, many patients with A-T (as a result of ATM mutations) exhibit SIgAD<sup>7</sup>. Additionally, microhomology levels are drastically elevated in S $\mu$ -Sa regions and are less evident at S $\mu$ -S $\gamma$  regions of B cells isolated from A-T patients<sup>305</sup>. The effect of SETX-deficiency on p-ATM foci induction following DNA damage may suggest that SETX-deficient mice are utilizing a-EJ rather than NHEJ during CSR, in a similar manner to ATM<sup>-/-</sup> B cells.

Recently, SETX has been implicated in SMA<sup>215</sup>. SMA is one of the leading neurodegenerative causes of early childhood mortality. SMA is caused by mutation of the survival of motor neuron 1 (SMN1) gene<sup>306</sup>. SMN1 was found to colocalize with SETX, and SMN1-deficiency, as is found in SMA patients, caused a subsequent decrease in SETX expression<sup>215</sup>. Given the R-loop resolving function of SETX, it was not surprising that R-loop levels were elevated in cells from SMA patients, which resulted in elevated numbers of DSBs and activation of the DDR. The consequences of these findings on the DDR differed in cells that were post-mitotic, such as neurons, compared to cells with the ability to replicate. In dividing cells, the DNA damage induced by R-loop accumulation is faithfully repaired by HR during cellular division. However, in post-mitotic neurons HR is unavailable and the consequences of DNA damage are more deleterious. Chronic low levels

of SMN1 resulted in decreased expression of DNA-PKcs leading to an impairment in NHEJ. Decreased DNA-PKcs prevented neurons from effectively repairing DNA damage and ultimately resulted in neuronal cell death<sup>215</sup>. The results of this study have clear consequences for SETX-related disorders and the role of SETX on CSR. CSR occurs during the G1 phase of the cell cycle, and therefore B cells are unable to utilize HR for DNA repair<sup>78–80,275</sup>. SETX-deficiency in SMA-derived neurons resulted in defective NHEJ by decreased expression of DNA-PKcs<sup>215</sup>. These findings may extend into B cells during CSR. Therefore, determining whether SETX<sup>-/-</sup> cells have lower expression of DNA-PKcs would be an interesting avenue for future studies.

### ***3.3.5 SETX Deficiency Promotes $\alpha$ -EJ Repair of DNA During CSR***

To explore whether SETX<sup>-/-</sup> influenced the DNA repair pathways used during CSR, we sequenced the S $\alpha$  region of cells that had switched to IgA using primers directed upstream of the S $\mu$  region and downstream of the S $\alpha$  region<sup>200</sup>. S-region recombination events leave a signature within the repaired DNA, upon which conclusions about the type of DDR pathway that has been utilized during CSR can be drawn. The NHEJ pathway is the default DNA repair pathway for the recombination of S-regions<sup>78,94,307,308</sup> resulting in a microhomology of 0-4 bp at the site of ligation between S-regions<sup>316</sup>. However, an  $\alpha$ -EJ pathway can also be used for DNA repair, although  $\alpha$ -EJ is a slower process than NHEJ and relies upon longer microhomologies, 3-20 bp, to complete ligation<sup>280,281,307–310</sup>. Given the fact that SETX interacts with 53BP1<sup>213</sup>, and that 53BP1 promotes NHEJ<sup>311</sup>, combined with the kinetic delay in switching to IgA that we observed in our earlier experiments, we

reasoned that SETX deficiency may alter the repair pathway being utilized by SETX<sup>-/-</sup> B cells.

Indeed we observed a difference in the trend of microhomology usage between WT and SETX-KO CH12 cells. The majority of WT recombination events contained 1nt of microhomology, consistent with NHEJ DNA repair, while SETX-KO increased the microhomology usage for S-region DNA repair. The effect of SETX-deficiency on microhomology usage is similar to that reported for ATM-deficient B cells undergoing CSR<sup>252,305</sup>, which have been demonstrated to display a significant increase in the level of microhomology used for repair during CSR. Interestingly, this increase in microhomology usage is not limited to ATM deficiency but was also observed in the context of 53BP1, MDC1, and H2AX deficiencies<sup>249,264</sup>. SETX colocalizes with 53BP1, MDC1, and  $\gamma$ -H2AX<sup>213</sup>. Further, we demonstrated that ATM phosphorylation, which correlates with activity<sup>312</sup>, is impaired in SETX deficient conditions following DNA damage.

Given the interactions between SETX and known mediators of NHEJ, it would not be surprising that in SETX-deficient conditions NHEJ may be impaired. PARP1 is an important mediator of the a-EJ pathway and has also been demonstrated to be activated in response to R-loop dependent DNA damage<sup>313</sup>. PARP1 interacts with DXH9, another R-loop helicase, and has been found within the R-loop interactome, along with DNA-PK<sup>313</sup>. Therefore, PARP1-mediated a-EJ would be expected to remain intact in SETX<sup>-/-</sup> conditions.

### **3.3.6 Limitations**

In the body of work described herein we have demonstrated a kinetic defect in IgA class switching in SETX-deficient conditions that is associated with altered DNA repair pathway usage. However, it is important to keep in mind the limitations of our model system. In an attempt to recapitulate AOA2 phenotypes, the SETX<sup>-/-</sup> mouse model was developed by Becherel *et al.* However, no neurodegenerative phenotype develops in this model<sup>194</sup>. Some AOA2 patients have mutations in SETX that result in a loss of R-loop resolving function but do not completely abrogate protein expression. Therefore, mutated SETX may still exhibit distinct phenotypes from those observed in our knockout mouse model. Additionally, although we explored the role of SETX on the DDR, our studies were conducted in MEFs rather than B cells. Therefore, it will be important to extend our findings to B cells during CSR. Finally, it is not clear whether the defect in CSR that we observed is related to the etiology of AOA2. Understanding the involvement of the immunological phenotypes associated with mutations in SETX on AOA2 and ALS4 will be important in the future.

### **3.3.7 Concluding Remarks**

It is clear that many neurodegenerative disorders share common features. Therefore, it is not surprising that SETX deficiency, which results in AOA2, shows phenotypic similarities to A-T. While in AOA2 ATM is not mutated, we do see a deficit in ATM activation. Common hallmarks of A-T include immunodeficiency and radiosensitivity, in addition to neurological disorders<sup>2</sup>. AOA2 patients do not display the ionizing sensitivity

reported for A-T patients<sup>314</sup> however, they do display similar neurodegenerative disorders, although less severe, and we have now reported a mild immunodeficiency in SETX-deficient mice. ATM is a central figure in the DDR, while SETX is not essential, this may explain the difference seen in the disease severity between A-T and AOA2, and the more subtle nature of phenotypes associated with SETX deficiency.

Herein, we have observed a deficiency in switching to IgA in the SETX<sup>-/-</sup> mouse model during a primary immune response, thereby effecting the kinetics of an IgA response to vaccination, as demonstrated in Figure 3.3.1. These findings raise the possibility that individuals suffering from AOA2, who also lack SETX, may have an IgA-associated immunodeficiency. The associated IgA immunodeficiency would not be SIgAD but rather a unique form of IgA deficiency specific to antigen-specific IgA cells following a primary exposure. Environmental insults have long been thought to play a role in the onset and/or progression of neurodegenerative diseases<sup>315,316</sup> with increased levels of inflammation thought to play a significant role in both disease onset and progression<sup>324</sup>. Given our findings, it will be interesting to determine whether AOA2 patients experience elevated levels of inflammation early in life due to greater rates of infection at mucosal sites where IgA is highly enriched. IgA in the gut plays a critical role in maintaining noninflammatory commensal bacteria and neutralizing invasive species<sup>317</sup>. Therefore, kinetic delays in IgA production may result in harmful inflammation originating from the gut. Exploring this rare population of AOA2 patients, and their immune responses, merits further study and may shed light on the etiology of AOA2.

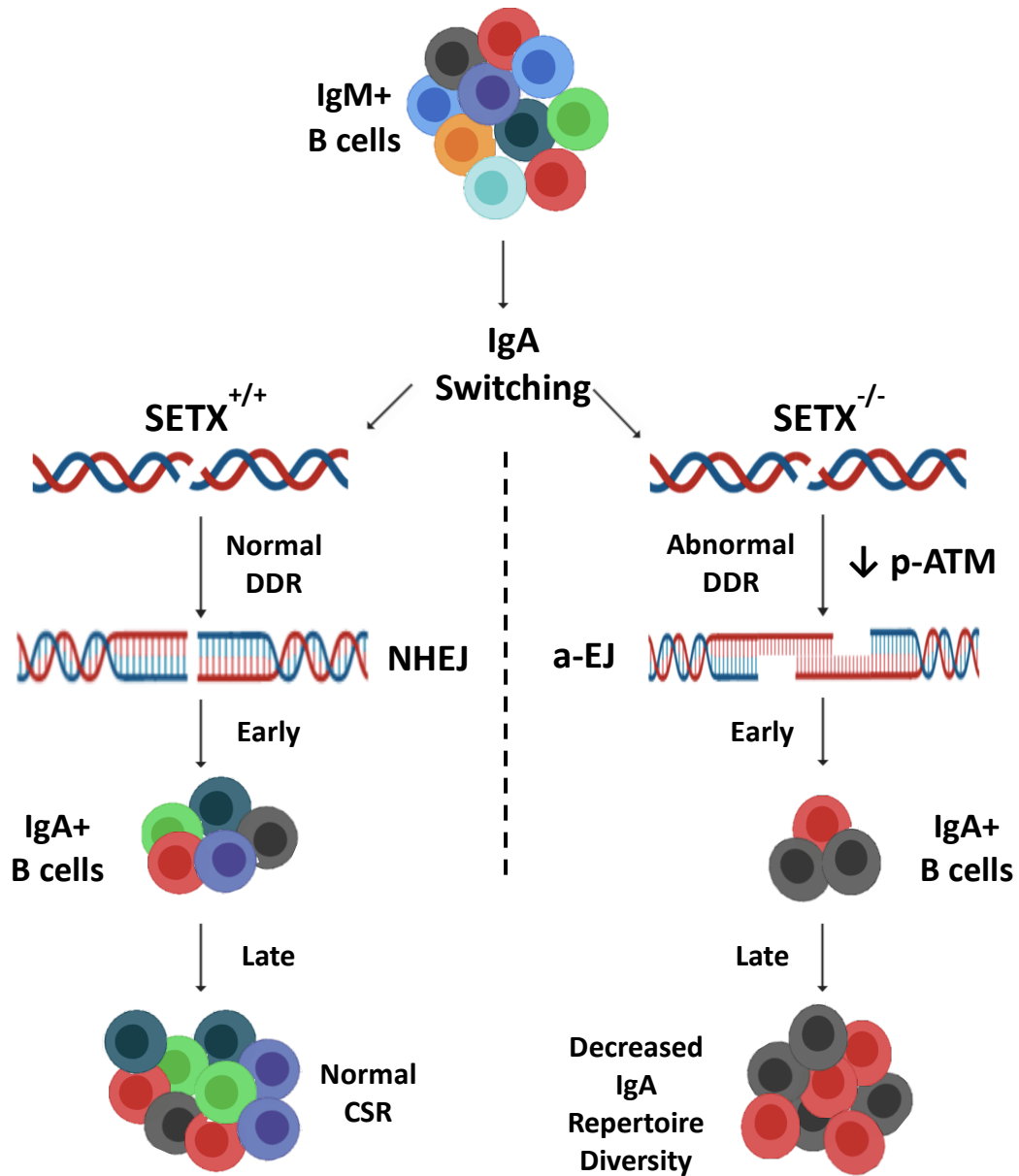


**Figure 3.3.1: A model for the role of SETX on IgA class switching**

We have demonstrated that SETX deficiency results in an IgA specific defect during CSR. SETX<sup>+/+</sup> and SETX<sup>-/-</sup> B cells demonstrated intact signals for the initiation of CSR, including R-loop accumulation and GLT expression, resulting in equivalent DSB induction in both SETX<sup>+/+</sup> and SETX<sup>-/-</sup> B cells. Following DNA damage, in SETX<sup>+/+</sup> conditions the DDR repaired inter S-region DSBs via NHEJ, and CSR proceeded normally. However, in SETX<sup>-/-</sup> B cells the DDR was abnormal, potentially through decreased ATM activity. The abnormal DDR resulted in a preference for a-EJ over NHEJ in SETX<sup>-/-</sup> B cells. In comparison to NHEJ, a-EJ is a slower process, with an increased probability of mutation at the site of repair, and a reliance on microhomology for the repair of DSBs. As a result of a-EJ usage for DNA repair, we observed decreased clonal diversity within the IgA repertoire in SETX<sup>-/-</sup> mice as fewer cells reach the IgA isotype during CSR.

## CHAPTER 4

# A Role for Viral Infection on the Onset and Progression of Amyotrophic Lateral Sclerosis

## 4.1 Introduction

### 4.1.1 Genetics of ALS

ALS has a strong genetic basis, with over 100 genes associated with the disease to-date<sup>318</sup>. ALS can be divided into two subcategories; sporadic ALS (sALS) and familial ALS (fALS). Inherited ALS is considered fALS whereas sALS refers to patients with no family history of ALS<sup>319</sup>. However, the utility of these ALS categories is currently being challenged given that the clinical features of ALS are indistinguishable between sALS and fALS<sup>135</sup>. The most studied and strongly-associated genetic factors involved in ALS include C9orf72, fused in sarcoma RNA binding protein (FUS), TAR DNA-binding protein 43 (TDP-43), and superoxide dismutase 1 (SOD1). Research on these proteins constitute the basis of our molecular understandings of ALS<sup>318</sup>. However, given the advancements in sequencing technology, new mutations are being uncovered in ALS at an increasing rate. For example, in 2019 the gene *DNAJC7* was shown to be mutated in some patients with ALS. It encodes for a heat-shock protein family member that, when mutated, results in the accumulation of misfolded proteins<sup>320</sup>. C9orf72 mutations are characterized by repeat nucleotide expansions which can cause both loss and gain of function, as well as accumulations of toxic RNA foci<sup>239</sup>. Toxic RNA foci sequester RNA binding proteins resulting in multiple downstream effects such as abnormal RNA splicing and altered transcriptional profiles<sup>321</sup>. FUS mutations have also been linked with ALS and can cause RNA binding defects, alterations in gene expression, and mitochondrial defects<sup>322</sup>. ALS-associated TDP-43 mutations cause abnormal protein cleavage products, toxic aggregation of TDP-43, and mislocalization of TDP-43 to the cytoplasm<sup>323</sup>. Interestingly, TDP-43

aggregates have been found in 97% of ALS patients independent of the causal mutated gene<sup>324</sup>. SOD1 mutations have been shown to result in a gain of function which causes elevated levels of reactive oxygen species (ROS) as well as protein misfolding and aggregation<sup>325,326</sup>.

#### ***4.1.2 Possible Etiology of ALS***

SOD1 is the most extensively studied of the ALS genes. SOD1<sup>G93A</sup> was the first, and most aggressive, mouse model of ALS and has made important contributions to the knowledge of ALS since its development in 1993<sup>327</sup>. SOD1 is an enzyme involved in the resolution of ROS by converting superoxide ions into hydrogen peroxide<sup>328</sup>. However, it remains unclear how mutations in SOD1 ultimately cause ALS. ALS-linked SOD1 mutations have been demonstrated to result in a gain of function and a subsequent elevation in ROS production<sup>329,330</sup>. SOD1 mutations have been associated with abnormal induction of the inflammatory response, as evidenced by the increased IFN expression observed in SOD1<sup>G93A</sup> mice astroglia in the spinal cord<sup>331</sup>. Further, SOD1 mutations may alter mitochondria and endoplasmic reticulum (ER) stress, likely through ROS related mechanisms<sup>332–335</sup>. In addition to the above proposed role of SOD1 in ALS, mutations in SOD1 result in the aggregation of mSOD1 in a prion-like fashion<sup>336,337</sup>. Even WT SOD1 has also been demonstrated to have a high propensity to misfold<sup>338</sup>. Therefore, mSOD1 has multiple consequences that may lead to disease onset and/or progression.

#### ***4.1.2.1 Toxic Protein Aggregation and Spreading***

A key hallmark of ALS, regardless of genetic cause, is the accumulation of misfolded proteins. Protein misfolding is a common consequence of mutation in many genes associated with ALS including FUS, TDP-43, and SOD1<sup>339</sup>. mSOD1 acts in a prion-like fashion wherein mSOD1 can interact with natively folded SOD1 and induce its misfolding, as well as interact with mSOD1 to form large aggregates of mSOD1<sup>336,337,340</sup>. There are multiple conformations of mSOD1, as recognized by different epitope specific antibodies<sup>341</sup>. Recent research has demonstrated that a prion-like mechanism of pathogenic mSOD1 transfer between cells can occur via both exosome-independent and -dependent mechanisms<sup>342,343</sup>. In this way SOD1 aggregation can spread from cell to cell within the CNS thus promoting disease progression. The toxicity of mSOD1 may originate from microglia and astrocytes within the CNS<sup>344</sup>. This was determined *in vitro* by co-culturing microglia-expressing SOD1<sup>G93A</sup> with normal neurons and demonstrating that SOD1<sup>G93A</sup> harbouring microglia exert toxic effects on neurons, although the mechanism is not entirely clear<sup>344-346</sup>. TDP-43 has also been extensively explored in the context of protein aggregation. In ALS, TDP-43 inclusions are widespread and result in both full length and fragmented TDP-43 being sequestered into cytoplasmic aggregates<sup>324</sup>. Protein aggregation is not an ALS specific phenomenon, but appears to be a more general feature of neurodegenerative diseases, with AD, Huntington's disease (HD), and PD all displaying protein aggregation as a consequence of disease<sup>347</sup>.

Protein aggregation results in the induction of the unfolded protein response (UPR). However, mSOD1 is resistant to proteolytic degradation due to the formation of  $\beta$ -sheet

enriched aggregates. This promotes the accumulation of SOD1 aggregates, and the formation of insoluble inclusions<sup>348</sup> within the cell. Interestingly, the accumulation of monomeric and oligomeric mSOD1 is likely a protective mechanism, as the aggregates themselves are nontoxic<sup>349</sup>. The UPR relies upon three ER stress sensors: double-stranded RNA-activated protein kinase-like ER kinase (PERK), inositol requiring enzyme 1 (IRE1), and activating transcription factor 6 (ATF6)<sup>350</sup>. All three ER stress sensors bind to and sequester GRP78. This binding is disrupted in times of stress, allowing GRP78 to interact with misfolded proteins, such as mSOD1<sup>351</sup>. Interestingly, ER stress actually appears to promote the accumulation of mSOD1 in ALS suggesting a positive feedback loop of stress and protein misfolding<sup>352</sup>. Therefore, cellular stress is likely a consequence of misfolded protein accumulation, especially due to the ubiquity of protein misfolding seen in the context of various forms of ALS<sup>338,353–357</sup>.

#### ***4.1.2.2 Glutamate Excitotoxicity***

Glutamate is a neurotransmitter that acts in an excitatory manner when released into the synaptic cleft<sup>358</sup>. Glutamate is removed from the synaptic cleft by astrocytes, which surround the synapse, through the transporter EAAT2, and is then reused for further neurotransmission<sup>359</sup>. EAAT2 is highly abundant in the CNS on the surface of astrocytes<sup>360</sup>. In ALS cases there is a downregulation of EAAT2 resulting in an accumulation of glutamate in the synapse which results in overactivation of neurons<sup>361–363</sup>. The downregulation of EAAT2 is not a result of a direct mutation but is rather a consequence of aberrant RNA processing<sup>362,364–366</sup>.

MNs appear to be uniquely sensitive to over-stimulation by glutamate<sup>367,368</sup>. Glutamate accumulation and MN excitation results in excitotoxicity which is a form of neuronal death. Excitotoxicity causes a Ca<sup>2+</sup> influx into the MN, resulting in a Ca<sup>2+</sup> imbalance<sup>375</sup>. This Ca<sup>2+</sup> influx results in an accumulation of Ca<sup>2+</sup> in the ER and mitochondria, resulting in dysfunctional organelles, and inducing elevated levels of ROS and cell death<sup>369–371</sup>. Further, influx of Ca<sup>2+</sup> leads to the misfolding of SOD1<sup>371,372</sup> prior to completion of *de novo* folding into its native conformation after synthesis<sup>373,374</sup>. Glutamate excitotoxicity has also been associated with HD, PD, and AD<sup>375</sup>. However, given the lack of benefit offered by riluzole treatment, which inhibits glutamate release and stimulation<sup>376</sup>, glutamate toxicity may not be a driving force of disease in ALS.

#### ***4.1.2.3 Mitochondrial Abnormalities***

Mitochondrial dysfunction has been associated with ALS and other neurodegenerative disorders, and results in the production of ROS. In patients with ALS mitochondria display a vacuolated phenotype<sup>377,378</sup>, a phenotype also observed in SOD1 and TDP-43 mouse models of ALS<sup>379</sup>. Further, aggregates of mitochondria can be observed in clusters along the axon of MNs<sup>379</sup>. Interestingly, many proteins associated with ALS, including SOD1<sup>380–382</sup>, TDP-43<sup>383</sup>, FUS<sup>384</sup>, and C9orf72<sup>385</sup>, have been demonstrated to interact with mitochondria, and play an active role in mitochondrial damage<sup>381,383,385</sup>.

SOD1 has the strongest association with mitochondria, with natively folded SOD1 being found in the intermembrane space<sup>386</sup>. In ALS, mSOD1 aggregation can result in the inhibition of the electron transport chain<sup>387,388</sup>. Multiple mSOD1 specific antibodies

localize to the matrix and surface of mitochondria in the spinal cord of SOD1<sup>G93A</sup> rats<sup>341</sup>. Mitochondria are sensitive to proteotoxic stress induced by aggregated proteins<sup>389</sup>. Additionally, TDP-43, FUS, and C9orf72 accumulate at mitochondria. Generally, ALS related proteins cause a decrease in ATP production and an elevation in ROS<sup>390</sup> that are associated with mitochondrial defects. Mitochondrial dysfunction occurs prior to disease onset<sup>391</sup> and may precipitate disease progression.

#### ***4.1.2.4 Oxidative and Endoplasmic Reticulum Stress***

A hallmark of mitochondrial dysfunction is ROS accumulation<sup>392</sup>. Oxidative damage can alter many cellular structures, including lipids, DNA, and proteins<sup>393</sup>. ROS induces inflammation, protein aggregation, and ER stress<sup>394-396</sup>. Extensive damage of mitochondria can occur as a result of elevations in ROS and has been extensively reported in ALS patients<sup>397,398</sup>. Given the ubiquity of proteins associated with ALS interacting with mitochondria, ROS and elevated oxidative stress is a hallmark of ALS<sup>381,383,385,397,398</sup>. The stress induced by ROS on mRNA has been studied in the SOD1<sup>G93A</sup> mouse model and promotes MN degeneration<sup>399</sup>. SOD1 is itself a target of ROS induced damage which is believed to further promote its misfolding and aggregation<sup>400</sup>, thereby inducing a positive feedback loop of protein misfolding and mitochondrial damage<sup>335,341</sup>.

In addition to oxidative stress, ER stress and the UPR is impacted in ALS. The ER is a site of protein synthesis and folding. It is also involved in secretion of proteins, and acts as an important store of Ca<sup>2+</sup> within the cell<sup>401,402</sup>. In ALS, protein aggregates are ubiquitinated although not appropriately degraded through the proteasome<sup>324,403,404</sup>. ER

stress has been observed to occur in both SOD1<sup>G93A</sup> models<sup>405</sup> and in ALS patients<sup>406</sup>. ER stress is thought to occur due to misfolded protein accumulation given that mSOD1 colocalizes with ER markers<sup>407</sup> and ER chaperones are upregulated in ALS patients<sup>408</sup>. An imbalance of Ca<sup>2+</sup> is another mechanism linked to ER stress<sup>409</sup>, potentially as a result of abnormal transporting of Ca<sup>2+</sup> between the ER and the mitochondria<sup>409</sup>. Further, a decrease in cellular Ca<sup>2+</sup>, within the ER, results in both mitochondrial and ER stress in the SOD1<sup>G93A</sup> model<sup>410,411</sup>.

#### ***4.1.2.5 Neuroinflammation***

ALS patients often have an elevated neuroinflammatory phenotype, including hallmarks such as elevated cytokine expression, glial activation, protein misfolding and aggregation, and immune cell infiltration into the CNS<sup>412</sup>, as demonstrated in Figure 4.1.1. Inflammatory cytokines are also elevated in the periphery of ALS patients, including TNF- $\alpha$ , IL-1 $\beta$ , and IL-6<sup>413</sup>. Microgliosis has been shown to correlate with ALS disease progression<sup>189,414</sup>. Microglia typically act in the healthy maintenance of the CNS by eliminating apoptotic cells and supporting both neurons and the other cells of the CNS such as astrocytes and oligodendrocytes<sup>415</sup>. However, in ALS patients microglia transition from a protective M2 phenotype<sup>416</sup> to a neurotoxic M1 phenotype<sup>186,417</sup> during disease progression. Upon this transition, M1 microglia proliferate and become overactivated, releasing proinflammatory cytokines, such as TNF- $\alpha$  and IL-1 $\beta$ , and toxic compounds, such as nitric oxide (NO), which have detrimental effects on MNs<sup>189</sup>. However, the current

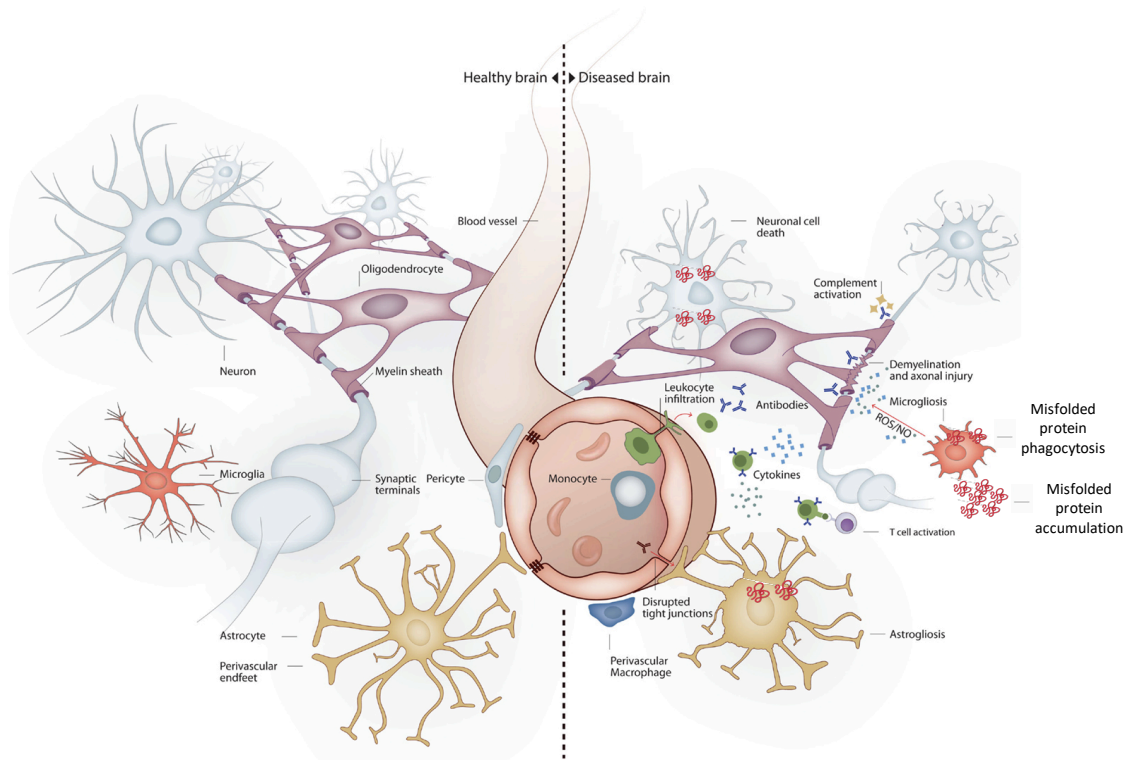


**Figure 4.1.1: Inflammation is mediated by glial cells within the CNS during neurodegenerative disorders**

Glial cells are an important component of the CNS. Glial cells maintain homeostasis within the CNS and provide support to neuronal cells to ensure efficient signal transduction and an anti-inflammatory environment. Additionally, glial cells have the ability to sense subtle inflammation changes in the environment of the CNS and also the periphery. Secretion of proinflammatory mediators in the CNS is mediated by astrocytes and microglia. A hallmark of neurodegeneration is the overactivation, and proinflammatory nature, of glial cells, resulting in an inflammatory milieu. Neuroinflammation is mediated by increased pro-inflammatory cytokine expression as well as the accumulation of misfolded proteins, resulting in the activation of glial cells. Astrocyte activation, or astroglial hypertrophy, is key to neurodegenerative disorders wherein astrocytes alter their morphology, in response to an inflammatory milieu, resulting in increased permeability of the BBB and enhanced inflammation via leukocyte infiltration. Microglial activation, or microgliosis, is another hallmark of neurodegenerative disorders. During microgliosis, microglia transition to a pro-inflammatory state in the presence of inflammatory cytokines and misfolded proteins. Inflammatory microglia exhibit a reduction in phagocytic potential as well as an elevation in the expression and secretion of pro-inflammatory cytokines and toxic factors. A pro-inflammatory environment promotes the degeneration of neuronal tissue and neurodegenerative disease progression. This figure is adapted from Sankowski *et al.* 2015<sup>418</sup>.

ALS literature is divided as to whether gliosis is a cause or consequence of dying MN within the CNS<sup>186,419</sup>.

Immune cell infiltration into the CNS is considered a hallmark of many neurodegenerative disorders, including ALS<sup>420</sup>. In ALS specifically, CD4<sup>+</sup> Foxp3<sup>+</sup> T-regulatory cells (T<sub>reg</sub>), have been found in the spinal cords of both mice and humans actively supporting glial cells<sup>421</sup>. Interestingly, the number of T<sub>reg</sub> cells in the periphery of ALS patients inversely correlates with disease progression<sup>422,423</sup>. These results suggest that CD4<sup>+</sup> T<sub>reg</sub> infiltration is a protective mechanism in ALS. Within the CNS T<sub>reg</sub> have been shown to suppress neuroinflammation and promote the neuroprotective effects of microglia<sup>424</sup>. In contrast, CD8<sup>+</sup> T cells have been found in the spinal cords of mice and humans with ALS, and can selectively kill MNs *in-vitro*<sup>425</sup>. Further, SOD1<sup>G93A</sup> mice crossed with RAG2<sup>-/-</sup> experience an acceleration in ALS progression, with similar effects observed in CD4<sup>-/-</sup>SOD1<sup>G93A</sup> mice. This demonstrates that CD4<sup>+</sup> T cells are protective in ALS<sup>421</sup>. While T cells appear to play a critical role in ALS, B cells appear to play little to no role in ALS progression<sup>426</sup>.

#### ***4.1.3 CNS Response to Peripheral Inflammation***

The CNS is an immune-privileged site. However, peripheral inflammation is detected by the nervous system to ensure appropriate control of immunological, physiological, and behavioural responses. Mechanisms that signal from the periphery to the CNS following a viral infection may include signalling through circumventricular organs

(CVOs), the BBB, immune cell tissue infiltration, and neuroimmunoregulatory mechanisms such as the immunological reflex<sup>420,427–429</sup>.

CVOs are highly vascularized areas within the midlines of the ventricles which act to transfer and propagate signals from the periphery into the CNS<sup>430</sup>. CVOs are characterized by large perivascular spaces, fenestrated capillaries, and specialized ependymal cells and are considered to be either sensory or secretory in nature<sup>428,431,432</sup>. The sensory CVOs have connections with nuclei in the hypothalamus and the brain stem and therefore have an important role in controlling the autonomic and endocrine functions<sup>431,432</sup>. CVOs play important roles in maintaining body temperature, osmolarity, and neuroinflammatory responses via receptors on the surfaces of neurons and astrocytes<sup>428</sup>. CD14 and TLR4 are both constitutively expressed in CVOs which, upon stimulation, causes microglial activation and the release of proinflammatory cytokines, leading to sickness behaviours and physiological responses, such as fever and cytokine expression, to combat infection<sup>433–435</sup>.

The BBB is a tight junction seal that separates the CNS from the periphery. The BBB consists of endothelial cells, astrocyte end feet, and pericytes, which together form a highly selective barrier protecting the CNS<sup>158</sup>. A common hallmark of neurodegenerative disorders is the loss of integrity of the BBB, typically late in disease progression, allowing potentially damaging stimuli and peripheral immune cells to enter the CNS and enhance disease progression<sup>163</sup>.

During peripheral infections, the immune response is coordinated by reflexive neural circuits. The immunological reflex consists of both the afferent and efferent arc<sup>427</sup>.

Signals are transmitted from the periphery to neurons through the use of cytokines. For example, neurons have been demonstrated to express IL1-R1 which interacts with IL-1 to induce signalling via NF-kB<sup>436,437</sup>. During IAV infection, pathogen associated molecular patterns (PAMPs) interact with TLRs to induce secretion of pro-inflammatory cytokines such as TNF- $\alpha$  and IL-1<sup>438,439</sup>. The vagus nerve senses IL-1 expression, and PAMPs, sending signals from the lungs to the hypothalamus to initiate fever and sickness syndrome<sup>440-443</sup>. Signaling from the periphery to brain is called the afferent arc, whereas signaling from the brain to periphery is termed the efferent arc<sup>427</sup>. The efferent arc is made up of cholinergic anti-inflammatory pathways<sup>444</sup>. Vagus nerve signals induce the release of acetylcholine which interacts with nicotinic acetylcholine receptor subunit  $\alpha$ -7 ( $\alpha$ 7nAChR).  $\alpha$ 7nAChR is widely expressed on immune cells which, when stimulated, causes downregulation of NF-kB translocation thereby suppressing pro-inflammatory cytokine expression, but leaving anti-inflammatory cytokine expression unaltered<sup>445-447</sup>.

#### ***4.1.4 The Role of Astrocytes in Neurodegenerative Disease***

Astrocytes can become reactive during chronic inflammatory conditions, a phenomenon known as astrogliosis. Astrogliosis exists on a spectrum ranging from mild to severe<sup>448</sup>. During mild astrogliosis there is a moderate upregulation of glial fibrillary acid protein (GFAP), a common marker of astrocyte reactivity<sup>449</sup>, without increases in cellular proliferation. Mild astrogliosis occurs when there is a perturbation that does not cause deep penetration into the CNS, or in response to a diffuse innate immune activation such as an infection<sup>448</sup>. At the other end of the spectrum, severe astrogliosis includes upregulation of

GFAP, hypertrophy of the cell body and processes, and excessive proliferation of astrocytes<sup>450</sup>. Severe astrogliosis results in the formation of a “glial scar”. A glial scar is an attempt to cordon off necrotic, inflammatory areas of the CNS from the healthy tissue<sup>451</sup>. Severe astrogliosis can be triggered by highly invasive infections, chronic neurodegeneration, or severe trauma<sup>450,452,453</sup>. Common triggers of astrogliosis include cytokines (IL-6, TNF $\alpha$ , IL-1, etc), LPS, TLR ligands, glutamate, ATP, ROS, hypoxia, and misfolded proteins<sup>448,454-459</sup>. The consequences of astrogliosis can be either protective or deleterious. Initially astrogliosis acts in a protective manner however, if left unchecked or if stimulation is persistent, astrogliosis can become deleterious. Glial scar formation is often associated with neurodegeneration/inflammation and can inhibit axon regeneration<sup>460-462</sup>. Astrogliosis can act protectively by sequestering glutamate, reducing ROS, degrading misfolded proteins, and limiting the spread of inflammatory mediators within the CNS<sup>458</sup>.

The role of astrocytes in common neurodegenerative disorders, such as AD and PD, has been extensively studied and while reactive astrocytes are present in both disorders, the function of the astrogliosis in these diseases remains unclear. A hallmark of AD is the accumulation of amyloid- $\beta$  (A $\beta$ ) plaques within the brain<sup>463</sup>, and reactive astrocytes are associated with A $\beta$  plaques<sup>464</sup>. Reactive astrocytes envelop A $\beta$  plaques to form glial scars, possibly in an attempt to prevent A $\beta$  mediated toxic effects<sup>465</sup>. Astrocytes also uptake and degrade A $\beta$ <sup>466-468</sup>. Comparatively, the role of astrogliosis is less well studied in PD. The exact etiology of PD remains elusive however, there is a loss of dopamine producing neurons and aggregation of misfolded  $\alpha$ -synuclein inside Lewy bodies<sup>469</sup>. Astrocytes within the substantia nigra, the area of the brain with dopamine producing neurons, were found to

have undergone mild astrogliosis in post-mortem specimens from PD patients<sup>470</sup>. Thus, the role and consequences of astrogliosis may differ from one neurodegenerative disorder to another.

Astrocytes have been implicated in ALS due to a downregulation of the receptor EAAT2, decreasing uptake of glutamate from within the synapse<sup>471</sup>. Glutamate signaling within MNs results in excitatory signaling. EAAT2 downregulation causes an accumulation of glutamate within the synapse, leading to overstimulation of MNs, and ultimately ends in a form of neuronal cell death described as excitotoxicity<sup>472</sup>. Interestingly, selective expression of mutant SOD1 within astrocytes was sufficient to cause MN toxicity. In this model, neurons were found to be dying due to hyperexcitability induced by factors released from astrocytes<sup>473</sup>. In SOD1 induced ALS, mSOD1 accumulates within astrocytes<sup>474</sup>. The knockdown of mSOD1 in the astrocytes of both the SOD1<sup>G37R</sup> and SOD1<sup>G85R</sup> mice models results in a decreased rate of disease progression and increased survival time<sup>331,346</sup>. Astrocytes in the SOD1<sup>G93A</sup> mouse model have been demonstrated to have elevated levels of cleaved caspase-3 in the presence of diseased MNs, and exhibited an altered morphology<sup>475</sup>. In diseased astrocytes, mitochondrial abnormalities result in elevated ROS and neurodegeneration<sup>476</sup>. Additionally, a key role of astrocytes is the signaling to neurons. In ALS the signals sent to neurons by astrocytes are proinflammatory, such as IFN- $\gamma$ <sup>477,478</sup>. While astrogliosis is observed in SOD1 mouse models of ALS, when SOD1 was sequestered to only astrocytes disease did not occur, despite the presence of astrogliosis<sup>479</sup> suggesting differences between *in-vitro*<sup>473</sup> and *in-vivo* roles of astrocytes<sup>479</sup>. Further, inhibition of astrocyte proliferation did not affect disease progression in the

SOD1<sup>G93A</sup> model<sup>480</sup>. Thus, while astrocytes and astrogliosis likely play an important role in ALS, their exact contribution to disease remains uncertain.

#### ***4.1.5 The Role of Microglia in Neurodegenerative Disease***

In addition to the regulation of a healthy CNS milieu, microglia can become over activated, a phenomenon known as microgliosis. Microgliosis is detrimental to the CNS and is a hallmark of neuroinflammation. Therefore, it is often associated with neurodegenerative disorders<sup>481</sup>. According to the “prion paradigm”, during neurodegenerative disorders misfolded proteins form a “seed” of endogenous protein aggregation which ultimately self-propagates and aggregates into larger insoluble masses. While the nature of seeding differs depending on disease, the prevailing theory of the prion paradigm is that the misfolding protein cascade remains similar between diseases<sup>482</sup>. Misfolded proteins are a well-known inducer of microgliosis<sup>186,417,483–485</sup> which suggests that microgliosis could be an important element in the etiology of neurodegenerative diseases.

During AD, microglia are initially stimulated to phagocytose A $\beta$  in a protective manner<sup>486</sup>. However, chronic stimulation of microglia by A $\beta$  results in microgliosis and elevated neuroinflammation. In a positive feedback loop, microglia express receptors such as TLR2, TLR4 and NLRP3, which recognize A $\beta$ , activating microglia and inducing the release of proinflammatory cytokines which in turn result in cellular damage and the release of damage associated molecular patterns (DAMPs)<sup>487–489</sup>. Microglia also recognize DAMPs which stimulates the secretion of proinflammatory cytokines such as TNF- $\alpha$  and

IL-1 $\beta$ , thereby propagating neurotoxicity and further A $\beta$  aggregation<sup>490</sup>. Interestingly, mouse knockouts of TLR2, TLR4, and NLRP3 in models of AD attenuate A $\beta$  aggregation and prevent cognitive damage<sup>491–494</sup>. During PD microgliosis is induced by detection of aggregated  $\alpha$ -synuclein<sup>495</sup>. Microgliosis during PD may accelerate disease progression through  $\alpha$ -synuclein recognition via TLR1/2<sup>496,497</sup>.

In addition to AD and PD, microgliosis has been implicated in ALS<sup>189</sup>. In SOD1 cases of ALS, mSOD1 released from damaged neurons results in microglial activation which in turn results in proinflammatory cytokine and ROS release, further damaging MNs. Misfolded protein recognition stimulates NF- $\kappa$ B signaling and IL-1 $\beta$  expression in microglia<sup>498,499</sup>. Upon inhibition of NF- $\kappa$ B signaling, MNs were saved from microglial mediated toxicity<sup>506</sup>. Additionally, microglia isolated from SOD1<sup>G93A</sup> mice do not display an M1/M2 classical activation pattern. Rather, they seem to have an intermediate phenotype. Activation of microglia in the SOD1<sup>G93A</sup> model is due to signals from multiple stimuli, such as misfolded proteins and neuronal cell death<sup>186</sup>. In this model, survival can be extended following the depletion of TLR4, further suggesting that microglial activation is an important mediator of disease progression<sup>500</sup>. Interestingly, microglia have been demonstrated to play an active role in the clearance of TDP-43 in TDP-43 mouse models of ALS. Therefore, in the context of TDP-43 healthy microglia may be neuroprotective<sup>416</sup>. Taken together, the interplay between astrocytes and microglia is likely of great importance in ALS, and the two cell types may be acting synergistically to accelerate disease progression.

#### ***4.1.6 Neurodegeneration, TLR Signaling, and Microgliosis***

TLR signaling is an important mediator of microglial activation, and yet is essential for enhancing survival in the SOD1<sup>G93A</sup> mouse model. TLR activation results in signaling through the adaptor TIR domain containing adaptor inducing IFN- $\beta$  (TRIF) and myeloid differentiation factor 88 (MyD88)<sup>501</sup>. Interestingly, deficiencies in TRIF accelerated ALS progression by causing dysfunctional astrocyte activation<sup>502</sup>. Bone marrow transplants from MyD88 deficient donors also accelerated disease progression<sup>503</sup>. However, TLR4 deficiency specifically in microglia and astrocytes extended survival and significantly delayed disease onset in SOD1<sup>G93A</sup> mice<sup>500</sup>. TLR4 signaling functions through both MyD88 and TRIF to propagate signals<sup>501</sup> and therefore the conflicting results, with regard to ALS-related survival, remain a mystery. However, the role of TLR4 signaling in ALS likely varies in a cell-type specific manner with TLR4 signaling being detrimental in microglia and astrocytes, yet protective in other cells.

The NF- $\kappa$ B pathway is involved in a variety of functions, including inflammation and immune responses<sup>504</sup>. The activation of the classical NF- $\kappa$ B pathway in microglia, and not astrocytes, results in MN death<sup>499</sup>. In microglia, NF- $\kappa$ B activation is induced by TLR signaling following sensing of a variety of PAMPs and DAMPs and triggers a proinflammatory response<sup>504</sup>. A common DAMP in ALS is misfolded proteins, which can be sensed through TLRs. Indeed, mSOD1 has been observed to activate microglia in a MyD88 dependent manner<sup>503</sup>. TLRs involved in the sensing of misfolded proteins include TLR2 and TLR4, as well as CD14<sup>484</sup>. Intriguingly, exposure of MNs to mSOD1 was insufficient to induce toxicity *in-vitro*. However, exposing microglia to mSOD1 resulted in

a proinflammatory activation<sup>484</sup>. Activated microglia and astrocytes can be toxic to MNs both *in-vitro* and *in-vivo*<sup>186,417,419,483,484,505–509</sup>. Interestingly, shRNA-mediated knockdown of SOD1 in astrocytes and MNs, along with suppression of NF-κB activation in microglia, increased mouse survival by 67 days in the SOD1<sup>G93A</sup> ALS model<sup>510</sup>. These results support the notion that targeting microglial activation and inducers of microglial priming simultaneously may prove to be a viable therapy for neurodegenerative disorders in the future.

#### ***4.1.7 Environmental Triggers of ALS***

The cross-talk between the immune system and portions of the CNS may represent a key target for ALS pathogenesis. Mutations in genes that have roles regulating immunity could influence the response to environmental factors and thereby contribute to disease pathogenesis<sup>511,512</sup>. Additionally, the penetrance of many ALS related genes is incomplete and therefore, genetics alone seem insufficient to fully explain all cases of ALS<sup>513–516</sup>.

Many environmental factors have been explored as risk factors for ALS. These include specific chemical exposures, heavy metals exposure, smoking, physical activity, military service, and viral infections<sup>511,512,517,518</sup>. Our group recently published a review evaluating the published links between viral infection and neurodegenerative diseases. It is clear that despite many associations, there have been few detailed mechanistic studies into the role of viral infection in contributing to ALS onset or progression<sup>518</sup>. Despite the paucity of mechanistic studies exploring viral infections and ALS, the correlative studies which have made associations between particular viruses and ALS often report post-mortem

identification of chronic neurotropic viruses, such as enteroviruses and retroviruses<sup>518</sup>. Recently, an ALS-like syndrome has been reported in Brazilian patients following infection with Chikungunya virus<sup>519</sup>. Interestingly, Chikungunya virus infection has also been demonstrated to infect astrocytes and microglia to induce apoptosis of glial cells and secretion of pro-inflammatory mediators<sup>520</sup>.

The associations between ALS and viral infections are predominantly based on elevated rates of detection of neurotropic viruses in the blood and post-mortem brain tissue of ALS patients, which was explored in the early 1990's<sup>521</sup>. Poliovirus was one of the first viruses linked to ALS due to the development of post-polio myelitis – a disease that closely resembles ALS<sup>522,523</sup>. Furthering this link, *in-vitro* models have shown that poliovirus 3C protease can cleave TDP-43, a causal protein of ALS, leading to its aberrant function<sup>524</sup>. Further, elegant work from the Luo laboratory has demonstrated that coxsackievirus B3 can induce TDP-43 cleavage through the 2A and 3C proteases, suggesting that TDP-43 cleavage may be a general property of enteroviral infection<sup>525</sup>. This recent work has provided much more convincing direct evidence that enteroviruses may be involved in ALS, and that this warrants more study.

Evidence linking endogenous retroviruses, such as human endogenous retrovirus K (HERV-K), to ALS has also been described. Mice expressing the *env* protein of HERV-K develop symptoms of progressive MN disease, characterized by decreased synaptic activity and dendritic spine abnormalities in pyramidal neurons<sup>526</sup>. Additionally, compared to control individuals who had elevated systemic inflammation, ALS patients had elevated levels of *env* transcripts within the CSF<sup>526</sup>. More recently, quantitative analyses of HERV-

K transcript abundance failed to find a difference between control and ALS patients in motor cortex samples<sup>527,528</sup>. Therefore, the role of HERV-K in ALS remains controversial and may only be relevant in a subset of ALS patients.

The *Herpesviridae* family of viruses have also been implicated in ALS, in addition to other neurodegenerative diseases. This is not too surprising given that Alphaherpesviruses are able to directly infect neuronal tissue and have been detected at elevated rates in patients with AD<sup>529</sup> and PD<sup>530</sup>. Prospective cohort studies indicated that incidence of AD correlated with herpes simplex virus type 1 (HSV-1) reactivation<sup>531</sup>. Additional epidemiological evidence demonstrated an enrichment of HSV-1 DNA in post-mortem brain samples of AD patients, wherein the viral DNA was found to be specifically localized within amyloid plaques<sup>532–534</sup>. Recently, it has been suggested that A $\beta$  seeding and plaque formation may be an anti-viral mechanism against HSV-1 infection and reactivation<sup>535</sup>.

HSV-1 is an enveloped neurotropic virus carrying a linear double-stranded DNA genome. Initially, the virus typically produces an active lytic infection in epithelial cells lining the oral or genital mucosa<sup>536</sup>. HSV-1 spreads from epithelial cells to neurons where it is transported to the trigeminal ganglia through retrograde transport along axons. Within the trigeminal ganglia, HSV-1 establishes latency in sensory neurons<sup>537</sup>. HSV-1 reactivates intermittently, and upon reactivation virions can follow axons toward the epithelium or, in rare cases, can travel further into the CNS and exert neurotoxic effects<sup>529</sup>.

Conversely, acute non-neurotropic infections have also been linked to neurodegenerative diseases. IAV, a member of the Orthomyxoviridae family, has a segmented negative sense, single stranded RNA genome<sup>538</sup>. IAV infections are typically

limited to the lung. However, evidence of IAV involvement in neurodegenerative diseases, especially PD, has been reported. Studies have found enrichment of IAV within the post-mortem brain samples of PD patients<sup>539</sup>. Interestingly, Hosseini et al. have demonstrated that non-neurotropic IAV strains, such as H3N2, are able to induce long-lasting neuroinflammation with accompanying structural changes to hippocampal neurons – a typical hallmark of AD<sup>540</sup>. Further, IAV infection also triggered multiple sclerosis in the autoimmune-prone 2D2 mice. IAV infection caused time-dependent transcriptomic changes in the cerebellum and spinal cord, mainly through the upregulation of immune response genes activated through IFN-1 and -2 receptor signaling<sup>541</sup>.

In addition to viral infections, bacterial infections have also been a focus of study. One of the first associated environmental associations with ALS was discovered in Guam in 1945<sup>542</sup>. The native population of Guam had a much higher incidence rate of ALS than would normally be expected based on population estimates<sup>543</sup>. Eventually it was discovered that a chemical produced by cyanobacteria,  $\beta$ -methylamino-L-alanine (BMAA), appeared to be causing the elevation in ALS rates within the Guamanian population<sup>511</sup>. This phenomenon has also been reported in France<sup>544</sup> and the USA<sup>545</sup>, in areas with higher BMAA levels. However, the mechanism responsible for the neurotoxicity caused by BMAA exposure remains unclear. Multiple potential mechanisms have been proposed, including glutathione depletion, astrogliosis, and the induction of protein misfolding and toxic aggregation<sup>546</sup>. Crosstalk between the brain and the gut microbiome has also recently been explored in both the context of ALS and other neurodegenerative disorders. The microbiota has been demonstrated to increase permeability of the BBB as well as affect

neuronal survival and neurogenesis<sup>547</sup>. The majority of studies exploring the microbiota have focused on PD<sup>548</sup> while the role of the microbiota on ALS is less clear. Recently Blacher *et al.* demonstrated that different bacteria present in the microbiome can act to ameliorate or enhance ALS development. Protective microbiota stimulated the release of nicotinamide into the CSF<sup>549</sup>.

The numerous studies that have identified the presence of various neurotropic viruses in ALS patients provide a possible etiological link between infections and ALS. However, many of these studies may suffer from an “enrichment bias”, as the viruses identified tend to cause persistent infections and can thus be found in the post-mortem tissues<sup>518</sup>. Indeed, acute viral infections may have a similar effect. However, these infections are cleared by the immune system relatively quickly, precluding post-mortem detection. This makes epidemiological association studies with viruses that cause acute infections much more difficult. In addition, although they are biologically very diverse, viral infections often cause perturbations in the same pathways underlying neuronal death as observed in ALS including ER stress, protein misfolding, mitochondrial manipulation, and stress granule (SG) induction<sup>518</sup>, as illustrated in Figure 4.1.2. Together, viral infections may be perturbing one, or multiple, pathophysiological pathways to induce the onset and/or progression of ALS.

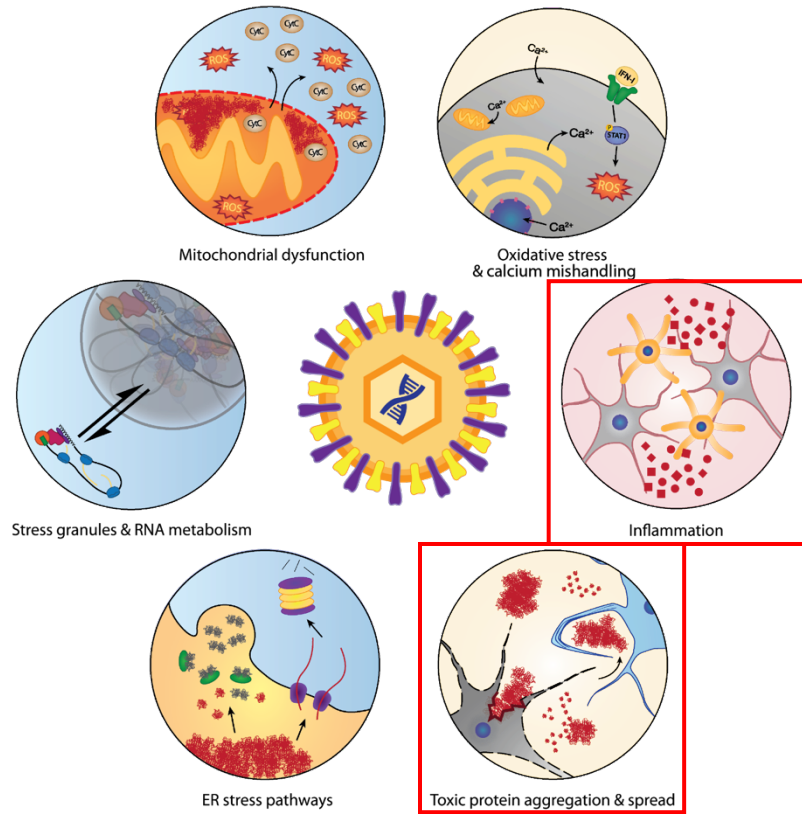


**Figure 4.1.2: Pathophysiological pathways associated with ALS are perturbed during viral infection**  
 Viral infections disrupt pathophysiological pathways associated with ALS. Potential etiological pathways associated with ALS include SG formation, RNA metabolic defects, mitochondrial and ER dysfunction, neuroinflammation, and misfolded protein spreading and aggregation. Viral interference with one or multiple of these pathways may lead to ALS onset and/or accelerated disease progression in individuals with a genetic predisposition towards ALS. Herein, we focus on the role of infection on inflammation and misfolded protein accumulation as they relate to ALS following viral infection. This figure is adapted from Celeste and Miller 2018<sup>518</sup>.

#### ***4.1.8 Implications for Environmental Factors as Triggers of ALS***

The role of the environment has long been accepted within the ALS field to be an important determinant of disease onset. Viral infections have been specifically explored as one such trigger. Herein, we have developed a compelling case for IAV accelerating disease – possibly through the overactivation of microglia. Given that priming of innate cells cannot be passed down to daughter cells<sup>550,551</sup>, there may be a key window of time in which environmental factors can trigger ALS.

Recent research has explored the role of neurotropic viral infection, namely rabies, HIV, and ZIKV, on spinal neurons derived from isogenic iPSCs with an induced mutation in FUS. Interestingly, all three of the RNA viruses tested exacerbated ALS phenotypes, *in-vitro*, including SG formation and neurodegeneration<sup>552</sup>. SG formation is a common hallmark of FUS-related ALS<sup>553</sup>. Viral infection increased the accumulation of SG's in iPSC-derived neurons. Further, viral infection altered the localization of FUS thereby exacerbating the deleterious effects of mutated-FUS and inducing neuronal death<sup>552</sup>. Therefore, it will be important to determine whether our findings in the SOD1<sup>G93A</sup> model extend to ALS cases caused by other mutations, and to sporadic ALS where the mutation may not be known.

ALS has been demonstrated to spread from an initial focal point<sup>554</sup>. A gap in our understanding of ALS is the mechanism(s) that govern this spread. Perhaps most intriguingly, these authors noted the characteristic spreading of ALS mechanisms, such as SG formation and protein mislocalization, was induced by viral infection *in vitro*<sup>552</sup>. Rabies was able to spread through neuronal circuitry<sup>552</sup>. The spread of rabies through the *in-vitro*

neural circuitry may be an example of how neurotropic viruses could mediate disease spread.<sup>552</sup> However, there are limitations to be noted in the interpretation of the study described above. Firstly, it was performed *in-vitro*, and so it is unclear the extent to which those observations can be extended to an *in vivo* setting. Furthermore, the viruses used were relatively rare and all three were neurotropic. For example, the Center for Disease Control (CDC) reported that only 23 cases of rabies were reported from 2008 – 2017<sup>555</sup>, HIV affects approximately 1.1 million in the USA<sup>556</sup>, and 148 cases of ZIKV were reported in US territories during 2018<sup>557</sup>. Comparatively, the number of ALS cases in the USA is approximately 16,000 people each year, or roughly 30,000 patients currently living with ALS, as described by the CDC<sup>558</sup>. Taken together, the likelihood of these specific viruses being an important trigger of ALS is low. However, many of the cellular and physiological responses to viral infection are similar and are more likely to serve as conserved mechanisms across many types of viruses.

Many of the proteins implicated in ALS are ubiquitously expressed<sup>318</sup>. Therefore, infection related exacerbation of ALS pathogenesis could conceivably occur in non-neuronal tissue, by non-neurotropic infections, and ultimately spread misfolded protein to neuronal tissue in a prion-like manner. Indeed, this model is consistent with the non-cell autonomous nature of ALS. mSOD1 has been demonstrated to spread to other cells in both exosomal independent and dependent manners. Upon uptake by neighbouring cells, mSOD1 acts in a prion-like manner and prompts further SOD1 misfolding<sup>342</sup>. Exosomes have been explored in the context of viral infections and can act as anti-viral mediators to signal to neighbouring cells that an infection is occurring. Additionally, viruses have the

ability to co-opt the exosomal secretion pathway as a manner of shuttling viral particles to the cell surface<sup>559</sup>. Influenza, specifically, has been demonstrated to incorporate exosomal markers into the virion<sup>560</sup>. Abundant host proteins are also associated with influenza virions<sup>560</sup>. SOD1 is highly abundant and ubiquitously expressed protein, making up approximately 1% of total cellular protein content<sup>561</sup>. Further, mSOD1 has been found on the surface of released exosomes rather than being packaged within them<sup>342</sup>. This presents the possibility for mSOD1 to be found on the surface of influenza virions, or on exosomes secreted during IAV infection<sup>562</sup>.

mSOD1 has been observed in the CSF of ALS patients by immunoprecipitation assays and sandwich ELISAs. Further, mSOD1 was detected in all patients with ALS assessed, regardless of the genetic basis of their disease (i.e. even in cases with WT SOD1)<sup>338</sup>. The accumulation of mSOD1 in the CSF of ALS patients was found to be toxic to NSC-34 cells (a neuronal cell line) and the toxic effect was lost following immunoprecipitation-mediated removal of SOD1 from the CSF<sup>338</sup>. Interestingly, mSOD1 was observed in the CSF of a subset of PD patients and patients with progressive supranuclear palsy<sup>338</sup>, suggesting that the misfolding of SOD1 is a general feature of some neurodegenerative disorders.

There is data to suggest that viral infections may serve as an important and potentially widespread environmental trigger of neurodegenerative disease. Viruses perturb many of the same pathophysiological pathways associated with ALS<sup>518</sup> and may trigger hallmarks of ALS such as protein misfolding and inflammation, which could in turn induce gliosis. Further, some cases of infection mediated onset of ALS may explain the spreading

phenomenon observed during the progression of ALS phenotypes in diagnosed patients<sup>554</sup>. Finally, given the commonalities between neurodegenerative disorders, viral infections may act as a trigger of neurodegenerative disorders in a general sense.

#### ***4.1.9 Hypothesis***

Herein, we hypothesize that IAV infection will accelerate ALS progression by promoting neurotoxic inflammatory processes. To explore this hypothesis, we have multiple aims.

1. To determine whether IAV infection accelerates the onset and/or progression of ALS in the SOD1<sup>G93A</sup> mouse model.
2. To determine whether a live viral infection is required for the acceleration of ALS progression in the SOD1<sup>G93A</sup> mouse model.
3. To determine whether IAV infection alters the pathophysiological pathways associated with ALS including inflammation and misfolded protein accumulation.

## 4.2 Results

### 4.2.1 IAV infection accelerates ALS progression

To explore whether an acute viral infection could alter ALS disease onset and/or progression we infected both WT and SOD1<sup>G93A</sup> mice. Mice were infected with a sublethal infection of IAV (300pfu, 0.1LD<sub>50</sub>) (Fig. 4.1) or a lethal infection of IAV (3000pfu, 1LD<sub>50</sub>) (Fig. 4.2) intranasally at day 60 and we explored the effect of infection on ALS pathology. Day 60 was chosen because at this age SOD1<sup>G93A</sup> mice are pre-symptomatic<sup>563</sup>, allowing us to determine whether infection could “trigger” ALS earlier than in uninfected mice, or whether it causes disease to progress more rapidly. ALS clinical signs were measured using the rotarod assay, which measures a combination of limb strength, coordination, and gait. Mice were placed on the rotarod and the latency until fall was measured. Importantly, WT and SOD1<sup>G93A</sup> mice were assessed pre-infection, at day 60. As expected, both genotypes performed equivalently prior to infection (Fig. 4.1A)

Following recovery from infection, we assessed ALS disease progression of the SOD1<sup>G93A</sup> mice (Fig. 4.1 and 4.2). All mice initially demonstrate an improvement in their performance on the rotarod as the animals gain experience with the skill. The 0.1LD<sub>50</sub> IAV infection resulted in an acceleration of disease progression, with infected mice reaching 50% of their initial fall time approximately 2 weeks earlier than uninfected mice (Fig. 4.1B and 4.1C). The performance of WT mice on the rotarod progressively improves throughout the duration of the experiment, regardless of prior infection (Fig. 4.1B). In addition to ALS clinical signs, we also assessed how 0.1LD<sub>50</sub> IAV infection affected the overall survival of the SOD1<sup>G93A</sup> mice (Fig 4.1D). Both the infected and uninfected SOD1<sup>G93A</sup> mice started to

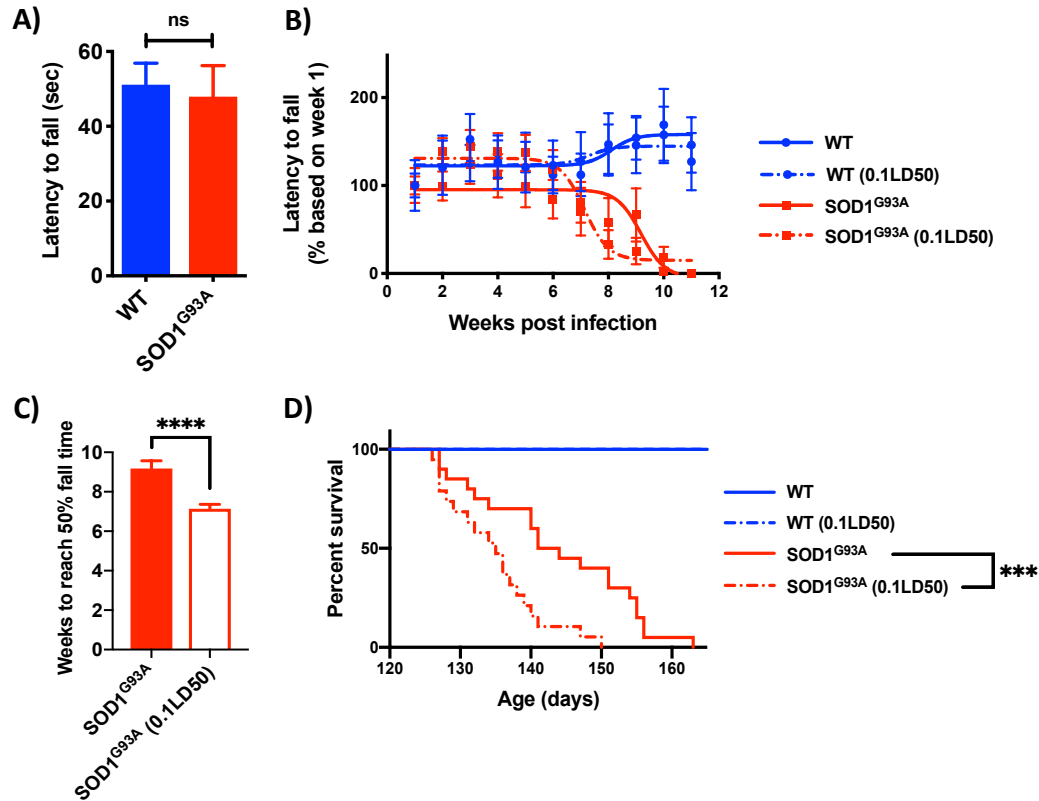


**Figure 4.1: Sublethal Influenza A infection accelerates ALS disease progression and reduces overall survival in the SOD1<sup>G93A</sup> ALS model**

WT and SOD1<sup>G93A</sup> mice were infected with 0.1LD<sub>50</sub> of IAV at 60 days of age. (A) WT (n = 9) and SOD1<sup>G93A</sup> (n=9) mice were assessed via the rotarod, prior to infection at day 60. (B) Following recovery of IAV infection mice were assessed for ALS clinical signs weekly using the rotarod. Latency to fall was averaged for each condition, and normalized to week 1 as 100%, and the data was analyzed using a sigmoidal curve fit. WT (uninfected) n = 13. WT (0.1LD<sub>50</sub>) n = 10. SOD1<sup>G93A</sup> (uninfected) n = 11. SOD1<sup>G93A</sup> (0.1LD<sub>50</sub>) n = 14. (C) Using the sigmoidal fit for each condition we extracted the point at which the fit reaches 50% of the maximum fall time and graphed ± standard error of the fit. Statistics were determined via a Student's T-test with p < 0.0001, \*\*\*\*. (D) The endpoint survival of each condition was assessed due to the mice succumbing from their ALS-like clinical signs. Endpoint was defined as the mice being unable to right for 30s on each side. Statistics were determined using the Mantel-Cox test with p < 0.001, \*\*\*. WT (uninfected) n = 13. WT (0.1LD<sub>50</sub>) n = 10. SOD1<sup>G93A</sup> (uninfected) n = 20. SOD1<sup>G93A</sup> (0.1LD<sub>50</sub>) n = 19.

succumb to ALS at the same time, approximately 130 days of age. Interestingly, infection of SOD1<sup>G93A</sup> mice at day 60 resulted in more rapid ALS symptom progression (Fig. 4.1C and 4.1D). 1LD<sub>50</sub> IAV infection resulted in a similar effect on ALS progression as 0.1LD<sub>50</sub> IAV infection (Fig. 4.2A and 4.2B). Again, we observed a decrease in survival time due to more rapid ALS disease progression following infection (Fig. 4.2C). These results demonstrate that a single sub-lethal IAV infection, prior to onset of ALS clinical signs, can accelerate ALS disease progression in the SOD1<sup>G93A</sup> mouse model.

#### ***4.2.2 IAV infection does not cause more severe morbidity in the SOD1<sup>G93A</sup> ALS mouse model***

Given the impact of IAV infection in accelerating ALS progression, we sought to determine whether SOD1<sup>G93A</sup> mice experienced more severe IAV infection than WT mice. We observed no difference in morbidity as measured by weight loss following the 0.1LD<sub>50</sub> IAV infection when comparing WT and SOD1<sup>G93A</sup> mice (Fig. 4.3A). Following a 1LD<sub>50</sub> IAV infection the difference between WT and SOD1<sup>G93A</sup> mice was minimal with regards to weight loss (Fig. 4.3B). Further, there were no differences observed between WT and SOD1<sup>G93A</sup> mice survival upon IAV infection at either 0.1LD<sub>50</sub> (Fig. 4.3C) or 1LD<sub>50</sub> (Fig. 4.3D). Thus, SOD1<sup>G93A</sup> mice do not seem more susceptible to severe IAV infection when compared to WT mice.

To confirm whether SOD1<sup>G93A</sup> expression had an effect on viral replication we performed viral growth curves in MEFs (Fig. 4.3E). Both WT and SOD1<sup>G93A</sup> MEFs were infected with IAV at a MOI of 3. Viral replication was then quantified using plaque assays.

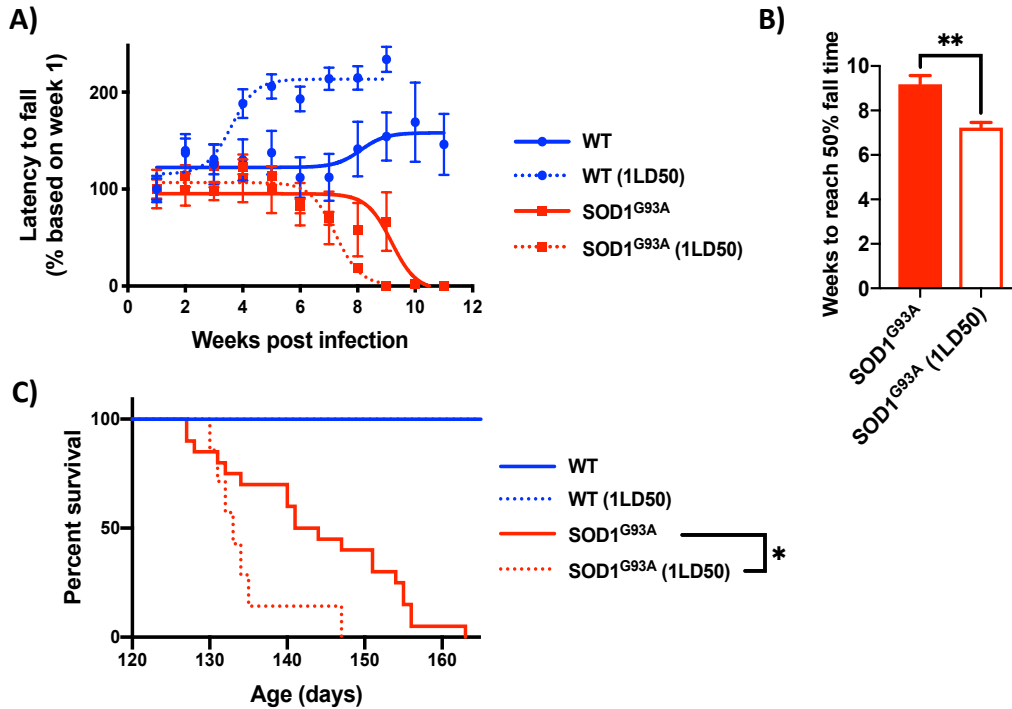


**Figure 4.2: Lethal Influenza A infection accelerates ALS disease progression and reduces overall survival in the SOD1<sup>G93A</sup> ALS model**

WT and SOD1<sup>G93A</sup> mice were infected with 1LD<sub>50</sub> of IAV at 60 days of age. (A) Following recovery of IAV infection mice were assessed for ALS clinical signs weekly using the rotarod. Latency to fall was averaged for each condition, and normalized to week 1 as 100%, the data was analyzed using a sigmoidal curve fit. WT (uninfected) n = 13. WT (1LD<sub>50</sub>) n = 7. SOD1<sup>G93A</sup> (uninfected) n = 11. SOD1<sup>G93A</sup> (1LD<sub>50</sub>) n = 7. (B) Using the sigmoidal fit for each condition we extracted the point at which the fit reaches 50% of the maximum fall time and graphed ± standard error of the fit. Statistics were determined via Student's T-test with p < 0.01, \*\*. (C) The endpoint survival of each condition was assessed due to the mice succumbing from their ALS-like clinical signs. Endpoint was defined as the mice being unable to right for 30s on each side. Statistics were determined using the Mantel-Cox test with p < 0.05, \*. WT (uninfected) n = 13. WT (1LD<sub>50</sub>) n = 7. SOD1<sup>G93A</sup> (uninfected) n = 20. SOD1<sup>G93A</sup> (1LD<sub>50</sub>) n = 7.

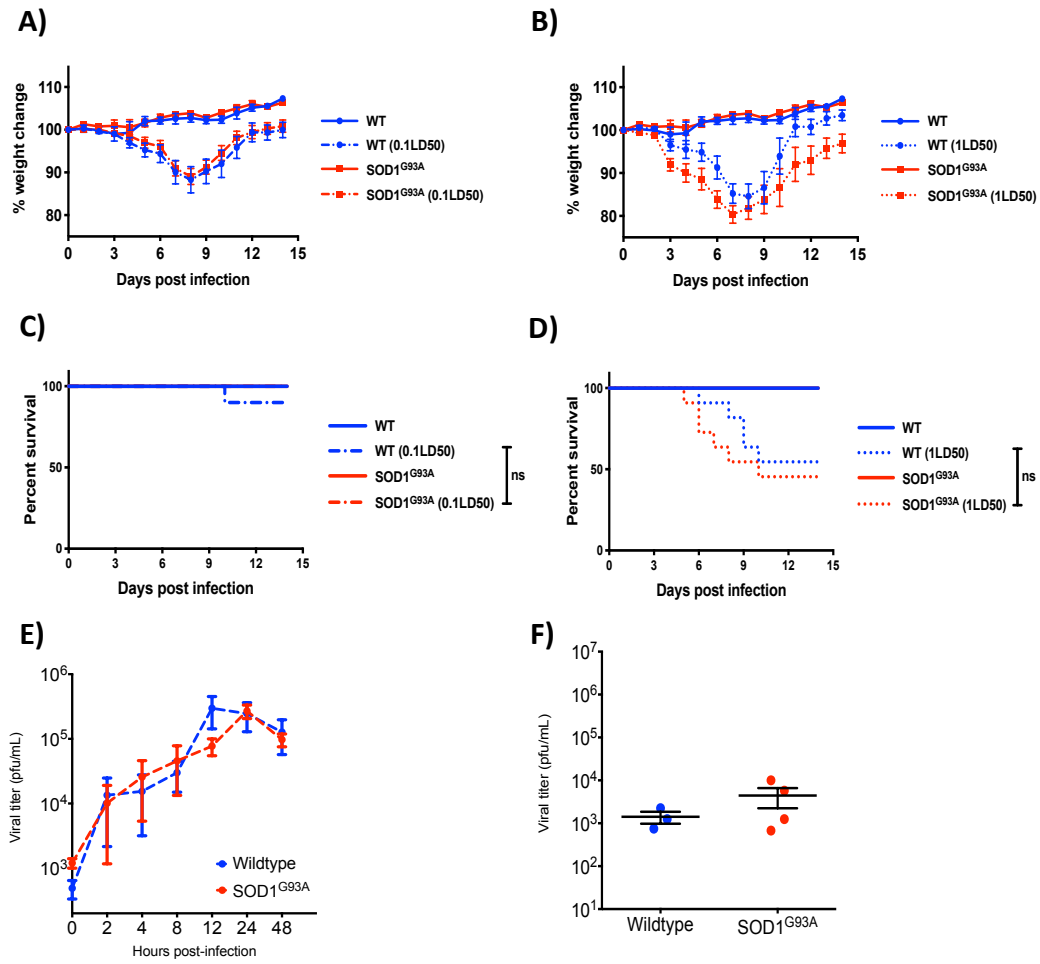


**Figure 4.3: SOD1<sup>G93A</sup> expressing mice exhibit similar morbidity to wildtype mice during an influenza A infection**

WT and SOD1<sup>G93A</sup> mice were infected with 0.1LD<sub>50</sub> or 1LD<sub>50</sub> of IAV at 60 days of age. WT (uninfected) n = 8. WT (0.1LD<sub>50</sub>) n = 10. WT (1LD<sub>50</sub>) n = 11. SOD1<sup>G93A</sup> (uninfected) n = 10. SOD1<sup>G93A</sup> (0.1LD<sub>50</sub>) n = 19. SOD1<sup>G93A</sup> (1LD<sub>50</sub>) n = 11. (A and B) Weight loss was monitored for 14 dpi with 0.1LD<sub>50</sub> or 1LD<sub>50</sub> of IAV. (C and D) The endpoint survival of the mice was assessed for 14 days following infection with 0.1LD<sub>50</sub> (C) or 1LD<sub>50</sub> (D) of IAV. Endpoint was defined as 20% weight loss. (E) WT and SOD1<sup>G93A</sup> MEFs were infected with MOI 3 of IAV and viral titres were assessed using the plaque assay. N = 3. (F) WT and SOD1<sup>G93A</sup> mice were infected with 0.1LD<sub>50</sub> IAV at 60 days of age. Lungs were homogenized 4 dpi and viral titres were assessed using the plaque assay. WT N = 3. SOD1<sup>G93A</sup> N = 4.

We found that SOD1<sup>G93A</sup> and WT MEFs were equally permissive to IAV replication. Additionally, we explored viral loads in the lungs of WT and SOD1<sup>G93A</sup> mice at day 4 post-infection (when peak viral titers are typically observed) with 0.1LD<sub>50</sub> of IAV. Consistent with our *in-vitro* data, we found no difference in viral load between WT and SOD1<sup>G93A</sup> mice (Fig. 4.3F). These results suggest that the SOD1<sup>G93A</sup> mutation has no effect on IAV replication or pathogenesis. Thus, the impact of IAV infection on acceleration of ALS progression is not likely due to differences in infection severity in the SOD1<sup>G93A</sup> model.

#### ***4.2.3 Effect of IAV infection on ALS progression does not require viral replication***

We have observed that a sublethal IAV infection accelerates ALS onset and progression (Fig. 4.1). However, the mechanism through which infection drives ALS progression in the SOD1<sup>G93A</sup> mice remained unclear. We therefore set out to characterize the role of the immune response to infection in accelerating ALS disease. We used inactivated IAV to explore the role of the immune response independent of viral replication. To this end, we administered SOD1<sup>G93A</sup> mice with 50 µg of formalin-inactivated IAV either via *i.m.* injection or *i.n.* administration (Fig 4.4). Following administration of inactivated IAV the mice were weighed for a 14 day period. As expected, the mice lost no weight (data not shown). Following this 2-week period, mice were subjected to the rotarod test, weekly, in an identical fashion to the IAV-infected mice described previously. We observed a difference between the control and *i.m.* administered inactivated IAV SOD1<sup>G93A</sup> mice (Fig 4.4A and 4.4B). Similar to the 0.1LD<sub>50</sub> infected SOD1<sup>G93A</sup> mice, *i.m.* vaccinated SOD1<sup>G93A</sup> mice reached 50% of their initial fall time for the rotarod test 2 weeks earlier than control

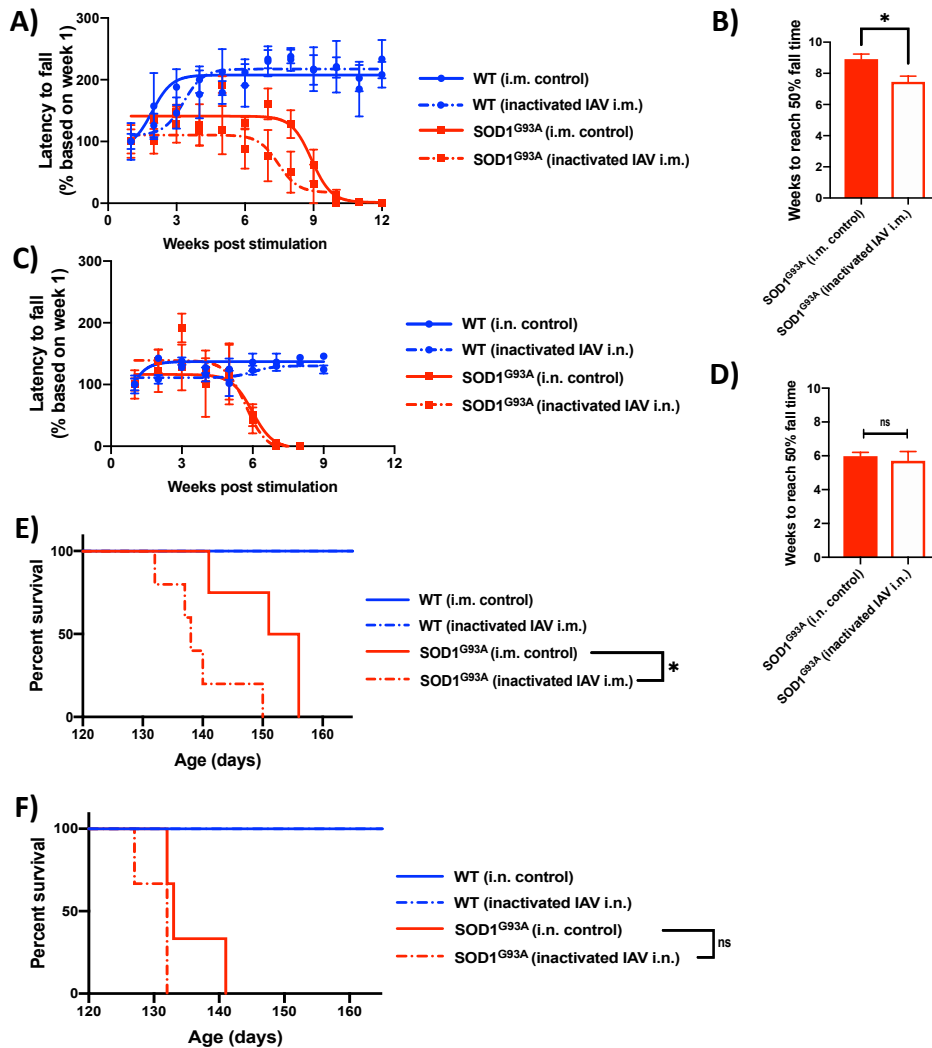


**Figure 4.4: Administration of inactivated influenza A results in an intermediate effect on ALS progression in the SOD1<sup>G93A</sup> ALS model**

WT and SOD1<sup>G93A</sup> mice were stimulated with 50µg of inactivated IAV via *i.m.* injection into the right hind limb or *i.n.* in 40µL volume at 60 days of age. WT (*i.m.* control) n = 4. WT (*i.m.* inactivated IAV) n = 11. SOD1<sup>G93A</sup> (*i.m.* control) n = 4. SOD1<sup>G93A</sup> (*i.m.* inactivated IAV) n = 5. WT (*i.n.* control) n = 4. WT (*i.n.* inactivated IAV) n = 5. SOD1<sup>G93A</sup> (*i.n.* control) n = 3. SOD1<sup>G93A</sup> (*i.n.* inactivated IAV) n = 3. (A and C) Following a 14 day period post-stimulation with inactivated IAV, WT and SOD1<sup>G93A</sup> mice were assessed for ALS clinical signs weekly using the rotarod. Latency to fall was averaged for each condition, and normalized to week 1 as 100%, and the data was analyzed using a sigmoidal curve fit. *i.m.* (A) and *i.n.* (C). (B and D) Using the sigmoidal fit for each condition we extracted the point at which the fit reaches 50% of the maximum fall time and graphed ± standard error of the fit. *i.m.* (B) and *i.n.* (D). Statistics were determined via one-way ANOVA with p < 0.05, \*, p < 0.01, \*\*, and p < 0.001, \*\*\*. (E and F) The endpoint survival of each condition was assessed due to the mice succumbing from their ALS-like clinical signs. Endpoint was defined as the mice being unable to right for 30s on each side. *i.m.* (E) and *i.n.* (F). Statistics were determined using the Mantel-Cox test with p < 0.05, \*.

mice. SOD1<sup>G93A</sup> mice develop specifically manifest disease in the hind limbs. Therefore, we hypothesized that the local inflammatory response that would have occurred following *i.m.* injection of inactivated IAV into the hindlimb may have been an especially potent insult that later affected the progression of ALS in the SOD1<sup>G93A</sup> mice. Thus, we also administered the inactivated IAV *i.n.* to mimic the route of a live IAV infection, though the extent of inflammation would have been much lower than during an actual infection. In contrast to what we observed after *i.m.* injection, administration of inactivated-IAV did not enhance the ALS progression compared to the control (Fig. 4.4C and 4.4D).

In addition to assessing the role of inactivated IAV on ALS progression, via the rotarod, we also monitored mice until reaching endpoint due to ALS clinical sign progression. Administration of inactivated IAV *i.m.* caused a significant decrease in survival time compared to the *i.m.* control (Fig 4.4E). However, there was no difference between the *i.n.* control and *i.n.* inactivated IAV treated SOD1<sup>G93A</sup> mice (Fig 4.4F). These results suggest that the immune response to infection is at least partially responsible for the accelerated progression of ALS in this model, and that the location and magnitude of inflammation seem to be important.

#### ***4.2.4 Cytokine profiles of SOD1<sup>G93A</sup> mice are similar to WT in vitro and in vivo***

Evidence that the immune response seemed to be sufficient to explain (at least partially) the acceleration of ALS disease led us to explore whether there were any abnormalities in the antiviral response. To explore the antiviral response *in vitro*, we stimulated WT and SOD1<sup>G93A</sup> MEFs with inactivated IAV (Fig. 4.5). We observed similar

expression levels of the antiviral genes *ISG15*, *DDX58*, *IFIT1*, and *IFITM3*, quantified using qRT-PCR, in WT and SOD1<sup>G93A</sup> MEFs (Fig. 4.5A). In addition to anti-viral gene expression, we explored the cytokine profile of SOD1<sup>G93A</sup> MEFs via a 32-plex cytokine array. In unstimulated conditions, SOD1<sup>G93A</sup> MEFs had higher expression of proinflammatory markers (Fig. 4.5B). Following stimulation with inactivated IAV, both WT and SOD1<sup>G93A</sup> MEFs demonstrated elevated cytokine levels relative to baseline, but there was no difference between the genotypes (Fig. 4.5C). These results suggest that expression of the SOD1<sup>G93A</sup> mutation does not affect host ISG expression or cytokine response to viral infection.

We next assessed the cytokine response *in vivo* to IAV infection. To do this, we infected WT and SOD1<sup>G93A</sup> mice at day 60 with 0.1LD<sub>50</sub> IAV. Following infection, we isolated and homogenized both the lungs and brains of mice at 4 and 30 dpi (64 and 90 days of age, respectively) and subjected the homogenates to the same 32-plex cytokine array as was used for *in vitro* analysis (Fig. 4.6). We did not observe an elevation in the cytokine profile of either the lung (Fig. 4.6A) or the brain (Fig. 4.6B) of the SOD1<sup>G93A</sup> mice compared to WT mice at either 4 days or 30 dpi. Each cytokine/chemokine analyzed was normalized to matched tissue from uninfected WT mice. At these times, baseline levels of cytokine expression were not elevated in the SOD1<sup>G93A</sup> mice lungs or brains compared to the WT mice. While there were no appreciable differences in cytokine production in either the lungs or brains of SOD1<sup>G93A</sup> mice compared to WT mice, we reasoned that SOD1<sup>G93A</sup> mice may be more sensitive to the effects of inflammation due to underlying dysregulated immune responses.

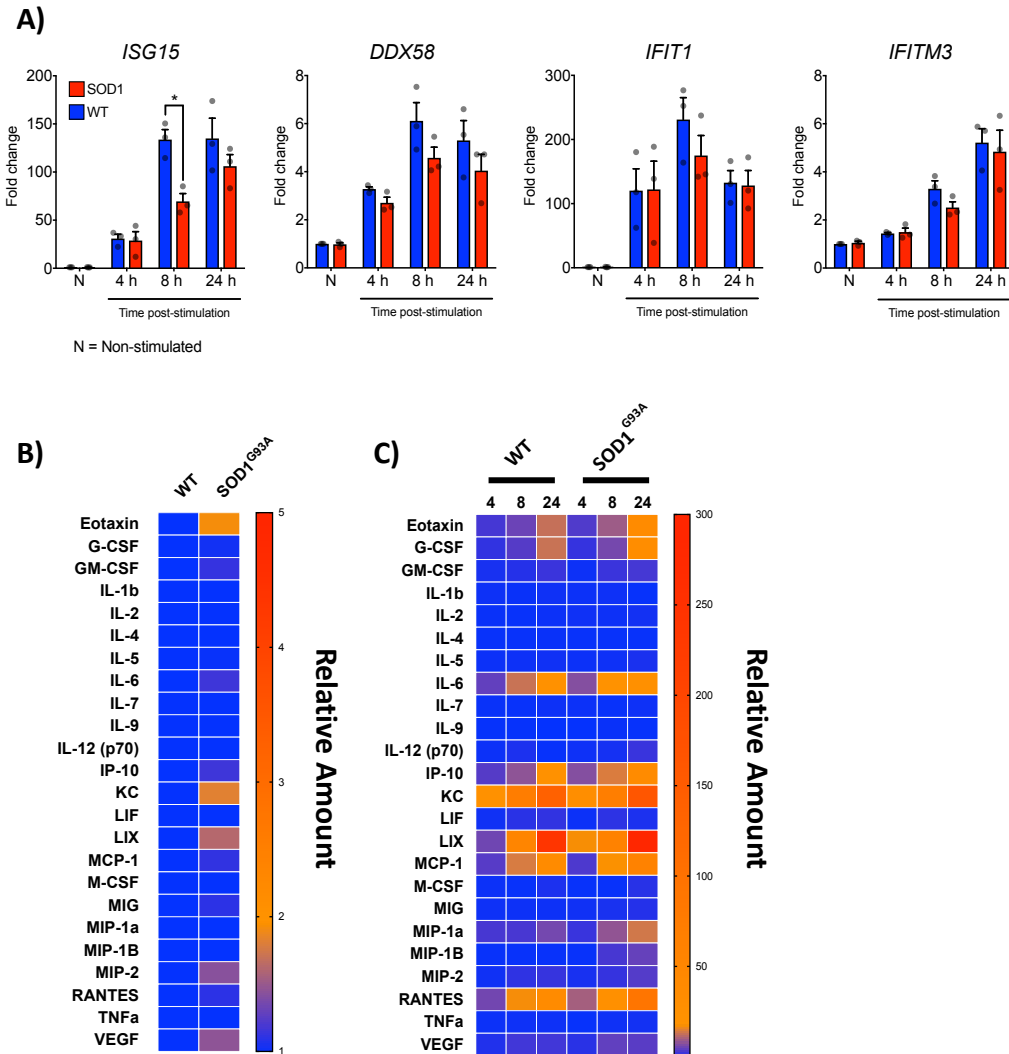


**Figure 4.5: *In vitro* inflammatory and antiviral response to inactivated influenza A virus in WT and SOD1<sup>G93A</sup> expressing conditions**

WT and SOD1<sup>G93A</sup> MEFs were stimulated with inactivated-IAV for 4, 8, and 24 h, following which media and RNA was isolated from MEFs. (A) Fold changes of antiviral gene transcript quantity at 4, 8, and 24 hours post-stimulation for ISG15, DDX58, IFIT1, and IFITM3 relative to non-stimulated WT conditions. Circles are plotted for data points from individual replicates, and error bars represent standard error of the mean. N = 3. p < 0.05, \*, determined via one-way ANOVA. (B) Multiplex cytokine/chemokine analysis was performed on cell culture supernatants from unstimulated MEFs. Heat map shows fold changes of protein concentration relative to non-stimulated WT conditions. N = 5. (C) Multiplex cytokine/chemokine analysis was performed on cell culture supernatants from MEFs stimulated with inactivated virus at 4, 8, and 24 h post-stimulation. Heat map shows fold changes of protein concentration relative to non-stimulated WT conditions. N = 5.

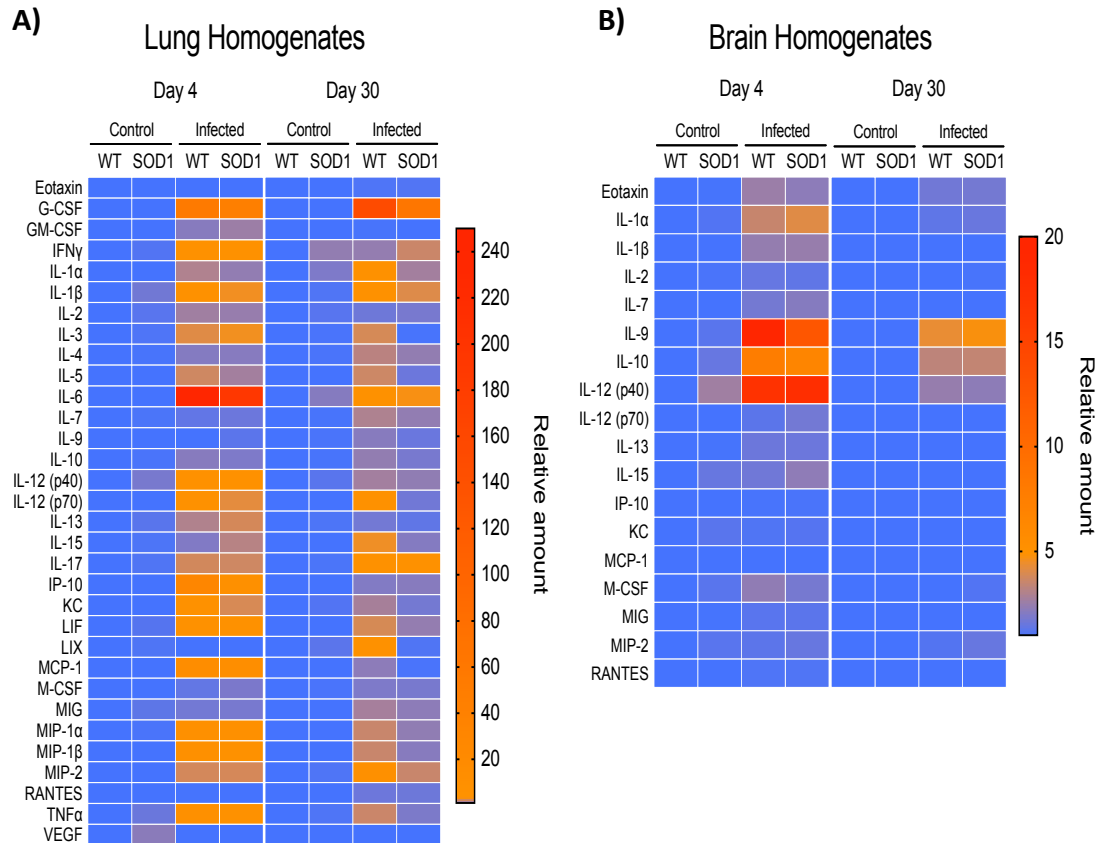


**Figure 4.6: *In vivo* inflammatory response to influenza A virus infection in WT and SOD1<sup>G93A</sup> mice.** Lungs and brain were extracted from WT and SOD1<sup>G93A</sup> mice at 4 and 30 dpi (64 and 90 days of age) following 0.1LD<sub>50</sub> IAV infection. (A) Multiplex cytokine/chemokine analysis was performed on WT and SOD1-G93A mice 4 and 30 days after influenza infection. Control animals were uninfected. Heat maps show fold changes of protein concentration relative to WT controls of the same age in lung homogenates. N = 3. (B) Multiplex cytokine/chemokine analysis was performed on WT and SOD1-G93A mice 4 and 30 days after influenza infection. Control animals were uninfected. Heat maps show fold changes of protein concentration relative to WT controls of the same age in brain homogenates. N = 3.

#### ***4.2.5 Microgliosis levels are elevated in SOD1<sup>G93A</sup> mice at later disease stages following IAV infection***

The loss of neurons and glial activation in the spinal cord are hallmarks of ALS progression in both mice and humans<sup>189,564</sup>. To determine whether infection might influence the extent of microglial activation, we infected SOD1<sup>G93A</sup> and WT mice with 0.1LD<sub>50</sub> at day 60 and isolated the lumbar spinal region at 120 days of age (60 dpi). At 120 days of age clinical signs of disease are clearly present, but animals are not at endpoint. We used Iba-1 and GFAP staining to quantify microgliosis (Fig. 4.7) and astrogliosis (Fig. 4.8), respectively, within the lumbar spinal cord.

Using Iba-1, a standard marker for activated microglia<sup>565</sup>, we observed an increase in the levels of activated microglia in the lumbar spinal region of SOD1<sup>G93A</sup> compared to WT mice (Fig. 4.7A). Further, infected SOD1<sup>G93A</sup> mice exhibited elevated levels of microgliosis compared to uninfected SOD1<sup>G93A</sup> at 120 days of age (Fig. 4.7B). Interestingly, previously-infected WT mice exhibit a minor increase in the level of microgliosis, in comparison to uninfected WT mice, but exhibited no ALS-like clinical signs (Fig. 4.7B). In addition to microglia, we also assessed the extent of astrogliosis using GFAP as a marker of astrocytes<sup>449</sup> in the spinal cord (Fig. 4.8A). There was a trend towards an elevation in astrogliosis in the infected SOD1<sup>G93A</sup> spinal cords in comparison to the uninfected SOD1<sup>G93A</sup> that was lower in magnitude to the differences observed in microgliosis, and narrowly missed reaching statistical significance (Fig. 4.8B). Similarly, to microgliosis, astrogliosis appeared to be elevated in WT infected mice compared to uninfected WT mice. However, the overall magnitude of astrogliosis detected in WT mice

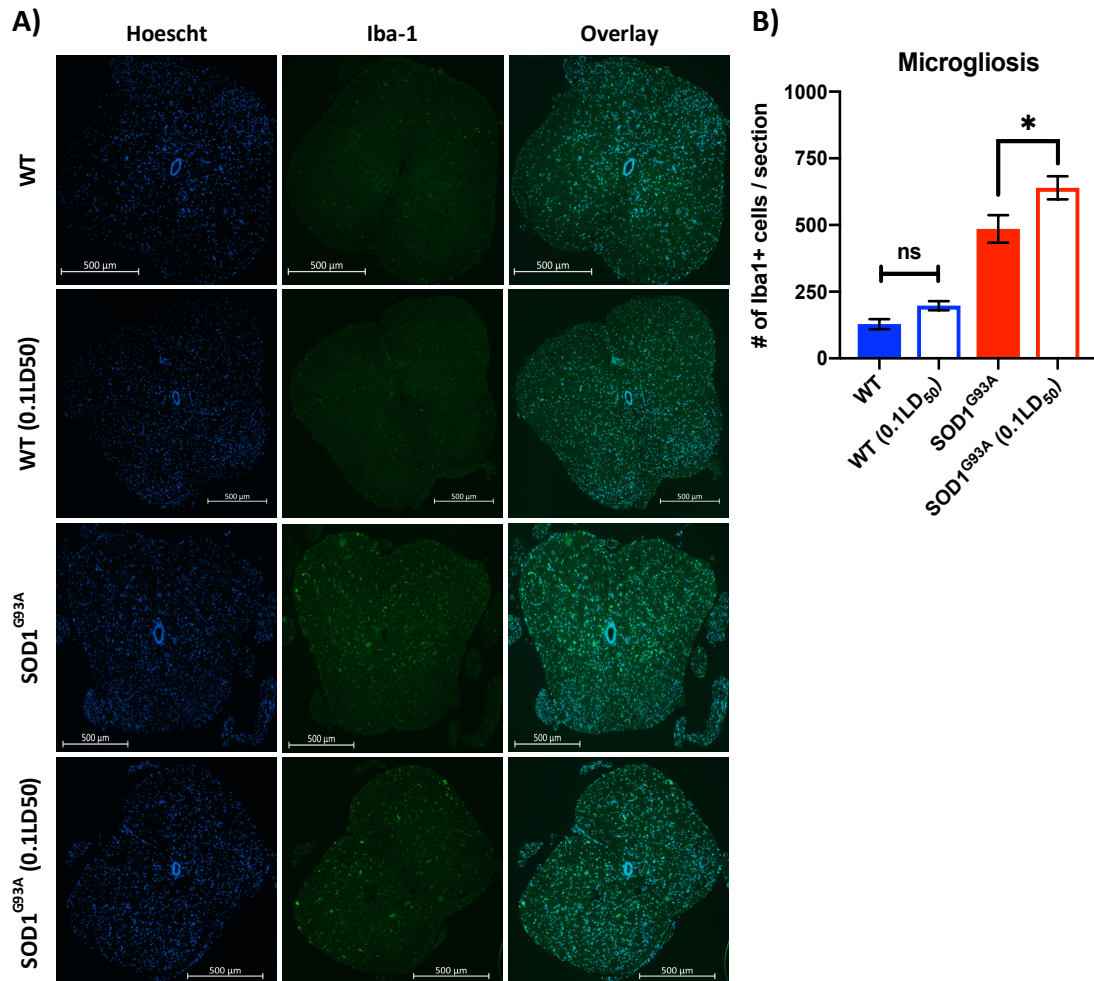


**Figure 4.7: Influenza A infection of SOD1<sup>G93A</sup> mice induces elevated levels of microgliosis**

WT and SOD1<sup>G93A</sup> mice were infected with 0.1LD<sub>50</sub> of IAV at 60 days of age. At day 120 mice were euthanized and the lumbar spinal region was extracted, fixed in 3.7% PFA for 48h, and sectioned. Scale bars represent 500  $\mu$ m. (A) Lumbar spinal sections were stained with Iba-1 for activated microglia and Hoechst33342 for DNA. Images were taken with the Zeiss at 5X magnification. (B) Iba-1+ microglia were counted in each treatment using ImageJ. N = 3, \*, p < 0.01, as determined via one-way ANOVA.

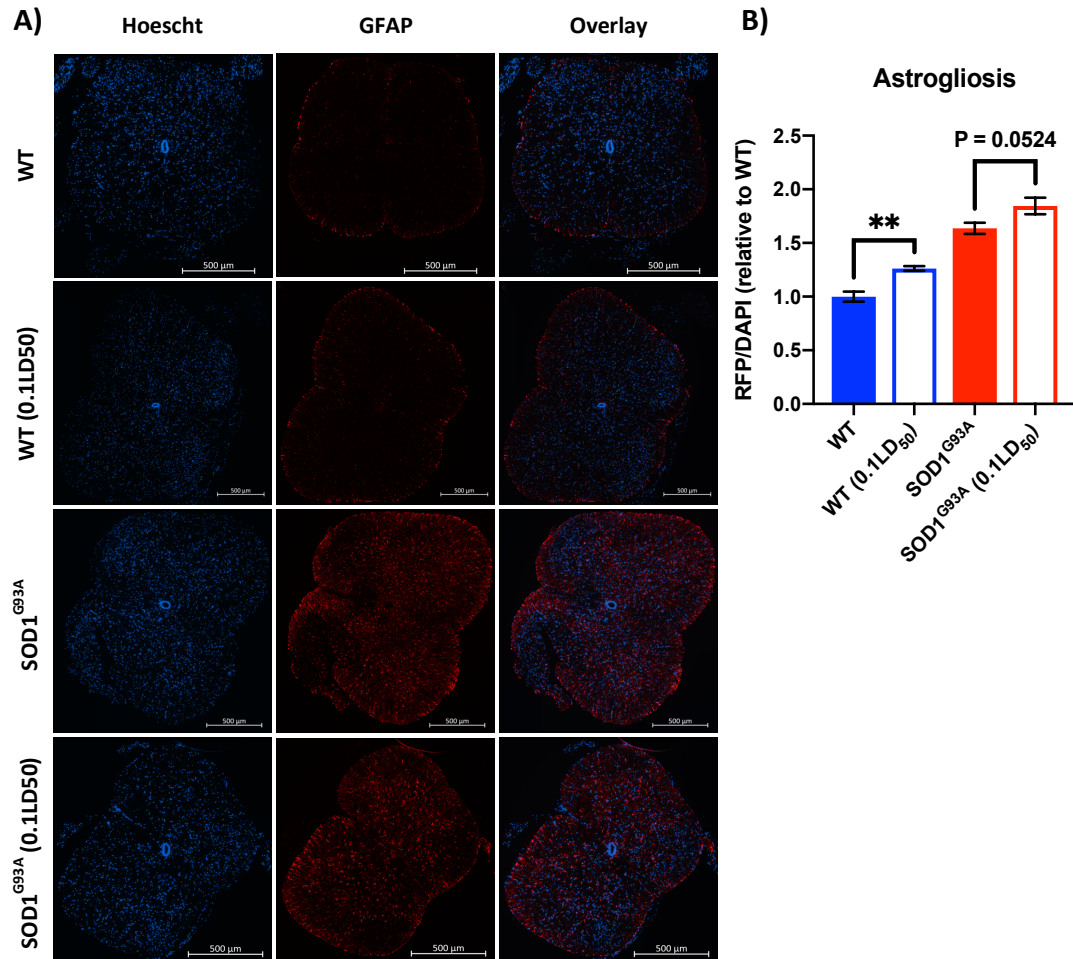


**Figure 4.8: Influenza A infection of SOD1<sup>G93A</sup> mice induces a slight elevation in astrogliosis**

WT and SOD1<sup>G93A</sup> mice were infected with 0.1LD<sub>50</sub> of IAV at 60 days of age. At day 120 mice were euthanized and the lumbar spinal region was extracted, fixed in 3.7% PFA for 48h, and sectioned. Scale bars represent 500 μm. (A) Lumbar spinal sections were stained with GFAP for activated astrocytes and Hoechst33342 for DNA. Images were taken with the Zeiss at 5X magnification. (B) GFAP integrated fluorescent intensity was quantified and quantified based on the Hoechst integrated fluorescent intensity using ImageJ. N = 3, \*\*, p < 0.01

was still much lower than those observed even in uninfected SOD1<sup>G93A</sup> animals (Fig. 4.8B). In conclusion, peripheral inflammation stimulated by IAV infection results in the exacerbation of microgliosis in in the lumbar spine of SOD1<sup>G93A</sup> mice.

#### ***4.2.6 Misfolded SOD1 levels are unaltered in the spinal cords of previously-infected SOD1<sup>G93A</sup> mice at day 60 post-infection***

The SOD1<sup>G93A</sup> mouse model is characterized by SOD1 misfolding as a hallmark of disease<sup>563</sup>. mSOD1 has been demonstrated to activate glial cells both *in-vitro* and *in-vivo*<sup>484,566–568</sup>, and as a result we reasoned that glial activation may be due to the accumulation of mSOD1 following IAV infection. We measured mSOD1 using the antibody AMF7-67, which specifically recognizes mSOD1<sup>341</sup> (Fig. 4.9). As expected, mSOD1 was not detected in the spinal cords of WT mice whereas a strong signal of mSOD1 was evident throughout the spinal cord of SOD1<sup>G93A</sup> mice (Fig. 4.9A). Interestingly, mSOD1 levels were unaltered in the SOD1<sup>G93A</sup> spinal cord of infected mice in comparison to uninfected SOD1<sup>G93A</sup> mice at day 120 (60 dpi) (Fig. 4.9B). Taken together, mSOD1 levels are not elevated to the same extent as glial activation in the spinal cord of day 120 previously infected SOD1<sup>G93A</sup> mice. However, elevation of mSOD1 may be seen immediately following infection with differences lost as mice reach closer to endpoint.

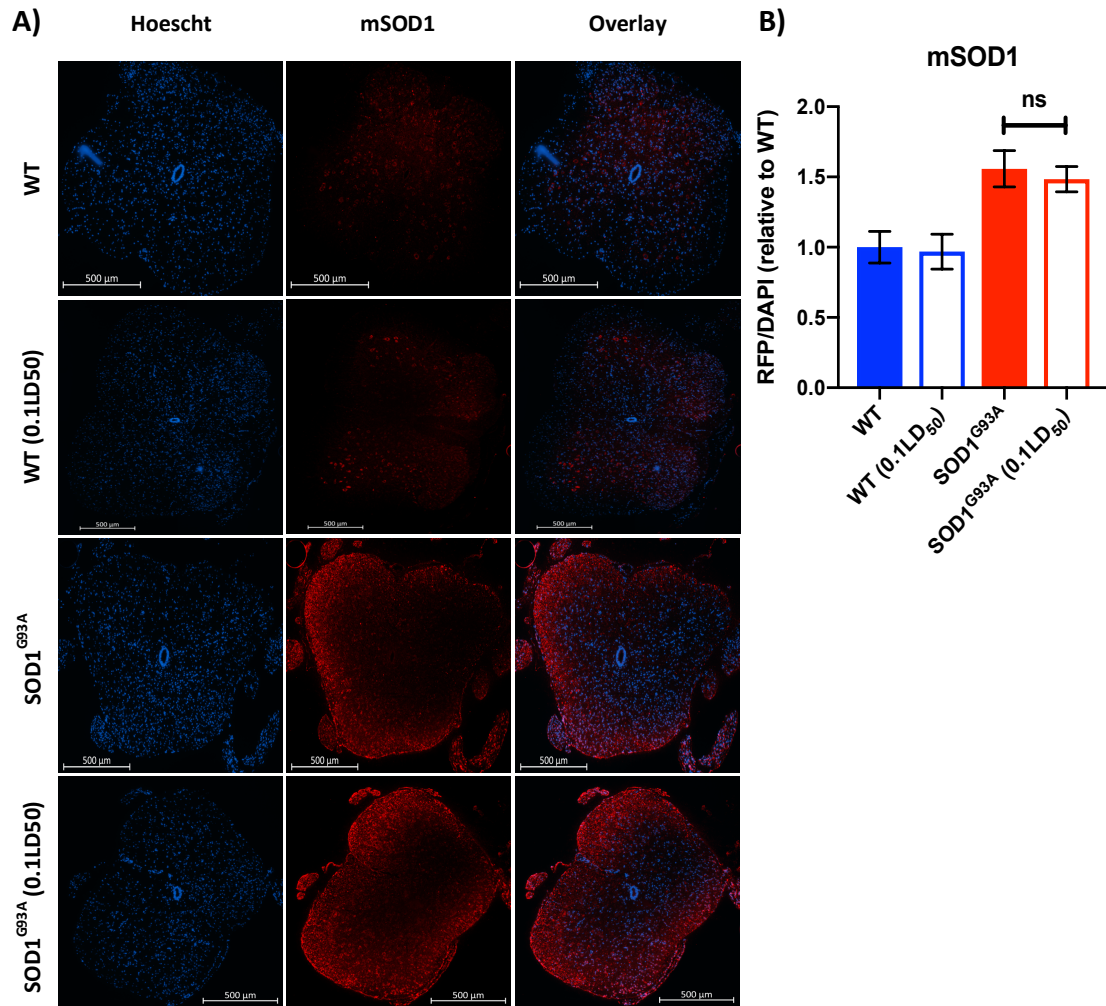


**Figure 4.9: Influenza A infection of SOD1<sup>G93A</sup> mice does not affect misfolded SOD1 accumulation**  
 WT and SOD1<sup>G93A</sup> mice were infected with 0.1LD<sub>50</sub> of IAV at 60 days of age. At day 120 mice were euthanized and the lumbar spinal region was extracted, fixed in 3.7% PFA for 48h, and sectioned. Scale bars represent 500  $\mu$ m. (A) Lumbar spinal sections were stained with AMF7-63, a marker of mSOD1, and Hoechst33342 for DNA. Images were taken with the Zeiss Imager M2 at 5X magnification. (B) mSOD1 integrated fluorescent intensity was quantified and quantified based on the Hoechst integrated fluorescent intensity using ImageJ. N = 3

## 4.3 Discussion

### *4.3.1 IAV Infection Accelerates ALS Progression Independent of Infection Severity*

ALS remains a devastating, untreatable disease, with an average survival of 2-5 years post-diagnosis. Much effort has been exerted to discover the etiology of ALS in order to design effective treatments<sup>135</sup>. Unfortunately, all available treatments offer modest increases in survival for patients and the current standard of care is mainly palliative in nature<sup>135-143</sup>. A plethora of pathophysiological phenotypes have been described for ALS. However, what remains unclear is which of these potential mechanisms are an underlying cause of ALS, and which may be a consequence. ALS is a multifactorial disease with a complex interplay between genetic and environmental factors likely being critical to determining the probability, timing and rate of disease onset and progression<sup>511,512</sup>. To explore this interplay, we utilized a well-studied ALS mouse model expressing the human SOD1<sup>G93A</sup> mutation<sup>327</sup>, and explored the potential for common viral infections to alter the onset and/or the progression of ALS.

Infection of the SOD1<sup>G93A</sup> model with a single sublethal infection (0.1LD<sub>50</sub>) of IAV accelerated ALS progression by approximately two weeks and decreased survival by approximately 7 days. Interestingly, this effect was not due to any intrinsic differences in the acute response to infection. Both the WT and SOD1<sup>G93A</sup> mice experienced comparable morbidity as measured by weight loss. Additionally, viral replication rates were similar in the lungs of WT and SOD1<sup>G93A</sup> mice and in MEFs. Together, these results suggested that the effects of viral infection on ALS progression are not due to the virus causing more severe infection of the SOD1<sup>G93A</sup> mice.

A more severe infection with 1LD<sub>50</sub> of IAV resulted in a comparable weight loss between WT and SOD1<sup>G93A</sup> infected mice, with half of both WT and SOD1<sup>G93A</sup> infected groups succumbing to infection. Mice that survived 1LD<sub>50</sub> infection experienced accelerated ALS-like clinical signs similar to those infected with 0.1LD<sub>50</sub>. However, 1LD<sub>50</sub> infection creates a selection bottleneck, wherein the more robust mice survive infection. Since the weaker mice (or mice that experience more severe clinical signs) reach endpoint due to acute infection, it is difficult to make firm conclusions about whether severity of infection causes more rapid progression of ALS disease using only this data. In the future, use of attenuated viruses that cause less severe infection than that caused by 0.1LD<sub>50</sub> will shed more light on this issue.

#### ***4.3.2 The Effects of IAV Infection on the SOD1<sup>G93A</sup> Model is not Virus Specific***

We also explored whether the effect of IAV infection on ALS progression was unique to influenza virus, or a more general response to viral infection. To this end we infected female SOD1<sup>G93A</sup> mice with HSV-1. HSV-1 infection accelerated disease progression by approximately 2 weeks, similar to the acceleration observed following an IAV infection. Interestingly, acute HSV-1 infection appeared much more severe in the SOD1<sup>G93A</sup> mice. Roughly 75% of SOD1<sup>G93A</sup> females succumbed to HSV-1 infection however, viral replication rates were unaltered relative to WT in vaginal lavage samples or *in-vitro*. HSV-1 differs from IAV in many ways, key among which is the ability of HSV-1 to infect neurons<sup>536</sup>, whereas the strain of IAV used herein is not neurotropic.

HSV-1 was of particular interest to study in addition to IAV due to its high seroprevalence and recent findings that HSV-1 is associated with AD and PD<sup>569</sup>. Recurrent HSV-1 infection induces cognitive defects and neurodegenerative hallmarks in mice including A $\beta$  expression, tau tangles, and neuroinflammation (IL-6, IL-1 $\beta$ , and astrogliosis) elevation<sup>570</sup>. However, IAV can also induce neuroinflammation and microgliosis following peripheral infection with either neurotropic or non-neurotropic strains<sup>540</sup>. Taken together, these data suggest that common neurotropic and non-neurotropic viral infections can accelerate the progression of ALS in SOD1<sup>G93A</sup> mice.

#### ***4.3.3 The Immune Response to Infection is Sufficient to Induce ALS Acceleration***

To separate the effects of viral infection from the immune response to the infection in the SOD1<sup>G93A</sup> model, we administered inactivated IAV. Inactivated-IAV was administered via both *i.m.* and *i.n.*, routes to explore whether route of administration alters the effect on ALS progression. Interestingly, inactivated-IAV administered *i.m.* accelerated the ALS progression of the SOD1<sup>G93A</sup> mice, albeit to a lesser extent than an infection. However, following *i.n.* administration of inactivated IAV, we observed that there was no effect on ALS progression. In terms of survival, inactivated-IAV, administered *i.m.*, resulted in SOD1<sup>G93A</sup> mice succumbing to ALS clinical signs faster than control SOD1<sup>G93A</sup> mice which received a saline injection. In contrast, SOD1<sup>G93A</sup> mice administered inactivated-IAV *i.n.* did not display a difference in ALS-related survival, compared to control SOD1<sup>G93A</sup> mice.

Intramuscular administration of inactivated-IAV occurs in the quadriceps, which is also the site at which disease manifests in the SOD1<sup>G93A</sup> model. A key feature of ALS is the loss of muscular innervation through the degradation of the neuromuscular junction (NMJ). In the SOD1<sup>G93A</sup> model of ALS, NMJ degradation begins prior to the onset of ALS clinical signs, as early as 56 days of age<sup>571</sup>. Therefore, local inflammation at the site of disease may exacerbate this process. In contrast, following *i.n.* administration, inflammation is likely much lower in the periphery and limited primarily to the lung, not a site of onset in the SOD1<sup>G93A</sup> model. Currently, influenza and pneumococcal vaccinations are recommended for ALS patients in order to reduce the risk of severe respiratory illness<sup>572</sup>. Interestingly, these results may suggest that patients with ALS may benefit from a non-injectable vaccine method rather than the typical injectable vaccines. Taken together, these results suggest that the inflammatory response is at least partially responsible for accelerated ALS progression in the SOD1<sup>G93A</sup> model.

#### ***4.3.4 Cytokine Responses Induced by IAV Infection are not Globally Altered in SOD1<sup>G93A</sup> Mice***

CNS innate immune cells such as microglia and astrocytes are known to become skewed towards an inflammatory phenotype in ALS and other neurodegenerative disorders, such as AD and PD<sup>573</sup>. Further, the SOD1<sup>G93A</sup> model and patients with ALS demonstrate a neuroinflammatory profile<sup>189</sup>. A proinflammatory phenotype is evident prior to symptom onset and correlates with disease progression<sup>417,499,574–579</sup>. In addition to CNS perturbations,

systemic changes have also been noted in ALS patients, with elevated levels of many proinflammatory cytokines detected in the blood<sup>580</sup>.

Given the role of inflammation in ALS, we postulated that infection induced inflammation may exacerbate disease progression. Anti-viral gene expression was similar in WT and SOD1<sup>G93A</sup> cells, which was consistent with our earlier results demonstrating equivalent viral replication in these same cells. SOD1<sup>G93A</sup> MEFs exhibited a slight elevation in cytokine production at baseline compared to WT MEFs. Interestingly, both WT and SOD1<sup>G93A</sup> MEFs responded to IAV with a similar profile and magnitude of cytokine/chemokine secretion. WT and SOD1<sup>G93A</sup> mice demonstrated elevated levels of cytokines/chemokines in both the lung and brain following infection relative to uninfected animals, confirming that peripheral infection induced inflammation in the CNS. However, the cytokine/chemokine profile was similar between both WT and SOD1<sup>G93A</sup> expressing mice. The similarity in cytokine profile observed in WT and SOD1<sup>G93A</sup> animals may be due to the fact that cytokines were measured in the lungs and the brain. However, the lumbar spinal cord is where disease primarily manifests in the SOD1<sup>G93A</sup> model. Indeed, the majority of studies on the SOD1<sup>G93A</sup> model demonstrate inflammation peaking after 100 days of age, with early signs of inflammation reported as early as 75 days of age<sup>578</sup>. Inflammation has been reported in the brains of SOD1<sup>G93A</sup> mice at later times of disease progression, although the most severe inflammation is observed in the spinal cord<sup>581</sup>. Taken together, these data suggest that prior infection does not induce major global changes in the inflammatory profile of SOD1<sup>G93A</sup> mice.

#### ***4.3.5 Peripheral Infection and Inflammation Induce Gliosis in the CNS***

Chronic insults induce the activation of glial cells. However, transient insults can have similar effects, depending upon the intensity of the insult<sup>412</sup>. Peripheral insults have been demonstrated to activate both microglia and astrocytes within the CNS. Notably, activated microglia have been reported in the brain of a PD mouse model following a highly pathogenic IAV infection<sup>540</sup>. Interestingly, IAV infection has been demonstrated to activate microglia within the brain of PD mice by multiple groups<sup>540,582–585</sup>. Investigators assessed the effects of both neurotropic (H5N1) and non-neurotropic (H1N1) strains of IAV on microglia within the substantia nigra and hippocampus, regions involved in PD and AD, respectively<sup>538</sup>. Neurotropic IAV was able to directly infect dopaminergic neurons within the substantia nigra causing a drastic elevation in microgliosis and the loss of the dopaminergic neurons. Comparatively, non-neurotropic H1N1 was not detected within the CNS yet infection elevated levels of microgliosis in both the substantia nigra and hippocampus<sup>540</sup>. Infection stimulated inflammatory encephalitis without the influx of peripheral lymphocytes into the CNS, which is unusual<sup>540</sup>. The BBB also remained intact following IAV infection. As such, the authors hypothesized gliosis may be triggered by increased levels of circulating cytokines<sup>585</sup>. Thus, peripheral viral infection can stimulate gliosis in the CNS, possibly as a consequence of increased circulating levels of inflammatory cytokines.

Activated microglia have also been observed in the brain of mice subjected to an *i.p.* administration of LPS as well as during live bacterial infection<sup>586</sup>. LPS stimulated microglia best recapitulate a “prototypical” activated phenotype (M1 microglia), as they

display a dramatic increase in expression of pro-inflammatory mediators<sup>586</sup>. Microglia isolated from SOD1<sup>G93A</sup> mice and stimulated with LPS differed from LPS induced WT microglia in their morphology and elevated secretion of monocyte chemoattractant protein-1 (MCP-1), demonstrating a distinct inflammatory phenotype following stimulation<sup>587</sup>. Further, microglia isolated from SOD1<sup>G93A</sup> mice demonstrated protein expression associated with other neurodegenerative disorders such as AD and PD<sup>186,193</sup>.

Pro-inflammatory (M1) microglia are characterized by the elevated expression of MHC-II, IL-1 $\beta$ , TNF- $\alpha$ , and iNOS. This phenotype can be induced by TLR4 signalling following LPS exposure, or by IFN- $\gamma$ <sup>189,192</sup>. In contrast, regenerative microglia (M2), which are activated following signalling by IL-4 and IL-13 and are characterized by ARG1, TGF- $\beta$ , and IL-10 expression<sup>187-190</sup>. Near the end-stage of disease, SOD1<sup>G93A</sup> mice exhibit extensive infiltration of T cells into the spinal cord<sup>186</sup>, resulting in an ALS-specific microglial phenotype. This phenotype was characterized by interactions between microglia and CD4 T cells that are presumed to be neuroprotective, in addition to microglial activation by soluble inflammatory mediators. As a result, microglia isolated from SOD1<sup>G93A</sup> expressed both neurotoxic and neuroprotective factors simultaneously<sup>186</sup>. Given the phenotypic heterogeneity of microglia in ALS, clinical trials using non-specific anti-inflammatory drugs might be destined for failure<sup>588</sup>. The fact that these microglial phenotypes are shared across many neurodegenerative disorders might further explain the previous failures of anti-inflammation treatments in neurodegenerative disorders<sup>589</sup>. Inflammation has a paradoxical role in neurodegenerative disorders, wherein it can play either a beneficial and detrimental role, depending upon timing and context.

Given the strong evidence that microglia can be activated by peripheral inflammation, we assessed previously-infected SOD1<sup>G93A</sup> mice for microglial activation within the spinal cord at 120 days of age, using Iba-1 as a marker<sup>565</sup>. As expected, elevated levels of microgliosis were evident within the spinal cords of uninfected SOD1<sup>G93A</sup> mice compared to WT mice. Interestingly, we observed an exacerbation in the level of microgliosis within the spinal cord of IAV infected SOD1<sup>G93A</sup> mice. Astrogliosis has also been reported in both SOD1<sup>G93A</sup> mice and ALS patients<sup>331,346,472,473,477–479</sup>. Accordingly, we demonstrated a slight elevation in astrogliosis within the spinal cords of previously IAV infected SOD1<sup>G93A</sup> mice, though the phenotype was milder than that observed for microglia. Comparatively, in WT mice, astrogliosis remained elevated up to 60 days post-IAV infection, while microgliosis was similar to baseline levels. Microgliosis in ALS is considered to promote disease progression<sup>189</sup>. Therefore, the elevated microgliosis observed in previously infected SOD1<sup>G93A</sup> mice may be driving the observed acceleration in disease progression.

#### ***4.3.6 Protein Misfolding and Microglial Priming***

The sensing of misfolded proteins by microglia is a common trigger of microgliosis in neurodegenerative disorders, including ALS<sup>590</sup>. Therefore, we explored how IAV infection influenced mSOD1 accumulation in the CNS. SOD1<sup>G93A</sup> mice accumulate aggregates of mSOD1 in the CNS<sup>563</sup>. This may be a protective mechanism, whereby toxic oligomers are sequestered into less toxic aggregates<sup>591</sup>. Onset of SOD1 misfolding can be detected at low levels around day 60 in SOD1<sup>G93A</sup> mice and accumulates in the CNS until

approximately day 120<sup>591</sup>. While SOD1<sup>G93A</sup> mice clearly had elevated levels of mSOD1 when compared to WT mice, we found no elevation in the levels of mSOD1 in the spinal cord of previously infected mice at day 120. It is possible that mSOD1 levels had peaked at day 120. Therefore, exploration of mSOD1 at early times after infection will give an indication of whether the timing and magnitude of mSOD1 accumulation is altered following infection.

Priming of microglia has been observed in neurodegenerative disorders such as AD and PD, as well as during normal aging<sup>592</sup>. Priming of microglia is a form of trained innate immunity, wherein innate immune cells exhibit “memory” of a previous insult<sup>590</sup>. Trained innate immunity is not due to a genetic alteration, but rather is a result of transcriptomic and epigenetic alterations, and therefore is not inherited following cell divisions<sup>550,551</sup>. Microglial priming is characterized by an over-activation of microglia cells following a secondary activating stimulus<sup>590</sup>. Common inducers of microglial priming in neurodegenerative disorders are the presence and accumulation of misfolded proteins<sup>590,593–595</sup> and neuroinflammation<sup>596–600</sup>. Therefore, inflammation induced by a peripheral infection may act as a secondary exposure to primed microglia within SOD1<sup>G93A</sup> mice, inducing an exacerbated inflammatory response within the CNS. Conversely, inflammation induced by a peripheral infection may act as a primary priming event, leading microglia to become hyper-inflammatory in response to the mSOD1 during disease progression in the SOD1<sup>G93A</sup> mice<sup>591</sup>.

#### **4.3.7 Limitations**

In the studies described herein we have demonstrated that IAV infection accelerates ALS disease progression in the SOD1<sup>G93A</sup> model of ALS. The SOD1<sup>G93A</sup> mouse model was designed to harbour a high copy number of the mutated human SOD1 gene which acts as a driver of ALS<sup>327</sup>. Some patients with ALS have mutations within SOD1, however, the copy number is unaltered. Overexpression of SOD1 may modify the molecular underpinnings of ALS and confound the observations made using the SOD1<sup>G93A</sup> model. Therefore, it will important to extend these findings into other models of ALS, such as SOD1 models with lower copy numbers or by using other ALS models (eg. TDP-43, C9ORF72, etc.). Extending our infection studies into other models of ALS will allow us to confirm whether our findings will be widely applicable to patients with diverse genetic bases of disease.

#### **4.3.8 Concluding Remarks**

Very few studies have examined the mechanism(s) through which viral infections influence ALS onset/progression. Herein, we have demonstrated that a single sublethal IAV infection in the SOD1<sup>G93A</sup> ALS model can significantly accelerate disease progression and decrease survival time. This phenotype was due to the exacerbation of inflammatory glial cell activation within the spinal cord, as a consequence of cross talk between peripheral inflammation and the CNS. In the case of our model, influenza virus infection accelerated ALS progression through a “hit-and-run” mechanism exacerbating pathophysiological pathways associated with disease. There may be a “critical window” of time during which infections are capable of triggering disease acceleration, as illustrated in Figure 4.3.1., also

infections during this critical window may help to explain the heterogeneity observed in patients with ALS. Further exploration of the involvement of innate immune cells and pathways within the CNS on disease progression may provide new therapeutic targets for ALS.

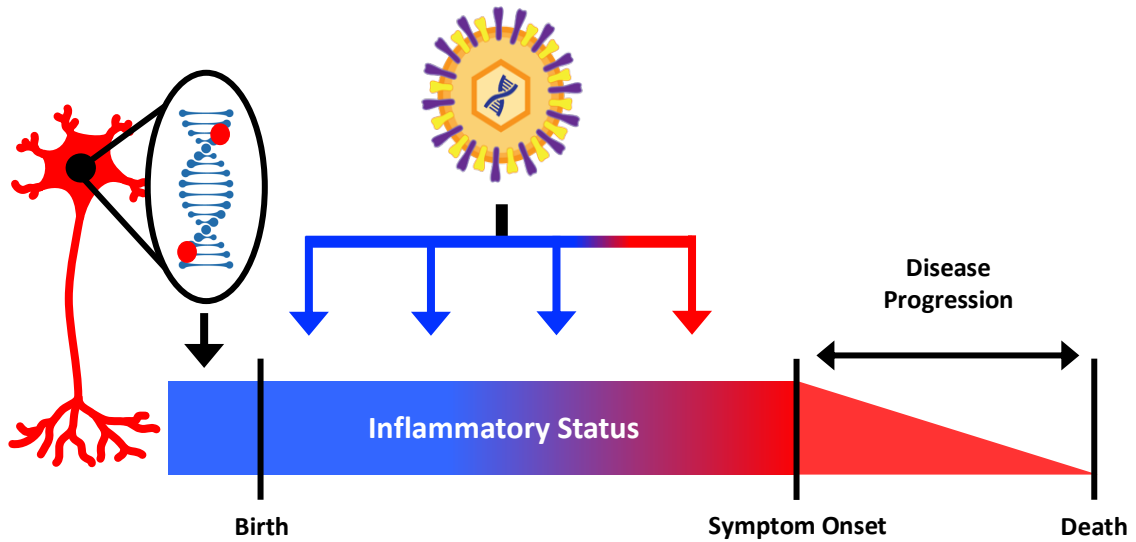


**Figure 4.3.1: A model for viral infection as an environmental trigger of ALS**

Timing of infection may be critical for infection induced ALS onset and progression. We have demonstrated that glial activation occurs, following peripheral infection, at a greater magnitude within the CNS of SOD1<sup>G93A</sup> mice. We propose that there is a critical window in which infection can mediate ALS progression, potentially via a microglial priming mechanism. In this model, genetic susceptibility for ALS predisposes microglia to a primed state. Infection is the secondary stimuli required to induce an inflammatory switch in the microglia. Enhanced peripheral inflammation, due to infection, hyper activates primed microglia within the spinal cord. Inflammatory microglia accelerate disease progression post-infection. Conversely, viral infection may be the primary trigger which primes microglia in the spinal cord. Pathophysiological mechanisms, such as the accumulation of misfolded proteins, is the secondary response causing hyper activation of primed microglia.

## 4.4 Appendix

### 4.4.1 HSV-1 infection is more severe in *SOD1<sup>G93A</sup>* mice

We wanted to determine whether the HSV-1, another common virus, albeit with a very different biology in comparison to IAV, would also accelerate ALS progression in the *SOD1<sup>G93A</sup>* mouse model. After HSV-1 infection ( $1 \times 10^5$  pfu/mouse) we observed no weight change differences between the *SOD1<sup>G93A</sup>* and WT mice (Fig. 4.10A). However, the *SOD1<sup>G93A</sup>* mice were more sensitive to HSV-1 infection in comparison to WT mice (Fig. 4.10B). Interestingly, the increased mortality to HSV-1 was not due to an increase in viral loads. During infection mice were vaginally lavaged and HSV-1 titres were assessed for up to 7 dpi. No differences were noted between WT and *SOD1<sup>G93A</sup>* mice (Fig. 4.10C). HSV-1 replication rates were also assessed *in vitro* using WT and *SOD1<sup>G93A</sup>* MEFs. The replication kinetics of HSV-1 were unaltered in the *SOD1<sup>G93A</sup>* expressing conditions when compared to the WT MEFs (Fig. 4.10D). Therefore, the increased mortality of *SOD1<sup>G93A</sup>* mice upon HSV-1 infection was not due to elevated viral loads/an increase in viral replication. We next wanted to explore whether HSV-1 infection accelerated ALS onset/progression as we observed after IAV infection of *SOD1<sup>G93A</sup>* mice.

To explore whether HSV-1 infection accelerated ALS disease progression we monitored the mice using the rotarod assay, in an identical fashion to IAV infected mice. HSV-1 infections were performed intravaginally using female mice. Interestingly, we observed a similar phenomenon to that of IAV-infected mice, wherein HSV-1 infected *SOD1<sup>G93A</sup>* animals reached 50% of their initial fall time approximately 2 weeks earlier than uninfected mice (Fig. 4.11A and 4.11B). Surprisingly, when looking at survival due

to ALS clinical signs we did not observe a difference between infected and uninfected SOD1<sup>G93A</sup> mice, which may be an artifact of the low number of animals tested so far (Fig 4.11C). To make firm conclusions regarding the role of HSV-1 infection on ALS progression we need to increase the number of experimental animals.

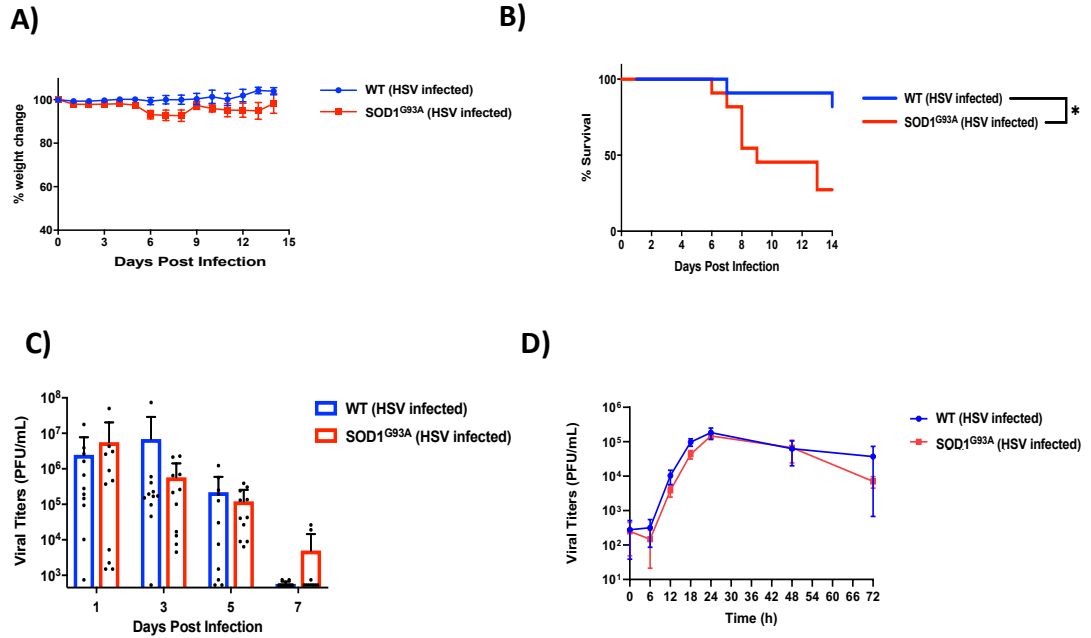


**Figure 4.10: SOD1<sup>G93A</sup> expressing mice exhibit enhanced morbidity to a HSV-1 infection**

WT and SOD1<sup>G93A</sup> mice were infected with 10<sup>5</sup> pfu of HSV-1 strain 17 syn at day 60 of age. (A) Weight loss was measured following infection for 14 days. WT (HSV infected) n = 11. SOD1<sup>G93A</sup> (HSV infected) n = 11. (B) The endpoint survival of the mice was assessed for 14 days following infection. Endpoint was defined as severe genital pathology or rectal paralysis. Statistics were determined using the Mantel-Cox test with p < 0.05, \*. (C) Viral titers were assessed from vaginal lavage samples 1, 3, 5, and 7 dpi in both WT and SOD1<sup>G93A</sup> mice. (D) WT and SOD1<sup>G93A</sup> MEFs were infected at MOI 2 with HSV-1 strain 17 syn and viral titres were assessed, via plaque assay, at 6, 12, 18, 24, 48, and 72h post-infection. N = 3

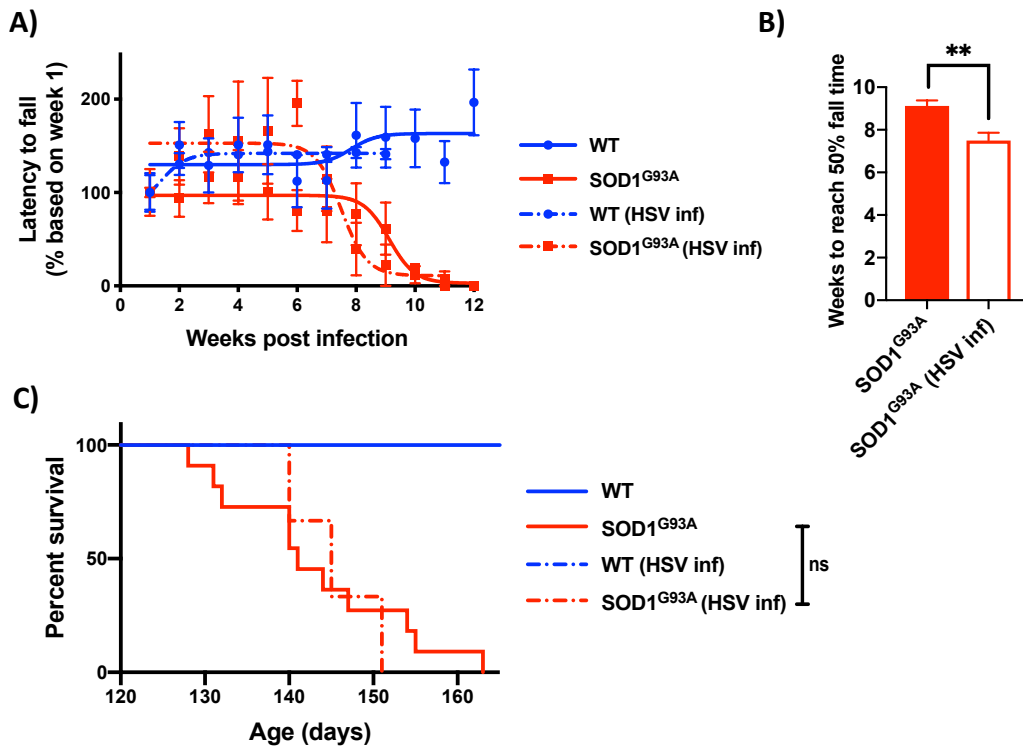


**Figure 4.11: HSV-1 infection accelerates ALS disease progression in the SOD1<sup>G93A</sup> ALS model**

WT and SOD1<sup>G93A</sup> mice were infected with 10<sup>5</sup> pfu of HSV-1 strain 17 syn at 60 days of age. (A) Following recovery of HSV infection mice were assessed for ALS clinical signs weekly using the rotarod. Latency to fall was averaged for each condition, and normalized to week 1 as 100%, and the data was analyzed using a sigmoidal curve fit. WT (uninfected) n = 13. WT (HSV infected) n = 5. SOD1<sup>G93A</sup> (uninfected) n = 11. SOD1<sup>G93A</sup> (HSV infected) n = 3. (B) Using the sigmoidal fit for each condition we extracted the point at which the fit reaches 50% of the maximum fall time and graphed ± standard error of the fit. Statistics were determined via student's T-test with p < 0.01, \*\*. (C) The endpoint survival of each condition was assessed due to the mice succumbing from their ALS-like clinical signs. Endpoint was defined as the mice being unable to right for 30s on each side.

# Chapter 5

## General Discussion

### ***5.1 IgA Deficiency and Neurodegeneration***

SETX-deficient mice demonstrated a kinetic defect in CSR to the IgA isotype. SIgAD is a common immunological disorder which often goes unnoticed<sup>287</sup>. SETX<sup>-/-</sup> mice do not display a true SIgAD, given that total IgA levels are unaffected. However, we demonstrated a kinetic defect in the accumulation of antigen-specific IgA. IgA is the most prevalent antibody at mucosal sites, such as the lungs and gut<sup>601</sup>. As previously discussed, SETX<sup>-/-</sup> mice share similarities with the ATM<sup>-/-</sup> mouse models for A-T, likely due to the decreased level of p-ATM present in SETX<sup>-/-</sup> cells following DNA damage. SIgAD is a common phenotype associated with A-T patients<sup>7</sup>. Patients with A-T experience elevated rates of recurrent respiratory infections<sup>7</sup>, and an ATM<sup>-/-</sup> mouse model exhibited elevated inflammation following acid-induced lung injury<sup>602</sup>. SIgAD often goes unnoticed however, patients with SIgAD have elevated rates of certain infections, particularly respiratory infections, as well as elevated rates of inflammatory bowel disease<sup>291,603</sup>. Therefore, patients with SETX-deficiencies, such as those with AOA2, may exhibit an elevated rate of infection at mucosal sites, resulting in elevated inflammation. Susceptibility to mucosal infections may occur to a lesser extent in AOA2 than patients with A-T, given the milder IgA phenotype seen in SETX<sup>-/-</sup> mice.

IgA also coats the surface of commensal bacteria in the gut preventing inflammation<sup>604</sup> and maintaining a healthy microbiome<sup>605</sup>. The link between the microbiota and neurodegenerative disorders has become an increasing focus for the field. The crosstalk between the brain and the gut microbiome has been explored in the context of ALS and other neurodegenerative disorders. The microbiota has been demonstrated to affect the

permeability of the BBB as well as neuronal survival and neurogenesis<sup>547</sup>. The majority of studies exploring the microbiota have focused on PD<sup>548</sup> while the role of the microbiota on ALS is less clear. Recently Blacher *et al.* demonstrated that different bacteria present in the microbiome can act to ameliorate or enhance ALS development. Protective effects were mediated by the release of nicotinamide into the CSF from the bacteria in the gut<sup>549</sup>. Interestingly, A-T mouse models exhibit variability in the onset of disease likely through the alterations in the microbiota and elevated levels of oxidative stress<sup>606</sup>. Microbiota disruption is associated with increased inflammation<sup>607</sup>, a common hallmark of neurodegenerative disorders.

Therefore, abnormalities in the IgA compartment of SETX-deficient patients may contribute to neurodegenerative disease via inflammatory mechanisms at mucosal sites. The interaction between the gut and the BBB is a relatively new field of research, with a “leaky” gut being extensively linked with neurodegenerative disorders<sup>608</sup>. Increased oxidative stress induced by disruption of the microbiota may be a cause of elevated levels of inflammation<sup>606,608</sup>. Indeed, SETX has been implicated in the defense against oxidative DNA damage and DSB repair<sup>212</sup>. Thus, IgA deficiency in the SETX<sup>-/-</sup> model of AOA2 may enhance sensitivity to mucosal pathogens, promoting the onset of neurodegeneration.

### ***5.2 Implications of SETX Deficiency on the DDR in Neurodegeneration***

The effect of SETX-deficiency on the DDR and NHEJ may also relate to patients with AOA2. The etiology of SETX related disorders is not well understood. Deficiencies in DNA DSB repair could be central to the etiology of AOA2. Whether DNA damage is

the cause or effect of neurodegenerative conditions is not completely understood. Neurons are post-mitotic and rely upon NHEJ as the main pathway for DNA repair following DNA damage<sup>92</sup>. SETX-deficient B cells demonstrated a deficiency in NHEJ and a promotion of a-EJ during CSR. Therefore, defects in NHEJ in neurons are also likely to occur in SETX deficient cells. Accumulation of DSBs has been observed in patients with neurodegenerative disorders and may be a common theme. Furthermore, DDR has been implicated in neurodegenerative disorders including AD, PD, and ALS<sup>609</sup>.

The accumulation of DSBs has been demonstrated to occur during the early stages of AD development in mouse models of disease<sup>610,611</sup>. Elevated levels of DSB in hippocampal neurons was associated with increased neuronal apoptosis<sup>610,611</sup>. Additionally, factors associated with DNA repair, such as BRCA1 and ATM expression levels and functional activities are reduced in AD patient brains, potentially explaining the elevation in DSBs observed in AD patients<sup>612-614</sup>. SETX interacts with both BRCA1 and ATM<sup>213</sup>, and we demonstrated that p-ATM levels were reduced in SETX-deficient conditions. This suggests parallels between pathways implicated in AD and AOA2. NHEJ rates are also decreased in AD neurons as a result of decreased expression of both Ku and DNA-PKcs<sup>615,616</sup>. Additionally, expression of DNA-PKcs has been previously demonstrated to be decreased in SETX-deficient conditions<sup>215</sup>. The DNA-PK complex acts as an inhibitor of other DNA repair pathways to promote NHEJ<sup>111</sup>. A deficiency in DNA-PKcs in B cells would be expected to cause a decrease in NHEJ with a concomitant increase in a-EJ<sup>113</sup>. This would be consistent with an indirect function of SETX on DNA repair during CSR. PD patients exhibit elevated levels of DSBs in dopaminergic neurons in the substantia nigra

rather than hippocampal neurons as observed in AD<sup>617</sup>. Like AD models, DSBs in PD dopaminergic neurons were observed to precede disease onset in mouse models<sup>617</sup>. Common hallmarks of DNA damage are likewise elevated in models of PD, including 53BP1,  $\gamma$ -H2AX, and p-ATM foci formation<sup>617</sup>.

The DDR has been implicated to play a role in ALS as well. Many of the genes implicated in ALS are important mediators of the DDR including C9orf72, FUS, and TDP-43. C9orf72 repeat expansions that occur in ALS result in an R-loop accumulation and ultimately elevated DNA damage in both mouse and human systems<sup>240,241</sup>. FUS has been found to accumulate at DNA damage sites, in a PARylation dependent manner and common markers of DNA damage have also been demonstrated to be elevated in mutated FUS conditions, including  $\gamma$ -H2AX foci accumulation<sup>618,619</sup>. TDP-43 is involved in the efficient recruitment of XRCC4-Ligase IV to sites of DNA damage thereby promoting efficient repair<sup>620,621</sup>. In ALS, TDP-43 becomes mislocalized to the cytoplasm thereby causing defects in the NHEJ repair pathway<sup>596</sup>. In neurons, TDP-43 depletion increased sensitization to DSBs resulting in increased cell death<sup>596</sup>. Together, the data presented here provide increasing evidence that the etiology of SETX- related disorders may be caused by defects in the DDR. Furthermore, defects in the DDR pathway may extend to other related neurodegenerative disorders.

### ***5.3 CNS Immunity and Glial Cell Activation***

Glial cells within the CNS maintain the healthy function of neurons and consist of microglia, astrocytes, and oligodendrocytes. Innate cell over-activation has been

demonstrated for many neurodegenerative disorders, such as AD and PD, in addition to disorders such as anxiety and depression<sup>412,622</sup>. ALS is considered to be a non-cell autonomous disease with microglia, astrocytes, and oligodendrocytes implicated in ALS progression<sup>151</sup>. Microglia and astrocytes have received the most attention in the context of ALS and seem to have the largest contribution to pathogenesis given their roles within the healthy CNS.

Microglia normally act as sensors of the CNS microenvironment, constantly surveying neurons for signs of damage and restructuring synaptic connections through phagocytic processes<sup>176</sup>. During chronic inflammatory stimuli, such as that which occurs in many neurodegenerative disorders, microglia become less ramified and adopt a M1 phenotype, becoming more phagocytic and releasing proinflammatory cytokines such as IL-1 $\beta$ , IL-6, and TNF $\alpha$ <sup>189,192</sup>. Astrocytes, on the other hand, play a major role in managing synaptic transmission by sequestering neurotransmitters from the synaptic cleft. Additionally, astrocytes act to absorb nutrients from blood vessels and transmit maintenance signals to other cells within the CNS<sup>169,171</sup>. During neurodegenerative disorders, astrocytes have been demonstrated to induce neurotoxicity through proinflammatory cytokine release, reduced trophic factor release, elevated ROS production, and reduced ability to uptake glutamate, causing excitotoxicity in neurons<sup>448</sup>.

Microgliosis and astrogliosis both correlate with neurodegenerative disease progression. Herein, we demonstrated that both microgliosis and astrogliosis were exacerbated in infected SOD1<sup>G93A</sup> mice. However, the elevation in microgliosis was more

profound. Therefore, the role of microgliosis during ALS might be key to disease progression in our model.

#### ***5.4 Microglial Priming in Neurodegenerative Disorders***

Neuroinflammation is a hallmark of many neurodegenerative disorders, as well as of physiological processes such as aging. The dysregulation of inflammatory responses that occurs during aging may play an important role in neurodegenerative disorders, and may partially explain why many of these disorders are strongly associated with aging<sup>623 624</sup>. Therefore, understanding microglial changes during aging may shed light on the potential roles for microglia in both AD and other neurodegenerative disorders. During aging, microglia have been observed to transition from a protective to a pro-inflammatory state. In fact, expression of CD11b, CD11c, TREM2 and CD68 is elevated during both aging and AD<sup>625,626</sup>.

A typical microglial response to chronic inflammation is the active killing of surrounding cells and a loss of all regenerative capacities. However, low levels of acute inflammation can stimulate normal microglial responses, which are protective in the CNS. After inflammatory signals have resolved, the microglia ultimately recover and return to rest. However, following recovery, microglia can exhibit inappropriate responses to secondary-stimuli, at which point microglia are said to be “primed”<sup>590</sup>. Currently the markers of primed microglia are not well understood. Primed microglia are typically characterized by hyper-activation following a secondary-stimuli<sup>590</sup>. Priming can be induced by LPS<sup>596–600</sup> and misfolded proteins<sup>590,593–595</sup>, which are sensed by microglia through

CD14, TLR2, TLR4, and scavenger receptors, and signal through the NF- $\kappa$ B pathway<sup>592,627</sup>. Other general markers of neurodegeneration have been shown to trigger microglial priming, namely CSF-1 and CCL2<sup>590</sup>. CSF-1 stimulates microglial proliferation through CSF-1R, which can also be activated by IL-34<sup>628</sup>. Similarly, CCL2, which signals through CCR2, promotes microglial proliferation and migration of microglia to sites of damage<sup>629</sup> including spinal cord MNs following sciatic nerve injury<sup>630</sup>. Therefore, microglial priming may promote inflammation in the CNS triggered by secondary stimuli.

Microglial priming has been most extensively studied in AD. However, neurodegenerative disorders share many common hallmarks and therefore, much of what has been learned in the AD model may also be applicable to ALS. The biochemical hallmarks of AD include extracellular A $\beta$  accumulations and intracellular Tau aggregates<sup>463,631</sup>. Aging is also a major risk factor for AD<sup>624</sup>, likely due to the accumulation of a proinflammatory, Th1 response during the normal aging process<sup>623</sup>. Additionally, brain injuries are associated with AD development, again due to the induction of a proinflammatory milieu<sup>632</sup>. In the context of neurodegenerative disorders, microglia have been demonstrated to become primed through multiple signals, including misfolded proteins. In AD, A $\beta$ , is recognized by microglia and engulfed<sup>633–637</sup>. However, studies of AD have also suggested that microglial priming results in A $\beta$  misfolding, as opposed to misfolding causing microglial priming<sup>493,638</sup>. Thus, the relationship between protein misfolding and microglia priming/activation is complex and incompletely understood.

Recent studies have suggested that microglial priming and protein misfolding acts in a cyclic manner, wherein priming causes elevated protein misfolding, which in turn

promotes further microglial priming and so on, in this manner perpetuating neurodegenerative disorders<sup>592</sup>. An additional protein associated with AD is tau, a microtubule associated protein<sup>639</sup>. Tau aggregates are a common characteristic of AD and other neurodegenerative disorders<sup>640</sup>. Similar to A $\beta$ , tau fibrils have been demonstrated to prime microglia<sup>641</sup>. Further, microgliosis has been proposed to be the earliest response in the CNS to tauopathies<sup>642</sup>.

Neuroinflammation induced by LPS causes cognitive impairment and sickness behaviours in C57BL/6J mice. Microglial activation was observed in the hypothalamus of LPS treated mice, concomitant with cognitive decline as measured by Morris water maze. Expression of IL-4 and IL-10 were reduced in the brain of LPS treated mice while TNF- $\alpha$ , IL-1 $\beta$ , PGE2, and NO expression levels were elevated<sup>643</sup>. The effect of LPS was dependent upon TLR4 signaling. Interestingly, inflamed brains also expressed A $\beta$ , supporting a role for neuroinflammation as a trigger of AD<sup>643</sup>.

IAV infection has been shown to trigger neuroinflammation. Peripheral IAV infection altered cognitive ability of mice and elevated proinflammatory cytokines including IL-1 $\beta$ , IL-6, TNF- $\alpha$ , and IFN- $\alpha$ . This was accompanied by a decrease in expression of BDNF, NGF (neurotrophic factors) and CD200 and CX3CL1 (immunomodulatory factors) within the hippocampus of infected mice. The magnitude of the changes in expression observed were relatively small, less than 2-fold, and but could still have a significant biological effect given the self-perpetuating nature of microglial priming<sup>540,584</sup>. Microglial activation has been observed following IAV infection with non-neurotropic strains. However, IAV can also induce encephalitis. Following H1N1 infection,

there was no evidence of virus in the CNS and the BBB remained intact. Nevertheless, microglial activation was detected in the substantia nigra and hippocampus. Prior to the onset of microgliosis there was a decrease in expression of neurotrophic factors such as BDNF and GDNF<sup>585</sup>. Comparatively, highly pathogenic IAV, H5N1, was able to infect the CNS and induced long term effects (up to 90 dpi) on cytokine expression and microglial activation, especially within the substantia nigra and hippocampus regions of the brain. In mouse models of PD, H5N1 mediated long terms changes, including phosphorylated  $\alpha$ -synuclein and microglial activation, but was not sufficient to induce PD alone<sup>582,583</sup>. While the aforementioned studies did not specifically interrogate microglial priming, the magnitude of activation in the microglial population observed in these studies would be consistent with primed microglia.

Clearly then, microglial priming is a common feature of many neurodegenerative diseases. Our observations are consistent with previous studies that have shown that peripheral IAV infection can trigger microglial activation. If these microglia have been primed (by mSOD1, for example), they may respond to peripheral inflammation by mounting a hyperinflammatory response, thereby accelerated the progression of ALS clinical signs. Therefore, strategies that specifically treat or prevent hyperactivation of microglia may be an attractive therapeutic strategy for ALS.

### ***5.5 The Mechanism of Motor Neuron Death Remains a Mystery in ALS***

The pathway of MN death in ALS is still poorly understood. Prior studies examined both necroptosis and apoptosis as potential forms of neuronal death. Apoptosis is a highly

controlled form of cell death which relies upon caspase activation<sup>644</sup>. Comparatively, necroptosis is a form of cell death exhibiting hallmarks of both necrosis and apoptosis<sup>645</sup>, but is independent of caspase activity and reliant upon RIPK3 and MLKL activity<sup>645–649</sup>. Neuronal death in ALS is Bax dependent<sup>650</sup> and caspase-independent<sup>651</sup>. Therefore, classical apoptosis does not seem to drive MN death during ALS, which led to the hypothesis that it may instead be driven by necroptosis<sup>651,652</sup>.

Necroptosis is particularly interesting in the context of ALS and other neurodegenerative disorders, as it is associated with inflammatory stimuli such as LPS and TNF- $\alpha$ <sup>647,653</sup>. Indeed, IAV infection can induce necroptosis in the lung<sup>654</sup>. However, recent research has demonstrated that necroptosis is dispensable for MN cell death in the SOD1<sup>G93A</sup> ALS model<sup>655</sup>. The terminal executioner of necroptosis (MLKL), was knocked out and these mice were crossed with SOD1<sup>G93A</sup> mice. Onset, progression, and survival was unchanged in MLKL<sup>-/-</sup> SOD1<sup>G93A</sup> mice relative to WT SOD1<sup>G93A</sup> mice. MN degeneration, microgliosis, and astrogliosis was also unchanged. RIPK1 accumulation was observed at end stages of disease, but neither RIPK3 or MLKL expression was detected<sup>655</sup>. RIPK3 and MLKL are required for necroptosis, and expression of both was undetected in the SOD1<sup>G93A</sup> mice. Additionally, RIPK3 deletion does not prevent MN death in the SOD1<sup>G93A</sup> model of ALS, further demonstrating that necroptosis appears to be insignificant in SOD1 models of ALS<sup>656</sup>. Therefore, the specific pathway responsible for MN death in ALS remains elusive.

### ***5.6 Peripheral Immune Cell Involvement in the Pathogenesis of ALS***

An additional hallmark of ALS is the influx of T cells into the CNS at later stages of disease. T cell influx can be beneficial or deleterious largely dependent upon whether the T cell entering the CNS is CD4<sup>+</sup> or CD8<sup>+</sup>, respectively. CD4<sup>+</sup> T cells help to ameliorate disease in the SOD1<sup>G93A</sup> model<sup>421</sup>. CD4<sup>+</sup> T cells provided supportive neuroprotection by regulating the trophic/cytotoxic balance of glial cells<sup>421</sup>. In SOD1<sup>G93A</sup>/RAG2<sup>-/-</sup> mice, deficient of B and T cells, disease onset occurred at the same time as in WT SOD1<sup>G93A</sup> mice. However, RAG2 deficient SOD1<sup>G93A</sup> mice demonstrated more rapid disease progression<sup>421</sup>. Therefore, the authors surmised that T cells are in fact beneficial to disease progression. The supposition that CD4<sup>+</sup> were responsible for mediating protection is supported by the observation that CD4<sup>-/-</sup> SOD1<sup>G93A</sup> mice experienced a similar increase in the rate of disease progression as that observed in RAG2<sup>-/-</sup> SOD1<sup>G93A</sup> mice<sup>421</sup>.

T<sub>reg</sub>, as characterized by CD4, CD25, and FoxP3 expression, are elevated in the periphery during the stable phase of disease in the SOD1<sup>G93A</sup> model. T<sub>reg</sub> levels decrease during disease progression<sup>657</sup>. The increase in peripheral CD4<sup>+</sup>CD25<sup>+</sup>FoxP3<sup>+</sup> T<sub>reg</sub> was observed at approximately 16 weeks of age in SOD1<sup>G93A</sup> mouse model, and levels decrease again by end stages<sup>657</sup>. IL-4 is co-expressed with FoxP3 in T<sub>reg</sub> and suppresses the toxic while enhancing the neuroprotective properties of microglia during ALS progression<sup>657</sup>. Further, T<sub>reg</sub> cell counts in ALS patients are correlated with the speed of disease progression. Increased CD4<sup>+</sup>CD25<sup>+</sup>, or total CD4<sup>+</sup> cells in the periphery correlated with a slower disease progression<sup>657</sup>. On the other hand, reduced T<sub>reg</sub> cell numbers, decreased FOXP3 and Gata3 expression, has been associated with rapid disease progression<sup>422</sup>.

These observations triggered studies exploring the potential utility of  $T_{reg}$  as a treatment for ALS.  $SOD1^{G93A}$  mice treated with IL-2 exhibited an expansion in  $T_{reg}$  and a subsequent increase in survival. The enhancement in survival is believed to be due to the suppression of astrocyte and microglial activation, which preserved the MN soma size, thus delaying disease progression<sup>424</sup>. However,  $T_{reg}$  isolated from ALS patients have been demonstrated to have decreased functionality and are less suppressive than those from healthy counterparts<sup>423</sup>. The suppressive ability was restorable following expansion *ex-vivo*. Therefore, while  $T_{reg}$  numbers are elevated in patients their functionality is likely suppressed when compared to healthy individuals<sup>423</sup>. To this end, a phase I study of the utility of expanded autologous  $T_{reg}$  in ALS patients has been conducted<sup>658</sup>. During the phase-I trial 3 patients were infused with autologous expanded  $T_{reg}$ , accompanied by IL-2 injections 3 times-weekly, to maintain the  $T_{reg}$  post-transplantation.  $T_{reg}$  infusions were deemed to be safe and well-tolerated in ALS patients.  $T_{reg}$  slowed disease progression at both early and late stages of disease following administration. A previous unpublished pilot study demonstrated no effect of IL-2 administration alone, therefore, the therapeutic effects were attributed to  $T_{reg}$  activity<sup>658</sup>.

Comparatively, while CD4+ T cells offer benefits to ALS patients CD8+ T cells are detrimental to ALS progression following invasion of the CNS<sup>421</sup>. Cytotoxic CD8+ T cells, expressing  $SOD1^{G93A}$ , trigger death of spinal MNs *in-vitro*<sup>425</sup>. Following CD8 depletion in the  $SOD1^{G93A}$  model there was a significant increase in the number of spinal MNs. However, no change in motor function or life expectancy was observed, suggesting that CD8 T cells play an active role in removal of non-functional MNs<sup>425</sup>. Therefore, CD8 T

cells likely only eliminate MNs that are already displaying ALS phenotypes yet CD8 T cells do not drive ALS disease progression by the targeting of healthy MNs.

Taken together, CD4+ T cells seem to play a protective role in ALS. Suppression of gliosis via T<sub>reg</sub> at the later disease stages appears to be a mechanism to combat abnormal inflammatory responses. The suppressive abilities of T cells wane over time, likely due to T cell exhaustion. It remains to be determined whether T cell invasion of the CNS is observed in our infection model of SOD1<sup>G93A</sup> mice. IAV infection induces robust CD4+ and CD8+ T cell responses<sup>659-661</sup>. Therefore, IAV infection may have an important impact on T cells in the SOD1<sup>G93A</sup> model. Whether IAV induced T cell responses are deleterious or beneficial to ALS disease progression remains to be determined.

### ***5.9 Concluding Remarks***

The immune system is broadly divided into innate and adaptive branches. Both branches of the immune system likely play an important role in neurodegenerative disorders. Innate cell activation within the CNS is a key hallmark of neuroinflammation and neurodegenerative disorders while adaptive cells can infiltrate the CNS and act to ameliorate inflammation. Additionally, both innate and adaptive immune responses occur in the periphery following infection and may transmit disease driving signals to the CNS. Herein, we have described immunological perturbations associated with two neurological disorders, AOA2 and ALS.

Patients with ARCA's often demonstrate immunodeficiency in addition to the neurological symptoms associated with disease. We have demonstrated that SETX, the causative gene of AOA2, results in an IgA specific deficiency. Interestingly deficiency in IgA production was most pronounced for antigen-specific IgA during a primary immune response. Total IgA titers were unaltered in SETX<sup>-/-</sup> mice. To the best of our knowledge this is a unique phenotype associated with SETX deficiency. In SETX deficient B cells, upstream targeting of AID to the IgH locus during CSR appeared to be unaltered, suggesting that SETX deficiency plays a role later, in the DDR and the repair of DNA during CSR. SETX deficiency reduced utilization of NHEJ and promoted a-EJ, potentially through decreased ATM activation. Additionally, the kinetic delay in IgA production, as well as decreased IgA diversity, may alter the response to infection and inflammation at mucosal sites resulting in increased basal inflammation levels in AOA2 patients, a common driver of neurodegenerative disorders. Further, the role of SETX in the DDR may have implications in neuronal cells. How MNs die during neurodegenerative disorders remains poorly understood. SETX deficiency may result in an impairment in the repair of DSBs leading to an accumulation of DNA damage and ultimately, disease onset. Our findings regarding role of SETX during repair of DNA damage may provide new therapeutic insights for patients with AOA2.

ALS is the most common MN disease, yet its etiology remains very poorly understood. ALS is a highly heterogeneous disease and is believed to be caused by a confluence of genetic and environmental factors. Herein, we demonstrated that IAV infection accelerates ALS disease progression in the SOD1<sup>G93A</sup> mouse model of ALS. IAV

infection induced microgliosis and astrogliosis within the lumbar spinal cord. In the future, it will be important to determine whether elevated microgliosis is the driver of the accelerated disease progression that we observed. Microglial priming would provide a compelling explanation for the exacerbation in microgliosis observed in ALS following viral infection. Microglia in ALS may be primed to respond with a hyperinflammatory phenotype upon secondary insult (such as infection). Whether microgliosis following infection is a general ALS response or a SOD1 model specific phenomenon remains to be determined. However, the ubiquity of gliosis observed in neurodegenerative disorders suggests that gliosis may be a key driver of disease in neuronal tissue. Thus, targeting of microglial priming, via pharmaceutical methods, may prove to be an important therapeutic target to prevent ALS disease progression in patients.

## Bibliography

1. Palau, F. & Espinós, C. Autosomal recessive cerebellar ataxias. *Orphanet Journal of Rare Diseases* **1**, 47 (2006).
2. Rothblum-Oviatt, C. *et al.* Ataxia telangiectasia: A review. *Orphanet J. Rare Dis.* **11**, 159–180 (2016).
3. Gatti, R. A. *et al.* Localization of an ataxia-telangiectasia gene to chromosome 11q22-23. *Nature* **336**, 577–580 (1988).
4. Becker-Catania, S. G. *et al.* Ataxia-telangiectasia: Phenotype/genotype studies of ATM protein expression, mutations, and radiosensitivity. *Mol. Genet. Metab.* **70**, 122–133 (2000).
5. Date, H. *et al.* Early-onset ataxia with ocular motor apraxia and hypoalbuminemia is caused by mutations in a new HIT superfamily gene. *Nat. Genet.* **29**, 184–188 (2001).
6. Moreira, M. & Koenig, M. Ataxia with Oculomotor Apraxia Type 2. *GeneReviews*® [Internet] (2004). Available at: [https://www.ncbi.nlm.nih.gov/books/NBK1154/pdf/Bookshelf\\_NBK1154.pdf](https://www.ncbi.nlm.nih.gov/books/NBK1154/pdf/Bookshelf_NBK1154.pdf).
7. Nowak-Wegrzyn, A., Crawford, T. O., Winkelstein, J. A., Carson, K. A. & Lederman, H. M. Immunodeficiency and infections in ataxia-telangiectasia. *J. Pediatr.* **144**, 505–511 (2004).
8. Mariani, L. L. *et al.* Comparing ataxias with oculomotor apraxia: A multimodal study of AOA1, AOA2 and at focusing on video-oculography and alpha-fetoprotein. *Sci. Rep.* **7**, 15284–15292 (2017).

9. Anheim, M. *et al.* Ataxia with oculomotor apraxia type 2: Clinical, biological and genotype/phenotype correlation study of a cohort of 90 patients. *Brain* **132**, 2688–2698 (2009).
10. Chen, Y. Z. *et al.* DNA/RNA helicase gene mutations in a form of juvenile amyotrophic lateral sclerosis (ALS4). *Am. J. Hum. Genet.* **74**, 1128–1135 (2004).
11. Bennett, C. L. *et al.* Senataxin mutations elicit motor neuron degeneration phenotypes and yield TDP-43 mislocalization in ALS4 mice and human patients. *Acta Neuropathol.* **136**, 425–443 (2018).
12. Berek, C., Berger, A. & Apel, M. Maturation of the immune response in germinal centers. *Cell* **67**, 1121–1129 (1991).
13. De Silva, N. S. & Klein, U. Dynamics of B cells in germinal centres. *Nat. Rev. Immunol.* **15**, 137–148 (2015).
14. Blink, E. J. *et al.* Early appearance of germinal center-derived memory B cells and plasma cells in blood after primary immunization. *J. Exp. Med.* **201**, 545–554 (2005).
15. Weisel, F. J., Zuccarino-Catania, G. V., Chikina, M. & Shlomchik, M. J. A Temporal Switch in the Germinal Center Determines Differential Output of Memory B and Plasma Cells. *Immunity* **44**, 116–130 (2016).
16. Kerfoot, S. M. *et al.* Germinal Center B Cell and T Follicular Helper Cell Development Initiates in the Interfollicular Zone. *Immunity* **34**, 947–960 (2011).
17. Baumjohann, D., Okada, T. & Ansel, K. M. Cutting Edge: Distinct Waves of BCL6 Expression during T Follicular Helper Cell Development. *J. Immunol.* **187**, 2089–

- 2092 (2011).
18. Kitano, M. *et al.* Bcl6 Protein Expression Shapes Pre-Germinal Center B Cell Dynamics and Follicular Helper T Cell Heterogeneity. *Immunity* **34**, 961–972 (2011).
  19. Bannard, O. *et al.* Germinal center centroblasts transition to a centrocyte phenotype according to a timed program and depend on the dark zone for effective selection. *Immunity* **39**, 912–924 (2013).
  20. Victora, G. D. *et al.* Germinal center dynamics revealed by multiphoton microscopy with a photoactivatable fluorescent reporter. *Cell* **143**, 592–605 (2010).
  21. Victora, G. D. *et al.* Identification of human germinal center light and dark zone cells and their relationship to human B-cell lymphomas. *Blood* **120**, 2240–2248 (2012).
  22. Dominguez-Sola, D. *et al.* The proto-oncogene MYC is required for selection in the germinal center and cyclic reentry. *Nat. Immunol.* **13**, 1083–1091 (2012).
  23. Allen, C. D. C. *et al.* Germinal center dark and light zone organization is mediated by CXCR4 and CXCR5. *Nat. Immunol.* **5**, 943–952 (2004).
  24. Attridge, K. *et al.* IL-21 Promotes CD4 T Cell Responses by Phosphatidylinositol 3-Kinase–Dependent Upregulation of CD86 on B Cells. *J. Immunol.* **192**, 2195–2201 (2014).
  25. Tze, L. E. *et al.* CD83 increases MHC II and CD86 on dendritic cells by opposing IL-10 - Driven MARCH1-mediated ubiquitination and degradation. *J. Exp. Med.* **208**, 149–165 (2011).
  26. Krzyzak, L. *et al.* CD83 Modulates B Cell Activation and Germinal Center

- Responses. *J. Immunol.* **196**, 3581–3594 (2016).
27. Guttridge, D. C., Albanese, C., Reuther, J. Y., Pestell, R. G. & Baldwin, A. S. NF- $\kappa$ B Controls Cell Growth and Differentiation through Transcriptional Regulation of Cyclin D1. *Mol. Cell. Biol.* **19**, 5785–5799 (1999).
  28. Feng, B., Cheng, S., Pear, W. S. & Liou, H. C. NF- $\kappa$ B inhibitor blocks B cell development at two checkpoints. *Med. Immunol.* **3**, 1 (2004).
  29. Almaden, J. V. *et al.* B-cell survival and development controlled by the coordination of NF- $\kappa$ B family members RelB and cRel. *Blood* **127**, 1276–1286 (2016).
  30. Saito, M. *et al.* A Signaling Pathway Mediating Downregulation of BCL6 in Germinal Center B Cells Is Blocked by BCL6 Gene Alterations in B Cell Lymphoma. *Cancer Cell* **12**, 280–292 (2007).
  31. Scharer, C. D., Barwick, B. G., Guo, M., Bally, A. P. R. & Boss, J. M. Plasma cell differentiation is controlled by multiple cell division-coupled epigenetic programs. *Nat. Commun.* **9**, 1698 (2018).
  32. Shinnakasu, R. *et al.* Regulated selection of germinal-center cells into the memory B cell compartment. *Nat. Immunol.* **17**, 861–869 (2016).
  33. Roychoudhuri, R. *et al.* BACH2 regulates CD8<sup>+</sup> T cell differentiation by controlling access of AP-1 factors to enhancers. *Nat. Immunol.* **17**, 851–860 (2016).
  34. Phan, T. G. *et al.* High affinity germinal center B cells are actively selected into the plasma cell compartment. *J. Exp. Med.* **203**, 2419–2424 (2006).
  35. Stavnezer, J., Guikema, J. E. J. & Schrader, C. E. Mechanism and Regulation of Class Switch Recombination. *Annu. Rev. Immunol.* **26**, 261–292 (2008).

36. Xu, Z., Zan, H., Pone, E. J., Mai, T. & Casali, P. Immunoglobulin class-switch DNA recombination: Induction, targeting and beyond. *Nature Reviews Immunology* **12**, 517–531 (2012).
37. Daniels, G. A. & Lieber, M. R. RNA: DNA complex formation upon transcription of immunoglobulin switch regions: Implications for the mechanism and regulation of class switch recombination. *Nucleic Acids Res.* **23**, 5006–5011 (1995).
38. Mizuta, R. *et al.* Molecular visualization of immunoglobulin switch region RNA/DNA complex by atomic force microscope. *J. Biol. Chem.* **278**, 4431–4434 (2003).
39. Shinkura, R. *et al.* The influence of transcriptional orientation on endogenous switch region function. *Nat. Immunol.* **4**, 435–441 (2003).
40. Kao, Y. P. *et al.* Detection and characterization of R-loops at the murine immunoglobulin *S<sub>α</sub>* region. *Mol. Immunol.* **54**, 208–216 (2013).
41. Dickerson, S. K., Market, E., Besmer, E. & Papavasiliou, F. N. AID mediates hypermutation by deaminating single stranded DNA. *J. Exp. Med.* **197**, 1291–1296 (2003).
42. Yu, K., Chedin, F., Hsieh, C. L., Wilson, T. E. & Lieber, M. R. R-loops at immunoglobulin class switch regions in the chromosomes of stimulated B cells. *Nat. Immunol.* **4**, 442–451 (2003).
43. Chaudhuri, J. *et al.* Transcription-targeted DNA deamination by the AID antibody diversification enzyme. *Nature* **422**, 726–730 (2003).
44. Schrader, C. E., Linehan, E. K., Mochevova, S. N., Woodland, R. T. & Stavnezer, J.

- Inducible DNA breaks in Ig S regions are dependent on AID and UNG. *J. Exp. Med.* **202**, 561–568 (2005).
45. Fear, D. J., McCloskey, N., O'Connor, B., Felsenfeld, G. & Gould, H. J. Transcription of Ig Germline Genes in Single Human B Cells and the Role of Cytokines in Isotype Determination. *J. Immunol.* **173**, 4529–4538 (2004).
46. Rush, J. S. & Hodgkin, P. D. B cells activated via CD40 and IL-4 undergo a division burst but require continued stimulation to maintain division, survival and differentiation. *Eur. J. Immunol.* **31**, 1150–1159 (2001).
47. Ehrhardt, R. O., Strober, W. & Harriman, G. R. Effect of transforming growth factor (TGF)-beta 1 on IgA isotype expression. TGF-beta 1 induces a small increase in sIgA+ B cells regardless of the method of B cell activation. *J. Immunol.* **148**, 3830–3836 (1992).
48. Roy, D., Yu, K. & Lieber, M. R. Mechanism of R-Loop Formation at Immunoglobulin Class Switch Sequences. *Mol. Cell. Biol.* **28**, 50–60 (2008).
49. Muramatsu, M. *et al.* Specific expression of activation-induced cytidine deaminase (AID), a novel member of the RNA-editing deaminase family in germinal center B cells. *J. Biol. Chem.* **274**, 18470–18476 (1999).
50. Petersen-Mahrt, S. K., Harris, R. S. & Neuberger, M. S. AID mutates E. coli suggesting a DNA deamination mechanism for antibody diversification. *Nature* **418**, 99–103 (2002).
51. Muramatsu, M. *et al.* Class switch recombination and hypermutation require activation-induced cytidine deaminase (AID), a potential RNA editing enzyme. *Cell*

- 102**, 553–563 (2000).
52. Barzilay, G. & Hickson, I. D. Structure and function of apurinic/aprimidinic endonucleases. *BioEssays* **17**, 713–719 (1995).
  53. Stavnezer, J. *et al.* Differential expression of APE1 and APE2 in germinal centers promotes error-prone repair and A:T mutations during somatic hypermutation. *Proc. Natl. Acad. Sci. U. S. A.* **111**, 9217–9222 (2014).
  54. Roco, J. A. *et al.* Class-Switch Recombination Occurs Infrequently in Germinal Centers. *Immunity* **51**, 337-350.e7 (2019).
  55. Stavnezer, J. & Schrader, C. E. Mismatch repair converts AID-instigated nicks to double-strand breaks for antibody class-switch recombination. *Trends Genet.* **22**, 23–28 (2006).
  56. Genschel, J., Bazemore, L. R. & Modrich, P. Human exonuclease I is required for 5' and 3' mismatch repair. *J. Biol. Chem.* **277**, 13302–13311 (2002).
  57. Genschel, J. & Modrich, P. Mechanism of 5'-directed excision in human mismatch repair. *Mol. Cell* **12**, 1077–1086 (2003).
  58. Kunkel, T. A. & Erie, D. A. DNA mismatch repair. *Annu. Rev. Biochem.* **74**, 681–710 (2005).
  59. Wilson, T. M. *et al.* MSH2-MSH6 stimulates DNA polymerase  $\eta$ , suggesting a role for A:T mutations in antibody genes. *J. Exp. Med.* **201**, 637–645 (2005).
  60. Casellas, R. *et al.* Ku80 is required for immunoglobulin isotype switching. *EMBO J.* **17**, 2404–2411 (1998).
  61. Manis, J. P. *et al.* Ku70 is required for late B cell development and immunoglobulin

- heavy chain class switching. *J. Exp. Med.* **187**, 2081–2089 (1998).
62. Schultz, L. B., Chehab, N. H., Malikzay, A. & Halazonetis, T. D. p53 binding protein 1 (53BP1) is an early participant in the cellular response to DNA double-strand breaks. *J. Cell Biol.* **151**, 1381–1390 (2000).
63. Reina-San-Martin, B. *et al.* H2AX is required for recombination between immunoglobulin switch regions but not for intra-switch region recombination or somatic hypermutation. *J. Exp. Med.* **197**, 1767–1778 (2003).
64. Mochan, T. A., Venere, M., DiTullio, R. A. & Halazonetis, T. D. 53BP1, an activator of ATM in response to DNA damage. *DNA Repair* **3**, 945–952 (2004).
65. Ward, I. M. *et al.* 53BP1 is required for class switch recombination. *J. Cell Biol.* **165**, 459–464 (2004).
66. Farrant, J. Germ-line transcripts and class switching. *Clin. Exp. Immunol.* **95**, 1–2 (1994).
67. Stavnezer, J. Immunoglobulin class switching. *Curr. Opin. Immunol.* **8**, 199–205 (1996).
68. Lorenz, M., Jung, S. & Radbruch, A. Switch transcripts in immunoglobulin class switching. *Science (80-. )*. **267**, 1825–1828 (1995).
69. Maul, R. W. & Gearhart, P. J. AID and somatic hypermutation. in *Advances in Immunology* **105**, 159–191 (Academic Press Inc., 2010).
70. Briney, B. S., Willis, J. R. & Crowe, J. E. Location and length distribution of somatic hypermutation-associated DNA insertions and deletions reveals regions of antibody structural plasticity. *Genes Immun.* **13**, 523–529 (2012).

71. Krokan, H. E. & Bjørås, M. Base excision repair. *Cold Spring Harb. Perspect. Biol.* **5**, a012583 (2013).
72. Pilzecker, B. & Jacobs, H. Mutating for good: DNA damage responses during somatic hypermutation. *Frontiers in Immunology* **10**, 438 (2019).
73. Zlatanou, A. *et al.* The hMsh2-hMsh6 Complex Acts in Concert with Monoubiquitinated PCNA and Pol  $\eta$  in Response to Oxidative DNA Damage in Human Cells. *Mol. Cell* **43**, 649–662 (2011).
74. Guo, C. *et al.* Mouse Rev1 protein interacts with multiple DNA polymerases involved in translesion DNA synthesis. *EMBO J.* **22**, 6621–6630 (2003).
75. Tissier, A. *et al.* Co-localization in replication foci and interaction of human Y-family members, DNA polymerase pol $\eta$  and REV1 protein. *DNA Repair (Amst)*. **3**, 1503–1514 (2004).
76. Ross, A. L. & Sale, J. E. The catalytic activity of REV1 is employed during immunoglobulin gene diversification in DT40. *Mol. Immunol.* **43**, 1587–1594 (2006).
77. Kano, C., Hanaoka, F. & Wang, J. Y. Analysis of mice deficient in both REV1 catalytic activity and POLH reveals an unexpected role for POLH in the generation of C to G and G to C transversions during Ig gene hypermutation. *Int. Immunol.* **24**, 169–174 (2012).
78. Schrader, C. E., Guikema, J. E. J., Linehan, E. K., Selsing, E. & Stavnezer, J. Activation-Induced Cytidine Deaminase-Dependent DNA Breaks in Class Switch Recombination Occur during G<sub>1</sub> Phase of the Cell Cycle and Depend upon

- Mismatch Repair . *J. Immunol.* **179**, 6064–6071 (2007).
79. Sharbeen, G., Yee, C. W. Y., Smith, A. L. & Jolly, C. J. Ectopic restriction of DNA repair reveals that UNG2 excises AID-induced uracils predominantly or exclusively during G1 phase. *J. Exp. Med.* **209**, 965–974 (2012).
80. Wiedemann, E. M., Peycheva, M. & Pavri, R. DNA Replication Origins in Immunoglobulin Switch Regions Regulate Class Switch Recombination in an R-Loop-Dependent Manner. *Cell Rep.* **17**, 2927–2942 (2016).
81. Wang, Q. *et al.* The cell cycle restricts activation-induced cytidine deaminase activity to early G1. *J. Exp. Med.* **214**, 49–58 (2017).
82. Le, Q. & Maizels, N. Cell Cycle Regulates Nuclear Stability of AID and Determines the Cellular Response to AID. *PLOS Genet.* **11**, e1005411 (2015).
83. Gitlin, A. D., Shulman, Z. & Nussenzweig, M. C. Clonal selection in the germinal centre by regulated proliferation and hypermutation. *Nature* **509**, 637–640 (2014).
84. Shulman, Z. *et al.* Germinal centers: Dynamic signaling by T follicular helper cells during germinal center B cell selection. *Science.* **345**, 1058–1062 (2014).
85. Liu, D. *et al.* T-B-cell entanglement and ICOSL-driven feed-forward regulation of germinal centre reaction. *Nature* **517**, 214–218 (2015).
86. Yeh, C. H., Nojima, T., Kuraoka, M. & Kelsoe, G. Germinal center entry not selection of B cells is controlled by peptide-MHCII complex density. *Nat. Commun.* **9**, 928 (2018).
87. Zhang, Y. *et al.* Germinal center B cells govern their own fate via antibody feedback. *J. Exp. Med.* **210**, 457–464 (2013).

88. Stewart, I., Radtke, D., Phillips, B., McGowan, S. J. & Bannard, O. Germinal Center B Cells Replace Their Antigen Receptors in Dark Zones and Fail Light Zone Entry when Immunoglobulin Gene Mutations are Damaging. *Immunity* **49**, 477-489.e7 (2018).
89. Jackson, S. P. & Bartek, J. The DNA-damage response in human biology and disease. *Nature* **461**, 1071–1078 (2009).
90. Sonoda, E., Hohegger, H., Saberi, A., Taniguchi, Y. & Takeda, S. Differential usage of non-homologous end-joining and homologous recombination in double strand break repair. *DNA Repair (Amst)*. **5**, 1021–1029 (2006).
91. Mao, Z., Bozzella, M., Seluanov, A. & Gorbunova, V. DNA repair by nonhomologous end joining and homologous recombination during cell cycle in human cells. *Cell Cycle* **7**, 2902–2906 (2008).
92. Santivasi, W. L. & Xia, F. The role and clinical significance of DNA damage response and repair pathways in primary brain tumors. *Cell and Bioscience* **3**, 10–16 (2013).
93. Rothkamm, K., Kruger, I., Thompson, L. H. & Lobrich, M. Pathways of DNA Double-Strand Break Repair during the Mammalian Cell Cycle. *Mol. Cell. Biol.* **23**, 5706–5715 (2003).
94. Kotnis, A., Du, L., Liu, C., Popov, S. W. & Pan-Hammarström, Q. Non-homologous end joining in class switch recombination: The beginning of the end. in *Philosophical Transactions of the Royal Society B: Biological Sciences* **364**, 653–665 (Royal Society, 2009).

95. Lieber, M. R. The Mechanism of Double-Strand DNA Break Repair by the Nonhomologous DNA End-Joining Pathway. *Annu. Rev. Biochem.* **79**, 181–211 (2010).
96. Blier, P. R., Griffith, A. J., Craft, J. & Hardin, J. A. Binding of Ku protein to DNA. Measurement of affinity for ends and demonstration of binding to nicks. *J. Biol. Chem.* **268**, 7594–7601 (1993).
97. Walker, J. R., Corpina, R. A. & Goldberg, J. Structure of the Ku heterodimer bound to dna and its implications for double-strand break repair. *Nature* **412**, 607–614 (2001).
98. Nick McElhinny, S. A., Snowden, C. M., McCarville, J. & Ramsden, D. A. Ku Recruits the XRCC4-Ligase IV Complex to DNA Ends. *Mol. Cell. Biol.* **20**, 2996–3003 (2000).
99. Sibanda, B. L. *et al.* Crystal structure of an Xrcc4-DNA ligase IV complex. *Nat. Struct. Biol.* **8**, 1015–1019 (2001).
100. Gu, J. *et al.* XRCC4:DNA ligase IV can ligate incompatible DNA ends and can ligate across gaps. *EMBO J.* **26**, 1010–1023 (2007).
101. West, R. B., Yaneva, M. & Lieber, M. R. Productive and Nonproductive Complexes of Ku and DNA-Dependent Protein Kinase at DNA Termini. *Mol. Cell. Biol.* **18**, 5908–5920 (1998).
102. Ma, Y. *et al.* The DNA-dependent protein kinase catalytic subunit phosphorylation sites in human artemis. *J. Biol. Chem.* **280**, 33839–33846 (2005).
103. Ma, Y., Schwarz, K. & Lieber, M. R. The Artemis:DNA-PKcs endonuclease cleaves

- DNA loops, flaps, and gaps. *DNA Repair (Amst)*. **4**, 845–851 (2005).
104. Goodarzi, A. A. *et al.* DNA-PK autophosphorylation facilitates Artemis endonuclease activity. *EMBO J*. **25**, 3880–3889 (2006).
  105. Leuther, K. K., Hammarsten, O., Kornberg, R. D. & Chu, G. Structure of DNA-dependent protein kinase: implications for its regulation by DNA. *EMBO J*. **18**, 1114–1123 (1999).
  106. Turchi, J. J., Henkels, K. & Zhou, Y. Cisplatin-DNA adducts inhibit translocation of the Ku subunits of DNA-PK. *Nucleic Acids Res*. **28**, 4634–4641 (2000).
  107. Uematsu, N. *et al.* Autophosphorylation of DNA-PKCS regulates its dynamics at DNA double-strand breaks. *J. Cell Biol*. **177**, 219–229 (2007).
  108. Rooney, S. *et al.* Defective DNA repair and increased genomic instability in Artemis-deficient murine cells. *J. Exp. Med*. **197**, 553–565 (2003).
  109. Du, L. *et al.* Involvement of artemis in nonhomologous end-joining during immunoglobulin class switch recombination. *J. Exp. Med*. **205**, 3031–3040 (2008).
  110. Gottlieb, T. M. & Jackson, S. P. The DNA-dependent protein kinase: requirement for DNA ends and association with Ku antigen. *Cell* **72**, 131–142 (1993).
  111. Perrault, R., Wang, H., Wang, M., Rosidi, B. & Iliakis, G. Backup pathways of NHEJ are suppressed by DNA-PK. *J. Cell. Biochem*. **92**, 781–794 (2004).
  112. Costantini, S., Woodbine, L., Andreoli, L., Jeggo, P. A. & Vindigni, A. Interaction of the Ku heterodimer with the DNA ligase IV/Xrcc4 complex and its regulation by DNA-PK. *DNA Repair (Amst)*. **6**, 712–722 (2007).
  113. Frit, P., Barboule, N., Yuan, Y., Gomez, D. & Calsou, P. Alternative end-joining

- pathway(s): Bricolage at DNA breaks. *DNA Repair (Amst)*. **17**, 81–97 (2014).
114. Cortizas, E. M. *et al.* Alternative End-Joining and Classical Nonhomologous End-Joining Pathways Repair Different Types of Double-Strand Breaks during Class-Switch Recombination. *J. Immunol.* **191**, 5751–5763 (2013).
115. Audebert, M., Salles, B. & Calsou, P. Involvement of poly(ADP-ribose) polymerase-1 and XRCC1/DNA ligase III in an alternative route for DNA double-strand breaks rejoining. *J. Biol. Chem.* **279**, 55117–55126 (2004).
116. Audebert, M., Salles, B., Weinfeld, M. & Calsou, P. Involvement of polynucleotide kinase in a poly(ADP-ribose) polymerase-1-dependent DNA double-strand breaks rejoining pathway. *J. Mol. Biol.* **356**, 257–265 (2006).
117. Lee-Theilen, M., Matthews, A. J., Kelly, D., Zheng, S. & Chaudhuri, J. CtIP promotes microhomology-mediated alternative end joining during class-switch recombination. *Nat. Struct. Mol. Biol.* **18**, 75–80 (2011).
118. Cheng, Q. *et al.* Ku counteracts mobilization of PARP1 and MRN in chromatin damaged with DNA double-strand breaks. *Nucleic Acids Res.* **39**, 9605–9619 (2011).
119. Chan, S. H., Yu, A. M. & McVey, M. Dual roles for DNA polymerase theta in alternative end-joining repair of double-strand breaks in *Drosophila*. *PLoS Genet.* **6**, 1–16 (2010).
120. Ma, J.-L., Kim, E. M., Haber, J. E. & Lee, S. E. Yeast Mre11 and Rad1 Proteins Define a Ku-Independent Mechanism To Repair Double-Strand Breaks Lacking Overlapping End Sequences. *Mol. Cell. Biol.* **23**, 8820–8828 (2003).
121. Haince, J. F. *et al.* PARP1-dependent kinetics of recruitment of MRE11 and NBS1

- proteins to multiple DNA damage sites. *J. Biol. Chem.* **283**, 1197–1208 (2008).
122. Robert, I., Dantzer, F. & Reina-San-Martin, B. Parp1 facilitates alternative NHEJ, whereas Parp2 suppresses IgH/c-myc translocations during immunoglobulin class switch recombination. *J. Exp. Med.* **206**, 1047–1056 (2009).
123. Wang, M. *et al.* PARP-1 and Ku compete for repair of DNA double strand breaks by distinct NHEJ pathways. *Nucleic Acids Res.* **34**, 6170–6182 (2006).
124. D’Amours, D. & Jackson, S. P. The Mre11 complex: At the crossroads of DNA repair and checkpoint signalling. *Nature Reviews Molecular Cell Biology* **3**, 317–327 (2002).
125. Sartori, A. A. *et al.* Human CtIP promotes DNA end resection. *Nature* **450**, 509–514 (2007).
126. Yun, M. H. & Hiom, K. CtIP-BRCA1 modulates the choice of DNA double-strand-break repair pathway throughout the cell cycle. *Nature* **459**, 460–463 (2009).
127. Truong, L. N. *et al.* Microhomology-mediated End Joining and Homologous Recombination share the initial end resection step to repair DNA double-strand breaks in mammalian cells. *Proc. Natl. Acad. Sci. U. S. A.* **110**, 7720–7725 (2013).
128. Yousefzadeh, M. J. *et al.* Mechanism of Suppression of Chromosomal Instability by DNA Polymerase POLQ. *PLoS Genet.* **10**, e1004654 (2014).
129. Saito, S., Maeda, R. & Adachi, N. Dual loss of human POLQ and LIG4 abolishes random integration. *Nat. Commun.* **8**, 16112 (2017).
130. Arana, M. E., Seki, M., Wood, R. D., Rogozin, I. B. & Kunkel, T. A. Low-fidelity DNA synthesis by human DNA polymerase theta. *Nucleic Acids Res.* **36**, 3847–3856

(2008).

131. Martomo, S. A., Saribasak, H., Yokoi, M., Hanaoka, F. & Gearhart, P. J. Reevaluation of the role of DNA polymerase  $\theta$  in somatic hypermutation of immunoglobulin genes. *DNA Repair (Amst)*. **7**, 1603–1608 (2008).
132. Wang, Z. *et al.* DNA polymerase (POLQ) is important for repair of DNA double-strand breaks caused by fork collapse. *J. Biol. Chem.* **294**, 3909–3919 (2019).
133. Masani, S., Han, L., Meek, K. & Yu, K. Redundant function of DNA ligase 1 and 3 in alternative end-joining during immunoglobulin class switch recombination. *Proc. Natl. Acad. Sci. U. S. A.* **113**, 1261–1266 (2016).
134. Lu, G. *et al.* Ligase I and ligase III mediate the DNA double-strand break ligation in alternative end-joining. *Proc. Natl. Acad. Sci. U. S. A.* **113**, 1256–1260 (2016).
135. Zarei, S. *et al.* A comprehensive review of amyotrophic lateral sclerosis. *Surgical Neurology International* **6**, 171 (2015).
136. Lacomblez, L., Bensimon, G., Leigh, P. N., Guillet, P. & Meininger, V. Dose-ranging study of riluzole in amyotrophic lateral sclerosis. *Lancet* **347**, 1425–1431 (1996).
137. Zoccolella, S. *et al.* Riluzole and amyotrophic lateral sclerosis survival: A population-based study in southern Italy. *Eur. J. Neurol.* **14**, 262–268 (2007).
138. Miller, R. G., Mitchell, J. D. & Moore, D. H. Riluzole for amyotrophic lateral sclerosis (ALS)/motor neuron disease (MND). *Cochrane Database Syst. Rev.* CD001447 (2002). doi:10.1002/14651858.cd001447.pub3
139. Fang, T. *et al.* Stage at which riluzole treatment prolongs survival in patients with

- amyotrophic lateral sclerosis: a retrospective analysis of data from a dose-ranging study. *Lancet Neurol.* **17**, 416–422 (2018).
140. Abe, K. *et al.* Safety and efficacy of edaravone in well defined patients with amyotrophic lateral sclerosis: a randomised, double-blind, placebo-controlled trial. *Lancet Neurol.* **16**, 505–512 (2017).
141. Sawada, H. Clinical efficacy of edaravone for the treatment of amyotrophic lateral sclerosis. *Expert Opin. Pharmacother.* **18**, 735–738 (2017).
142. Cruz, M. P. Edaravone (Radicava): A novel neuroprotective agent for the treatment of amyotrophic lateral sclerosis. *P and T* **43**, 25–28 (2018).
143. Luo, L. *et al.* Efficacy and safety of edaravone in treatment of amyotrophic lateral sclerosis—a systematic review and meta-analysis. *Neurological Sciences* **40**, 235–241 (2019).
144. Turnbull, J. Is edaravone harmful? (A placebo is not a control). *Amyotroph. Lateral Scler. Front. Degener.* **19**, 477–482 (2018).
145. Shellikeri, S. *et al.* The neuropathological signature of bulbar-onset ALS: A systematic review. *Neuroscience and Biobehavioral Reviews* **75**, 378–392 (2017).
146. Rowland, L. P. & Shneider, N. A. Amyotrophic lateral sclerosis. *New England Journal of Medicine* **344**, 1688–1700 (2001).
147. Pramatarova, A., Laganière, J., Roussel, J., Brisebois, K. & Rouleau, G. A. Neuron-specific expression of mutant superoxide dismutase 1 in transgenic mice does not lead to motor impairment. *J. Neurosci.* **21**, 3369–3374 (2001).
148. Lino, M. M., Schneider, C. & Caroni, P. Accumulation of SOD1 Mutants in

- Postnatal Motoneurons Does Not Cause Motoneuron Pathology or Motoneuron Disease. *J. Neurosci.* **22**, 4825–4832 (2002).
149. Ilieva, H., Polymenidou, M. & Cleveland, D. W. Non-cell autonomous toxicity in neurodegenerative disorders: ALS and beyond. *Journal of Cell Biology* **187**, 761–772 (2009).
150. Philips, T. & Rothstein, J. D. Glial cells in amyotrophic lateral sclerosis. *Experimental Neurology* **262**, 111–120 (2014).
151. Chen, H., Kankel, M. W., Su, S. C., Han, S. W. S. & Ofengeim, D. Exploring the genetics and non-cell autonomous mechanisms underlying ALS/FTLD. *Cell Death and Differentiation* **25**, 646–660 (2018).
152. Beers, D. R. & Appel, S. H. Immune dysregulation in amyotrophic lateral sclerosis: mechanisms and emerging therapies. *The Lancet Neurology* **18**, 211–220 (2019).
153. Clement, A. M. *et al.* Wild-type nonneuronal cells extend survival of SOD1 mutant motor neurons in ALS mice. *Science*. **302**, 113–117 (2003).
154. Chaplin, D. D. Overview of the immune response. *J. Allergy Clin. Immunol.* **125**, S3-23 (2010).
155. Barker, C. F. & Billingham, R. E. Immunologically privileged sites. *Adv. Immunol.* **25**, 1–54 (1978).
156. Carson, M. J., Doose, J. M., Melchior, B., Schmid, C. D. & Ploix, C. C. CNS immune privilege: Hiding in plain sight. *Immunological Reviews* **213**, 48–65 (2006).
157. Ransohoff, R. M. & Brown, M. A. Innate immunity in the central nervous system. *Journal of Clinical Investigation* **122**, 1164–1171 (2012).

158. Daneman, R. & Prat, A. The blood–brain barrier. *Cold Spring Harb. Perspect. Biol.* **7**, a020412 (2015).
159. Worzfeld, T. & Schwaninger, M. Apicobasal polarity of brain endothelial cells. *Journal of Cerebral Blood Flow and Metabolism* **36**, 340–362 (2016).
160. Armulik, A. *et al.* Pericytes regulate the blood–brain barrier. *Nature* **468**, 557–561 (2010).
161. Alvarez, J. I., Katayama, T. & Prat, A. Glial influence on the blood brain barrier. *GLIA* **61**, 1939–1958 (2013).
162. Noell, S. *et al.* Evidence for a role of dystroglycan regulating the membrane architecture of astroglial endfeet. *Eur. J. Neurosci.* **33**, 2179–2186 (2011).
163. Sweeney, M. D., Sagare, A. P. & Zlokovic, B. V. Blood–brain barrier breakdown in Alzheimer disease and other neurodegenerative disorders. *Nature Reviews Neurology* **14**, 133–150 (2018).
164. Kakaroubas, N., Brennan, S., Keon, M. & Saksena, N. K. Pathomechanisms of Blood–Brain Barrier Disruption in ALS. *Neurosci. J.* **2019**, 2537698 (2019).
165. Azevedo, F. A. C. *et al.* Equal numbers of neuronal and nonneuronal cells make the human brain an isometrically scaled-up primate brain. *J. Comp. Neurol.* **513**, 532–541 (2009).
166. Matias, I., Morgado, J. & Gomes, F. C. A. Astrocyte Heterogeneity: Impact to Brain Aging and Disease. *Front. Aging Neurosci.* **11**, 59 (2019).
167. Li, Q. & Barres, B. A. Microglia and macrophages in brain homeostasis and disease. *Nature Reviews Immunology* **18**, 225–242 (2018).

168. Michalski, J. P. & Kothary, R. Oligodendrocytes in a nutshell. *Frontiers in Cellular Neuroscience* **9**, 340 (2015).
169. Macvicar, B. A. & Newman, E. A. Astrocyte regulation of blood flow in the brain. *Cold Spring Harb. Perspect. Biol.* **7**, a020388 (2015).
170. Zonta, M. *et al.* Neuron-to-astrocyte signaling is central to the dynamic control of brain microcirculation. *Nat. Neurosci.* **6**, 43–50 (2003).
171. Chung, W. S., Allen, N. J. & Eroglu, C. Astrocytes control synapse formation, function, and elimination. *Cold Spring Harb. Perspect. Biol.* **7**, a020370 (2015).
172. Mederos, S., González-Arias, C. & Perea, G. Astrocyte–Neuron Networks: A Multilane Highway of Signaling for Homeostatic Brain Function. *Front. Synaptic Neurosci.* **10**, 45 (2018).
173. Rouach, N., Koulakoff, A., Abudara, V., Willecke, K. & Giaume, C. Astroglial metabolic networks sustain hippocampal synaptic transmission. *Science*. **322**, 1551–1555 (2008).
174. Suzuki, A. *et al.* Astrocyte-neuron lactate transport is required for long-term memory formation. *Cell* **144**, 810–823 (2011).
175. Matsui, T. *et al.* Astrocytic glycogen-derived lactate fuels the brain during exhaustive exercise to maintain endurance capacity. *Proc. Natl. Acad. Sci. U. S. A.* **114**, 6358–6363 (2017).
176. Nimmerjahn, A., Kirchhoff, F. & Helmchen, F. Neuroscience: Resting microglial cells are highly dynamic surveillants of brain parenchyma in vivo. *Science*. **308**, 1314–1318 (2005).

177. Harrison, J. K. *et al.* Role for neuronally derived fractalkine in mediating interactions between neurons and CX3CR1-expressing microglia. *Proc. Natl. Acad. Sci. U. S. A.* **95**, 10896–10901 (1998).
178. Wolf, Y., Yona, S., Kim, K. W. & Jung, S. Microglia, seen from the CX3CR1 angle. *Front. Cell. Neurosci.* **7**, 26 (2013).
179. Schafer, D. P. *et al.* Microglia Sculpt Postnatal Neural Circuits in an Activity and Complement-Dependent Manner. *Neuron* **74**, 691–705 (2012).
180. Stevens, B. *et al.* The Classical Complement Cascade Mediates CNS Synapse Elimination. *Cell* **131**, 1164–1178 (2007).
181. Davalos, D. *et al.* ATP mediates rapid microglial response to local brain injury in vivo. *Nat. Neurosci.* **8**, 752–758 (2005).
182. Marín-Teva, J. L. *et al.* Microglia Promote the Death of Developing Purkinje Cells. *Neuron* **41**, 535–547 (2004).
183. Sedel, F., Béchade, C., Vyas, S. & Triller, A. Macrophage-Derived Tumor Necrosis Factor  $\alpha$ , an Early Developmental Signal for Motoneuron Death. *J. Neurosci.* **24**, 2236–2246 (2004).
184. Marín-Teva, J. L., Cuadros, M. A., Martín-Oliva, D. & Navascués, J. Microglia and neuronal cell death. *Neuron Glia Biology* **7**, 25–40 (2012).
185. Brown, G. C. & Neher, J. J. Microglial phagocytosis of live neurons. *Nat. Rev. Neurosci.* **15**, 209–216 (2014).
186. Chiu, I. M. *et al.* A neurodegeneration-specific gene-expression signature of acutely isolated microglia from an amyotrophic lateral sclerosis mouse model. *Cell Rep.* **4**,

- 385–401 (2013).
187. Park, H. J., Oh, S. H., Kim, H. N., Jung, Y. J. & Lee, P. H. Mesenchymal stem cells enhance  $\alpha$ -synuclein clearance via M2 microglia polarization in experimental and human parkinsonian disorder. *Acta Neuropathol.* **132**, 685–701 (2016).
  188. Lobo-Silva, D., Carriche, G. M., Castro, A. G., Roque, S. & Saraiva, M. Balancing the immune response in the brain: IL-10 and its regulation. *Journal of Neuroinflammation* **13**, 297 (2016).
  189. Geloso, M. C. *et al.* The dual role of microglia in ALS: Mechanisms and therapeutic approaches. *Front. Aging Neurosci.* **9**, 242 (2017).
  190. Rossi, C. *et al.* Interleukin 4 modulates microglia homeostasis and attenuates the early slowly progressive phase of amyotrophic lateral sclerosis article. *Cell Death Dis.* **9**, 250 (2018).
  191. Olah, M. *et al.* Identification of a microglia phenotype supportive of remyelination. *Glia* **60**, 306–321 (2012).
  192. Kalkman, H. O. & Feuerbach, D. Antidepressant therapies inhibit inflammation and microglial M1-polarization. *Pharmacology and Therapeutics* **163**, 82–93 (2016).
  193. Walker, D. G. & Lue, L. F. Immune phenotypes of microglia in human neurodegenerative disease: Challenges to detecting microglial polarization in human brains. *Alzheimer's Research and Therapy* **7**, 56 (2015).
  194. Becherel, O. J. *et al.* Senataxin Plays an Essential Role with DNA Damage Response Proteins in Meiotic Recombination and Gene Silencing. *PLoS Genet.* **9**, e1003435 (2013).

195. Durkin, M., Qian, X., Popescu, N. & Lowy, D. Isolation of Mouse Embryo Fibroblasts. *Bio. Protoc.* **3**, e908 (2013).
196. Lim, J. *et al.* Nuclear Proximity of Mtr4 to RNA Exosome Restricts DNA Mutational Asymmetry. *Cell* **169**, 523-537.e15 (2017).
197. Margine, I., Palese, P. & Krammer, F. Expression of functional recombinant hemagglutinin and neuraminidase proteins from the novel H7N9 influenza virus using the baculovirus expression system. *J. Vis. Exp.* e51112 (2013). doi:10.3791/51112
198. Pinna, D., Corti, D., Jarrossay, D., Sallusto, F. & Lanzavecchia, A. Clonal dissection of the human memory B-cell repertoire following infection and vaccination. *Eur. J. Immunol.* **39**, 1260–1270 (2009).
199. McIntyre, T. M., Kehry, M. R. & Snapper, C. M. Novel in vitro model for high-rate IgA class switching. *J. Immunol.* **154**, 3156–61 (1995).
200. Ribeiro de Almeida, C. *et al.* RNA Helicase DDX1 Converts RNA G-Quadruplex Structures into R-Loops to Promote IgH Class Switch Recombination. *Mol. Cell* **70**, 650-662.e8 (2018).
201. Halász, L. *et al.* RNA-DNA hybrid (R-loop) immunoprecipitation mapping: An analytical workflow to evaluate inherent biases. *Genome Res.* **27**, 1063–1073 (2017).
202. Turchaninova, M. A. *et al.* High-quality full-length immunoglobulin profiling with unique molecular barcoding. *Nat. Protoc.* **11**, 1599–1616 (2016).
203. Byers, S. L., Wiles, M. V., Dunn, S. L. & Taft, R. A. Mouse Estrous Cycle Identification Tool and Images. *PLoS One* **7**, e35538 (2012).

204. Richner, M., Jager, S. B., Siupka, P. & Vaegter, C. B. Hydraulic extrusion of the spinal cord and isolation of dorsal root ganglia in rodents. *J. Vis. Exp.* e55226 (2017). doi:10.3791/55226
205. Skourti-Stathaki, K., Proudfoot, N. J. & Gromak, N. Human Senataxin Resolves RNA/DNA Hybrids Formed at Transcriptional Pause Sites to Promote Xrn2-Dependent Termination. *Mol. Cell* **42**, 794–805 (2011).
206. Aguilera, A. & Gómez-González, B. DNA-RNA hybrids: The risks of DNA breakage during transcription. *Nature Structural and Molecular Biology* **24**, 439–443 (2017).
207. Grunseich, C. *et al.* Senataxin Mutation Reveals How R-Loops Promote Transcription by Blocking DNA Methylation at Gene Promoters. *Mol. Cell* **69**, 426–437.e7 (2018).
208. Cohen, S. *et al.* Senataxin resolves RNA:DNA hybrids forming at DNA double-strand breaks to prevent translocations. *Nat. Commun.* **9**, 533 (2018).
209. Miller, M. S. *et al.* Senataxin suppresses the antiviral transcriptional response and controls viral biogenesis. *Nat. Immunol.* **16**, 485–494 (2015).
210. Becherel, O. J. *et al.* Disruption of Spermatogenesis and Infertility in Ataxia with Oculomotor Apraxia Type 2 (AOA2). *Cerebellum* **18**, 448–456 (2019).
211. Catford, S. R., O’Byrne, M. K., McLachlan, R. I., Delatycki, M. B. & Rombauts, L. Germ cell arrest associated with a SETX mutation in ataxia oculomotor apraxia type 2. *Reprod. Biomed. Online* **38**, 961–965 (2019).
212. Suraweera, A. *et al.* Senataxin, defective in ataxia oculomotor apraxia type 2, is

- involved in the defense against oxidative DNA damage. *J. Cell Biol.* **177**, 969–979 (2007).
213. Yuce, O. & West, S. C. Senataxin, Defective in the Neurodegenerative Disorder Ataxia with Oculomotor Apraxia 2, Lies at the Interface of Transcription and the DNA Damage Response. *Mol. Cell. Biol.* **33**, 406–417 (2013).
214. Hatchi, E. *et al.* BRCA1 recruitment to transcriptional pause sites is required for R-loop-driven DNA damage repair. *Mol. Cell* **57**, 636–647 (2015).
215. Kannan, A., Bhatia, K., Branzei, D. & Gangwani, L. Combined deficiency of Senataxin and DNA-PKcs causes DNA damage accumulation and neurodegeneration in spinal muscular atrophy. *Nucleic Acids Res.* **46**, 8326–8346 (2018).
216. Yeo, A. J. *et al.* R-Loops in Proliferating Cells but Not in the Brain: Implications for AOA2 and Other Autosomal Recessive Ataxias. *PLoS One* **9**, e90219 (2014).
217. Hiscott, J. Triggering the innate antiviral response through IRF-3 activation. *Journal of Biological Chemistry* **282**, 15325–15329 (2007).
218. Burma, S., Chen, B. P., Murphy, M., Kurimasa, A. & Chen, D. J. ATM Phosphorylates Histone H2AX in Response to DNA Double-strand Breaks. *J. Biol. Chem.* **276**, 42462–42467 (2001).
219. Skourti-Stathaki, K. & Proudfoot, N. J. A double-edged sword: R loops as threats to genome integrity and powerful regulators of gene expression. *Genes and Development* **28**, 1384–1396 (2014).
220. Lee, D. Y. & Clayton, D. A. Properties of a primer RNA-DNA hybrid at the mouse

- mitochondrial DNA leading-strand origin of replication. *J. Biol. Chem.* **271**, 24262–24269 (1996).
221. Crossley, M. P., Bocek, M. & Cimprich, K. A. R-Loops as Cellular Regulators and Genomic Threats. *Molecular Cell* **73**, 398–411 (2019).
222. Sanz, L. A. *et al.* Prevalent, Dynamic, and Conserved R-Loop Structures Associate with Specific Epigenomic Signatures in Mammals. *Mol. Cell* **63**, 167–178 (2016).
223. Roy, D. & Lieber, M. R. G Clustering Is Important for the Initiation of Transcription-Induced R-Loops In Vitro, whereas High G Density without Clustering Is Sufficient Thereafter. *Mol. Cell. Biol.* **29**, 3124–3133 (2009).
224. Roy, D., Zhang, Z., Lu, Z., Hsieh, C.-L. & Lieber, M. R. Competition between the RNA Transcript and the Nontemplate DNA Strand during R-Loop Formation In Vitro: a Nick Can Serve as a Strong R-Loop Initiation Site. *Mol. Cell. Biol.* **30**, 146–159 (2010).
225. Westover, K. D., Bushnell, D. A. & Kornberg, R. D. Structural basis of transcription: Nucleotide selection by rotation in the RNA polymerase II active center. *Cell* **119**, 481–489 (2004).
226. Kent, T., Kashkina, E., Anikin, M. & Temiakov, D. Maintenance of RNA-DNA hybrid length in bacterial RNA polymerases. *J. Biol. Chem.* **284**, 13497–13504 (2009).
227. Roberts, R. W. & Crothers, D. M. Stability and properties of double and triple helices: Dramatic effects of RNA or DNA backbone composition. *Science.* **258**, 1463–1466 (1992).

228. Duquette, M. L., Handa, P., Vincent, J. A., Taylor, A. F. & Maizels, N. Intracellular transcription of G-rich DNAs induces formation of G-loops, novel structures containing G4 DNA. *Genes Dev.* **18**, 1618–1629 (2004).
229. Gan, W. *et al.* R-loop-mediated genomic instability is caused by impairment of replication fork progression. *Genes Dev.* **25**, 2041–2056 (2011).
230. García-Rubio, M. L. *et al.* The Fanconi Anemia Pathway Protects Genome Integrity from R-loops. *PLoS Genet.* **11**, e1005674 (2015).
231. García-Muse, T. & Aguilera, A. Transcription-replication conflicts: How they occur and how they are resolved. *Nature Reviews Molecular Cell Biology* **17**, 553–563 (2016).
232. Salas-Armenteros, I. *et al.* Human THO –Sin3A interaction reveals new mechanisms to prevent R-loops that cause genome instability. *EMBO J.* **36**, 3532–3547 (2017).
233. Akman, G. *et al.* Pathological ribonuclease H1 causes R-loop depletion and aberrant DNA segregation in mitochondria. *Proc. Natl. Acad. Sci. U. S. A.* **113**, E4276–E4285 (2016).
234. Parajuli, S. *et al.* Human ribonuclease H1 resolves R-loops and thereby enables progression of the DNA replication fork. *J. Biol. Chem.* **292**, 15216–15224 (2017).
235. Zhao, H., Zhu, M., Limbo, O. & Russell, P. RNase H eliminates R-loops that disrupt DNA replication but is nonessential for efficient DSB repair. *EMBO Rep.* **19**, e45335 (2018).
236. Marinello, J. *et al.* Dynamic effects of topoisomerase  $\alpha$  inhibition on R-loops and

- short transcripts at active promoters. *PLoS One* **11**, e0147053 (2016).
237. Manzo, S. G. *et al.* DNA Topoisomerase I differentially modulates R-loops across the human genome. *Genome Biol.* **19**, 100 (2018).
238. Puno, M. R. & Lima, C. D. Structural basis for MTR4-ZCCHC8 interactions that stimulate the MTR4 helicase in the nuclear exosome-targeting complex. *Proc. Natl. Acad. Sci. U. S. A.* **115**, E5506–E5515 (2018).
239. DeJesus-Hernandez, M. *et al.* Expanded GGGGCC Hexanucleotide Repeat in Noncoding Region of C9ORF72 Causes Chromosome 9p-Linked FTD and ALS. *Neuron* **72**, 245–256 (2011).
240. Haeusler, A. R. *et al.* C9orf72 nucleotide repeat structures initiate molecular cascades of disease. *Nature* **507**, 195–200 (2014).
241. Walker, C. *et al.* C9orf72 expansion disrupts ATM-mediated chromosomal break repair. *Nat. Neurosci.* **20**, 1225–1235 (2017).
242. Elden, A. C. *et al.* Ataxin-2 intermediate-length polyglutamine expansions are associated with increased risk for ALS. *Nature* **466**, 1069–1075 (2010).
243. Hart, M. P., Brettschneider, J., Lee, V. M. Y., Trojanowski, J. Q. & Gitler, A. D. Distinct TDP-43 pathology in ALS patients with ataxin 2 intermediate-length polyQ expansions. *Acta Neuropathol.* **124**, 221–230 (2012).
244. Salvi, J. S. *et al.* Roles for Pbp1 and Caloric Restriction in Genome and Lifespan Maintenance via Suppression of RNA-DNA Hybrids. *Dev. Cell* **30**, 177–191 (2014).
245. Basu, U. *et al.* The RNA exosome targets the AID cytidine deaminase to both strands of transcribed duplex DNA substrates. *Cell* **144**, 353–363 (2011).

246. Li, L., Monckton, E. A. & Godbout, R. A Role for DEAD Box 1 at DNA Double-Strand Breaks. *Mol. Cell. Biol.* **28**, 6413–6425 (2008).
247. Arnold, L. W., Grdina, T. A., Whitmore, A. C. & Haughton, G. Ig isotype switching in B lymphocytes. Isolation and characterization of clonal variants of the murine Ly-1+ B cell lymphoma, CH12, expressing isotypes other than IgM. *J. Immunol.* **140**, 4355–4363 (1988).
248. Eckmann, L., Morzycka-Wroblewska, E., Smith, J. R. & Kagnoff, M. F. Cytokine-induced differentiation of IgA B cells: studies using an IgA expressing B-cell lymphoma. *Immunology* **76**, 235–241 (1992).
249. Panchakshari, R. A. *et al.* DNA double-strand break response factors influence end-joining features of IgH class switch and general translocation junctions. *Proc. Natl. Acad. Sci. U. S. A.* **115**, 762–767 (2018).
250. Shiloh, Y. ATM and related protein kinases: Safeguarding genome integrity. *Nature Reviews Cancer* **3**, 155–168 (2003).
251. Nowak, R. Discovery of AT gene sparks biomedical research bonanza. *Science.* **268**, 1700–1701 (1995).
252. Lumsden, J. M. *et al.* Immunoglobulin class switch recombination is impaired in Atm-deficient mice. *J. Exp. Med.* **200**, 1111–1121 (2004).
253. Bhatti, S. *et al.* ATM protein kinase: The linchpin of cellular defenses to stress. *Cellular and Molecular Life Sciences* **68**, 2977–3006 (2011).
254. Bain, A. L., Harris, J. L. & Khanna, K. K. Identification of ATM-interacting proteins by co-immunoprecipitation and glutathione-s-transferase (GST) pull-down assays.

- in *Methods in Molecular Biology* **1599**, 163–181 (Humana Press Inc., 2017).
255. Khair, L. *et al.* ATM Increases Activation-Induced Cytidine Deaminase Activity at Downstream S Regions during Class-Switch Recombination. *J. Immunol.* **192**, 4887–4896 (2014).
  256. Ward, I. M. & Chen, J. Histone H2AX Is Phosphorylated in an ATR-dependent Manner in Response to Replicational Stress. *J. Biol. Chem.* **276**, 47759–47762 (2001).
  257. Stiff, T. *et al.* ATM and DNA-PK Function Redundantly to Phosphorylate H2AX after Exposure to Ionizing Radiation. *Cancer Res.* **64**, 2390–2396 (2004).
  258. Kuo, L. J. & Yang, L. X. Gamma-H2AX- A novel biomaker for DNA double-strand breaks. *In Vivo* **22**, 305–310 (2008).
  259. Rogakou, E. P., Boon, C., Redon, C. & Bonner, W. M. Megabase chromatin domains involved in DNA double-strand breaks in vivo. *J. Cell Biol.* **146**, 905–915 (1999).
  260. Rogakou, E. P., Pilch, D. R., Orr, A. H., Ivanova, V. S. & Bonner, W. M. DNA double-stranded breaks induce histone H2AX phosphorylation on serine 139. *J. Biol. Chem.* **273**, 5858–5868 (1998).
  261. Podhorecka, M., Skladanowski, A. & Bozko, P. H2AX phosphorylation: Its role in DNA damage response and cancer therapy. *Journal of Nucleic Acids* **2010**, 920161 (2010).
  262. Franco, S. *et al.* H2AX prevents DNA breaks from progressing to chromosome breaks and translocations. *Mol. Cell* **21**, 201–214 (2006).
  263. Yin, B. *et al.* Histone H2AX stabilizes broken DNA strands to suppress chromosome

- breaks and translocations during V(D)J recombination. *J. Exp. Med.* **206**, 2625–2639 (2009).
264. Lou, Z. *et al.* MDC1 maintains genomic stability by participating in the amplification of ATM-dependent DNA damage signals. *Mol. Cell* **21**, 187–200 (2006).
265. Savic, V. *et al.* Formation of Dynamic  $\gamma$ -H2AX Domains along Broken DNA Strands Is Distinctly Regulated by ATM and MDC1 and Dependent upon H2AX Densities in Chromatin. *Mol. Cell* **34**, 298–310 (2009).
266. Xie, A. *et al.* Distinct Roles of Chromatin-Associated Proteins MDC1 and 53BP1 in Mammalian Double-Strand Break Repair. *Mol. Cell* **28**, 1045–1057 (2007).
267. Panier, S. & Boulton, S. J. Double-strand break repair: 53BP1 comes into focus. *Nature Reviews Molecular Cell Biology* **15**, 7–18 (2014).
268. Ward, I. M., Minn, K., Jorda, K. G. & Chen, J. Accumulation of checkpoint protein 53BP1 at DNA breaks involves its binding to phosphorylated histone H2AX. *J. Biol. Chem.* **278**, 19579–19582 (2003).
269. Chapman, J. R. *et al.* RIF1 Is Essential for 53BP1-Dependent Nonhomologous End Joining and Suppression of DNA Double-Strand Break Resection. *Mol. Cell* **49**, 858–871 (2013).
270. Callen, E. *et al.* 53BP1 mediates productive and mutagenic DNA repair through distinct phosphoprotein interactions. *Cell* **153**, 1266–1280 (2013).
271. Guo, X. *et al.* Acetylation of 53BP1 dictates the DNA double strand break repair pathway. *Nucleic Acids Res.* **46**, 689–703 (2018).
272. Feng, L. *et al.* Cell cycle-dependent inhibition of 53BP1 signaling by BRCA1. *Cell*

- Discov.* **1**, 15019 (2015).
273. Bothmer, A. *et al.* 53BP1 regulates DNA resection and the choice between classical and alternative end joining during class switch recombination. *J. Exp. Med.* **207**, 855–865 (2010).
274. Reina-San-Martin, B., Chen, J., Nussenzweig, A. & Nussenzweig, M. C. Enhanced intra-switch region recombination during immunoglobulin class switch recombination in 53BP1<sup>-/-</sup> B cells. *Eur. J. Immunol.* **37**, 235–239 (2007).
275. Feldman, S. *et al.* 53BP1 Contributes to Igh Locus Chromatin Topology during Class Switch Recombination. *J. Immunol.* **198**, 2434–2444 (2017).
276. Celeste, A. *et al.* Genomic instability in mice lacking histone H2AX. *Science.* **296**, 922–927 (2002).
277. Celeste, A. *et al.* H2AX haploinsufficiency modifies genomic stability and tumor susceptibility. *Cell* **114**, 371–383 (2003).
278. Ward, I. M. *et al.* 53BP1 cooperates with p53 and functions as a haploinsufficient tumor suppressor in mice. *Mol. Cell. Biol.* **25**, 10079–10086 (2005).
279. Weyemi, U. *et al.* Histone H2AX deficiency causes neurobehavioral deficits and impaired redox homeostasis. *Nat. Commun.* **9**, 1526 (2018).
280. Yan, C. T. *et al.* IgH class switching and translocations use a robust non-classical end-joining pathway. *Nature* **449**, 478–482 (2007).
281. Boboila, C. *et al.* Alternative end-joining catalyzes class switch recombination in the absence of both Ku70 and DNA ligase. *J. Exp. Med.* **207**, 417–427 (2010).
282. Bothmer, A. *et al.* Regulation of DNA End Joining, Resection, and Immunoglobulin

- Class Switch Recombination by 53BP1. *Mol. Cell* **42**, 319–329 (2011).
283. Feng, Y. L. *et al.* H2AX facilitates classical non-homologous end joining at the expense of limited nucleotide loss at repair junctions. *Nucleic Acids Res.* **45**, 10614–10633 (2017).
284. Deenick, E. K., Hasbold, J. & Hodgkin, P. D. Switching to IgG3, IgG2b, and IgA is division linked and independent, revealing a stochastic framework for describing differentiation. *J. Immunol.* **163**, 4707–4714 (1999).
285. Zhang, Z. Z., Pannunzio, N. R., Hsieh, C. L., Yu, K. & Lieber, M. R. The role of G-density in switch region repeats for immunoglobulin class switch recombination. *Nucleic Acids Res.* **42**, 13186–13193 (2014).
286. So, S., Davis, A. J. & Chen, D. J. Autophosphorylation at serine 1981 stabilizes ATM at DNA damage sites. *J. Cell Biol.* **187**, 977–990 (2009).
287. Yel, L. Selective IgA Deficiency. *Journal of Clinical Immunology* **30**, 10–16 (2010).
288. Brandtzaeg, P. *et al.* The clinical condition of IgA-deficient patients is related to the proportion of IgD- and IgM-producing cells in their nasal mucosa. *Clin. Exp. Immunol.* **67**, 626–636 (1987).
289. Janzi, M. *et al.* Selective IgA deficiency in early life: Association to infections and allergic diseases during childhood. *Clin. Immunol.* **133**, 78–85 (2009).
290. Barka, N. *et al.* Multireactive pattern of serum autoantibodies in asymptomatic individuals with immunoglobulin A deficiency. *Clin. Diagn. Lab. Immunol.* **2**, 469–472 (1995).
291. Edwards, E., Razvi, S. & Cunningham-Rundles, C. IgA deficiency: Clinical

- correlates and responses to pneumococcal vaccine. *Clin. Immunol.* **111**, 93–97 (2004).
292. Iber, D. & Maini, P. K. A mathematical model for germinal centre kinetics and affinity maturation. *J. Theor. Biol.* **219**, 153–175 (2002).
293. Allen, C. D. C., Okada, T., Tang, H. L. & Cyster, J. G. Imaging of germinal center selection events during affinity maturation. *Science.* **315**, 528–531 (2007).
294. Schwickert, T. A. *et al.* In vivo imaging of germinal centres reveals a dynamic open structure. *Nature* **446**, 83–87 (2007).
295. Hwang, J. K., Alt, F. W. & Yeap, L.-S. Related Mechanisms of Antibody Somatic Hypermutation and Class Switch Recombination. *Microbiol. Spectr.* **3**, MDNA3-0037–2014 (2015).
296. Huang, F.-T. *et al.* Sequence dependence of chromosomal R-loops at the immunoglobulin heavy-chain Smu class switch region. *Mol. Cell. Biol.* **27**, 5921–5932 (2007).
297. Manis, J. P. *et al.* 53BP1 links DNA damage-response pathways to immunoglobulin heavy chain class-switch recombination. *Nat. Immunol.* **5**, 481–487 (2004).
298. Ghezraoui, H. *et al.* 53BP1 cooperation with the REV7–shieldin complex underpins DNA structure-specific NHEJ. *Nature* **560**, 122–127 (2018).
299. Bennett, C. L. *et al.* Protein interaction analysis of senataxin and the ALS4 L389S mutant yields insights into senataxin post-translational modification and uncovers mutant-specific binding with a brain cytoplasmic RNA-encoded peptide. *PLoS One* **8**, e78837 (2013).

300. Wuerffel, R. *et al.* S-S Synapsis during Class Switch Recombination Is Promoted by Distantly Located Transcriptional Elements and Activation-Induced Deaminase. *Immunity* **27**, 711–722 (2007).
301. Jhunjhunwala, S. *et al.* The 3D Structure of the Immunoglobulin Heavy-Chain Locus: Implications for Long-Range Genomic Interactions. *Cell* **133**, 265–279 (2008).
302. Sleigh, M. J. The mechanism of DNA breakage by phleomycin in vitro. *Nucleic Acids Res.* **3**, 891–902 (1976).
303. Bekker-Jensen, S. *et al.* Spatial organization of the mammalian genome surveillance machinery in response to DNA strand breaks. *J. Cell Biol.* **173**, 195–206 (2006).
304. Stucki, M. *et al.* MDC1 directly binds phosphorylated histone H2AX to regulate cellular responses to DNA double-strand breaks. *Cell* **123**, 1213–1226 (2005).
305. Pan, Q. *et al.* Alternative end joining during switch recombination in patients with Ataxia-Telangiectasia. *Eur. J. Immunol.* **32**, 1300–1308 (2002).
306. Lefebvre, S. *et al.* Identification and characterization of a spinal muscular atrophy-determining gene. *Cell* **80**, 155–165 (1995).
307. Soulas-Sprauel, P. *et al.* Role for DNA repair factor XRCC4 in immunoglobulin class switch recombination. *J. Exp. Med.* **204**, 1717–1727 (2007).
308. Chang, H. H. Y., Pannunzio, N. R., Adachi, N. & Lieber, M. R. Non-homologous DNA end joining and alternative pathways to double-strand break repair. *Nature Reviews Molecular Cell Biology* **18**, 495–506 (2017).
309. Pan-Hammarström, Q. *et al.* Impact of DNA ligase IV on nonhomologous end

- joining pathways during class switch recombination in human cells. *J. Exp. Med.* **201**, 189–194 (2005).
310. Kracker, S. *et al.* Impaired induction of DNA lesions during immunoglobulin class-switch recombination in humans influences end-joining repair. *Proc. Natl. Acad. Sci. U. S. A.* **107**, 22225–22230 (2010).
311. Zimmermann, M. & De Lange, T. 53BP1: Pro choice in DNA repair. *Trends in Cell Biology* **24**, 108–117 (2014).
312. Kozlov, S. V. *et al.* Autophosphorylation and ATM activation: Additional sites add to the complexity. *J. Biol. Chem.* **286**, 9107–9119 (2011).
313. Cristini, A., Groh, M., Kristiansen, M. S. & Gromak, N. RNA/DNA Hybrid Interactome Identifies DXH9 as a Molecular Player in Transcriptional Termination and R-Loop-Associated DNA Damage. *Cell Rep.* **23**, 1891–1905 (2018).
314. Nahas, S. A., Duquette, A., Roddier, K., Gatti, R. A. & Brais, B. Ataxia-oculomotor apraxia 2 patients show no increased sensitivity to ionizing radiation. *Neuromuscul. Disord.* **17**, 968–969 (2007).
315. Cannon, J. R. & Greenamyre, J. T. The role of environmental exposures in neurodegeneration and neurodegenerative diseases. *Toxicol. Sci.* **124**, 225–250 (2011).
316. Amor, S. *et al.* Inflammation in neurodegenerative diseases - an update. *Immunology* **142**, 151–166 (2014).
317. Gutzeit, C., Magri, G. & Cerutti, A. Intestinal IgA production and its role in host-microbe interaction. *Immunological Reviews* **260**, 76–85 (2014).

318. Brown, R. H. & Al-Chalabi, A. Amyotrophic lateral sclerosis. *New England Journal of Medicine* **377**, 162–172 (2017).
319. Ajroud-Driss, S. & Siddique, T. Sporadic and hereditary amyotrophic lateral sclerosis (ALS). *Biochimica et Biophysica Acta - Molecular Basis of Disease* **1852**, 679–684 (2015).
320. Farhan, S. M. K. *et al.* Exome sequencing in amyotrophic lateral sclerosis implicates a novel gene, DNAJC7, encoding a heat-shock protein. *Nat. Neurosci.* **22**, 1966–1974 (2019).
321. Sicot, G. & Gomes-Pereira, M. RNA toxicity in human disease and animal models: From the uncovering of a new mechanism to the development of promising therapies. *Biochimica et Biophysica Acta - Molecular Basis of Disease* **1832**, 1390–1409 (2013).
322. Shang, Y. & Huang, E. J. Mechanisms of FUS mutations in familial amyotrophic lateral sclerosis. *Brain Research* **1647**, 65–78 (2016).
323. Mackenzie, I. R. A. & Rademakers, R. The role of transactive response DNA-binding protein-43 in amyotrophic lateral sclerosis and frontotemporal dementia. *Current Opinion in Neurology* **21**, 693–700 (2008).
324. Neumann, M. *et al.* Ubiquitinated TDP-43 in frontotemporal lobar degeneration and amyotrophic lateral sclerosis. *Science*. **314**, 130–133 (2006).
325. Andersen, P. M. Amyotrophic lateral sclerosis associated with mutations in the CuZn superoxide dismutase gene. *Current Neurology and Neuroscience Reports* **6**, 37–46 (2006).

326. Boylan, K. Familial ALS. *Neurol Clin* **33**, 807–830 (2015).
327. Rosen, D. R. *et al.* Mutations in Cu/Zn superoxide dismutase gene are associated with familial amyotrophic lateral sclerosis. *Nature* **362**, 59–62 (1993).
328. Perry, J. J. P., Shin, D. S., Getzoff, E. D. & Tainer, J. A. The structural biochemistry of the superoxide dismutases. *Biochimica et Biophysica Acta - Proteins and Proteomics* **1804**, 245–262 (2010).
329. Sau, D. *et al.* Mutation of SOD1 in ALS: A gain of a loss of function. *Hum. Mol. Genet.* **16**, 1604–1618 (2007).
330. Bunton-Stasyshyn, R. K. A., Saccon, R. A., Fratta, P. & Fisher, E. M. C. SOD1 Function and Its Implications for Amyotrophic Lateral Sclerosis Pathology: New and Renascent Themes. *Neuroscientist* **21**, 519–529 (2015).
331. Wang, R., Yang, B. & Zhang, D. Activation of interferon signaling pathways in spinal cord astrocytes from an ALS mouse model. *Glia* **59**, 946–958 (2011).
332. Pasinelli, P. *et al.* Amyotrophic lateral sclerosis-associated SOD1 mutant proteins bind and aggregate with Bcl-2 in spinal cord mitochondria. *Neuron* **43**, 19–30 (2004).
333. Vande Velde, C., Miller, T. M., Cashman, N. R. & Cleveland, D. W. Selective association of misfolded ALS-linked mutant SOD1 with the cytoplasmic face of mitochondria. *Proc. Natl. Acad. Sci. U. S. A.* **105**, 4022–4027 (2008).
334. Vande Velde, C. *et al.* Misfolded SOD1 associated with motor neuron mitochondria alters mitochondrial shape and distribution prior to clinical onset. *PLoS One* **6**, e22031 (2011).

335. Pickles, S. *et al.* Mitochondrial damage revealed by immunoselection for ALS-linked misfolded SOD1. *Hum. Mol. Genet.* **22**, 3947–3959 (2013).
336. Münch, C., O’Brien, J. & Bertolotti, A. Prion-like propagation of mutant superoxide dismutase-1 misfolding in neuronal cells. *Proc. Natl. Acad. Sci. U. S. A.* **108**, 3548–3553 (2011).
337. Sibilla, C. & Bertolotti, A. Prion properties of SOD1 in amyotrophic lateral sclerosis and potential therapy. *Cold Spring Harb. Perspect. Biol.* **9**, a024141 (2017).
338. Tokuda, E. *et al.* Wild-type Cu/Zn-superoxide dismutase is misfolded in cerebrospinal fluid of sporadic amyotrophic lateral sclerosis. *Mol. Neurodegener.* **14**, 42 (2019).
339. Polymenidou, M. & Cleveland, D. W. The seeds of neurodegeneration: Prion-like spreading in ALS. *Cell* **147**, 498–508 (2011).
340. Gurney, M. E. *et al.* Motor neuron degeneration in mice that express a human Cu,Zn superoxide dismutase mutation. *Science.* **264**, 1772–1775 (1994).
341. Pickles, S. *et al.* ALS-linked misfolded SOD1 species have divergent impacts on mitochondria. *Acta Neuropathol. Commun.* **4**, 43 (2016).
342. Grad, L. I., Pokrishevsky, E., Silverman, J. M. & Cashman, N. R. Exosome-dependent and independent mechanisms are involved in prion-like transmission of propagated Cu/Zn superoxide dismutase misfolding. *Prion* **8**, 331–335 (2014).
343. Grad, L. I. *et al.* Intercellular propagated misfolding of wild-type Cu/Zn superoxide dismutase occurs via exosome-dependent and -independent mechanisms. *Proc. Natl. Acad. Sci. U. S. A.* **111**, 3620–3625 (2014).

344. Yamanaka, K. *et al.* Mutant SOD1 in cell types other than motor neurons and oligodendrocytes accelerates onset of disease in ALS mice. *Proc. Natl. Acad. Sci. U. S. A.* **105**, 7594–7599 (2008).
345. Boillée, S. *et al.* Onset and progression in inherited ALS determined by motor neurons and microglia. *Science.* **312**, 1389–1392 (2006).
346. Yamanaka, K. *et al.* Astrocytes as determinants of disease progression in inherited amyotrophic lateral sclerosis. *Nat. Neurosci.* **11**, 251–253 (2008).
347. Sweeney, P. *et al.* Protein misfolding in neurodegenerative diseases: Implications and strategies. *Transl. Neurodegener.* **6**, 6 (2017).
348. Chia, R. *et al.* Superoxide dismutase 1 and tgSOD1G93A mouse spinal cord seed fibrils, suggesting a propagative cell death mechanism in amyotrophic lateral sclerosis. *PLoS One* **5**, e10627 (2010).
349. Zhu, C., Beck, M. V., Griffith, J. D., Deshmukh, M. & Dokholyan, N. V. Large SOD1 aggregates, unlike trimeric SOD1, do not impact cell viability in a model of amyotrophic lateral sclerosis. *Proc. Natl. Acad. Sci. U. S. A.* **115**, 4661–4665 (2018).
350. Gardner, B. M., Pincus, D., Gotthardt, K., Gallagher, C. M. & Walter, P. Endoplasmic reticulum stress sensing in the unfolded protein response. *Cold Spring Harb. Perspect. Biol.* **5**, a013169 (2013).
351. Tobisawa, S. *et al.* Mutant SOD1 linked to familial amyotrophic lateral sclerosis, but not wild-type SOD1, induces ER stress in COS7 cells and transgenic mice. *Biochem. Biophys. Res. Commun.* **303**, 496–503 (2003).
352. Medinas, D. B. *et al.* Endoplasmic reticulum stress leads to accumulation of wild-

- type SOD1 aggregates associated with sporadic amyotrophic lateral sclerosis. *Proc. Natl. Acad. Sci. U. S. A.* **115**, 8209–8214 (2018).
353. Rakhit, R. *et al.* An immunological epitope selective for pathological monomer-misfolded SOD1 in ALS. *Nat. Med.* **13**, 754–759 (2007).
354. Bosco, D. A. *et al.* Mutant FUS proteins that cause amyotrophic lateral sclerosis incorporate into stress granules. *Hum. Mol. Genet.* **19**, 4160–4175 (2010).
355. Forsberg, K. *et al.* Novel antibodies reveal inclusions containing non-native SOD1 in sporadic ALS patients. *PLoS One* **5**, e11552 (2010).
356. Pokrishevsky, E. *et al.* Aberrant localization of FUS and TDP43 is associated with misfolding of SOD1 in amyotrophic lateral sclerosis. *PLoS One* **7**, e35050 (2012).
357. Parakh, S. & Atkin, J. D. Protein folding alterations in amyotrophic lateral sclerosis. *Brain Research* **1648**, 633–649 (2016).
358. Zhou, Y. & Danbolt, N. C. Glutamate as a neurotransmitter in the healthy brain. *Journal of Neural Transmission* **121**, 799–817 (2014).
359. O’Kane, R. L., Martínez-López, I., DeJoseph, M. R., Viña, J. R. & Hawkins, R. A. Na<sup>+</sup>-dependent glutamate transporters (EAAT1, EAAT2, and EAAT3) of the blood-brain barrier. A mechanism for glutamate removal. *J. Biol. Chem.* **274**, 31891–31895 (1999).
360. Foran, E. & Trotti, D. Glutamate transporters and the excitotoxic path to motor neuron degeneration in amyotrophic lateral sclerosis. *Antioxidants and Redox Signaling* **11**, 1587–1602 (2009).
361. Bristol, L. A. & Rothstein, J. D. Glutamate transporter gene expression in

- amyotrophic lateral sclerosis motor cortex. *Ann. Neurol.* **39**, 676–679 (1996).
362. Lin, C. L. G. *et al.* Aberrant RNA processing in a neurodegenerative disease: The cause for absent EAAT2, a glutamate transporter, in amyotrophic lateral sclerosis. *Neuron* **20**, 589–602 (1998).
363. Sasaki, S., Komori, T. & Iwata, M. Excitatory amino acid transporter 1 and 2 immunoreactivity in the spinal cord in amyotrophic lateral sclerosis. *Acta Neuropathol.* **100**, 138–144 (2000).
364. Meyer, T. *et al.* The RNA of the glutamate transporter EAAT2 is variably spliced in amyotrophic lateral sclerosis and normal individuals. *J. Neurol. Sci.* **170**, 45–50 (1999).
365. Honig, L. S., Chambliss, D. D., Bigio, E. H., Carroll, S. L. & Elliott, J. L. Glutamate transporter EAAT2 splice variants occur not only in ALS, but also in AD and controls. *Neurology* **55**, 1082–1088 (2000).
366. Bendotti, C. *et al.* Transgenic SOD1 G93A mice develop reduced GLT-1 in spinal cord without alterations in cerebrospinal fluid glutamate levels. *J. Neurochem.* **79**, 737–746 (2001).
367. Van Den Bosch, L. & Robberecht, W. Different receptors mediate motor neuron death induced by short and long exposures to excitotoxicity. in *Brain Research Bulletin* **53**, 383–388 (2000).
368. Van Den Bosch, L., Vandenberghe, W., Klaassen, H., Van Houtte, E. & Robberecht, W. Ca<sup>2+</sup>-permeable AMPA receptors and selective vulnerability of motor neurons. *J. Neurol. Sci.* **180**, 29–34 (2000).

369. Carriedo, S. G., Sensi, S. L., Yin, H. Z. & Weiss, J. H. AMPA exposures induce mitochondrial Ca<sup>2+</sup> overload and ROS generation in spinal motor neurons in vitro. *J. Neurosci.* **20**, 240–250 (2000).
370. Urushitani, M. *et al.* N-methyl-D-aspartate receptor-mediated mitochondrial Ca(2+) overload in acute excitotoxic motor neuron death: a mechanism distinct from chronic neurotoxicity after Ca(2+) influx. *J. Neurosci. Res.* **63**, 377–387 (2001).
371. Tradewell, M. L., Cooper, L. A., Minotti, S. & Durham, H. D. Calcium dysregulation, mitochondrial pathology and protein aggregation in a culture model of amyotrophic lateral sclerosis: Mechanistic relationship and differential sensitivity to intervention. *Neurobiol. Dis.* **42**, 265–275 (2011).
372. Tateno, M. *et al.* Calcium-permeable AMPA receptors promote misfolding of mutant SOD1 protein and development of amyotrophic lateral sclerosis in a transgenic mouse model. *Hum. Mol. Genet.* **13**, 2183–2196 (2004).
373. Leal, S. S., Cardoso, I., Valentine, J. S. & Gomes, C. M. Calcium ions promote superoxide dismutase 1 (SOD1) aggregation into non-fibrillar amyloid: A link to toxic effects of calcium overload in amyotrophic lateral sclerosis (ALS)? *J. Biol. Chem.* **288**, 25219–25228 (2013).
374. Estácio, S. G., Leal, S. S., Cristóvão, J. S., Faísca, P. F. N. & Gomes, C. M. Calcium binding to gatekeeper residues flanking aggregation-prone segments underlies non-fibrillar amyloid traits in superoxide dismutase 1 (SOD1). *Biochim. Biophys. Acta - Proteins Proteomics* **1854**, 118–126 (2015).
375. Maragakis, N. J., Dykes-Hoberg, M. & Rothstein, J. D. Altered Expression of the

- Glutamate Transporter EAAT2b in Neurological Disease. *Ann. Neurol.* **55**, 469–477 (2004).
376. Doble, A. The pharmacology and mechanism of action of riluzole. *Neurology* **47**, S233-241 (1996).
377. Sasaki, S. & Iwata, M. Mitochondrial alterations in the spinal cord of patients with sporadic amyotrophic lateral sclerosis. *J. Neuropathol. Exp. Neurol.* **66**, 10–16 (2007).
378. Sasaki, S., Horie, Y. & Iwata, M. Mitochondrial alterations in dorsal root ganglion cells in sporadic amyotrophic lateral sclerosis. *Acta Neuropathol.* **114**, 633–639 (2007).
379. Magrané, J., Cortez, C., Gan, W. B. & Manfredi, G. Abnormal mitochondrial transport and morphology are common pathological denominators in SOD1 and TDP43 ALS mouse models. *Hum. Mol. Genet.* **23**, 1413–1424 (2014).
380. Higgins, C. M. J., Jung, C., Ding, H. & Xu, Z. Mutant Cu, Zn superoxide dismutase that causes motoneuron degeneration is present in mitochondria in the CNS. *J. Neurosci.* **22**, RC215 (2002).
381. Mattiazzi, M. *et al.* Mutated human SOD1 causes dysfunction of oxidative phosphorylation in mitochondria of transgenic mice. *J. Biol. Chem.* **277**, 29626–29633 (2002).
382. Higgins, C. M. J., Jung, C. & Xu, Z. ALS-associated mutant SODIG93A causes mitochondrial vacuolation by expansion of the intermembrane space by involvement of SOD1 aggregation and peroxisomes. *BMC Neurosci.* **4**, 16 (2003).

383. Wang, W. *et al.* The inhibition of TDP-43 mitochondrial localization blocks its neuronal toxicity. *Nat. Med.* **22**, 869–878 (2016).
384. Deng, J. *et al.* FUS Interacts with HSP60 to Promote Mitochondrial Damage. *PLoS Genet.* **11**, e1005357 (2015).
385. Lopez-Gonzalez, R. *et al.* Poly(GR) in C9ORF72-Related ALS/FTD Compromises Mitochondrial Function and Increases Oxidative Stress and DNA Damage in iPSC-Derived Motor Neurons. *Neuron* **92**, 383–391 (2016).
386. Fischer, L. R. *et al.* SOD1 targeted to the mitochondrial intermembrane space prevents motor neuropathy in the Sod1 knockout mouse. *Brain* **134**, 196–209 (2011).
387. Vijayvergiya, C., Beal, M. F., Buck, J. & Manfredi, G. Mutant superoxide dismutase 1 forms aggregates in the brain mitochondrial matrix of amyotrophic lateral sclerosis mice. *J. Neurosci.* **25**, 2463–2470 (2005).
388. Ferri, A. *et al.* Familial ALS-superoxide dismutases associate with mitochondria and shift their redox potentials. *Proc. Natl. Acad. Sci. U. S. A.* **103**, 13860–13865 (2006).
389. Hashimoto, M., Rockenstein, E., Crews, L. & Masliah, E. Role of Protein Aggregation in Mitochondrial Dysfunction and Neurodegeneration in Alzheimer's and Parkinson's Diseases. *NeuroMolecular Med.* **4**, 21–35 (2003).
390. Smith, E. F., Shaw, P. J. & De Vos, K. J. The role of mitochondria in amyotrophic lateral sclerosis. *Neuroscience Letters* **710**, 132933 (2019).
391. Kirkinetzos, I. G. *et al.* Cytochrome c association with the inner mitochondrial membrane is impaired in the CNS of G93A-SOD1 mice. *J. Neurosci.* **25**, 164–172 (2005).

392. Ježek, J., Cooper, K. F. & Strich, R. Reactive oxygen species and mitochondrial dynamics: The yin and yang of mitochondrial dysfunction and cancer progression. *Antioxidants* **7**, E13 (2018).
393. Pizzino, G. *et al.* Oxidative Stress: Harms and Benefits for Human Health. *Oxidative Medicine and Cellular Longevity* **2017**, 8416763 (2017).
394. Gregersen, N. & Bross, P. Protein misfolding and cellular stress: An overview. in *Methods in Molecular Biology* **648**, 3–23 (Humana Press Inc., 2010).
395. Bhandary, B., Marahatta, A., Kim, H. R. & Chae, H. J. An involvement of oxidative stress in endoplasmic reticulum stress and its associated diseases. *International Journal of Molecular Sciences* **14**, 434–456 (2013).
396. Mittal, M., Siddiqui, M. R., Tran, K., Reddy, S. P. & Malik, A. B. Reactive oxygen species in inflammation and tissue injury. *Antioxidants and Redox Signaling* **20**, 1126–1167 (2014).
397. Bogdanov, M. *et al.* Increased oxidative damage to DNA in ALS patients. *Free Radic. Biol. Med.* **29**, 652–658 (2000).
398. Mitsumoto, H. *et al.* Oxidative stress biomarkers in sporadic ALS. *Amyotroph. Lateral Scler.* **9**, 177–183 (2008).
399. Chang, Y. *et al.* Messenger RNA Oxidation Occurs Early in Disease Pathogenesis and Promotes Motor Neuron Degeneration in ALS. *PLoS One* **3**, e2849 (2008).
400. Rakhit, R. *et al.* Oxidation-induced misfolding and aggregation of superoxide dismutase and its implications for amyotrophic lateral sclerosis. *J. Biol. Chem.* **277**, 47551–47556 (2002).

401. Samtleben, S. *et al.* Direct imaging of ER calcium with targeted-esterase induced dye loading (TED). *J. Vis. Exp.* e50317 (2013). doi:10.3791/50317
402. Jan, C. H., Williams, C. C. & Weissman, J. S. Principles of ER cotranslational translocation revealed by proximity-specific ribosome profiling. *Science*. **346**, 1257521 (2014).
403. Arai, T. *et al.* TDP-43 is a component of ubiquitin-positive tau-negative inclusions in frontotemporal lobar degeneration and amyotrophic lateral sclerosis. *Biochem. Biophys. Res. Commun.* **351**, 602–611 (2006).
404. Blokhuis, A. M., Groen, E. J. N., Koppers, M., Van Den Berg, L. H. & Pasterkamp, R. J. Protein aggregation in amyotrophic lateral sclerosis. *Acta Neuropathologica* **125**, 777–794 (2013).
405. Dal Canto, M. C. & Gurney, M. E. Neuropathological changes in two lines of mice carrying a transgene for mutant human Cu,Zn SOD, and in mice overexpressing wild type human SOD: a model of familial amyotrophic lateral sclerosis (FALS). *Brain Res.* **676**, 25–40 (1995).
406. Oyanagi, K. *et al.* Spinal anterior horn cells in sporadic amyotrophic lateral sclerosis show ribosomal detachment from, and cisternal distention of the rough endoplasmic reticulum. *Neuropathol. Appl. Neurobiol.* **34**, 650–658 (2008).
407. Kikuchi, H. *et al.* Spinal cord endoplasmic reticulum stress associated with a microsomal accumulation of mutant superoxide dismutase-1 in an ALS model. *Proc. Natl. Acad. Sci. U. S. A.* **103**, 6025–6030 (2006).
408. Atkin, J. D. *et al.* Induction of the unfolded protein response in familial amyotrophic

- lateral sclerosis and association of protein-disulfide isomerase with superoxide dismutase 1. *Journal of Biological Chemistry* **281**, 30152–30165 (2006).
409. Grosskreutz, J., Van Den Bosch, L. & Keller, B. U. Calcium dysregulation in amyotrophic lateral sclerosis. *Cell Calcium* **47**, 165–174 (2010).
410. Jaiswal, M. K. & Keller, B. U. Cu/Zn superoxide dismutase typical for familial amyotrophic lateral sclerosis increases the vulnerability of mitochondria and perturbs Ca<sup>2+</sup> Homeostasis in SOD1G93A mice. *Mol. Pharmacol.* **75**, 478–489 (2009).
411. Jaiswal, M. *et al.* Impairment of mitochondrial calcium handling in a mtSOD1 cell culture model of motoneuron disease. *BMC Neurosci.* **10**, 64 (2009).
412. Liu, J. & Wang, F. Role of neuroinflammation in amyotrophic lateral sclerosis: Cellular mechanisms and therapeutic implications. *Frontiers in Immunology* **8**, 1005 (2017).
413. Hu, Y. *et al.* Increased peripheral blood inflammatory cytokine levels in amyotrophic lateral sclerosis: A meta-analysis study. *Sci. Rep.* **7**, 9094 (2017).
414. Radford, R. A. *et al.* The established and emerging roles of astrocytes and microglia in amyotrophic lateral sclerosis and frontotemporal dementia. *Frontiers in Cellular Neuroscience* **9**, 414 (2015).
415. Cherry, J. D., Olschowka, J. A. & O'Banion, M. K. Neuroinflammation and M2 microglia: The good, the bad, and the inflamed. *Journal of Neuroinflammation* **11**, 98 (2014).
416. Spiller, K. J. *et al.* Microglia-mediated recovery from ALS-relevant motor neuron

- degeneration in a mouse model of TDP-43 proteinopathy. *Nat. Neurosci.* **21**, 329–340 (2018).
417. Liao, B., Zhao, W., Beers, D. R., Henkel, J. S. & Appel, S. H. Transformation from a neuroprotective to a neurotoxic microglial phenotype in a mouse model of ALS. *Exp. Neurol.* **237**, 147–152 (2012).
418. Sankowski, R., Mader, S. & Valdés-Ferrer, S. I. Systemic inflammation and the brain: Novel roles of genetic, molecular, and environmental cues as drivers of neurodegeneration. *Front. Cell. Neurosci.* **9**, 28 (2015).
419. Ohgomori, T., Yamada, J., Takeuchi, H., Kadomatsu, K. & Jinno, S. Comparative morphometric analysis of microglia in the spinal cord of SOD1G93A transgenic mouse model of amyotrophic lateral sclerosis. *Eur. J. Neurosci.* **43**, 1340–1351 (2016).
420. Engelhardt, J. I., Tajti, J. & Appel, S. H. Lymphocytic Infiltrates in the Spinal Cord in Amyotrophic Lateral Sclerosis. *Arch. Neurol.* **50**, 30–36 (1993).
421. Beers, D. R., Henkel, J. S., Zhao, W., Wang, J. & Appel, S. H. CD4<sup>+</sup> T cells support glial neuroprotection, slow disease progression, and modify glial morphology in an animal model of inherited ALS. *Proc. Natl. Acad. Sci. U. S. A.* **105**, 15558–15563 (2008).
422. Henkel, J. S. *et al.* Regulatory T-lymphocytes mediate amyotrophic lateral sclerosis progression and survival. *EMBO Mol. Med.* **5**, 64–79 (2013).
423. Beers, D. R. *et al.* ALS patients' regulatory T lymphocytes are dysfunctional, and correlate with disease progression rate and severity. *JCI Insight* **2**, e89530 (2017).

424. Sheean, R. K. *et al.* Association of regulatory T-Cell Expansion with progression of amyotrophic lateral sclerosis a study of humans and a transgenic mouse model. *JAMA Neurol.* **75**, 681–689 (2018).
425. Coque, E. *et al.* Cytotoxic CD8 + T lymphocytes expressing ALS-causing SOD1 mutant selectively trigger death of spinal motoneurons. *Proc. Natl. Acad. Sci. U. S. A.* **116**, 2312–2317 (2019).
426. Naor, S. *et al.* Development of ALS-like disease in SOD-1 mice deficient of B lymphocytes. *J. Neurol.* **256**, 1228–1235 (2009).
427. Olofsson, P. S., Rosas-Ballina, M., Levine, Y. A. & Tracey, K. J. Rethinking inflammation: Neural circuits in the regulation of immunity. *Immunol. Rev.* **248**, 188–204 (2012).
428. Miyata, S. New aspects in fenestrated capillary and tissue dynamics in the sensory circumventricular organs of adult brains. *Frontiers in Neuroscience* **9**, 390 (2015).
429. Patel, J. P. & Frey, B. N. Disruption in the Blood-Brain Barrier: The Missing Link between Brain and Body Inflammation in Bipolar Disorder? *Neural Plasticity* **2015**, 708306 (2015).
430. Gross, P. M. & Weindl, A. Peering through the windows of the brain. *Journal of Cerebral Blood Flow and Metabolism* **7**, 663–672 (1987).
431. Johnson, A. K. & Gross, P. M. Sensory circumventricular organs and brain homeostatic pathways. *FASEB Journal* **7**, 678–686 (1993).
432. Cottrell, G. T. & Ferguson, A. V. Sensory circumventricular organs: Central roles in integrated autonomic regulation. *Regulatory Peptides* **117**, 11–23 (2004).

433. Parnet, P., Kelley, K. W., Bluthé, R. M. & Dantzer, R. Expression and regulation of interleukin-1 receptors in the brain. Role in cytokines-induced sickness behavior. *J. Neuroimmunol.* **125**, 5–14 (2002).
434. Chakravarty, S. & Herkenham, M. Toll-like receptor 4 on nonhematopoietic cells sustains CNS inflammation during endotoxemia, independent of systemic cytokines. *J. Neurosci.* **25**, 1788–1796 (2005).
435. Nakano, Y. *et al.* Astrocytic TLR4 expression and LPS-induced nuclear translocation of STAT3 in the sensory circumventricular organs of adult mouse brain. *J. Neuroimmunol.* **278**, 144–158 (2015).
436. Friedman, W. J. Cytokines regulate expression of the type 1 interleukin-1 receptor in rat hippocampal neurons and glia. *Exp. Neurol.* **168**, 23–31 (2001).
437. Holló, K. *et al.* Interleukin-1 receptor type 1 is overexpressed in neurons but not in glial cells within the rat superficial spinal dorsal horn in complete Freund adjuvant-induced inflammatory pain. *J. Neuroinflammation* **14**, 125 (2017).
438. Wu, H., Li, L. & Su, X. Vagus nerve through  $\alpha 7$  nAChR modulates lung infection and inflammation: Models, cells, and signals. *BioMed Research International* **2014**, 283525 (2014).
439. Pulendran, B. & Maddur, M. S. Innate immune sensing and response to influenza. *Curr. Top. Microbiol. Immunol.* **386**, 23–71 (2015).
440. Maier, S. F., Goehler, L. E., Fleshner, M. & Watkins, L. R. The role of the vagus nerve in cytokine-to-brain communication. in *Annals of the New York Academy of Sciences* **840**, 289–300 (Blackwell Publishing Inc., 1998).

441. Ek, M., Kurosawa, M., Lundeberg, T. & Ericsson, A. Activation of vagal afferents after intravenous injection of interleukin-1 $\beta$ : Role of endogenous prostaglandins. *J. Neurosci.* **18**, 9471–9479 (1998).
442. Goehler, L. E., Gaykema, R. P. a., HamMacK, S. E., Maier, S. F. & Watkins, L. R. Interleukin-1 induces c-Fos immunoreactivity in primary afferent neurons of the vagus nerve. *Brain Res.* **804**, 306–310 (1998).
443. Hansen, M. K., O'Connor, K. A., Goehler, L. E., Watkins, L. R. & Maier, S. F. The contribution of the vagus nerve in interleukin-1beta-induced fever is dependent on dose. *Am. J. Physiol. - Regul. Integr. Comp. Physiol.* **280**, R929-934 (2001).
444. Pavlov, V. A., Wang, H., Czura, C. J., Friedman, S. G. & Tracey, K. J. The Cholinergic Anti-inflammatory Pathway: A Missing Link in Neuroimmunomodulation. *Molecular Medicine* **9**, 125–134 (2003).
445. Borovikova, L. V. *et al.* Vagus nerve stimulation attenuates the systemic inflammatory response to endotoxin. *Nature* **405**, 458–462 (2000).
446. Wang, H. *et al.* Nicotinic acetylcholine receptor  $\alpha 7$  subunit is an essential regulator of inflammation. *Nature* **421**, 384–388 (2003).
447. Yoshikawa, H. *et al.* Nicotine inhibits the production of proinflammatory mediators in human monocytes by suppression of I- $\kappa$ B phosphorylation and nuclear factor- $\kappa$ B transcriptional activity through nicotinic acetylcholine receptor  $\alpha 7$ . *Clin. Exp. Immunol.* **146**, 116–123 (2006).
448. Sofroniew, M. V. Astrogliosis. *Cold Spring Harb. Perspect. Biol.* **7**, a020420 (2015).
449. Eng, L. F. & Ghirnikar, R. S. GFAP and Astrogliosis. in *Brain Pathology* **4**, 229–

237 (1994).

450. Wanner, I. B. *et al.* Glial scar borders are formed by newly proliferated, elongated astrocytes that interact to corral inflammatory and fibrotic cells via STAT3-dependent mechanisms after spinal cord injury. *J. Neurosci.* **33**, 12870–12886 (2013).
451. Sofroniew, M. V. Molecular dissection of reactive astrogliosis and glial scar formation. *Trends in Neurosciences* **32**, 638–647 (2009).
452. Faulkner, J. R. *et al.* Reactive Astrocytes Protect Tissue and Preserve Function after Spinal Cord Injury. *J. Neurosci.* **24**, 2143–2155 (2004).
453. Voskuhl, R. R. *et al.* Reactive astrocytes form scar-like perivascular barriers to leukocytes during adaptive immune inflammation of the CNS. *J. Neurosci.* **29**, 11511–11522 (2009).
454. Woiciechowsky, C., Schöning, B., Stoltenburg-Didinger, G., Stockhammer, F. & Volk, H. D. Brain-IL-1 $\beta$  triggers astrogliosis through induction of IL-6: Inhibition by propranolol and IL-10. *Med. Sci. Monit.* **10**, BR325-330 (2004).
455. Lin, H.-W. *et al.* Astrogliosis is delayed in type 1 interleukin-1 receptor-null mice following a penetrating brain injury. *J. Neuroinflammation* **3**, 15 (2006).
456. Maragakis, N. J. & Rothstein, J. D. Mechanisms of Disease: Astrocytes in neurodegenerative disease. *Nature Clinical Practice Neurology* **2**, 679–689 (2006).
457. Phatnani, H. & Maniatis, T. Astrocytes in neurodegenerative disease. *Cold Spring Harb. Perspect. Biol.* **7**, a020628 (2015).
458. Haim, L. Ben, Carrillo-de Sauvage, M. A., Ceyzériat, K. & Escartin, C. Elusive roles

- for reactive astrocytes in neurodegenerative diseases. *Frontiers in Cellular Neuroscience* **9**, 278 (2015).
459. Li, K., Li, J., Zheng, J. & Qin, S. Reactive Astrocytes in Neurodegenerative Diseases. *Aging Dis.* **10**, 664 (2019).
460. Tan, A. M., Zhang, W. & Levine, J. M. NG2: A component of the glial scar that inhibits axon growth. *Journal of Anatomy* **207**, 717–725 (2005).
461. Yiu, G. & He, Z. Glial inhibition of CNS axon regeneration. *Nature Reviews Neuroscience* **7**, 617–627 (2006).
462. Wanner, I. B. *et al.* A new in vitro model of the glial scar inhibits axon growth. *Glia* **56**, 1691–1709 (2008).
463. Bondi, M. W., Edmonds, E. C. & Salmon, D. P. Alzheimer’s disease: Past, present, and future. *Journal of the International Neuropsychological Society* **23**, 818–831 (2017).
464. Kraft, A. W. *et al.* Attenuating astrocyte activation accelerates plaque pathogenesis in APP/PS1 mice. *FASEB J.* **27**, 187–198 (2013).
465. Mathur, R. *et al.* A reduced astrocyte response to  $\beta$ -amyloid plaques in the ageing brain associates with cognitive impairment. *PLoS One* **10**, e0118463 (2015).
466. Funato, H. *et al.* Astrocytes containing amyloid  $\beta$ -protein (A $\beta$ )-positive granules are associated with a $\beta$ 40-positive diffuse plaques in the aged human brain. *Am. J. Pathol.* **152**, 983–992 (1998).
467. Nagele, R. G., D’Andrea, M. R., Lee, H., Venkataraman, V. & Wang, H. Y. Astrocytes accumulate A $\beta$ 42 and give rise to astrocytic amyloid plaques in

- Alzheimer disease brains. *Brain Res.* **971**, 197–209 (2003).
468. Wyss-Coray, T. *et al.* Adult mouse astrocytes degrade amyloid- $\beta$  in vitro and in situ. *Nat. Med.* **9**, 453–457 (2003).
469. Kordower, J. H. *et al.* Disease duration and the integrity of the nigrostriatal system in Parkinson's disease. *Brain* **136**, 2419–2431 (2013).
470. Tong, J. *et al.* Low levels of astroglial markers in Parkinson's disease: Relationship to  $\alpha$ -synuclein accumulation. *Neurobiol. Dis.* **82**, 243–253 (2015).
471. Barbeito, L. H. *et al.* A role for astrocytes in motor neuron loss in amyotrophic lateral sclerosis. in *Brain Research Reviews* **47**, 263–274 (2004).
472. Sasabe, J. *et al.* D-Amino acid oxidase controls motoneuron degeneration through D-serine. *Proc. Natl. Acad. Sci. U. S. A.* **109**, 627–632 (2012).
473. Fritz, E. *et al.* Mutant SOD1-expressing astrocytes release toxic factors that trigger motoneuron death by inducing hyperexcitability. *J. Neurophysiol.* **109**, 2803–2814 (2013).
474. Bruijn, L. I. *et al.* ALS-linked SOD1 mutant G85R mediates damage to astrocytes and promotes rapidly progressive disease with SOD1-containing inclusions. *Neuron* **18**, 327–338 (1997).
475. Rossi, D. *et al.* Focal degeneration of astrocytes in amyotrophic lateral sclerosis. *Cell Death Differ.* **15**, 1691–1700 (2008).
476. Cassina, P. *et al.* Mitochondrial dysfunction in SOD1G93A-bearing astrocytes promotes motor neuron degeneration: Prevention by mitochondrial-targeted antioxidants. *J. Neurosci.* **28**, 4115–4122 (2008).

477. Aebischer, J. *et al.* IFN $\gamma$  triggers a LIGHT-dependent selective death of motoneurons contributing to the non-cell-autonomous effects of mutant SOD1. *Cell Death Differ.* **18**, 754–768 (2011).
478. Wang, R., Yang, B. & Zhang, D. Activation of interferon signaling pathways in spinal cord astrocytes from an ALS mouse model. *Glia* **59**, 946–958 (2011).
479. Gong, Y. H., Parsadanian, A. S., Andreeva, A., Snider, W. D. & Elliott, J. L. Restricted expression of G86R Cu/Zn superoxide dismutase in astrocytes results in astrocytosis but does not cause motoneuron degeneration. *J. Neurosci.* **20**, 660–665 (2000).
480. Lepore, A. C. *et al.* Selective ablation of proliferating astrocytes does not affect disease outcome in either acute or chronic models of motor neuron degeneration. *Exp. Neurol.* **211**, 423–432 (2008).
481. Perry, V. H., Nicoll, J. A. R. & Holmes, C. Microglia in neurodegenerative disease. *Nature Reviews Neurology* **6**, 193–201 (2010).
482. Walker, L. C. & Jucker, M. Neurodegenerative Diseases: Expanding the Prion Concept. *Annu. Rev. Neurosci.* **38**, 87–103 (2015).
483. Xiao, Q. *et al.* Mutant SOD1G93A microglia are more neurotoxic relative to wild-type microglia. *J. Neurochem.* **102**, 2008–2019 (2007).
484. Zhao, W. *et al.* Extracellular mutant SOD1 induces microglial-mediated motoneuron injury. *Glia* **58**, 231–243 (2010).
485. Zhao, W. *et al.* TDP-43 activates microglia through NF- $\kappa$ B and NLRP3 inflammasome. *Exp. Neurol.* **273**, 24–35 (2015).

486. D'Andrea, M. R., Cole, G. M. & Ard, M. D. The microglial phagocytic role with specific plaque types in the Alzheimer disease brain. *Neurobiol. Aging* **25**, 675–683 (2004).
487. Coraci, I. S. *et al.* CD36, a class B scavenger receptor, is expressed on microglia in Alzheimer's disease brains and can mediate production of reactive oxygen species in response to  $\beta$ -amyloid fibrils. *Am. J. Pathol.* **160**, 101–112 (2002).
488. Martin, E., Boucher, C., Fontaine, B. & Delarasse, C. Distinct inflammatory phenotypes of microglia and monocyte-derived macrophages in Alzheimer's disease models: effects of aging and amyloid pathology. *Aging Cell* **16**, 27–38 (2017).
489. Venegas, C. *et al.* Microglia-derived ASC specks crossseed amyloid- $\beta$  in Alzheimer's disease. *Nature* **552**, 355–361 (2017).
490. Meraz-Ríos, M. A., Toral-Rios, D., Franco-Bocanegra, D., Villeda-Hernández, J. & Campos-Peña, V. Inflammatory process in Alzheimer's Disease. *Front. Integr. Neurosci.* **7**, 59 (2013).
491. Song, M. *et al.* TLR4 mutation reduces microglial activation, increases A $\beta$  deposits and exacerbates cognitive deficits in a mouse model of Alzheimer's disease. *J. Neuroinflammation* **8**, 92 (2011).
492. Liu, S. *et al.* TLR2 Is a Primary Receptor for Alzheimer's Amyloid  $\beta$  Peptide To Trigger Neuroinflammatory Activation. *J. Immunol.* **188**, 1098–1107 (2012).
493. Heneka, M. T. *et al.* NLRP3 is activated in Alzheimer's disease and contributes to pathology in APP/PS1 mice. *Nature* **493**, 674–678 (2013).
494. Xu, C. *et al.* Targeting of NLRP3 inflammasome with gene editing for the

- amelioration of inflammatory diseases. *Nat. Commun.* **9**, 4092 (2018).
495. Halliday, G. M. & Stevens, C. H. Glia: Initiators and progressors of pathology in Parkinson's disease. *Movement Disorders* **26**, 6–17 (2011).
496. Su, X. *et al.* Synuclein activates microglia in a model of Parkinson's disease. *Neurobiol. Aging* **29**, 1690–1701 (2008).
497. Kim, C. *et al.* Neuron-released oligomeric  $\alpha$ -synuclein is an endogenous agonist of TLR2 for paracrine activation of microglia. *Nat. Commun.* **4**, 1562 (2013).
498. Meissner, F., Molawi, K. & Zychlinsky, A. Mutant superoxide dismutase 1-induced IL-1 $\beta$  accelerates ALS pathogenesis. *Proc. Natl. Acad. Sci. U. S. A.* **107**, 13046–13050 (2010).
499. Frakes, A. E. *et al.* Microglia induce motor neuron death via the classical NF- $\kappa$ B pathway in amyotrophic lateral sclerosis. *Neuron* **81**, 1009–1023 (2014).
500. Lee, J. Y., Lee, J. D., Phipps, S., Noakes, P. G. & Woodruff, T. M. Absence of toll-like receptor 4 (TLR4) extends survival in the hSOD1G93A mouse model of amyotrophic lateral sclerosis. *J. Neuroinflammation* **12**, 90 (2015).
501. Kawasaki, T. & Kawai, T. Toll-like receptor signaling pathways. *Front. Immunol.* **5**, 461 (2014).
502. Komine, O. *et al.* Innate immune adaptor TRIF deficiency accelerates disease progression of ALS mice with accumulation of aberrantly activated astrocytes. *Cell Death Differ.* **25**, 2130–2146 (2018).
503. Kang, J. & Rivest, S. MyD88-deficient bone marrow cells accelerate onset and reduce survival in a mouse model of amyotrophic lateral sclerosis. *J. Cell Biol.* **179**,

- 1219–1230 (2007).
504. Shih, R. H., Wang, C. Y. & Yang, C. M. NF-kappaB signaling pathways in neurological inflammation: A mini review. *Front. Mol. Neurosci.* **8**, 77 (2015).
505. Gravel, M. *et al.* Il-10 controls early microglial phenotypes and disease onset in ALS caused by misfolded superoxide dismutase 1. *J. Neurosci.* **36**, 1031–1048 (2016).
506. Qian, K. *et al.* Sporadic ALS Astrocytes Induce Neuronal Degeneration In Vivo. *Stem Cell Reports* **8**, 843–855 (2017).
507. Di Giorgio, F. P., Carrasco, M. A., Siao, M. C., Maniatis, T. & Eggan, K. Non-cell autonomous effect of glia on motor neurons in an embryonic stem cell-based ALS model. *Nat. Neurosci.* **10**, 608–614 (2007).
508. Nagai, M. *et al.* Astrocytes expressing ALS-linked mutated SOD1 release factors selectively toxic to motor neurons. *Nat. Neurosci.* **10**, 615–622 (2007).
509. Marchetto, M. C. N. *et al.* Non-Cell-Autonomous Effect of Human SOD1G37R Astrocytes on Motor Neurons Derived from Human Embryonic Stem Cells. *Cell Stem Cell* **3**, 649–657 (2008).
510. Frakes, A. E., Braun, L., Ferraiuolo, L., Guttridge, D. C. & Kaspar, B. K. Additive amelioration of ALS by co-targeting independent pathogenic mechanisms. *Ann. Clin. Transl. Neurol.* **4**, 76–86 (2017).
511. Oskarsson, B., Horton, D. K. & Mitsumoto, H. Potential Environmental Factors in Amyotrophic Lateral Sclerosis. *Neurologic Clinics* **33**, 877–888 (2015).
512. Bozzoni, V. *et al.* Amyotrophic lateral sclerosis and environmental factors. *Functional Neurology* **31**, 7–19 (2016).

513. Zinman, L. *et al.* A mechanism for low penetrance in an ALS family with a novel SOD1 deletion. *Neurology* **72**, 1153–1159 (2009).
514. Al-Chalabi, A. & Lewis, C. M. Modelling the effects of penetrance and family size on rates of sporadic and familial disease. *Hum. Hered.* **71**, 281–288 (2011).
515. Chen, S., Sayana, P., Zhang, X. & Le, W. Genetics of amyotrophic lateral sclerosis: An update. *Mol. Neurodegener.* **8**, 28 (2013).
516. Murphy, N. A. *et al.* Age-related penetrance of the C9orf72 repeat expansion. *Sci. Rep.* **7**, 2116 (2017).
517. Xue, Y. C., Feuer, R., Cashman, N. & Luo, H. Enteroviral Infection: The Forgotten Link to Amyotrophic Lateral Sclerosis? *Front. Mol. Neurosci.* **11**, 63 (2018).
518. Celeste, D. B. & Miller, M. S. Reviewing the evidence for viruses as environmental risk factors for ALS: A new perspective. *Cytokine* **108**, 173–178 (2018).
519. Andrade, F. C., Vergetti, V., Cozza, G., Falcao, M. C. & Azevedo, G. Amyotrophic Lateral Sclerosis-like Syndrome after Chikungunya. *Cureus* **11**, e5876 (2019).
520. van Duijl-Richter, M. K. S., Hoornweg, T. E., Rodenhuis-Zybert, I. A. & Smit, J. M. Early events in chikungunya virus infection—from virus cell binding to membrane fusion. *Viruses* **7**, 3647–3674 (2015).
521. Martyn, C. N. & Osmond, C. The environment in childhood and risk of motor neuron disease. *J. Neurol. Neurosurg. Psychiatry* **55**, 997–1001 (1992).
522. Okumura, H., Kurland, L. T. & Waring, S. C. Amyotrophic Lateral Sclerosis and Polio: Is There an Association? *Ann. N. Y. Acad. Sci.* **753**, 245–256 (1995).
523. Shing, S. L. H. *et al.* Post-polio Syndrome: More than just a lower motor neuron

- disease. *Front. Neurol.* **10**, 773 (2019).
524. Sun, D., Chen, S., Cheng, A. & Wang, M. Roles of the picornaviral 3c proteinase in the viral life cycle and host cells. *Viruses* **8**, 82 (2016).
525. Fung, G. *et al.* Cytoplasmic translocation, aggregation, and cleavage of TDP-43 by enteroviral proteases modulate viral pathogenesis. *Cell Death Differ.* **22**, 2087–2097 (2015).
526. Li, W. *et al.* Human endogenous retrovirus-K contributes to motor neuron disease. *Sci. Transl. Med.* **7**, 307ra153 (2015).
527. Mayer, J. *et al.* Transcriptional profiling of HERV-K(HML-2) in amyotrophic lateral sclerosis and potential implications for expression of HML-2 proteins. *Mol. Neurodegener.* **13**, 39 (2018).
528. Garson, J. A. *et al.* Quantitative analysis of human endogenous retrovirus-K transcripts in postmortem premotor cortex fails to confirm elevated expression of HERV-K RNA in amyotrophic lateral sclerosis. *Acta Neuropathol. Commun.* **7**, 45 (2019).
529. Harris, S. A. & Harris, E. A. Molecular mechanisms for herpes simplex virus type 1 pathogenesis in Alzheimer's disease. *Front. Aging Neurosci.* **10**, 48 (2018).
530. Caggiu, E. *et al.* Inflammation, Infectious Triggers, and Parkinson's Disease. *Front. Neurol.* **10**, 122 (2019).
531. Letenneur, L. *et al.* Seropositivity to Herpes Simplex Virus antibodies and risk of Alzheimer's disease: A population-based cohort study. *PLoS One* **3**, e3637 (2008).
532. Itzhaki, R. F. *et al.* Herpes simplex virus type 1 in brain and risk of Alzheimer's

- disease. *Lancet* **349**, 241–244 (1997).
533. Wozniak, M., Mee, A. P. & Itzhaki, R. F. Herpes simplex virus type 1 DNA is located within Alzheimer's disease amyloid plaques. *J. Pathol.* **217**, 131–138 (2009).
534. Steel, A. J. & Eslick, G. D. Herpes viruses increase the risk of Alzheimer's disease: A meta-analysis. *J. Alzheimer's Dis.* **47**, 351–364 (2015).
535. Eimer, W. A. *et al.* Alzheimer's Disease-Associated  $\beta$ -Amyloid Is Rapidly Seeded by Herpesviridae to Protect against Brain Infection. *Neuron* **99**, 56-63.e3 (2018).
536. Brown, J. C. Herpes simplex virus latency: The DNA repair-Centered pathway. *Advances in Virology* **2017**, 7028194 (2017).
537. Theil, D. *et al.* Latent Herpesvirus Infection in Human Trigeminal Ganglia Causes Chronic Immune Response. *Am. J. Pathol.* **163**, 2179–2184 (2003).
538. Bouvier, N. M. & Palese, P. The biology of influenza viruses. *Vaccine* **26**, D49–D53 (2008).
539. Ravenholt, R. T. & Foegen, W. H. 1918 influenza, encephalitis lethargica, parkinsonism. *Lancet (London, England)* **2**, 860–864 (1982).
540. Hosseini, S. *et al.* Long-term neuroinflammation induced by influenza a virus infection and the impact on hippocampal neuron morphology and function. *J. Neurosci.* **38**, 3060–3080 (2018).
541. Blackmore, S. *et al.* Influenza infection triggers disease in a genetic model of experimental autoimmune encephalomyelitis. *Proc. Natl. Acad. Sci. U. S. A.* **114**, E6107–E6116 (2017).

542. Reed, D. M., Torres, J. M. & Brody, J. A. Amyotrophic Lateral Sclerosis and Parkinsonism-Dementia on Guam, 1945–1972. *Am. J. Epidemiol.* **101**, 302–310 (1975).
543. Galasko, D. *et al.* Clinical features and changing patterns of neurodegenerative disorders on Guam, 1997–2000. *Neurology* **58**, 90–97 (2002).
544. Masseret, E. *et al.* Dietary BMAA exposure in an amyotrophic lateral sclerosis cluster from southern France. *PLoS One* **8**, e83406 (2013).
545. Caller, T. A. *et al.* A cluster of amyotrophic lateral sclerosis in New Hampshire: A possible role for toxic cyanobacteria blooms. in *Amyotrophic Lateral Sclerosis* **10**, 101–108 (2009).
546. Yin, H. Z. *et al.* Intrathecal infusion of BMAA induces selective motor neuron damage and astrogliosis in the ventral horn of the spinal cord. *Exp. Neurol.* **261**, 1–9 (2014).
547. Logsdon, A. F., Erickson, M. A., Rhea, E. M., Salameh, T. S. & Banks, W. A. Gut reactions: How the blood–brain barrier connects the microbiome and the brain. *Exp. Biol. Med.* **243**, 159–165 (2018).
548. Miraglia, F. & Colla, E. Microbiome, Parkinson’s Disease and Molecular Mimicry. *Cells* **8**, 222 (2019).
549. Blacher, E. *et al.* Potential roles of gut microbiome and metabolites in modulating ALS in mice. *Nature* **572**, 474–480 (2019).
550. Kleinnijenhuis, J. *et al.* Bacille Calmette-Guérin induces NOD2-dependent nonspecific protection from reinfection via epigenetic reprogramming of monocytes.

- Proc. Natl. Acad. Sci. U. S. A.* **109**, 17537–17542 (2012).
551. Netea, M. G. *et al.* Trained immunity: A program of innate immune memory in health and disease. *Science*. **352**, aaf1098 (2016).
552. Bellmann, J. *et al.* Viral Infections Exacerbate FUS-ALS Phenotypes in iPSC-Derived Spinal Neurons in a Virus Species-Specific Manner. *Front. Cell. Neurosci.* **13**, 480 (2019).
553. Sama, R. R. K. *et al.* FUS/TLS assembles into stress granules and is a prosurvival factor during hyperosmolar stress. *J. Cell. Physiol.* **228**, 2222–2231 (2013).
554. Braak, H. *et al.* Amyotrophic lateral sclerosis - A model of corticofugal axonal spread. *Nature Reviews Neurology* **9**, 708–714 (2013).
555. Rabies | CDC. Available at: <https://www.cdc.gov/rabies/index.html>. (Accessed: 1st December 2019)
556. U.S. Statistics | HIV.gov. Available at: <https://www.hiv.gov/hiv-basics/overview/data-and-trends/statistics>. (Accessed: 1st December 2019)
557. 2018 Case Counts in the US | Zika Virus | CDC. Available at: <https://www.cdc.gov/zika/reporting/2018-case-counts.html>. (Accessed: 1st December 2019)
558. Mehta, P. *et al.* Prevalence of Amyotrophic Lateral Sclerosis — United States, 2014. *MMWR. Morb. Mortal. Wkly. Rep.* **67**, 216–218 (2018).
559. Anderson, M. R., Kashanchi, F. & Jacobson, S. Exosomes in Viral Disease. *Neurotherapeutics* **13**, 535–546 (2016).
560. Hutchinson, E. C. *et al.* Conserved and host-specific features of influenza virion

- architecture. *Nat. Commun.* **5**, 4816 (2014).
561. Pardo, C. A. *et al.* Superoxide dismutase is an abundant component in cell bodies, dendrites, and axons of motor neurons and in a subset of other neurons. *Proc. Natl. Acad. Sci. U. S. A.* **92**, 954–958 (1995).
562. Alenquer, M. & Amorim, M. J. Exosome biogenesis, regulation, and function in viral infection. *Viruses* **7**, 5066–5083 (2015).
563. Turner, B. J. & Talbot, K. Transgenics, toxicity and therapeutics in rodent models of mutant SOD1-mediated familial ALS. *Progress in Neurobiology* **85**, 94–134 (2008).
564. Yamanaka, K. & Komine, O. The multi-dimensional roles of astrocytes in ALS. *Neuroscience Research* **126**, 31–38 (2018).
565. Ahmed, Z. *et al.* Actin-binding proteins coronin-1a and IBA-1 are effective microglial markers for immunohistochemistry. *J. Histochem. Cytochem.* **55**, 687–700 (2007).
566. Boillée, S. *et al.* Onset and progression in inherited ALS determined by motor neurons and microglia. *Science.* **312**, 1389–1392 (2006).
567. Yamanaka, K. *et al.* Mutant SOD1 in cell types other than motor neurons and oligodendrocytes accelerates onset of disease in ALS mice. *Proc. Natl. Acad. Sci. U. S. A.* **105**, 7594–7599 (2008).
568. Yamanaka, K. *et al.* Astrocytes as determinants of disease progression in inherited amyotrophic lateral sclerosis. *Nat. Neurosci.* **11**, 251–253 (2008).
569. Marttila, R. J., Rinne, U. K. & Tiilikainen, A. Virus antibodies in Parkinson's

- disease. Herpes simplex and measles virus antibodies in serum and CSF and their relation to HLA types. *J. Neurol. Sci.* **54**, 227–238 (1982).
570. De Chiara, G. *et al.* Recurrent herpes simplex virus-1 infection induces hallmarks of neurodegeneration and cognitive deficits in mice. *PLOS Pathog.* **15**, e1007617 (2019).
571. Clark, J. A., Southam, K. A., Blizzard, C. A., King, A. E. & Dickson, T. C. Axonal degeneration, distal collateral branching and neuromuscular junction architecture alterations occur prior to symptom onset in the SOD1G93A mouse model of amyotrophic lateral sclerosis. *J. Chem. Neuroanat.* **76**, 35–47 (2016).
572. Karam, C. Y., Paganoni, S., Joyce, N., Carter, G. T. & Bedlack, R. Palliative Care Issues in Amyotrophic Lateral Sclerosis: An Evidenced-Based Review. *American Journal of Hospice and Palliative Medicine* **33**, 84–92 (2016).
573. Glass, C. K., Saijo, K., Winner, B., Marchetto, M. C. & Gage, F. H. Mechanisms Underlying Inflammation in Neurodegeneration. *Cell* **140**, 918–934 (2010).
574. Yang, W. W. *et al.* Relationship between neuropathology and disease progression in the SOD1G93A ALS mouse. *Exp. Neurol.* **227**, 287–295 (2011).
575. Sanagi, T. *et al.* Appearance of phagocytic microglia adjacent to motoneurons in spinal cord tissue from a presymptomatic transgenic rat model of amyotrophic lateral sclerosis. *J. Neurosci. Res.* **88**, 2736–2746 (2010).
576. Jara, J. H. *et al.* Evidence for an early innate immune response in the motor cortex of ALS. *J. Neuroinflammation* **14**, 129 (2017).
577. Noh, M. Y., Cho, K. A., Kim, H., Kim, S. M. & Kim, S. H. Erythropoietin modulates

- the immune-inflammatory response of a SOD1G93A transgenic mouse model of amyotrophic lateral sclerosis (ALS). *Neurosci. Lett.* **574**, 53–58 (2014).
578. Jeyachandran, A., Mertens, B., McKissick, E. A. & Mitchell, C. S. Type I vs. Type II cytokine levels as a function of SOD1 G93A mouse amyotrophic lateral sclerosis disease progression. *Front. Cell. Neurosci.* **9**, 462 (2015).
579. Apolloni, S. *et al.* Histamine regulates the inflammatory profile of SOD1-G93A microglia and the histaminergic system is dysregulated in amyotrophic lateral sclerosis. *Front. Immunol.* **8**, 1689 (2017).
580. Lu, C.-H. *et al.* Systemic inflammatory response and neuromuscular involvement in amyotrophic lateral sclerosis. *Neurol. - Neuroimmunol. Neuroinflammation* **3**, e244 (2016).
581. Leichsenring, A., Linnartz, B., Zhu, X. R., Lübbert, H. & Stichel, C. C. Ascending neuropathology in the CNS of a mutant SOD1 mouse model of amyotrophic lateral sclerosis. *Brain Res.* **1096**, 180–195 (2006).
582. Jang, H. *et al.* Highly pathogenic H5N1 influenza virus can enter the central nervous system and induce neuroinflammation and neurodegeneration. *Proc. Natl. Acad. Sci. U. S. A.* **106**, 14063–14068 (2009).
583. Jang, H. *et al.* Inflammatory effects of highly pathogenic H5N1 influenza virus infection in the CNS of mice. *J. Neurosci.* **32**, 1545–1559 (2012).
584. Jurgens, H. A., Amancherla, K. & Johnson, R. W. Influenza Infection Induces Neuroinflammation, Alters Hippocampal Neuron Morphology, and Impairs Cognition in Adult Mice. *J. Neurosci.* **32**, 3958–3968 (2012).

585. Sadasivan, S., Zanin, M., O'Brien, K., Schultz-Cherry, S. & Smeyne, R. J. Induction of microglia activation after infection with the non-neurotropic A/CA/04/2009 H1N1 influenza virus. *PLoS One* **10**, e0124047 (2015).
586. Hoogland, I. C. M., Houbolt, C., van Westerloo, D. J., van Gool, W. A. & van de Beek, D. Systemic inflammation and microglial activation: Systematic review of animal experiments. *Journal of Neuroinflammation* **12**, 114 (2015).
587. Sargsyan, S. A., Blackburn, D. J., Barber, S. C., Monk, P. N. & Shaw, P. J. Mutant SOD1 G93A microglia have an inflammatory phenotype and elevated production of MCP-1. *Neuroreport* **20**, 1450–1455 (2009).
588. Gordon, P. H. *et al.* Efficacy of minocycline in patients with amyotrophic lateral sclerosis: a phase III randomised trial. *Lancet Neurol.* **6**, 1045–1053 (2007).
589. Gilgun-Sherki, Y., Melamed, E. & Offen, D. Anti-Inflammatory Drugs in the Treatment of Neurodegenerative Diseases: Current State. *Curr. Pharm. Des.* **12**, 3509–3519 (2006).
590. Perry, V. H. & Holmes, C. Microglial priming in neurodegenerative disease. *Nature Reviews Neurology* **10**, 217–224 (2014).
591. Gill, C. *et al.* SOD1-positive aggregate accumulation in the CNS predicts slower disease progression and increased longevity in a mutant SOD1 mouse model of ALS. *Sci. Rep.* **9**, 6724 (2019).
592. Li, J.-W., Zong, Y., Cao, X.-P., Tan, L. & Tan, L. Microglial priming in Alzheimer's disease. *Ann. Transl. Med.* **6**, 176–176 (2018).
593. Roberts, K. *et al.* Extracellular aggregated Cu/Zn superoxide dismutase activates

- microglia to give a cytotoxic phenotype. *Glia* **61**, 409–419 (2013).
594. Wu, Z. *et al.* Differential pathways for interleukin-1 $\beta$  production activated by chromogranin A and amyloid  $\beta$  in microglia. *Neurobiol. Aging* **34**, 2715–2725 (2013).
595. Rojanathammanee, L., Floden, A. M., Manocha, G. D. & Combs, C. K. Attenuation of microglial activation in a mouse model of Alzheimer’s disease via NFAT inhibition. *J. Neuroinflammation* **12**, 42 (2015).
596. Cunningham, C., Wilcockson, D. C., Champion, S., Lunnon, K. & Perry, V. H. Central and systemic endotoxin challenges exacerbate the local inflammatory response and increase neuronal death during chronic neurodegeneration. *J. Neurosci.* **25**, 9275–9284 (2005).
597. Püntener, U., Booth, S. G., Perry, V. H. & Teeling, J. L. Long-term impact of systemic bacterial infection on the cerebral vasculature and microglia. *J. Neuroinflammation* **9**, 668 (2012).
598. Pei, Z. *et al.* MAC1 mediates LPS-induced production of superoxide by microglia: The role of pattern recognition receptors in dopaminergic neurotoxicity. *Glia* **55**, 1362–1373 (2007).
599. Hoogland, I. C. M. *et al.* Microglial activation after systemic stimulation with lipopolysaccharide and *Escherichia coli*. *Front. Cell. Neurosci.* **12**, 110 (2018).
600. Koss, K., Churchward, M. A., Tsui, C. & Todd, K. G. In Vitro Priming and Hyper-Activation of Brain Microglia: an Assessment of Phenotypes. *Mol. Neurobiol.* **56**, 6409–6425 (2019).

601. Van Egmond, M. *et al.* IgA and the IgA Fc receptor. *Trends in Immunology* **22**, 205–211 (2001).
602. Eickmeier, O. *et al.* Altered mucosal immune response after acute lung injury in a murine model of Ataxia Telangiectasia. *BMC Pulm. Med.* **14**, 93 (2014).
603. Cunningham-Rundles, C. Physiology of IgA and IgA deficiency. *J. Clin. Immunol.* **21**, 303–309 (2001).
604. Pasquier, B. *et al.* Identification of Fc $\alpha$ RI as an inhibitory receptor that controls inflammation: Dual role of FcR $\gamma$  ITAM. *Immunity* **22**, 31–42 (2005).
605. Mantis, N. J., Rol, N. & Corthésy, B. Secretory IgA's complex roles in immunity and mucosal homeostasis in the gut. *Mucosal Immunology* **4**, 603–611 (2011).
606. Yamamoto, M. L. *et al.* Intestinal bacteria modify lymphoma incidence and latency by affecting systemic inflammatory state, oxidative stress, and leukocyte genotoxicity. *Cancer Res.* **73**, 4222–4232 (2013).
607. Hakansson, A. & Molin, G. Gut microbiota and inflammation. *Nutrients* **3**, 637–687 (2011).
608. Obrenovich, M. Leaky Gut, Leaky Brain? *Microorganisms* **6**, 107 (2018).
609. Coppedè, F. & Migliore, L. DNA damage in neurodegenerative diseases. *Mutation Research - Fundamental and Molecular Mechanisms of Mutagenesis* **776**, 84–97 (2015).
610. Yu, H., Harrison, F. E. & Xia, F. Altered DNA repair; An early pathogenic pathway in Alzheimer's disease and obesity. *Sci. Rep.* **8**, 5600 (2018).
611. Shanbhag, N. M. *et al.* Early neuronal accumulation of DNA double strand breaks

- in Alzheimer's disease. *Acta Neuropathol. Commun.* **7**, 77 (2019).
612. Herrup, K., Li, J. & Chen, J. The role of ATM and DNA damage in neurons: Upstream and downstream connections. *DNA Repair (Amst)*. **12**, 600–604 (2013).
613. Pao, G. M. *et al.* Role of BRCA1 in brain development. *Proc. Natl. Acad. Sci. U. S. A.* **111**, E1240–E1248 (2014).
614. Suberbielle, E. *et al.* DNA repair factor BRCA1 depletion occurs in Alzheimer brains and impairs cognitive function in mice. *Nat. Commun.* **6**, 8897 (2015).
615. Davydov, V., Hansen, L. A. & Shackelford, D. A. Is DNA repair compromised in Alzheimer's disease? *Neurobiol. Aging* **24**, 953–968 (2003).
616. Shackelford, D. A. DNA end joining activity is reduced in Alzheimer's disease. *Neurobiol. Aging* **27**, 596–605 (2006).
617. Milanese, C. *et al.* Activation of the DNA damage response in vivo in synucleinopathy models of Parkinson's disease. *Cell Death Dis.* **9**, 818 (2018).
618. Singatulina, A. S. *et al.* PARP-1 Activation Directs FUS to DNA Damage Sites to Form PARG-Reversible Compartments Enriched in Damaged DNA. *Cell Rep.* **27**, 1809–1821 (2019).
619. Deng, Q. *et al.* FUS is phosphorylated by DNA-PK and accumulates in the cytoplasm after DNA damage. *J. Neurosci.* **34**, 7802–7813 (2014).
620. Guerrero, E. N. *et al.* Amyotrophic lateral sclerosis-associated TDP-43 mutation Q331K prevents nuclear translocation of XRCC4-DNA ligase 4 complex and is linked to genome damage-mediated neuronal apoptosis. *Hum. Mol. Genet.* **28**, 2459–2476 (2019).

621. Mitra, J. *et al.* Motor neuron disease-associated loss of nuclear TDP-43 is linked to DNA double-strand break repair defects. *Proc. Natl. Acad. Sci. U. S. A.* **116**, 4696–4705 (2019).
622. Ramirez, K., Fornaguera-Trias, J. & Sheridan, J. F. Stress-induced microglia activation and monocyte trafficking to the brain underlie the development of anxiety and depression. in *Current Topics in Behavioral Neurosciences* **31**, 155–172 (Springer Verlag, 2017).
623. Holtman, I. R. *et al.* Induction of a common microglia gene expression signature by aging and neurodegenerative conditions: a co-expression meta-analysis. *Acta Neuropathol. Commun.* **3**, 31 (2015).
624. Xia, X., Jiang, Q., McDermott, J. & Han, J. D. J. Aging and Alzheimer’s disease: Comparison and associations from molecular to system level. *Aging Cell* **17**, e12802 (2018).
625. Hart, A. D., Wytenbach, A., Hugh Perry, V. & Teeling, J. L. Age related changes in microglial phenotype vary between CNS regions: Grey versus white matter differences. *Brain. Behav. Immun.* **26**, 754–765 (2012).
626. Hopperton, K. E., Mohammad, D., Trépanier, M. O., Giuliano, V. & Bazinet, R. P. Markers of microglia in post-mortem brain samples from patients with Alzheimer’s disease: A systematic review. *Molecular Psychiatry* **23**, 177–198 (2018).
627. Letiembre, M. *et al.* Innate immune receptor expression in normal brain aging. *Neuroscience* **146**, 248–254 (2007).
628. Lin, H. *et al.* Discovery of a cytokine and its receptor by functional screening of the

- extracellular proteome. *Science*. **320**, 807–811 (2008).
629. Hinojosa, A. E., Garcia-Bueno, B., Leza, J. C. & Madrigal, J. L. M. CCL2/MCP-1 modulation of microglial activation and proliferation. *J. Neuroinflammation* **8**, 77 (2011).
630. Zhang, J. & De Koninck, Y. Spatial and temporal relationship between monocyte chemoattractant protein-1 expression and spinal glial activation following peripheral nerve injury. *J. Neurochem.* **97**, 772–783 (2006).
631. Zhang, F. & Jiang, L. Neuroinflammation in Alzheimer’s disease. *Neuropsychiatric Disease and Treatment* **11**, 243–256 (2014).
632. Ramos-Cejudo, J. *et al.* Traumatic Brain Injury and Alzheimer’s Disease: The Cerebrovascular Link. *EBioMedicine* **28**, 21–30 (2018).
633. Koenigsnecht, J. & Landreth, G. Microglial phagocytosis of fibrillar  $\beta$ -amyloid through a  $\beta$ 1 integrin-dependent mechanism. *J. Neurosci.* **24**, 9838–9846 (2004).
634. Simard, A. R., Soulet, D., Gowing, G., Julien, J. P. & Rivest, S. Bone marrow-derived microglia play a critical role in restricting senile plaque formation in Alzheimer’s disease. *Neuron* **49**, 489–502 (2006).
635. Pan, X. D. *et al.* Microglial phagocytosis induced by fibrillar  $\beta$ -amyloid is attenuated by oligomeric  $\beta$ -amyloid: Implications for Alzheimer’s disease. *Mol. Neurodegener.* **6**, 45 (2011).
636. Keren-Shaul, H. *et al.* A Unique Microglia Type Associated with Restricting Development of Alzheimer’s Disease. *Cell* **169**, 1276-1290.e17 (2017).
637. Lai, A. Y. & McLaurin, J. Clearance of amyloid- $\beta$  peptides by microglia and

- macrophages: The issue of what, when and where. *Future Neurology* **7**, 165–176 (2012).
638. Wendeln, A.-C. *et al.* Innate immune memory in the brain shapes neurological disease hallmarks. *Nature* **556**, 332–338 (2018).
639. Wang, Y. & Mandelkow, E. Tau in physiology and pathology. *Nature Reviews Neuroscience* **17**, 5–21 (2016).
640. Gao, Y.-L. *et al.* Tau in neurodegenerative disease. *Ann. Transl. Med.* **6**, 175 (2018).
641. Morales, I., Jiménez, J. M., Mancilla, M. & Maccioni, R. B. Tau oligomers and fibrils induce activation of microglial cells. *J. Alzheimer's Dis.* **37**, 849–856 (2013).
642. Yoshiyama, Y. *et al.* Synapse Loss and Microglial Activation Precede Tangles in a P301S Tauopathy Mouse Model. *Neuron* **53**, 337–351 (2007).
643. Zhao, J. *et al.* Neuroinflammation induced by lipopolysaccharide causes cognitive impairment in mice. *Sci. Rep.* **9**, 5790 (2019).
644. Elmore, S. Apoptosis: A Review of Programmed Cell Death. *Toxicologic Pathology* **35**, 495–516 (2007).
645. Dhuriya, Y. K. & Sharma, D. Necroptosis: A regulated inflammatory mode of cell death. *Journal of Neuroinflammation* **15**, 199 (2018).
646. Vercammen, D. *et al.* Inhibition of caspases increases the sensitivity of L929 cells to necrosis mediated by tumor necrosis factor. *J. Exp. Med.* **187**, 1477–1485 (1998).
647. Xiaoqing, S. *et al.* RIP3, a novel apoptosis-inducing kinase. *J. Biol. Chem.* **274**, 16871–16875 (1999).
648. Cho, Y. S. *et al.* Phosphorylation-Driven Assembly of the RIP1-RIP3 Complex

- Regulates Programmed Necrosis and Virus-Induced Inflammation. *Cell* **137**, 1112–1123 (2009).
649. Moriwaki, K. & Chan, F. K. M. Necroptosis-independent signaling by the RIP kinases in inflammation. *Cellular and Molecular Life Sciences* **73**, 2325–2334 (2016).
650. Gould, T. W. *et al.* Complete dissociation of motor neuron death from motor dysfunction by Bax deletion in a mouse model of ALS. *J. Neurosci.* **26**, 8774–8786 (2006).
651. Re, D. B. *et al.* Necroptosis drives motor neuron death in models of both sporadic and familial ALS. *Neuron* **81**, 1001–1008 (2014).
652. Ito, Y. *et al.* RIPK1 mediates axonal degeneration by promoting inflammation and necroptosis in ALS. *Science*. **353**, 603–608 (2016).
653. He, S. *et al.* Receptor Interacting Protein Kinase-3 Determines Cellular Necrotic Response to TNF- $\alpha$ . *Cell* **137**, 1100–1111 (2009).
654. Wang, Y. *et al.* Influenza Virus Infection Induces ZBP1 Expression and Necroptosis in Mouse Lungs. *Front. Cell. Infect. Microbiol.* **9**, 286 (2019).
655. Wang, T. *et al.* Necroptosis is dispensable for motor neuron degeneration in a mouse model of ALS. *Cell Death Differ.* (2019). doi:10.1038/s41418-019-0457-8
656. Dermentzaki, G. *et al.* Deletion of Ripk3 prevents motor neuron death In Vitro but not In Vivo. *eNeuro* **6**, ENEURO.0308-18.2018 (2019).
657. Beers, D. R. *et al.* Endogenous regulatory T lymphocytes ameliorate amyotrophic lateral sclerosis in mice and correlate with disease progression in patients with

- amyotrophic lateral sclerosis. *Brain* **134**, 1293–1314 (2011).
658. Thonhoff, J. R. *et al.* Expanded autologous regulatory T-lymphocyte infusions in ALS A phase I, first-in-human study. *Neurol. Neuroimmunol. NeuroInflammation* **5**, e465 (2018).
659. Askonas, B. A., Taylor, P. M. & Esquivel, F. Cytotoxic T Cells in Influenza Infection. *Ann. N. Y. Acad. Sci.* **532**, 230–237 (1988).
660. Bender, B. S., Croghan, T., Zhang, L. & Small, P. A. Transgenic mice lacking class I major histocompatibility complex-restricted T cells have delayed viral clearance and increased mortality after influenza virus challenge. *J. Exp. Med.* **175**, 1143–1145 (1992).
661. Topham, D. J. & Doherty, P. C. Clearance of an influenza A virus by CD4<sup>+</sup> T cells is inefficient in the absence of B cells. *J. Virol.* **72**, 882–885 (1998).